DOT/FAA/AR-05/16

Contaminated Billet Study

Office of Aviation Research
Washington, D.C. 20591

September 2005

Final Report

This document is available to the U.S. public through the National Technical Information Service (NTIS), Springfield, VA 22161.



U.S. Department of Transportation
Federal Aviation Administration

AUTHENTICATED
U.S. GOVERNMENT
INFORMATION
GPO

NOTICE

This document is disseminated under the sponsorship of the U.S. Department of Transportation in the interest of information exchange. The United States Government assumes no liability for the contents or use thereof. The United States Government does not endorse products or manufacturers. Trade or manufacturers names appear herein solely because they are considered essential to the objective of this report. This document does not constitute FAA certification policy. Consult your local FAA aircraft certification office as to its use.

This report is available at the Federal Aviation Administration William J. Hughes Technical Center's Full-Text Technical Reports page: actlibrary.tc.faa.gov in Adobe Acrobat portable document format (PDF).

Technical Report Documentation Page

1. Report No.	2. Government Accession No.	3. Recipient's Catalog No.
DOT/FAA/AR-05/16		

4. Title and Subtitle	5. Report Date
CONTAMINATED BILLET STUDY	September 2005
	6. Performing Organization Code

7. Author(s)	8. Performing Organization Report No.
Lisa Brasche[1], Thomas Chiou[1], Bruce Thompson[1], Kevin Smith[2], Bill Meeker[1], Frank Margetan[1], Paul Panetta[1], Rick Chenail[2], Fredrick Galli[2], Jeff Umbach[2], Dave Raulerson[2], Andrei Degtyar[2], Jon Bartos[3,] Dave Copley[3], Bob McElligott[3], Pat Howard[3],, and Manohar Bashyam[3]	

9. Performing Organization Name and Address	10. Work Unit No. (TRAIS)
Iowa State University[1] Center for Nondestructive Evaluation Ames, IA 50011 Pratt & Whitney[2] East Hartford, CT General Electric Aircraft Engines[3] Cincinnati, OH	
	11. Contract or Grant No. DTFA0398FIA029

12. Sponsoring Agency Name and Address	13. Type of Report and Period Covered
U.S. Department of Transportation Federal Aviation Administration Office of Aviation Research Washington, DC 20591	Final Report
	14. Sponsoring Agency Code ANE-110

15. Supplementary Notes

The FAA William J. Hughes Technical Center Technical Monitor was Cu Nguyen.

16. Abstract

During the Engine Titanium Consortium (ETC) Phase I program, the existence of a contaminated heat of titanium billet was made known to ETC and the Federal Aviation Administration. During processing of the billet, for a nonaerospace customer, a power outage led to a vacuum leak and resulted in numerous natural hard alpha defects. Because of the unique opportunity offered by the over 60 natural defects, an assessment was made that determined the defects were typical of those found in rotor grade material. The material was purchased for use in nondestructive evaluation and lifing studies. The 12 billets were inspected using multizone and conventional inspection with a subset of the heat inspected using a phased array method. Upon analysis of the inspection data, 10 of the 64 indications were selected for detailed metallographic characterization. The ten defects were serially sectioned at 5-mil increments, and the metallographic data was used to construct solid models for use in probability of detection studies. Several billets were also used in reproducibility and noise studies. Results of the inspection, defect characterization, and solid model generation are provided in this report along with use of the data in preliminary probability of detection calculations.

17. Key Words	18. Distribution Statement
Titanium billet, Hard alpha, Ultrasonic inspection, Probability of detection	This document is available to the public through the National Technical Information Service (NTIS), Springfield, Virginia 22161.

19. Security Classif. (of this report)	20. Security Classif. (of this page)	21. No. of Pages	22. Price
Unclassified	Unclassified	237	

TABLE OF CONTENTS

		Page
EXECUTIVE SUMMARY		xi
1.	INTRODUCTION	1
1.1	Purpose	1
1.2	Background	1
1.3	Program Objectives	3
1.4	Related Activities and Documents	4
2.	APPROACH	4
2.1	Initial Assessment of Heat	5
2.2	Inspection Summary	11
2.3	Description of Multizone Inspection	12
2.4	Defect Characterization	15
3.	DISCUSSION OF RESULTS	23
3.1	Inspection of the Contaminated Heat	23
3.2	Phased Array Inspection of the CBS Billets	31
3.3	Defect Characterization	36
3.4	Generation of Geometrical Data for Use in PoD Calculations	40
3.4.1	Geometrical Modeling	42
3.4.2	Ultrasonic Modeling	47
3.4.3	Error Analyses	49
3.5	Utilization of Data for PoD Analysis	53
3.6	Noise Analysis Studies	53
3.7	Reproducibility Studies Using the CBS Billets	63
3.7.1	Reproducibility Studies—Rolls-Royce	63
3.7.2	Reproducibility Studies—ETC	67
3.8	Misses Assessment	77
3.9	Disposition of CBS Materials	82
4.	CONCLUSIONS	90
5.	REFERENCES	91

APPENDICES

A—Literature Survey Completed by AlliedSignal in Phase I—Engine Titanium Consortium Program

B—Defect Characterization Protocol

C—Inspection Results for Contaminated Billet

D—Ultrasonic C-Scan Results for Indications Selected for Use in Probability of Detection Studies

E—Defect Characterization Data

F—Reconstruction of Hard Alpha Defects Using Metallographic Sectioning Data

G—Ultrasonic Modeling of Hard Alpha Defects

LIST OF FIGURES

Figure		Page
1	Manufacturing Cycle for Critical Rotating Components	2
2	Comparison of Typical Conversion Process Used to Produce Rotor-Grade Billets and the Conversion Process Used to Produce the CBS Billets	6
3	Photomacrograph Documents Removal of Indication From Billet Sample	6
4	Cylindrical Slug Taken From Billet B3W1 Was Cross-Sectioned Approximately 0.3″ Below the Plane of the Photomacrograph Shown in Figure 3	7
5	Electron Microprobe Backscattered Electron Image of Defect Taken From Billet B3W1	9
6	Microprobe Results in Medium Nitrogen	9
7	Electron Microprobe Shows Areas of Highest Nitrogen Content	10
8	Location of Billets Within the Ignot, Which Came From the Bottom Half of the Ingot	11
9	Spherically Focused Transducer, Offset 1/6 of Billet Radius to Produce 45º Longitudinal Wave	12
10	Multizone Concept That Uses Bicylindrical Transducers Designed to Focus Within 1″ Zones From Billet Surface to 1/2″ Beyond Center	12
11	Ultrasonic and Metallographic Analysis Steps Used to Characterize the Defects	15
12	Orientation of Sectioning Plane With Respect to Inspection Direction	16
13	Section Planes for Practice Defect	17
14	Microprobe Measurement Points for Practice Defect	18
15	Results for Nitrogen Scan Perpendicular (Transverse 1) to the Long Axis of the Defect With Zero Located at the Defect Core	20
16	Results for Nitrogen Scan Parallel to the Long Axis of the Defect With Zero Located at the End of the Defect Core	21
17	(a) Results for Oxygen Scan Perpendicular to the Long Axis (Transverse 1) of the Defect With Zero Located at the Defect Core and (b) Results for Oxygen Scan Parallel to the Long Axis of the Defect With Zero Located at the End of the Defect Core	22

18	Results for Ammonium Bifluoride and Kroll's Etchants	23
19	Venn Diagram Showing the Number of Indications Detected per Inspection Method	24
20	Example of Inspection Results for Billet B1AW1	26
21	Example of C-Scan Used in Selection of Defects for Further Characterization	27
22	Distribution of Amplitude Expressed as %FSH and SNR Results	29
23	Amplitude and SNR Results as a Function of Depth	30
24	Comparison of Single-Focus Transducer and Phased Array	31
25	Seven-Element Annular Array Developed for the CBS Evaluation	32
26	Setup Used in Billet Inspection	33
27	Comparison of Amplitude and SNR for Phased Array and Multizone Inspection of CBS Billets	36
28	Process Used for Ultrasonic Characterization of the Indications	37
29	Ultrasonic Characterization for B3W3 Indication B	38
30	Ultrasonic Characterization at Cube State Prior to Metallographic Sectioning of B3W3 Indication B	38
31	Selected Metallographic Sections for Sample B3W3-B	39
32	Microprobe Results for Section 5 (Approximately 20 mils) in Defect B3W3-B	39
33	Microprobe Results for Section 11 (Approximately 65 mils) in Defect B3W3-B	40
34	Peak Amplitudes of Inclusion and Void With and Without the Hard Alpha Shells for Different Inclusion Diameters	42
35	Polishes 8-13 of the Realigned and Reduced Cross-Section Images Used to Reconstruct Defect B1AW2-X	43
36	Stacking Orientation of the Metallographs of Hard Alpha Defect B1AW2-X	43
37	Example of More Complicated Void Connections	44
38	Raw vs NURB Void Boundary Trace Projection: Right Void of B1AW2-X	45
39	Three Angle Views of the Surface Model for Defect B1AW2-X	46

40	Actual Dimensions of Defect B1AW2-X	46
41	Example of Flaw Illumination By Ultrasonic Beam	47
42	Block Orientation for Experimental Ultrasonic Measurements	48
43	Comparison of Ultrasonic C-Scan Results, Model and Experiment	48
44	Decibel Amplitude Errors at 0- (peak), 40-, and 80-mils Scan Offset for All Six Sides of Defect B1AW2-X	50
45	Structural Plateaus in Defect B2W2-C's Geometric Model	50
46	Comparison Between Model and Experiment: dB Error of Peak Amplitude vs Log of Projected Flaw Area	51
47	Decibel Model Errors vs the Scan Offsets for Cases of Five Defects	52
48	Distribution of dB Model Errors of Peak Amplitudes in the Optimal Orientation	52
49	Summary of dB Model Errors of Peak Amplitudes in Optimal Orientation	53
50	C-Scan Image of 11″ Section of Billet B3W3	54
51	Sample Sectioning Plan for Noise Studies	55
52	Macrostructure Results for High- and Low-Noise Samples	56
53	Microstructure of High- and Low-Noise Samples	56
54	Velocity Results for High- and Low-Noise Samples	57
55	Attenuation and FOM Results for High- and Low-Noise Samples	58
56	Steps Required to Validate Theory of Noise Models	59
57	Electron Backscatter Kikuchi Diffraction Results for High-Noise Samples	60
58	Electron Backscatter Kikuchi Diffraction Results for Low-Noise Samples	61
59	Two-Point Correlation From High- and Low-Noise Regions of the Samples	62
60	Comparison of Predicted and Observed Values of Backscattering Coefficient	63
61	Amplitude Data for Various Transducers Used in the Rolls-Royce Study	67
62	Variability Analysis for Amplitude From Multizone Inspection	73
63	Variability Analysis for Amplitude From Conventional Inspection	73

64	Comparison of Multizone and Conventional Inspection Variability	74
65	Reproducibility Results for Indication B1BW1A-B From Field Studies	74
66	Factors Evaluated During Reproducibility Study	75
67	Main Effects Plot and Interactions Plot	76
68	Comparison of SNR for Laboratory Design of Equipment and Round-Robin Field Study	77
69	C-Scan of Indications D and C From Billet Segment B3W1BB Also Detected in Prior Inspections	79
70	C-Scan and Waveform Results for Indication B of Billet Segment B3W1BB	80
71	C-Scan and Waveform Results for New Indication Found in Billet Segment B1BW3CB	81
72	C-Scan and Waveform Results for New Indication Found in Billet Segment B1BW3CB Using 10-MHz Phased Array Inspection	82
73	C-Scan Results for Indication B1BW1-G Used in HIP-to-Heal Sample	89

LIST OF TABLES

Table		Page
1	Concentration Measurements for B3W1	8
2	Results of Point Microprobe Measurements for Practice Defect	19
3	Summary of Inspection Parameters for Each of the Inspection Methods	24
4	Tabulation of the Ten Indications Selected for Detailed Characterization and Reconstruction	28
5	Zoning Arrangement for Phased Array Inspection of CBS 6″ Diameter Billet	34
6	Signal to Noise and Amplitude Data From Phased Array Inspection	35
7	Billets Used in Rolls-Royce Reproducibility Study	64
8	Tabulation of Detections in Rolls-Royce Reproducibility Study	65
9	Transducers Used in Rolls-Royce Comparison Study	65
10	Amplitude Data From Transducer Comparison Study	66
11	Summary of Prior Ultrasonic Inspection Results for Billets Selected for Reproducibility Study	68
12	Test Matrix Used for Reproducibility Study	69
13	Summary of Conventional Indications Recorded as False Calls in Billet B1BW1A	70
14	Summary of Statistics of Multizone Reproducibility Study	70
15	Summary of Amplitude Statistics for Conventional Inspection	71
16	Summary of Signal Minus Noise Statistics for Conventional Inspection	71
17	Percent Efficiency of Multizone Inspection During Reproducibility Studies	72
18	Percent Efficiency of Conventional Inspection During Reproducibility Studies	72
19	Results of Full Factorial Experiment Performed in Laboratory Environment	76
20	Mults Used in the Misses Assessment	78
21	Listing of Samples Remaining From Original Billet Material	83
22	Inspection Amplitudes and SNR for Indication B1BW1-G Used in HIP-to-Heal Sample	89

LIST OF ACRONYMS

1D	One-dimensional
2D	Two-dimensional
3D	Three-dimensional
AANC	Airworthiness Assurance Nondestructive Inspection Validation Center
Al	Aluminum
C	Carbon
CA	Conventional angle
CBS	Contaminated Billet Study
CHM	Cold hearth melting
CL	Conventional longitudinal
ETC	Engine Titanium Consortium
FAA	Federal Aviation Administration
FATS	Focussed Array Transducer System
FBH	Flat-bottom hole
FOM	Figure of merit
FSH	Full-screen height
GE	General Electric Aircraft Engines
HIP	Hot isostatic press
ISU	Iowa State University
MZ	Multizone
N	Nitrogen
NURBS	Nonuniform rational b-splines
OD	Outside diameter
PC	Personal computer
PoD	Probability of detection
POP	Pulse-on-position
RAM	Random access memory
RF	Radio frequency
ROI	Region of interest
SNR	Signal-to-noise ratio
Ti	Titanium
TRMD	Turbine Rotor Materials Design
V	Vanadium
VAR	Vacuum arc remelting
WORM	Write-once-read-many

EXECUTIVE SUMMARY

During the Engine Titanium Consortium (ETC) Phase I program, the existence of a contaminated heat of titanium billet was made known to ETC and the Federal Aviation Administration. During processing of the billet for a nonaerospace customer, a power outage led to a vacuum leak and resulted in numerous natural hard alpha defects. Because of the unique opportunity offered by over 60 natural defects, an assessment was made that determined the defects were typical of those found in rotor grade material. The material was purchased for use in nondestructive evaluation and lifing studies. The 12 billets were inspected using multizone and conventional inspection with a subset of the heat inspected using a phased array method. Upon analysis of the inspection data, 10 of the 64 indications were selected for detailed metallographic characterization. The ten defects were serially sectioned at 5-mil increments, and the metallographic data was used to construct solid models for use in probability of detection studies. Several billets were also used in reproducibility and noise studies. The results of the inspection, defect characterization, and solid model generation are provided in this report along with use of the data in preliminary probability of detection (PoD) calculations. The following primary conclusions were arrived at:

- More than two times as many indications were found with multizone inspection than with the dual probe (longitudinal and angle inspection) conventional inspection. Detection occurred over the full depth of the billet for both methods. Conventional inspection detection was not correlated to the multizone amplitudes, i.e., the conventional misses occurred over the range of amplitudes.

- Phased array inspection was demonstrated to have similar capability to the multizone results with the advantage of simpler fixturing.

- In chemical analysis studies of the defects, the nitrogen concentration was found to drop to less than 1% within 10 mils from the defect center (center of the voiding). The implications of these results are that the nugget and diffusion zone contribute little to the detection of the defect. Ultrasonic response is dominated by the presence of cracks and voiding.

- Defect characterization of ten defects provides detailed understanding of hard alpha defects for use by metallurgists, life management, design, and inspection personnel. The data also provides input for PoD calculations and for use in model validation.

- Using the solid model results, the sizes of the defects were tabulated and used in subsequent PoD calculations. Preliminary results indicate inconsistencies between PoD calculations generated from prior data and the recent Contaminated Billet Study characterization. Additional effort is underway to extend the PoD calculations to include the full dataset of 60 indications and to further understand the input to prior PoD calculations.

- Several reproducibility studies were performed using a subset of the billets. Variability of amplitude response up to 10 dB was found for both conventional and multizone

methods. Inspection setup and transducer alignment were identified as key contributors to the variability.

- Of the ten hard alpha defects selected for metallographic sectioning, seven were not detected by conventional inspection. All of the missed defects were very large, having hard alpha core areas in the 15,000 to 100,000 square mils of range.

1. INTRODUCTION.

1.1 PURPOSE.

The safety of jet engines is dependent on the use of inspection technology for the detection of critical defects and accurate quantification of the performance of the various inspection methods for use in design and lifing calculations. Typically, the performance is quantified through the use of statistical tools and is reported as a probability of detection (PoD). However, the accuracy of the PoD results is dependent on having a significant number of data points for a given flaw type for use in the calculations.

The major flaw type of concern in titanium alloys used in production of jet engines is hard alpha defects that are caused by nitrogen and/or oxygen impurities in the metal. The hard alpha defects are often accompanied by cracks and voids, which may be located using present ultrasonic and eddy-current inspection procedures. Subsurface hard alpha defects that are found in production are almost always accompanied by cracks or voids. These hard alpha regions, being more brittle than nominal material, generally crack prior to surrounding material, thereby acting as a fatigue crack origin.

Naturally occurring hard alpha defects in rotor grade material have been reported at occurrences of less than one per million pounds. Therefore, their availability for study and evaluation is limited. In February 1995, while performing a routine inspection for a nonaerospace customer, a titanium supplier found multiple indications with conventional ultrasonic inspection. Upon sectioning two of the indications, hard alpha was confirmed, and the existence of the heat was made known to the Engine Titanium Consortium (ETC). Because of the opportunity this heat offered, ETC proposed to the Federal Aviation Administration (FAA) William J. Hughes Technical Center to purchase the heat for inspection, processing, and life management studies as part of the ETC research and for use by the FAA Turbine Rotor Materials Design (TRMD) program performed by Southwest Research Institute. The program became known as the Contaminated Billet Study (CBS) and has provided a unique opportunity for study by both the inspection and the lifing communities.

Through use of the heat for various inspection studies and subsequent metallographic and chemical analysis, a considerable amount was learned about the physical properties and detectability of this defect type. The inspection results, subsequent sectioning, and use of this heat for PoD studies are the subject of this report.

1.2 BACKGROUND.

Hard alpha defects are also know as high interstitial defects [1] and are defined as an interstitially stabilized alpha phase region of substantially higher hardness than the surrounding material, arising from very high local nitrogen, oxygen, or carbon concentrations that increase the beta transus and produce the high hardness, often brittle, alpha phase. Also commonly called a type I defect, low-density inclusion, or hard alpha, the defects are often associated with voids and cracks. Defects may occur because of the inadvertent use of burned sponge or contaminated raw stock, improperly processed electrodes, or vacuum leaks. Because of the deleterious effect

of these defects on the fatigue life of titanium alloys, any billet or forging found to contain a defect is removed from use in critical rotating components. Manufacture of rotating components of jet engines involves a multiple-step process that is designed to arrive at optimal material and mechanical properties. A schematic of the typical process is shown in figure 1. Raw materials are selected to ensure cleanliness of the final product. They are consolidated into a compact, used in preparation of the final ingot. Typical ingot diameters are 24″ or greater and are fabricated using either triple vacuum arc remelting (VAR) or cold hearth melting (CHM) followed by a VAR step. Ingots are visually inspected for indications of surface contamination before further processing to billet. Conversion of ingot to billet typically involves the use of V-die or rotary Gesellschaft fur Maschinenbau-und-fertigungstechnik processes to reduce the billet diameter to the appropriate size and arrive at acceptable microstructural conditions (i.e., grain size and alpha/beta ratios). After billet conversion, the surface is prepared for inspection and the billet is inspected with immersion ultrasonic inspection. If hard alpha defects are found, the entire heat in which any hard alpha defect occurs will be downgraded from premium quality and is no longer acceptable for use in critical rotating components. Those billets found acceptable will be cut into sections of appropriate length for a given forging design known as mults. The mults are then forged into a sonic shape for ultrasonic inspection. If no defects are found, the sonic-shaped component will be machined to final shape and then will be typically inspected with fluorescent penetrant inspection and surface etching, e.g., blue etch anodize, prior to entering service.

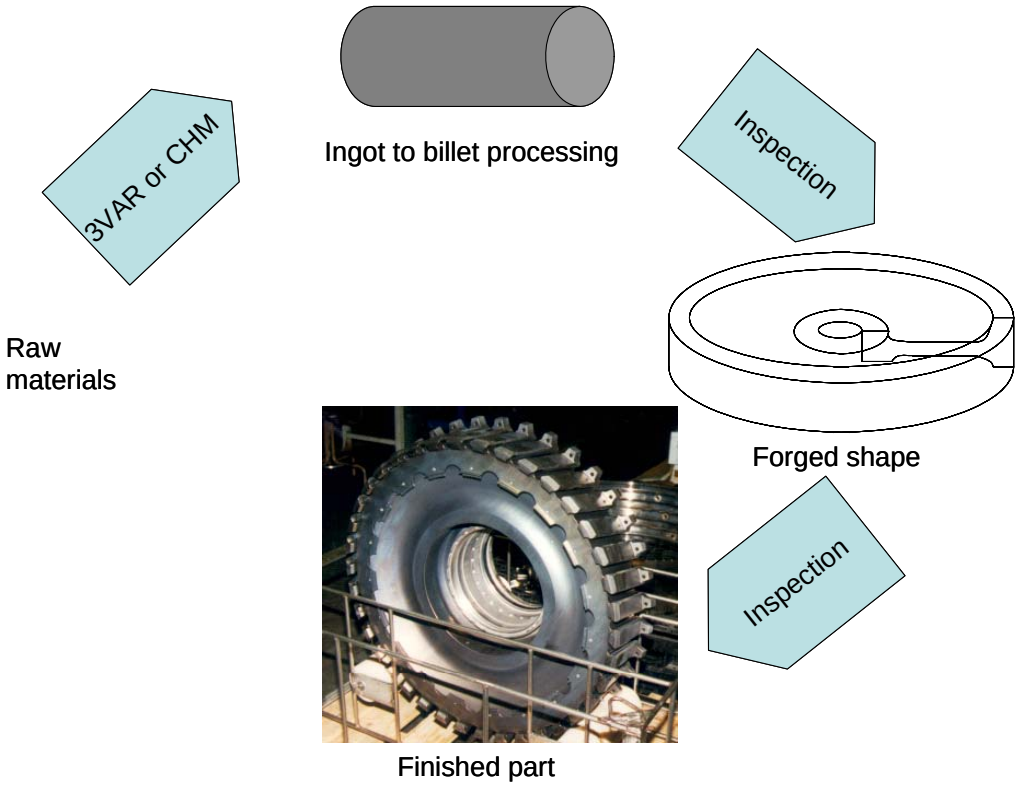


FIGURE 1. MANUFACTURING CYCLE FOR CRITICAL ROTATING COMPONENTS

The FAA and the aviation industry have placed much attention on the occurrence and detection of hard alpha defects since the 1989 Sioux City accident [2]. The FAA established an internal team to review the production, use, and management of titanium components and published the results of their efforts in the Titanium Rotating Component Review Team Report [3]. Recommendations included improvements for the inspection of titanium, which led to the establishment of the Engine Titanium Consortium. After the incident, the Jet Engine Titanium Quality Committee was formed under the auspices of the FAA, with membership including all the U.S. and European aircraft engine producers, for the purpose of rapid dissemination of titanium alloy melt-related defect issues and data and included activities leading to Advisory Circular (AC) 33.15-1, "Manufacturing Process of Premium Quality Titanium Alloy Rotating Engine Components" [1]. To address life management related issues, the Rotor Integrity Subcommittee was established through the auspices of the Aerospace Industries Association. Through cooperative efforts with the FAA, AC 33.14-1, "Damage Tolerance for High Energy Turbine Engine Rotors [4]," was also generated. A companion research program known as the Turbine Rotor Materials Design was initiated at Southwest Research Institute to support the needs of the lifing community.

In 1995, the ETC held its first of three open forums to place the results of the program in the public domain. At the meeting, the existence of a contaminated heat of Ti-6Al-4V was made known to the ETC team. An initial inspection indicated multiple defects, and a preliminary destructive analysis confirmed the existence of hard alpha defects. The ETC team requested approval from the FAA to purchase the heat of material for use by the ETC and TRMD research programs. A research program was put in place to use the material to improve the understanding of detectability of hard alpha and to provide quantitative data for use in inspection and lifing decisions.

1.3 PROGRAM OBJECTIVES.

The program objectives were:

- to provide a quantitative assessment of various ultrasonic approaches to billet inspection.
- to provide basic knowledge and data to improve the detection of hard alpha by developing an understanding of the acoustic, physical, and chemical properties of hard alpha defects.
- to provide reference samples containing naturally occurring hard alpha defects for evaluation of future inspection techniques, validation of PoD and ultrasonic methodologies, and support of technology transfer to titanium billet suppliers.
- to support the development of a probabilistically based, damage tolerance design code to augment the current safe-life philosophy for life management of commercial aircraft turbine engine rotors components.

1.4 RELATED ACTIVITIES AND DOCUMENTS.

The ETC was established in 1993 and included Iowa State University (ISU), General Electric Aircraft Engines (GE), Honeywell Engine Systems & Services, and Pratt & Whitney in a partnership to perform research that contributes to improvements in flight safety. The Phase I program, which was completed in 1998, led to improvements in production inspection of titanium billet [5], improved physics models for ultrasonics [6 and 7], and a feasibility study for phased array for ultrasonic inspection of billets [8]. In-service inspection efforts led to a commercially available portable scanner [9] and eddy-current probes [10] as well as improved probe designs [11] and eddy-current probe design tools [12]. Considerable progress was also made in developing a new approach [13] to quantifying inspection performance as reported in the FAA report DOT/FAA/AR-01/96, "A Methodology for the Assessment of the Capability of Inspection Systems for Detection of Subsurface Flaws in Engine Components" [14]. As part of the Phase I program, a literature survey was completed that detailed the defect types that occur in titanium billet. A summary of the results of that survey are provided in appendix A.

A companion research program [15], TRMD, was funded by the FAA with the objective to develop a probabilistically based damage tolerance design code to augment the current safe-life approach for life management of commercial aircraft gas turbine rotors and disks. Initial application of the code focused on melt-related hard alpha anomalies in titanium. Tests were also performed to determine the mechanical properties of hard alpha and titanium disk alloys, and a forging code was developed to predict the shape and orientation of hard alpha anomalies during processing. The probabilistic damage tolerance code that was developed for low-cycle fatigue of titanium rotors and disks containing hard alpha anomalies is called Design Assessment of Reliability With INspection (DARWIN®). It was developed by Southwest Research Institute in collaboration with Honeywell, formerly AlliedSignal Engines; GE; Pratt & Whitney; and Rolls-Royce Allison. Included in the TRMD program were efforts to validate deformation codes used in forging design and optimization. The objective of that portion of the program [16] was to develop a finite element microcode to simulate the deformation of a hard alpha inclusion during forming processes. Several of the CBS indications were provided to the TRMD program for use in validation of the deformation code and for use in generating material properties data with the results provided in FAA reports [16] and presentations.

2. APPROACH.

The approach for this research effort included the following steps, with details provided in sections 2.1-2.4.

- Determination of cause of the hard alpha defects in the available heat and suitability for further study
- Inspection of heat using multizone (MZ), conventional, and phased array inspection methods
- Analysis of inspection data and distribution of indications for further PoD and forging studies

- Detailed ultrasonic characterization of ten defects selected for use in PoD studies
- Metallographic sectioning with chemical analysis of the ten defects
- Coordination with the TRMD program in their use of three defects used for forging studies
- Use of metallographic section data to reconstruct the defect morphologies and subsequent PoD analysis

2.1 INITIAL ASSESSMENT OF HEAT.

In February 1995, the FAA-funded programs, the ETC and TRMD, were made aware of the existence of a contaminated heat of Ti-6Al-4V. The contaminated heat, number 883588-02, occurred as the result of a loss of power during melting. Following completion of the double VAR processing, the ingot was split in two and converted to the final billet diameter of 6″. The forging process is detailed in figure 2. Note that this is not the standard practice for rotor-grade materials, which are typically either triple VAR or CHM/VAR processed and rotary forged from ingot to final billet geometry. However, the original customer did not intend to use the material for aerospace applications, hence, the difference in processing. The supplier indicated that this heat was formulated from 72% revert, 28% sponge, and was chamber-welded. The primary ingot was piggy-back melted; the first electrode was melted uneventfully. Partway into the second melt, a total melt shop power outage occurred. The power outage shutdown the vacuum pumps, and a pressure spike occurred before the furnace was backfilled with argon. After power returned, melting was resumed to complete the primary ingot. The primary ingot was inverted and remelted to complete the processing. The initial inspection of the heat was completed using conventional 5-MHz transducers in two wave modes, longitudinal and refracted shear, which led to the detection of multiple indications. Based on the ultrasonic results, the heat was dispositioned for further commercial use. To ensure that the defect types were typical of hard alpha defects found in rotor-quality materials, an assessment was made with input from the ETC and TRMD teams along with representatives from the metallurgy staff at the original equipment manufacturers (OEM). Based on the chemical analysis and metallographic sectioning of the initial defects, it was determined that these defects were representative and, therefore, appropriate for further study, as described in the paragraphs below.

To determine the appropriateness of the material for further study, a chemical and metallographic analysis was performed on two of the indications, one of which is shown in figure 3. The bulk composition consisted of C-0.02, N-0.014, Fe-0.18, Al-5.56, V-4.10, O-0.18, and Y-<50 parts per million, within the range of typical Ti-6Al-4V. The purpose of the study was to characterize the inclusion as a typical hard alpha inclusion, compared to inclusions previously removed from billet product or from forged components. As reported by Bogan [17], the inclusion was a hard, brittle, cracked, and voided hard alpha, containing up to 12.6% nitrogen and surrounded by a diffusion zone and could be considered typical of those encountered in billet and forged products. Microprobe data showed that the highest nitrogen areas contained approximately 1.5%-2.0% vanadium with approximately 0.1%-0.9% aluminum.

Typical Process

- 36″ dia. ingot
- Heat 2100 ° F
  20″ RCS
- Heat 1750 ° F
  16″ RCS
- Heat 1975 ° F
  13″ RCS H_2O quench from dies
- Heat 1750 ° F
  9″ Octagon
- Heat 1750 ° F
  GFM Forge to 6.375″ dia.
  Bar turn to size 6″ dia.

RCS - Round corners square
OCT - octagon shape

CBS Process

36″ dia. ingot, 78″ length

- Heat 2100 ° F
  Upset forge to 50″ length,
  Rotate 90, draw to 32″ x 42″
- Heat 2100 ° F
  27″x 38”
- Heat 1750 ° F
  18.375″ x 35.375″
  Grind to 18″ x 35″
  Ship to customer
- Further processing at customer to 6.4″ x 28.7″; hard alpha detection; returned to RMI
- Flame cut
  B1 in half, slit in thirds
  B2 slit in thirds
  B3 slit in thirds
  Produced 12 pcs @ 6.4″ x 9.5″
- Heat 1750 ° F
  6″ RCS
- Heat 1750 ° F
  6.5″ OCT
  Bar turn to size 6″ dia.

FIGURE 2. COMPARISON OF TYPICAL CONVERSION PROCESS USED TO PRODUCE ROTOR-GRADE BILLETS AND THE CONVERSION PROCESS USED TO PRODUCE THE CBS BILLETS
(Note: the original customer for this material was not an aerospace customer.)

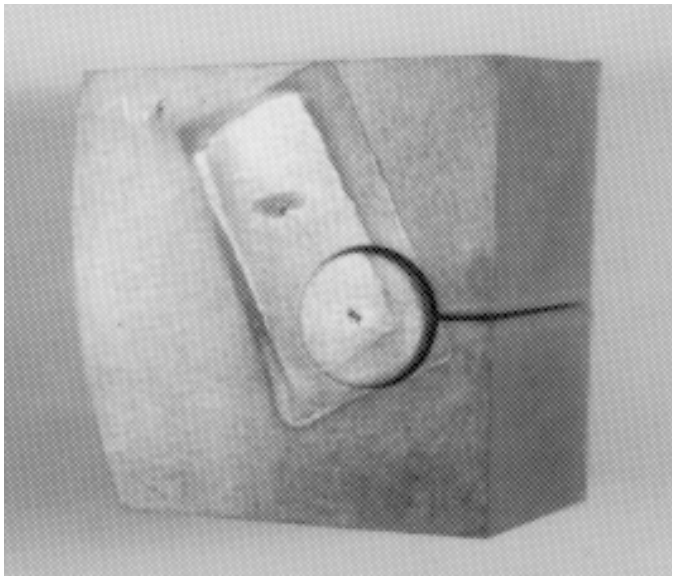


FIGURE 3. PHOTOMACROGRAPH DOCUMENTS REMOVAL OF INDICATION FROM BILLET SAMPLE
(Note the two indications visible in this sample were taken from B3W1. The indications were located at 0.875″ and 1.15″ from the billet surface.)

The presence of alloy content at the core of the inclusion indicates that the defect formation occurred in the alloyed state. The presence of oxygen in reduced nitrogen areas and the general absence of carbon all suggest an air leak type of hard alpha formation. An optical micrograph of the indication is shown in figure 4. The cylindrical slug was cross-sectioned approximately 0.3″ below the plane of the photomacrograph shown in figure 3. The 25X magnification photomicrograph maintains orientation between top and bottom views with the billet center shown to the right. The core of the inclusion (stabilized alpha with cracks and voids) is seen to be approximately 0.10″ in cross-sectional dimension with a diffusion zone extending to 0.20″ radially by approximately 0.12″ tangentially. Microprobe measurements were used to complete the analysis of B3W1 and are tabulated in table 1. The results of the microprobe analysis of this indication are shown in figures 5 through 7.

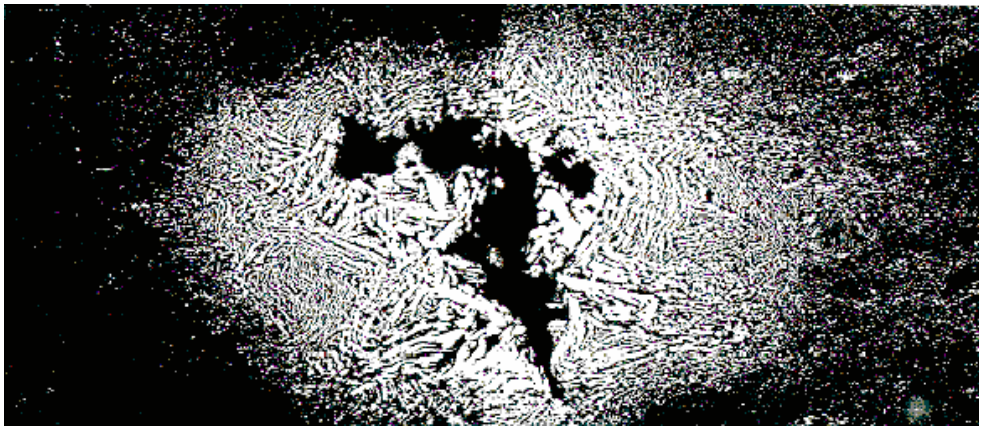


FIGURE 4. CYLINDRICAL SLUG TAKEN FROM BILLET B3W1 WAS CROSS-SECTIONED APPROXIMATELY 0.3″ BELOW THE PLANE OF THE PHOTOMACROGRAPH SHOWN IN FIGURE 3
(The 25X magnification photomicrograph shown here maintains orientation between top and bottom views with the billet center shown to the right.)

TABLE 1. CONCENTRATION MEASUREMENTS FOR B3W1

Point	Ti	Al	V	O	C	N
6	86.47	0.06	1.48	<ML	<ML	12.1
7	85.68	0.42	2.88	0.1	<ML	11.4
8	87.36	0.35	1.99	<ML	<ML	12.6
9	86.69	0.14	1.56	<ML	<ML	12.0
10	85.98	0.57	1.86	<ML	<ML	11.6
11	87.85	0.87	2.14	<ML	<ML	10.2
12	86.55	0.48	2.11	<ML	<ML	11.7
13	87.24	0.43	1.87	<ML	<ML	11.3
14	86.89	0.19	1.67	<ML	<ML	11.8
15	89.92	0.98	2.03	0.4	<ML	7.4
16	86.41	0.48	1.79	<ML	<ML	11.9
17	86.92	0.85	2.85	<ML	<ML	10.9
18	87.46	0.29	1.65	<ML	<ML	11.8
19	86.81	0.33	1.64	<ML	<ML	11.5
20	86.93	0.09	1.43	<ML	<ML	12.2
21	87.38	0.07	1.32	<ML	<ML	12.1
22	86.87	0.11	1.43	<ML	<ML	12.3
23	89.14	1.17	2.45	<ML	<ML	7.9
24	91.58	0.75	2.86	<ML	<ML	7.0
25	90.08	0.71	2.15	<ML	<ML	7.5
26	93.23	0.79	2.21	<ML	<ML	5.6
27	91.13	0.78	2.01	0.2	<ML	6.7
28	89.87	1.18	2.84	<ML	<ML	6.6
29	90.24	6.02	3.86	<ML	<ML	1.3
30	89.89	6.25	2.53	<ML	<ML	1.6
31	89.85	5.21	2.36	<ML	<ML	2.1
32	90.25	4.83	2.21	0.4	<ML	3
33	90.37	1.15	2.15	0.1	<ML	6.4
34	90.76	2.61	2.08	<ML	<ML	4.3
35	90.81	5.57	2.56	<ML	<ML	1.7
36	88.94	4.16	2.58	0.9	<ML	4.4
37	90.03	4.81	2.48	<ML	<ML	3.4
38	90.08	4.59	2.26	<ML	<ML	3
39	90.77	3.04	1.98	<ML	<ML	4
40	90.72	1.68	1.98	<ML	<ML	5.8
41	91.24	5.95	2.06	0.2	<ML	1.3
42	91.78	3.67	1.98	0.2	<ML	3.2
43	89.02	7.89	2.88	<ML	<ML	1
44	89.02	6.69	2.95	1.2	<ML	1.3
45	98.74	3.83	2.15	0.5	<ML	2.8
46	89.72	2.94	2.65	<ML	<ML	4.7
47	91.12	6.86	2.29	<ML	<ML	1.4
48	90.68	4.45	2.22	<ML	<ML	3.3
49	92.58	1.54	1.64	<ML	<ML	4.7
50	98.96	7.17	2.39	<ML	<ML	0.6
51	98.66	6.44	2.59	<ML	<ML	1.1
52	91.44	6.98	2.45	<ML	<ML	0.5
53	91.71	7.17	2.15	<ML	<ML	0.3
54	91.31	6.73	2.44	0.3	<ML	0.7
55	92.06	4.53	1.98	<ML	<ML	2
56	90.85	4.69	1.96	0.5	<ML	2.6
57	90.11	5.45	2.58	0.7	<ML	1.7
58	91.38	6.41	2.34	<ML	<ML	0.8
59	91.17	6.45	2.30	<ML	<ML	0.8
60	98.96	6.53	2.50	<ML	<ML	0.6
61	91.05	6.78	2.86	<ML	<ML	0.4
62	91.06	6.22	2.89	<ML	<ML	0.8
63	92.18	6.82	2.09	<ML	<ML	0.5
64	91.94	7.05	2.10	<ML	<ML	<ML

<ML - less than measuraable levels

O, C, N levels are not absolute concentrations but are relative to an average baseline value taken well away from the void area

Points correspond to locations marked in figures 4 through 7.

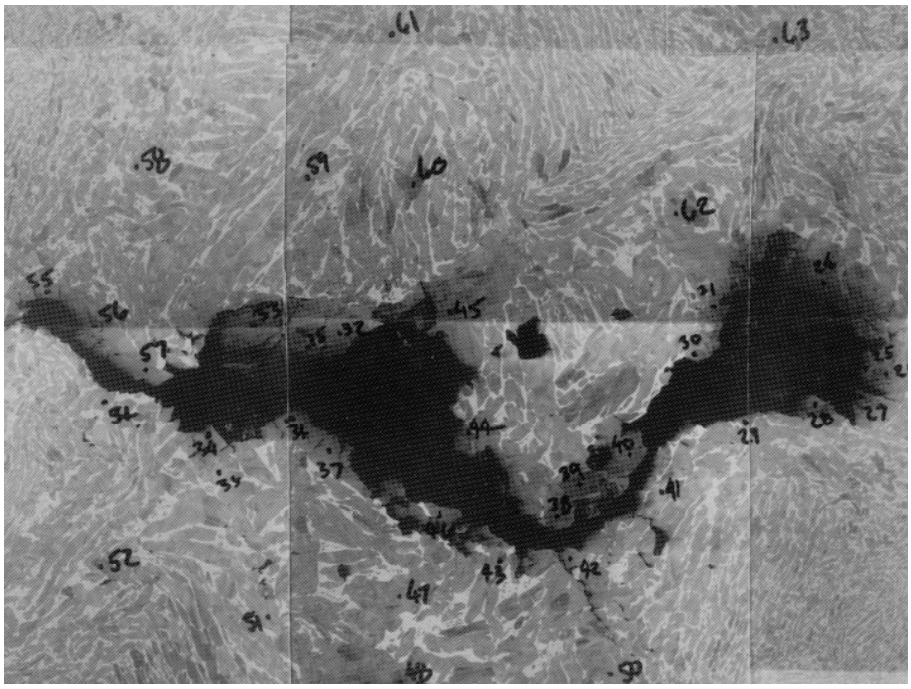


FIGURE 5. ELECTRON MICROPROBE BACKSCATTERED ELECTRON IMAGE OF DEFECT TAKEN FROM BILLET B3W1
(Numbers indicate location of microprobe measurements. Billet center is to right of image.)

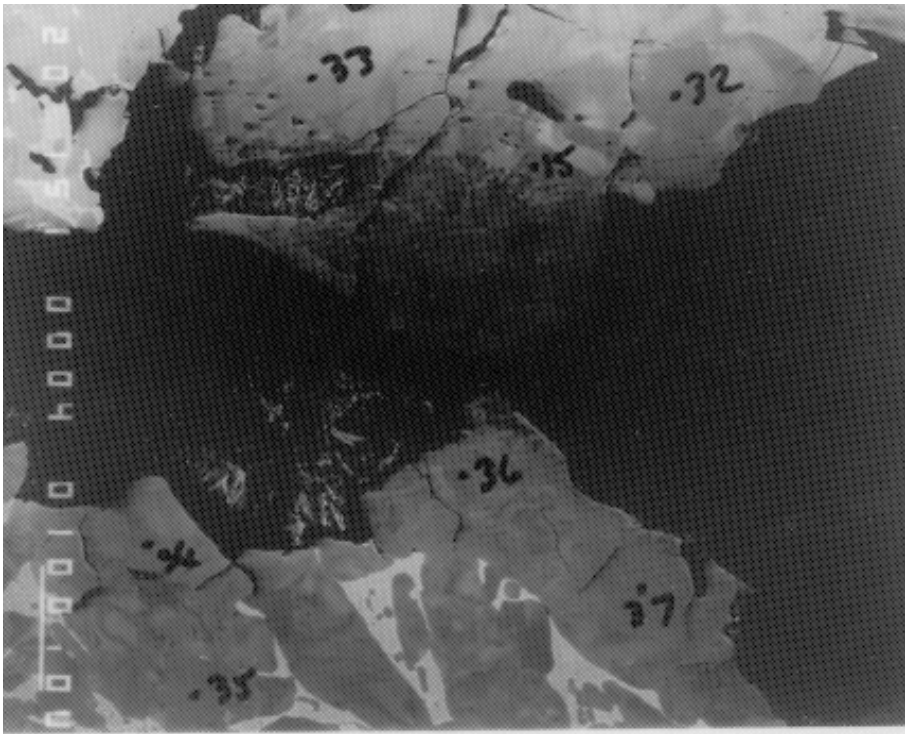


FIGURE 6. MICROPROBE RESULTS IN MEDIUM NITROGEN
(Range from 3.0% nitrogen at point 32 to 6.4% at point 33.)

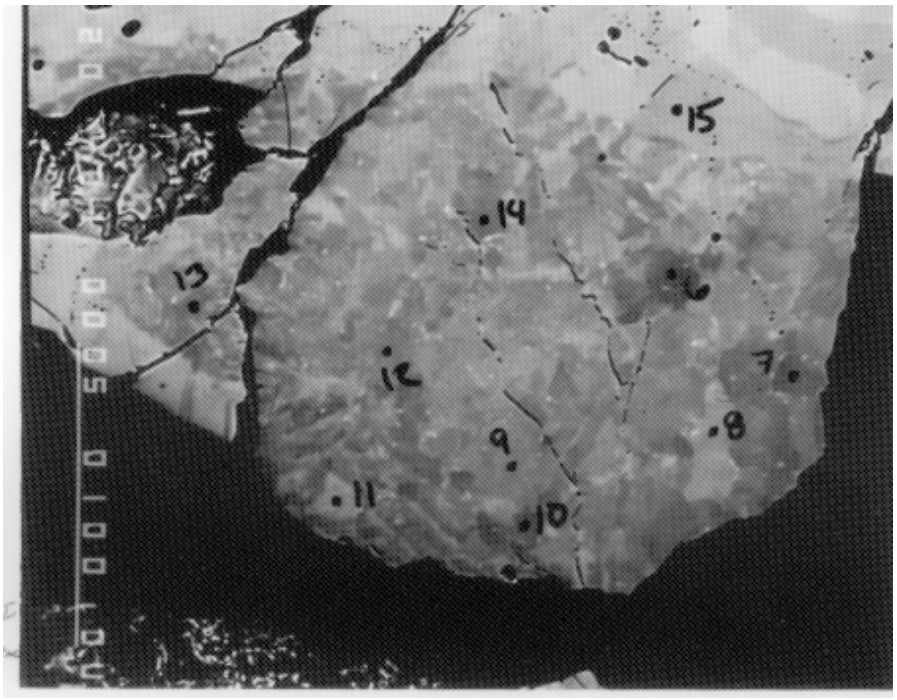


FIGURE 7. ELECTRON MICROPROBE SHOWS AREAS OF HIGHEST NITROGEN CONTENT
(The range of nitrogen content is from 7.4% N at point 15 up to 12.6% at point 8. The average nitrogen content in this area is 11.2%. Also note cracking in this area of the sample. The original micrograph was at 400X magnification.)

In addition to microprobe analysis, microhardness measurements were also made. The Knoop 500-gram microhardness ranged from a high of 805 (Rc 63) in the central core nugget, gradually decreasing to a value of 313 (Rc 30) in the normal microstructure. In May 1995, a joint ETC/TRMD assessment was made even though the heat was double VAR, the hard alpha defect was representative of typical defects found in triple VAR rotor-grade material. The ETC purchased the heat on behalf of the FAA for use in the inspection and lifing and deformation modeling programs.

The purchase included 6325 pounds of heat, representing half of the heat. The heat was converted into twelve 6″ diameter billets ranging from 87″ to 131″ in length. The location of the billets within the original ingot is shown in figure 8. The billet designations are listed first (B3W1, B3W2, etc.) followed by the length of the billet in inches. The number of indications detected by each of the inspection methods is listed for multizone, conventional longitudinal (CL), and conventional angle (CA). Four additional multizones were found upon detailed analysis of the data by ETC personnel that were not found (i.e., missed) by the production inspection analysis. The number of indications found in each billet by the original inspection and by the additional analysis (+ n) performed by ETC is indicated in figure 8.

B3W1 Len = 117” MZ = 4 CL = 3 CA = 3	B3W2 Len = 119.5” MZ = 8 CL = 2 CA = 3	B3W3 Len = 124.5” MZ = 4 CL = 2 CA = 3
B2W1 Len = 133” MZ = 4 CL = 2 CA = 3	B2W2 Len = 123” MZ = 3 + 1 CL = 0 CA = 0	B2W3 Len = 131” MZ = 3 CL = 0 CA = 1
B1BW1 Len = 104” MZ = 8 CL = 3 CA = 4	B1BW2 Len = 100.5” MZ = 5 CL = 4 CA = 2	B1BW3 Len = 107.5 MZ = 4 CL = 0 CA = 0
B1AW1 Len = 112.5” MZ = 5 CL = 1 CA = 3	B1AW2 Len = 117” MZ = 6 + 1 CL = 4 CA = 3	B1AW3 Len = 111” MZ = 5 + 2 CL = 2 CA = 2

FIGURE 8. LOCATION OF BILLETS WITHIN THE IGNOT, WHICH CAME FROM THE BOTTOM HALF OF THE INGOT

2.2 INSPECTION SUMMARY.

To fully characterize the heat and provide necessary data for PoD estimates, three inspection techniques were used:

1. Conventional dual transducer inspection: a 5-MHz longitudinal, cylindrically focused transducer at normal incidence (element size was 1″ by 0.5″ with an inspection water path of 3.5″ and a focal length of 8″) and a 5-MHz refracted longitudinal, spherically focused transducer (diameter of 0.75″ and water path of 3.5″) at an incident angle of 9.6º to produce a 45º longitudinal wave. The refracted angle was accomplished by offseting the transducer by 1/6 of the billet radius. The setup for the refracted longitudinal inspection is shown in figure 9. Note, the original inspection used refracted shear rather than refracted longitudinal.

2. Multizone inspection: 5-MHz bicylindrical focus, five zones. The multizone approach is based on the use of a bicylindrically focused transducer, which is designed to focus at 1″ zones, as shown conceptually in figure 10. Additional details of the multizone inspection process are provided in section 2.3.

3. Phased array inspection: 10-MHz center element for near-surface inspection, 5-MHz outer elements (seven) for the other four zones. Additional details of the phased array inspection are provided in section 3.2.

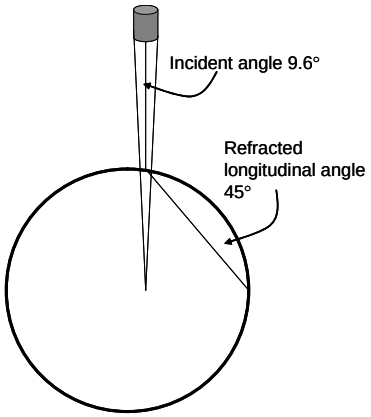


FIGURE 9. SPHERICALLY FOCUSED TRANSDUCER, OFFSET 1/6 OF BILLET RADIUS TO PRODUCE 45º LONGITUDINAL WAVE

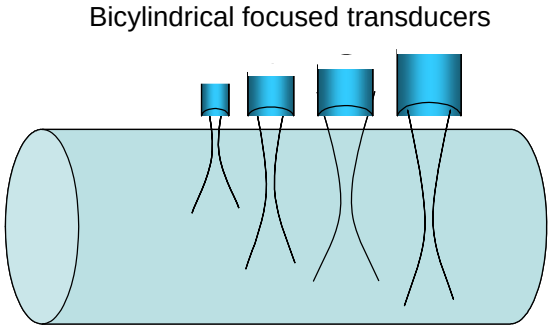


FIGURE 10. MULTIZONE CONCEPT THAT USES BICYLINDRICAL TRANSDUCERS DESIGNED TO FOCUS WITHIN 1″ ZONES FROM BILLET SURFACE TO 1/2″ BEYOND CENTER

2.3 DESCRIPTION OF MULTIZONE INSPECTION.

The multizone system is a real-time, personal computer (PC)-based platform that employs custom built analog electronics using up to eight parallel (nonmultiplexed) channels, each with a remote pulser/receiver matched to the ultrasonic transducer. Scanned helically, the billet is divided into concentric zones with a focused transducer used to acquire peak-detected C-scan image data for each zone. The depth of each zone is established by the depth of focus of that transducer. C-scan image data from all channels are displayed simultaneously on a 1024 x 1280 cathode ray tube, which scrolls as the inspection advances along the billet length. At the time of the CBS inspection, the data were written to optical storage upon completion of the inspection. Custom postscan analysis software was developed to detect flaws using signal-to-noise-based algorithms as well as amplitude rejection.

Motivation in the design of the multizone system was the use of focused transducers to overcome material noise and therefore improve detection. However, multiple compound focused transducers were required to inspect the billet volume to uniform sensitivity. The transducers were fitted with dual curvature lenses to produce a diffraction-limited symmetrical focus. This

configuration provided more uniform sensitivity versus depth for a given scan rate. The inspection zones were determined by the transducer focal zone parameters, i.e., diameter, d, and focal length, F. Each transducer inspects a depth of material roughly equal to the -3 dB depth of field ε_z and at a spatial sampling rate at least one-half the -6 dB beam diameter ε_x.

$$\varepsilon_z = 3.6\lambda[F/d]^2 \, c_1/c_2$$

$$\varepsilon_x = 1.03 \, \lambda[F/d]$$

The value c_1 is the sound velocity in water (0.058 in/μsec), c_2 is the sound velocity in titanium (0.243 in/μsec), and λ is the wavelength (0.049 in. in titanium at 5 MHz). A typical multizone transducer produces 5 MHz, F/8.0 beams that are approximately 0.1″ diameter and 0.8″ depth of field for titanium. At deeper depths, larger F numbers are used due to the limitation in element diameters produced by commercial vendors. By increasing the transducer size and depth in the material of its focal zone, overlapping foci are produced to uniformly inspect the billet volume, as shown in figure 10.

The ultrasonic instrument used custom analog electronics with up to eight parallel, nonmultiplexed channels. The parallel, nonmultiplexed architecture was used to eliminate any unattenuated sound that might interfere with a given channel's signal. A multiplexed solution also introduces possible speed limitations. Each transducer has its own remote pulser/receiver, which is matched to that specific transducer. The user can set various parameters for each channel such as attenuation, signal gate delay and width, and triggering rate. The data generated for each channel/zone is an analog, peak-to-peak C-scan voltage ranging from 0 to 10 volts, which is sent to the computer for display and storage.

The recommended computer configuration considered state of the art at the time of the CBS study was an Intel-based PC (e.g., 486, Pentium, etc.) with a large amount of random access memory (RAM) (64 MB or larger is recommended) running MSDOS and Windows. The RAM permits storage of data from all eight channels in memory as it is acquired. This eliminates time-consuming disk accesses during acquisition. Standard data acquisition boards were used for digital handshaking signals between the computer and the electronics and for digitization of the analog C-scan data. A 21″ 1280 x 1024 resolution color monitor allowed all eight channels to be displayed simultaneously during acquisition. The archival storage requirement was achieved using a write-once-read-many (WORM) optical disk for archiving the image data.

For inspection, the billet was immersed in a water tank and rotated about its axis. The maximum billet rotation speed was approximately 30 revolutions per minute. The transducers, aligned normal to the billet surface, were mounted on a stage or follower that rides on a track over the tank. As the billet rotates, the follower moves axially along the billet length and the material is inspected in a helical pattern. An axial encoder was mounted on the follower and was used to report axial position of the transducers during the scan. A rotary encoder was coupled to an adapter that is attached to the end of the billet using double-sided adhesive. The encoder generated a once-per-revolution index or home pulse, which was used by the computer acquisition software to determine the 0° location on the billet. The rotary encoder also generated

a 2048 pulse-per-revolution signal. This signal provided a position-dependent trigger for the ultrasonic transducers known as a pulse-on-position or POP pulse. The POP signal was used by the electronics to synchronize the triggering of the transducers for all eight channels to the billet rotation. Each channel divided down the 2048 master POP to the sample rate required to inspect the particular zone.

Outer zones with larger radii required more samples than inner zones to fully inspect the material. The sample count for a given zone was a function of the zone circumference and the beam diameter ε_x of the transducer. While transducers covering the larger radii zones fire more often than their smaller radii counterparts, all transducers fire simultaneously when they do trigger. This greatly minimized the possibility of any unattenuated sound from any channel interfering with the signal from any other channel.

Prior to inspection, the user must start the acquisition software on the computer. Based on the billet material and diameter, the operator is instructed on how to configure the electronics. Parameters such as attenuation, signal gate delay and width, and POP rate were set using thumbwheel switches on the electronics for the required number of channels. Information such as operator ID, billet length, and identification numbers must be entered into the software as well. Once the electronics are configured and the acquisition software is running, the rotary encoder begins triggering the electronics. The electronics fire the transducers and produce analog C-scan data values. These analog signals, along with axial position information, are sent to the PC acquisition software for storage in RAM and display. Upon scan completion, the user is given the opportunity to enter any comments about the scan. The data are then transferred from computer memory to disk and later archived to the WORM optical disk for permanent storage.

The implementation of digital data acquisition allows postscan analysis, which is not possible with any current conventional billet inspection system. A typical multizone inspection on a single billet can generate 30 MB or more of ultrasonic image data. These data can include flaw signals obscured by an acoustic noise level that varies both circumferentially and axially along the billet. An image analysis software package was developed to aid the operators in finding indications. This package, which runs on the system PC, provides a Microsoft Windows-based graphical user interface for displaying and manipulating the inspection results. Using data analysis tools such as maximum value axial cross sections and image magnification, the operator is able to locate signals that are above the local acoustic noise and display them at high resolution. The operator can then isolate potential rejectable signals and a surrounding area of homogeneous noise for each indication. Using those two regions-of-interest (ROI), the operator can calculate the signal-to-noise ratio (SNR) for each indication where SNR is defined as

$$SNR = \frac{P_s - \mu_n}{P_n - \mu_n}$$

where P_s is the maximum value of the signal ROI, P_n is the third highest (to exclude electrical noise spikes) value in the noise ROI, and m_n is the mean of noise ROI. Material acceptance criterion based on both peak amplitude and SNR are applied to the indication to make the accept

or reject decision. The PC can quickly review 30+ MB of data, allowing the task to be completed before the billet is removed from the tank. Since the scan positional information is stored along with the image data, the operator can return the transducer to the location on the billet where an indication exists to verify its location and mark the billet for sectioning to remove the material surrounding the indication. The multizone inspection system and postinspection data analysis described here are representative of the approach used in inspection of the CBS billets.

2.4 DEFECT CHARACTERIZATION.

The contaminated billet material offered an unprecedented opportunity for analysis of hard alpha defects. Defect characterization data combined with the ultrasonic inspection data provided improved understanding of the relationship between flaw morphology and detectability. A full protocol was developed for the defect characterization and is provided in appendix B. Characterization included ultrasonic measurements in several configurations, followed by metallographic sectioning. Digital images were recorded for each of the defect slices for use in the three-dimensional (3D) reconstruction of the flaws. Microprobe measurements were made on selected slices in each indication. Figure 11 provides a flow chart of the characterization steps.

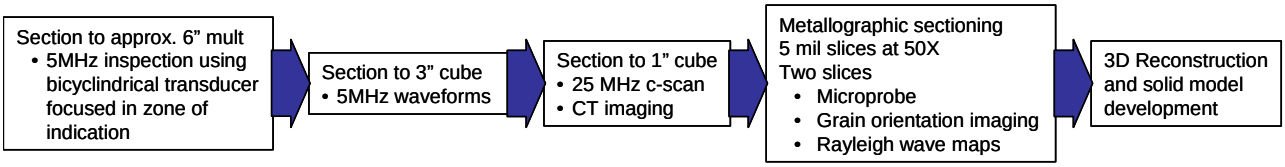


FIGURE 11. ULTRASONIC AND METALLOGRAPHIC ANALYSIS STEPS USED TO CHARACTERIZE THE DEFECTS

It was anticipated that pores and cracks would dominate the signals from hard alpha inclusions; therefore, a complete characterization of their morphology was the highest priority. To accurately predict the ultrasonic response of such irregularly shaped objects, definition of the surface to a resolution less than the ultrasonic wavelength is needed. At 5 MHz, the longitudinal ultrasonic wavelength is approximately 1.2 mm (0.048 in.) in titanium. Ideally, one would like the resolution to be about 10% of this, 120 μm (0.005 in.). Thus, 0.005″ was selected as the distance between sectioning planes. The sectioning planes should contain the direction of insonification, i.e., the sample can be sectioned in either the axial-radial plane or the circumferential-radial plane. Axial circumferential sectioning is not recommended, since there would be the possibility that a thin crack, which might have contributed strongly to the ultrasonic response, would fall between the planes. Furthermore, such sectioning would make it difficult to locate the positions of sharp concentration steps. The axial-radial plane was selected as the sectioning plane, as shown in figure 12, to minimize the number of polishes required.

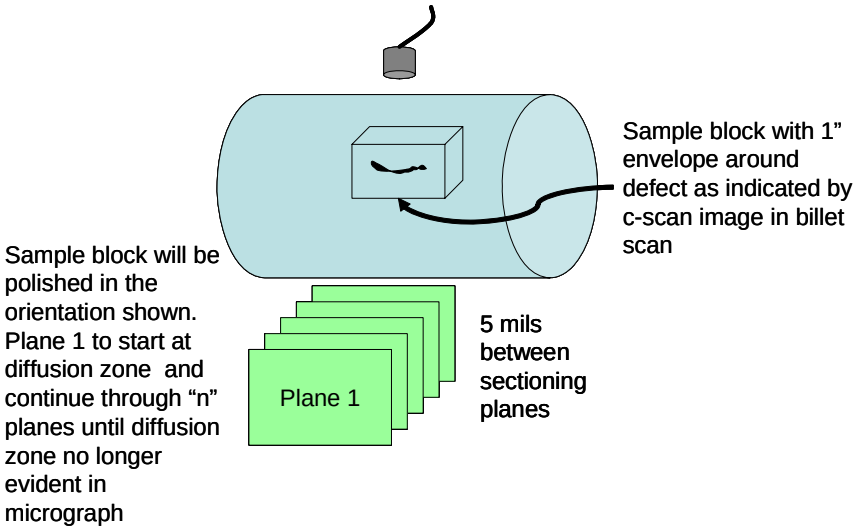


FIGURE 12. ORIENTATION OF SECTIONING PLANE WITH RESPECT TO INSPECTION DIRECTION

A practice defect was selected for developing and testing the characterization protocols. The defect was taken from billet B3W1. Note that the sectioning process used for this defect did not follow the orientation with respect to the billet axis as used with the other ten CBS indications. The purpose of characterization of this defect was to arrive at the etchants and microprobe processes. Five successive sections were made, as shown in figure 13. Note the change from diffusion zone to voiding as the sectioning progressed through the defect. The fifth section was used to evaluate the microprobe process. The sample was analyzed for titanium, aluminum, vanadium, nitrogen, and oxygen. Carbon could not be analyzed because the mounting material used required carbon coating of the sample. All analyses were performed at an accelerating voltage of 10 kV and a beam current of approximately 60 nA. A point analysis was used for the general survey, while selected area raster analyses at 4000X magnification were employed for the concentration profiles. The following analyses were performed:

- A general survey of approximately 25 points in and around the defect. Locations, which included primarily alpha phase, were chosen whenever possible for the point measurements.

- Two transverse concentration profiles ranging from ±50 mils of the defect center.

- One longitudinal concentration profile ranging from the defect center to 300 mils into the alloy.

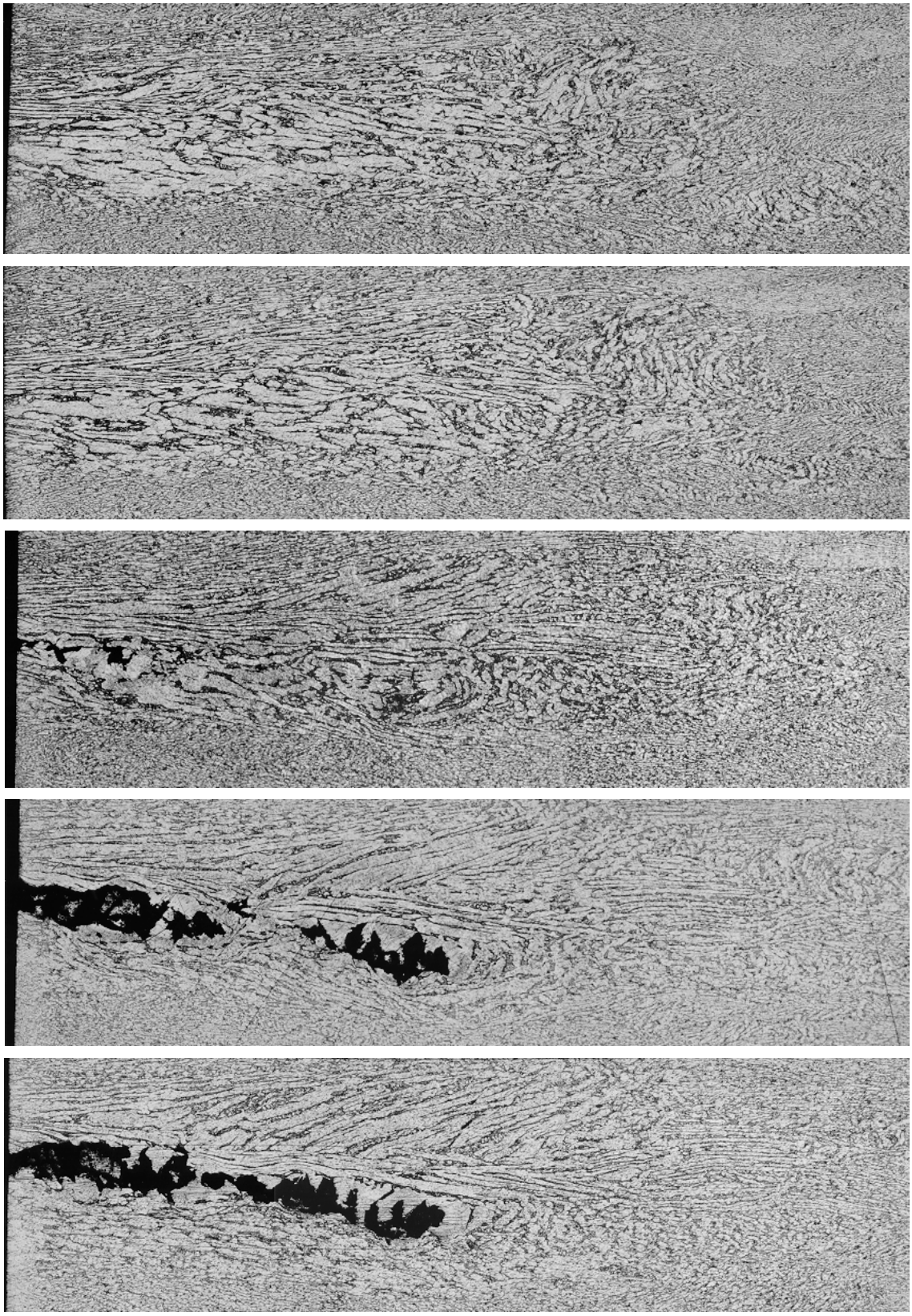
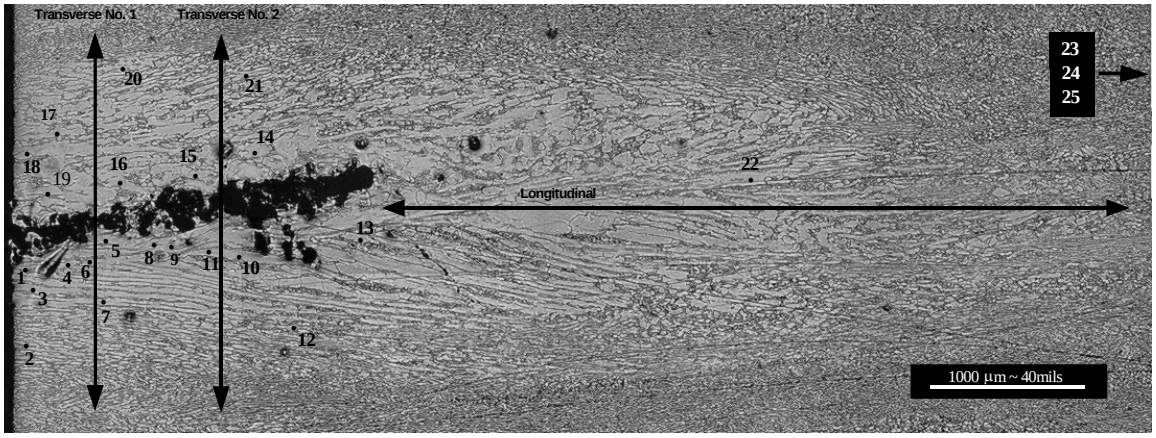


FIGURE 13. SECTION PLANES FOR PRACTICE DEFECT

Figure 14 shows the location of 25 point scans and 3 line scans completed on the practice defect. The results for the 25 points are tabulated in table 2. The results for the nitrogen line scans are shown in figures 15 (transverse scan) and 16 (longitudinal scan). Figure 17 provides the results for the oxygen scans. The scans show that the variation in nitrogen concentration was much more prominent transversely across the defect (see figure 15) than parallel to (in the plane of) the defect (see figure 16). This is consistent with the metallographic appearance and indicates that both the defect and the surrounding diffusion zone are flattened and elongated. In the diffusion zone there were no points where the composition changed abruptly. Note that within 10 mils of the defect center, the nitrogen concentration has dropped to less than 1 percent nitrogen. The ETC team was interested in understanding the concentration profile that determines whether there are significant ultrasonic impedance differences that will impact the inspection response. Based on the microprobe results and the need to understand the concentration profile, the decision was made to confine future microprobe analyses to line scans.

ETC Contaminated Billet Study - "Practice" Hard Alpha Titanium Defect



Optical image of defect. Numbers and arrows indicate approximate locations of point analyses and line scans.

FIGURE 14. MICROPROBE MEASUREMENT POINTS FOR PRACTICE DEFECT

In addition to arriving at the measurement process for microprobe analysis, a comparison of etchants was completed using the practice defect. A comparison was made to determine which etchant provided the best micrographs for hard alpha core/diffusion zone studies. Two etchants were compared, ammonium bifluoride and krolls etchant, as shown in figure 18. Note the more prominent indication of the diffusion zone in figure 18(a). Based on these results, the decision was made to use ammonium bifluoride in the defect characterization studies.

TABLE 2. RESULTS OF POINT MICROPROBE MEASUREMENTS FOR PRACTICE DEFECT

Point No.	Titanium	Aluminum	Vanadium	Oxygen	Nitrogen
0 (Center)	88.1	1.1	1.2	<0.1	8.6
1	89.8	5.6	1.9	0.3	1.4
2	89.6	6.9	2.0	0.3	0.6
3	88.1	5.8	2.2	0.3	1.5
4	86.9	5.2	2.0	0.3	2.1
5	86.8	3.7	1.4	0.3	2.9
6	86.6	5.9	1.7	0.3	1.3
7	84.2	7.0	1.8	0.3	0.6
8	85.1	5.6	1.8	0.3	2.0
9	86.2	5.7	2.0	0.3	1.5
10	85.2	5.9	1.7	0.3	0.9
11	85.4	5.8	1.9	0.3	1.1
12	89.2	6.7	1.6	0.3	0.7
13	87.8	5.3	1.7	0.3	1.2
14	88.6	4.9	2.0	0.3	1.3
15	85.8	5.0	1.7	0.3	1.9
16	86.3	4.9	1.8	0.3	1.5
17	86.2	6.3	1.9	0.3	0.9
18	84.3	6.4	1.8	0.3	0.9
19	83.8	6.0	2.0	0.3	1.2
20	85.2	7.1	1.6	0.3	0.3
21	83.9	7.0	1.6	0.3	0.4
22	84.8	6.7	1.7	0.3	0.4
23	85.0	7.2	1.6	0.3	0.4
24	83.2	7.3	1.7	0.3	0.5
25	85.7	7.2	1.7	0.3	0.2

All concentrations shown in weight percent. The location of the points is provided in figure 14.

LOCATION (mils)	NITROGEN (weight %)
-50	0.3
-50	0
-45	0.3
-40	0.1
-40	0.2
-35	0.3
-35	0.2
-30	0.5
-30	0.4
-25	0.1
-25	0.5
-20	0.6
-20	0.1
-15	0.8
-15	0.8
-10	1.0
-10	0.8
-8	1.3
-6	1.3
-5	0.7
-5	1.2
-3	3.4
-3	1.0
-2	5.5
-1	5.9
-1	2.8
0	6.5

LOCATION (mils)	NITROGEN (weight %)
0	7.3
1	4.3
1	3.3
2	1.9
2	2.6
3	1.9
4	1.0
4	1.1
5	1.3
5	1.6
6	0.8
6	0.8
7	1.0
8	1.2
8	0.9
10	1.1
10	0.7
11	0.8
15	0.7
15	0.7
20	0.7
20	0.8
25	0.3
25	0.1
30	0
35	0.1
40	0.2
40	0.2
45	0.2
45	0.2
50	0.2
50	0.2

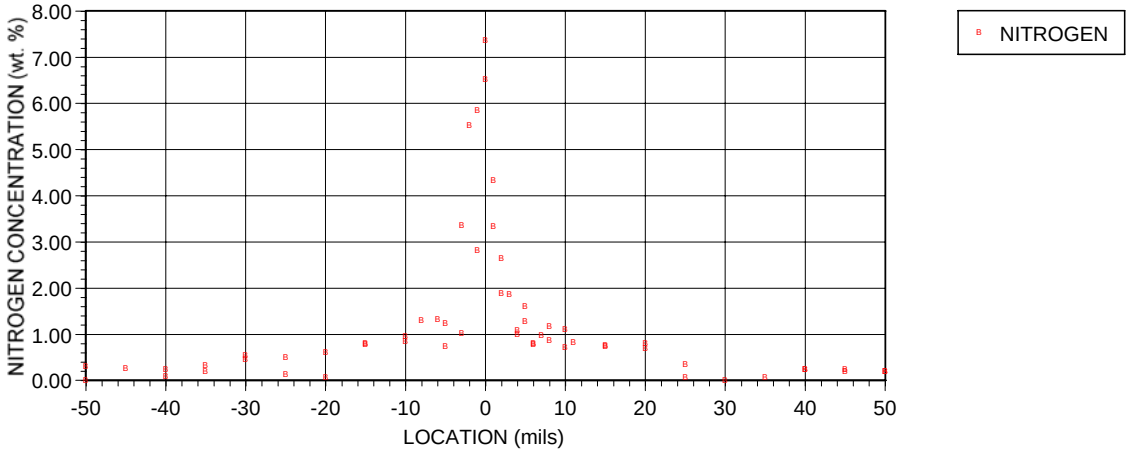


FIGURE 15. RESULTS FOR NITROGEN SCAN PERPENDICULAR (TRANSVERSE 1) TO THE LONG AXIS OF THE DEFECT WITH ZERO LOCATED AT THE DEFECT CORE
(The location of the scan is provided in figure 14.)

LOCATION (mils)	NITROGEN (weight %)
1	2.1
2	1.2
5	1.7
7	0.9
10	0.9
15	0.6
20	0.7
25	0.8
30	0.4
35	0.8
40	0.1
45	0.1
50	0.4
60	0.7
70	0.7
80	0.6
90	0.2
100	0.2
120	0.4
140	0.8
160	0.1
200	0.2
300	0.2

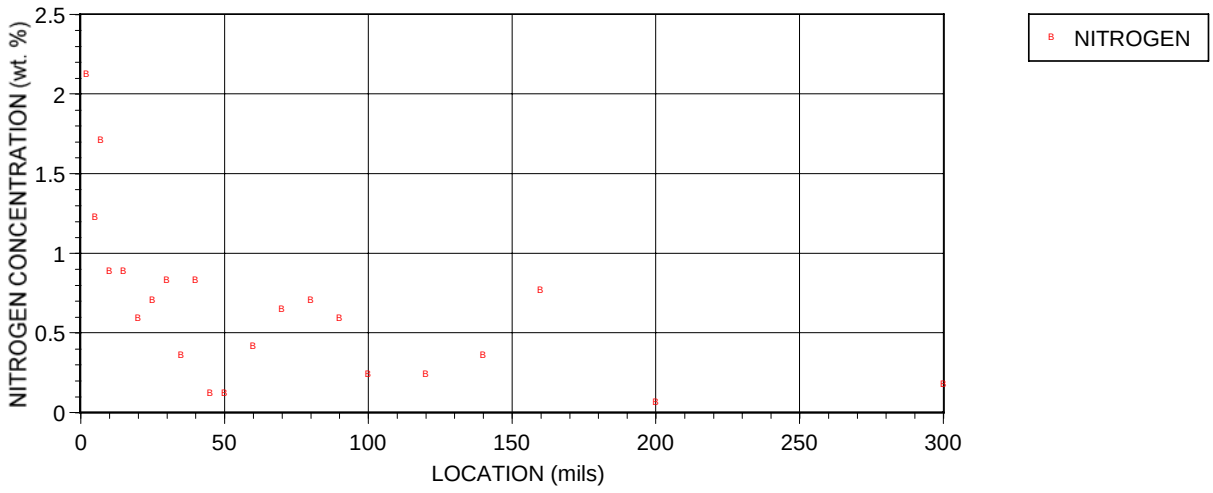
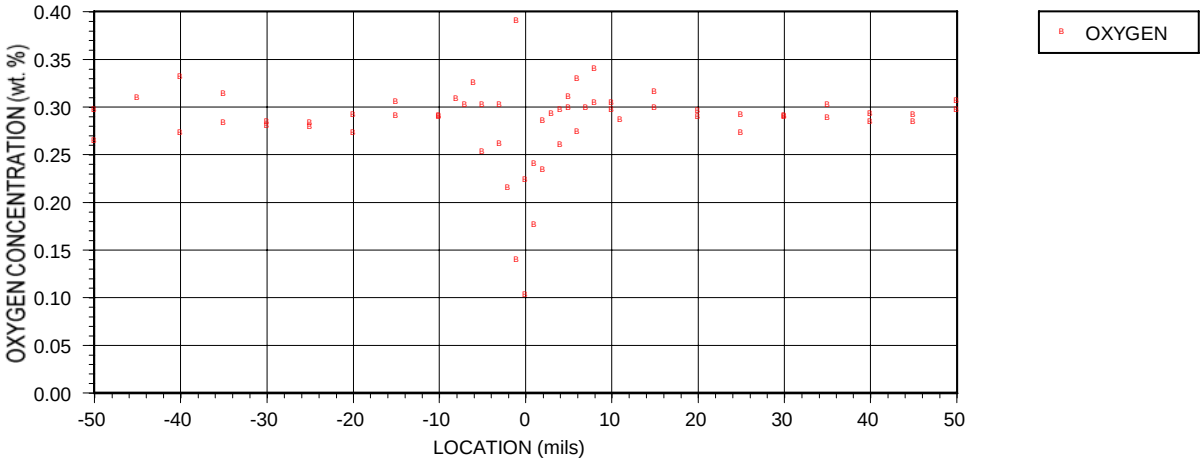
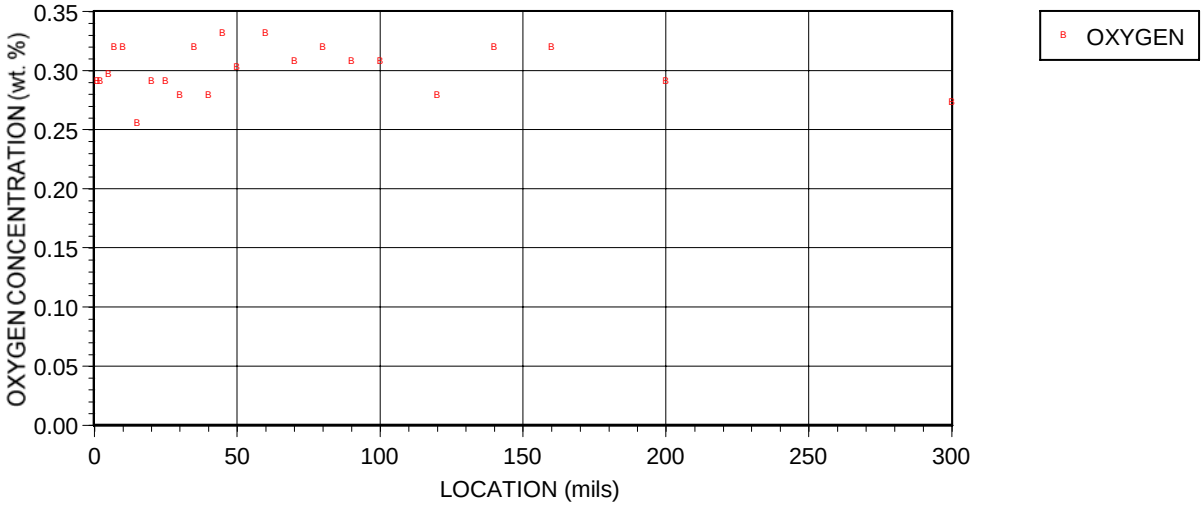


FIGURE 16. RESULTS FOR NITROGEN SCAN PARALLEL TO THE LONG AXIS OF THE DEFECT WITH ZERO LOCATED AT THE END OF THE DEFECT CORE
(The location of the scan is provided in figure 14.)

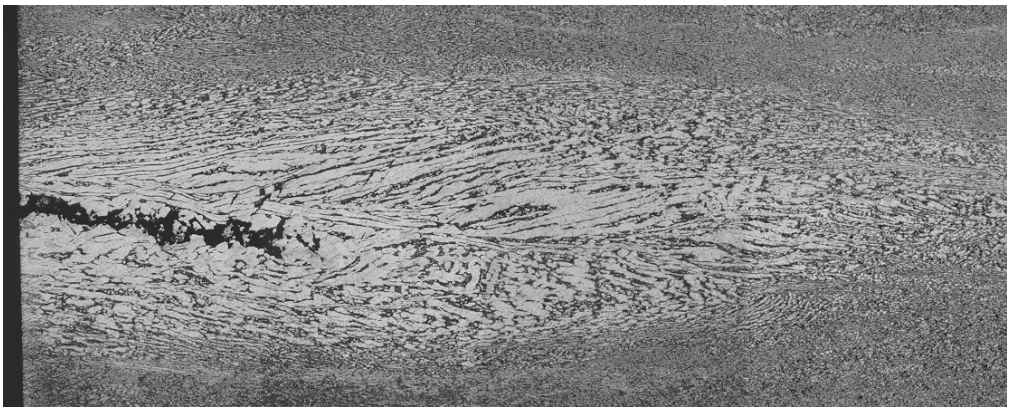


(a)

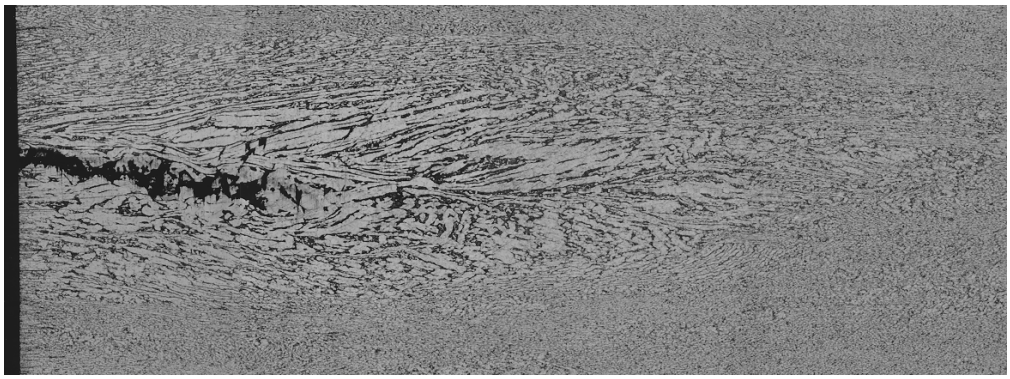


(b)

FIGURE 17. (a) RESULTS FOR OXYGEN SCAN PERPENDICULAR TO THE LONG AXIS (TRANSVERSE 1) OF THE DEFECT WITH ZERO LOCATED AT THE DEFECT CORE AND (b) RESULTS FOR OXYGEN SCAN PARALLEL TO THE LONG AXIS OF THE DEFECT WITH ZERO LOCATED AT THE END OF THE DEFECT CORE
(The location of the scans is provided in figure 14.)



(a)



(b)

FIGURE 18. RESULTS FOR (a) AMMONIUM BIFLUORIDE AND (b) KROLL'S ETCHANTS

3. DISCUSSION OF RESULTS.

3.1 INSPECTION OF THE CONTAMINATED HEAT.

The full heat was inspected at the billet supplier in September 1995 using the conventional dual-transducer inspection and multizone inspection methods. Modifications to hardware and software were made to the multizone system to also enable digital data collection for the two conventional inspection methods (CL and CA). This allowed amplitude and SNR analysis using the same software as for the multizone data. Setup parameters are summarized in table 3. A summary of the number of indications found for each method, with the exception of phased array, is shown in the figure 19. Note that the metallurgical review criteria for conventional inspection implies that indications in the CBS inspection with an amplitude greater than 45% would require cutup to determine if the response was from a rejectable defect. Therefore, in the evaluation of this heat, any conventional signals with an amplitude greater than 45% were included as indications.

TABLE 3. SUMMARY OF INSPECTION PARAMETERS FOR EACH OF THE INSPECTION METHODS

	Multizone	Conventional Longitudinal (CL)	Conventional Refracted Longitudinal (CA)
Transducer description	5-MHz, bicylindrical focused probes (4 zones)	5-MHz cylindrically focused transducer element size 1″ x 0.5″ with an inspection water path of 3.5″ and a focal length of 8″	5-MHz spherically focused transducer, diameter of 0.75″ and water path of 3.5″
Calibration	#2 FBH	#3 FBH	0.02″ diameter hole
Index per revolution	0.042″	0.042″	0.042″
Rejection amplitude*	70%	70%	70%
Rejection S/N	2.5	Signals greater than 3 dB above noise, but not less than 30% FSH, are subject to metallurgical review	Signals greater than 3 dB above noise, but not less than 30% FSH, are subject to metallurgical review

*Inspection is set up such that response to calibration target, e.g., #2 or #3 flat-bottom hole (FBH), is equivalent to 80% full-screen height (FSH). Rejection occurs when signal response exceeds 70% FSH.

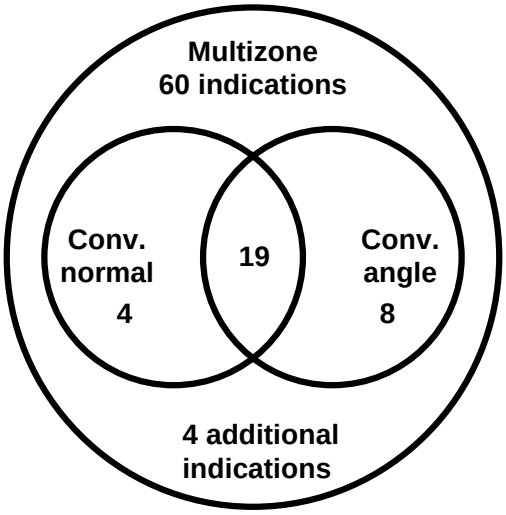


FIGURE 19. VENN DIAGRAM SHOWING THE NUMBER OF INDICATIONS DETECTED PER INSPECTION METHOD

The 12 CBS billets were previously inspected for the initial customer in November 1994, and the results were provided to the ETC as part of the purchase. In the initial inspection, precautions were not taken to prevent saturation of the ultrasonic signal. To enable capture of digital data using approved multizone and conventional inspection methods and to ensure that saturation of the signals did not occur, the complete heat was reinspected in September 1995.

Billet maps were generated for each of the billets and were used in comparisons and to guide selection of indications for the various studies described in section 3. Figure 20 provides the inspection results for one of the billets as an example. The complete set is provided in appendix C. These maps summarize the inspection results for each of the billets. The billet ID is provided in the upper left corner of each sheet. Below this is a summary of results. In the first column, indications were identified alphabetically with the left most indication beginning with A. The second column lists the distance from the end of the billet. Indication depths are provided in the next six columns of figure 20 for each of the inspection times (September 1995 and November 1994) and inspection methods (conventional normal, conventional longitudinal, multizone). Graphical representations, referred to as billet maps, provide the amplitude response and SNR for each of the indications, as was determined during each of the inspections. The SNR values quoted were computed in accordance with the multizone definition and calculated using digitally recorded C-scan data for both the multizone and conventional inspection methods.

C-scan images were also generated for each of the indications and estimates made of the indication size. An example of the C-scan results is shown in figure 21. The billet ID and indication ID are listed (e.g., B3W3-B) along with the zone in which the indication was found. Inches from top indicates the axial location of the defect within the billet. The amplitude, SNR, and depth are tabulated from the billet maps (see figure 20). The axial and circumferential lengths were estimated using the indication sizes from the C-scan images. The estimates of the axial length were straight-forward. The estimates of the circumferential length were based on the formula $x = 2\pi r\theta$, where θ was the circumferential extent of the image in pixels divided by the total number of pixels in a 360° revolution. No correction was made for the effects of beam size.

The C-scan images were reviewed to select 10 representative defects for use in the metallographic cutups to support PoD studies. The initial review led to the characterization of the indications into three categories: low amplitude, small spatial extent; high amplitude, small spatial extent; and high amplitude, large spatial extent. The C-scan results for the indications selected for use in the metallographic studies are provided in appendix D. A summary of the PoD indications is provided in table 4. Defects were also selected by the TRMD program for use in forging studies. The results of that program are provided in separate reports [15 and 16].

B1AW1

		September 1995 Inspection			November 1994 Inspection		
Stamped I.D.	Inches from top	Multizone Depth	Conv. Normal Depth	Conv. Angle Depth	Multizone Depth	Conv. Normal Depth	Conv. Angle Depth
A	3.3	0.2			0.3		
B	25.9	0.6		0.6	0.6	0.5	0.5
C	66.4	1.6	1.8	1.6	1.6		
D	92.7	1.7			1.8		
E	95.2	0.6		0.6	0.7	0.5	0.5

Additional indication reported on Nov 1994
Multizone, 12" from top, 0.94" deep,
amplitude 53%, 2.11 SNR (not rejectable)

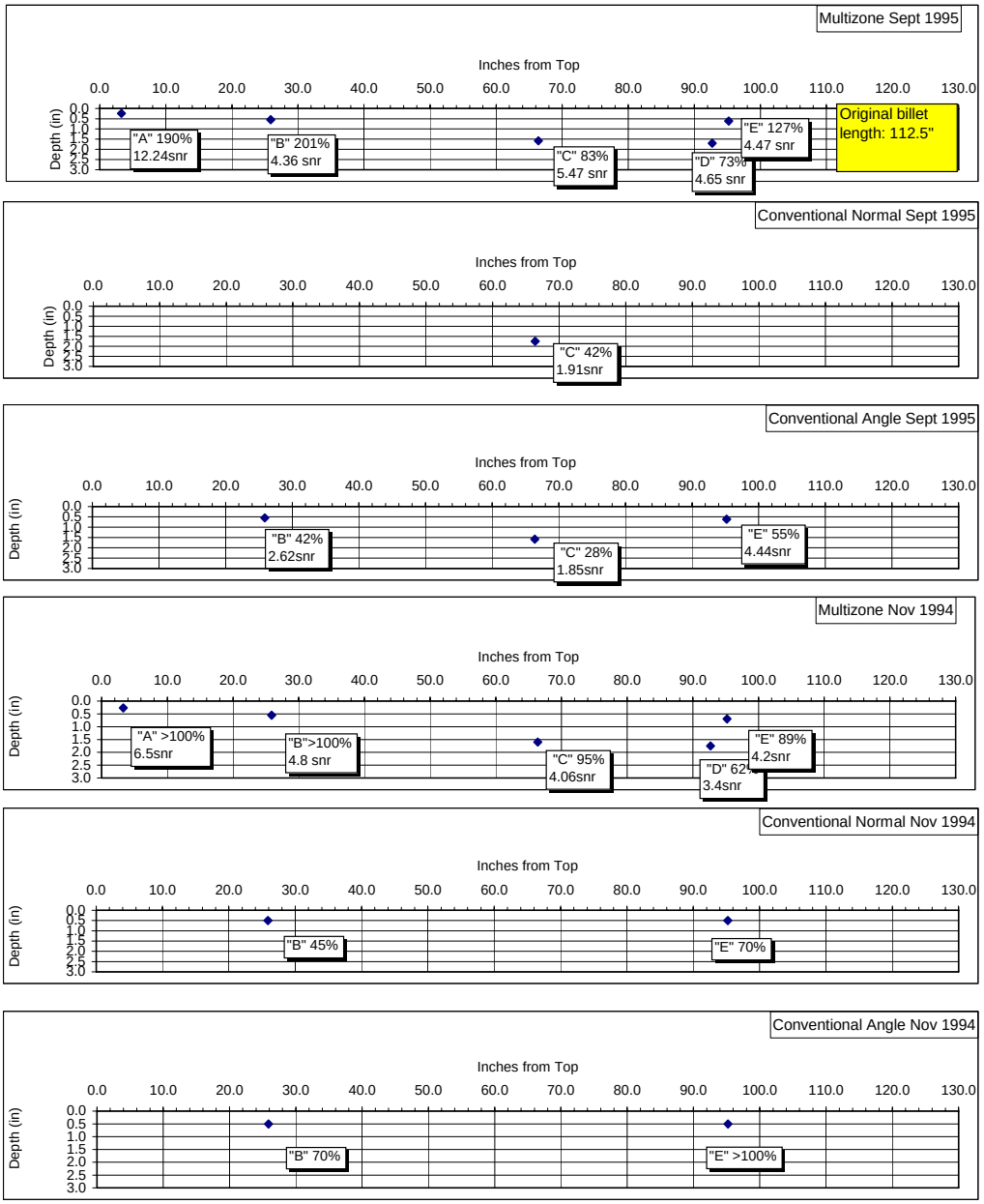
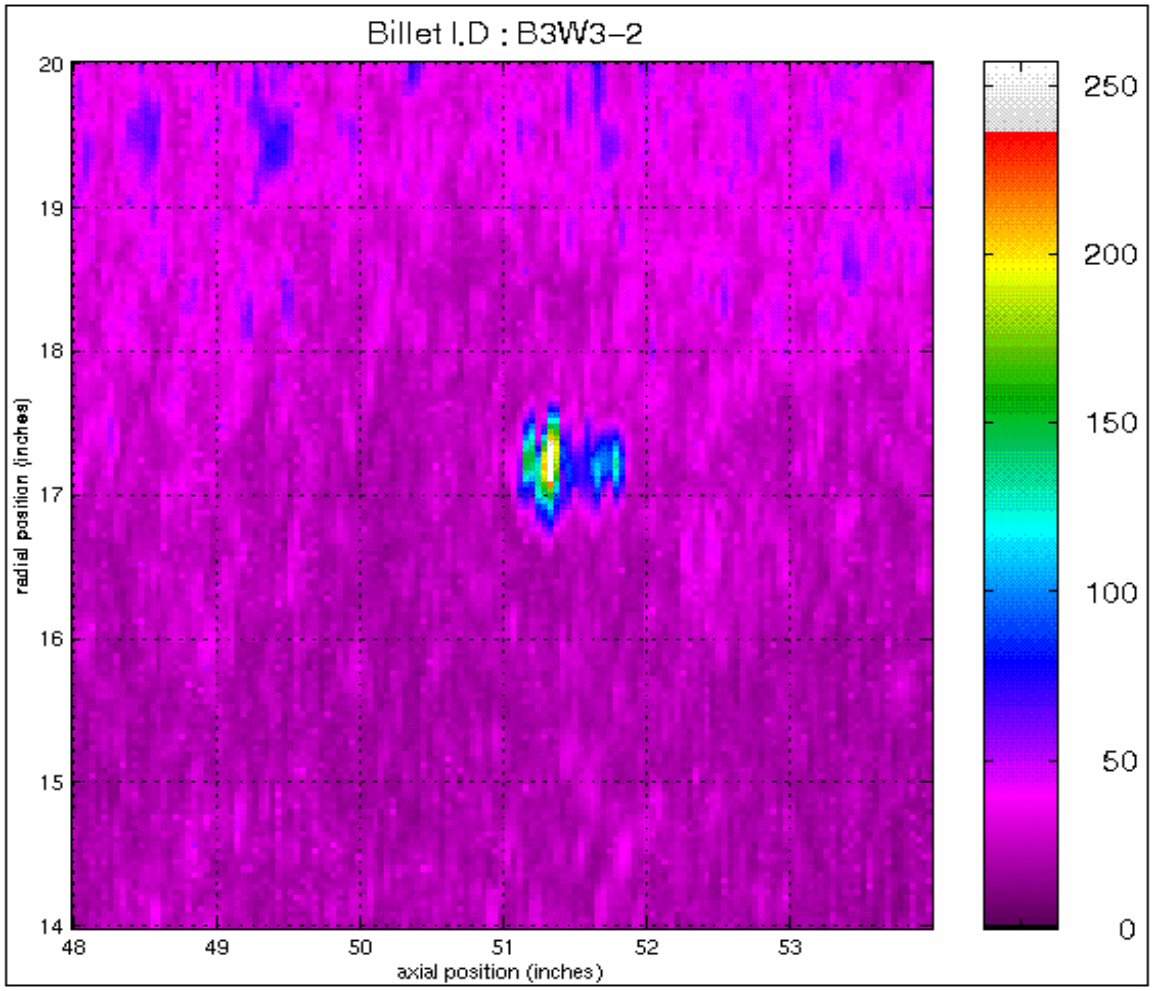


FIGURE 20. EXAMPLE OF INSPECTION RESULTS FOR BILLET B1AW1
(Results for all 12 billets are provided in appendix C.)



Billet ID: B3We-B

Zone: 1

Inches from top: 51

	Amplitude (%)	SNR	Depth (in)	Axial Length (in)	Racial Length (in)
Multizone	120	5.74	0.8	0.7152	0.2160
Conventional Longitudinal	50	2.39	1.0		
Conventional Angle	60	4.37	1.0		

Billet Length: 124.5

FIGURE 21. EXAMPLE OF C-SCAN USED IN SELECTION OF DEFECTS FOR FURTHER CHARACTERIZATION
(The complete set of defects used in the metallographic studies is provided in appendix D.)

TABLE 4. TABULATION OF THE TEN INDICATIONS SELECTED FOR DETAILED CHARACTERIZATION AND RECONSTRUCTION

Sample	Indication ID	Inspection Results			
		Multizone Amplitude SNR	Conventional Longitudinal Amplitude SNR	Conventional Angle Amplitude SNR	Depth (inches)
PoD-1	B3W3-B	MZ=120%, 5.74	CL=50%, 2.39	CA=60%, 4.37	0.8
PoD-2	B1BW3-C	MZ=127%, 6.67	CL=miss	CA=miss	0.5
PoD-3	B1BW3-D	MZ=74%, 5.06	CL=miss	CA=miss	1.5
PoD-4	B1AW3-E	MZ=47%, 2.52	CL=miss	CA=miss	1.6
PoD-5	B1AW3-D	MZ=101%, 4.49	CL=miss	CA=miss	1.1
PoD-6	B1AW3-A	MZ=142%, 5.02	CL=50%, 2.92	CA=60%, 2.48	0.7
PoD-7	B2W2-C	MZ=74%, 4.09	CL=miss	CA=miss	0.2
PoD-8	B1AW2-D	MZ=134%, 5.46	CL=50% 2.61	CA=miss	0.7
PoD-8X	B1AW2-X*	MZ=94%, 5.05	CL=miss	CA=miss	0.5
PoD-9	B1AW2-B	MZ=225%, 21.7	CL=miss	CA=miss	0.2

*Indication B1AW2-X was found near the originally selected indication, B1AW2-D and further sectioned for evaluation completing the set of ten indications.

Analysis of the inspection results included consideration of the amplitude and SNR. Figure 22 shows the distribution of amplitude and SNR for the indications. Note that no correlation was found between the multizone response and the conventional inspection results, i.e., indications detected by the conventional methods occurred over the same range of amplitude and SNR as the multizone inspection results. However, as reported earlier, more indications were found with multizone than with the conventional detection methods. Analysis of the indication response as a function of depth is plotted in figure 23. Note that detections occurred for all three methods at all inspection depths.

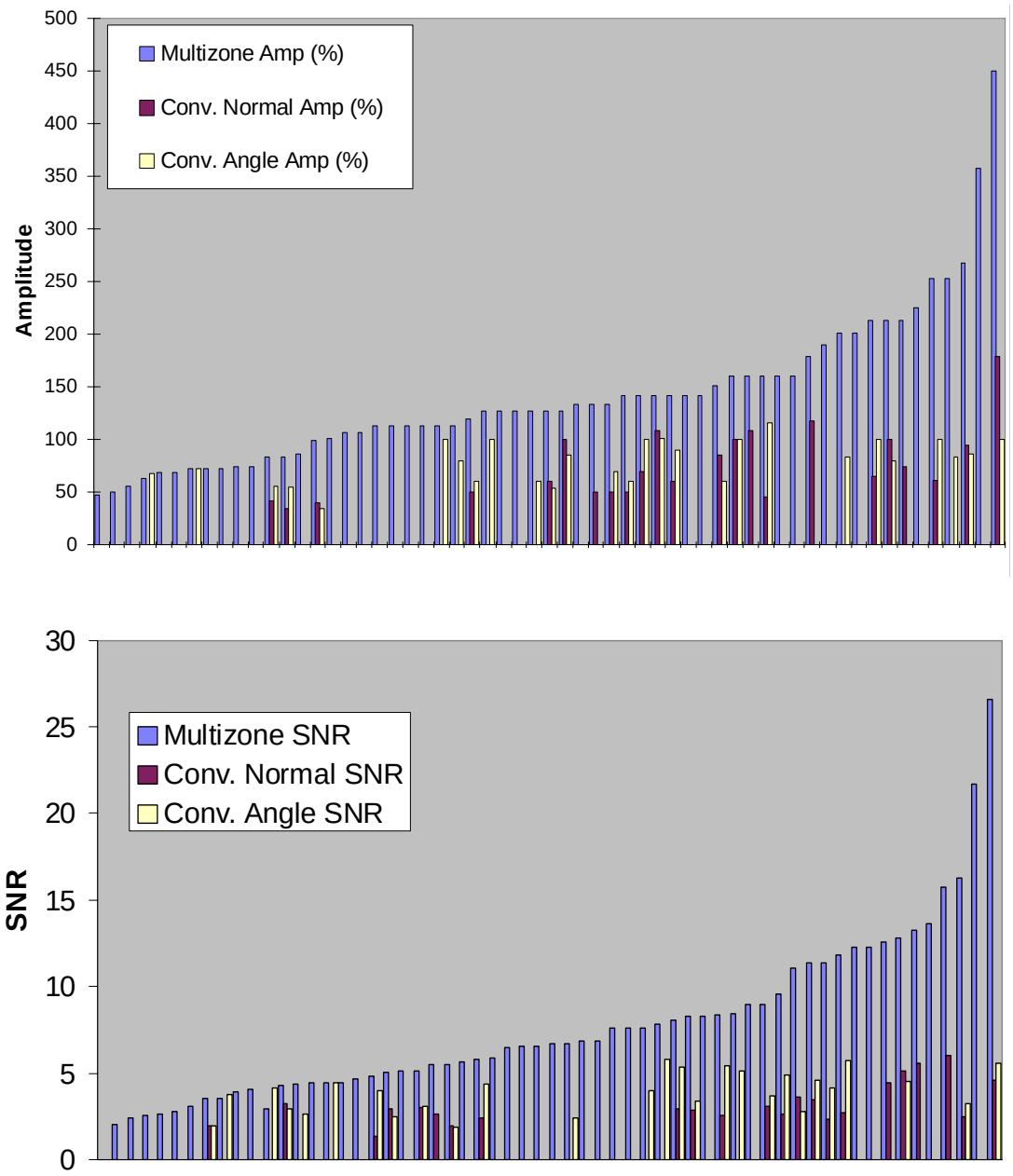


FIGURE 22. DISTRIBUTION OF AMPLITUDE EXPRESSED AS %FSH (TOP) AND SNR RESULTS (BOTTOM)

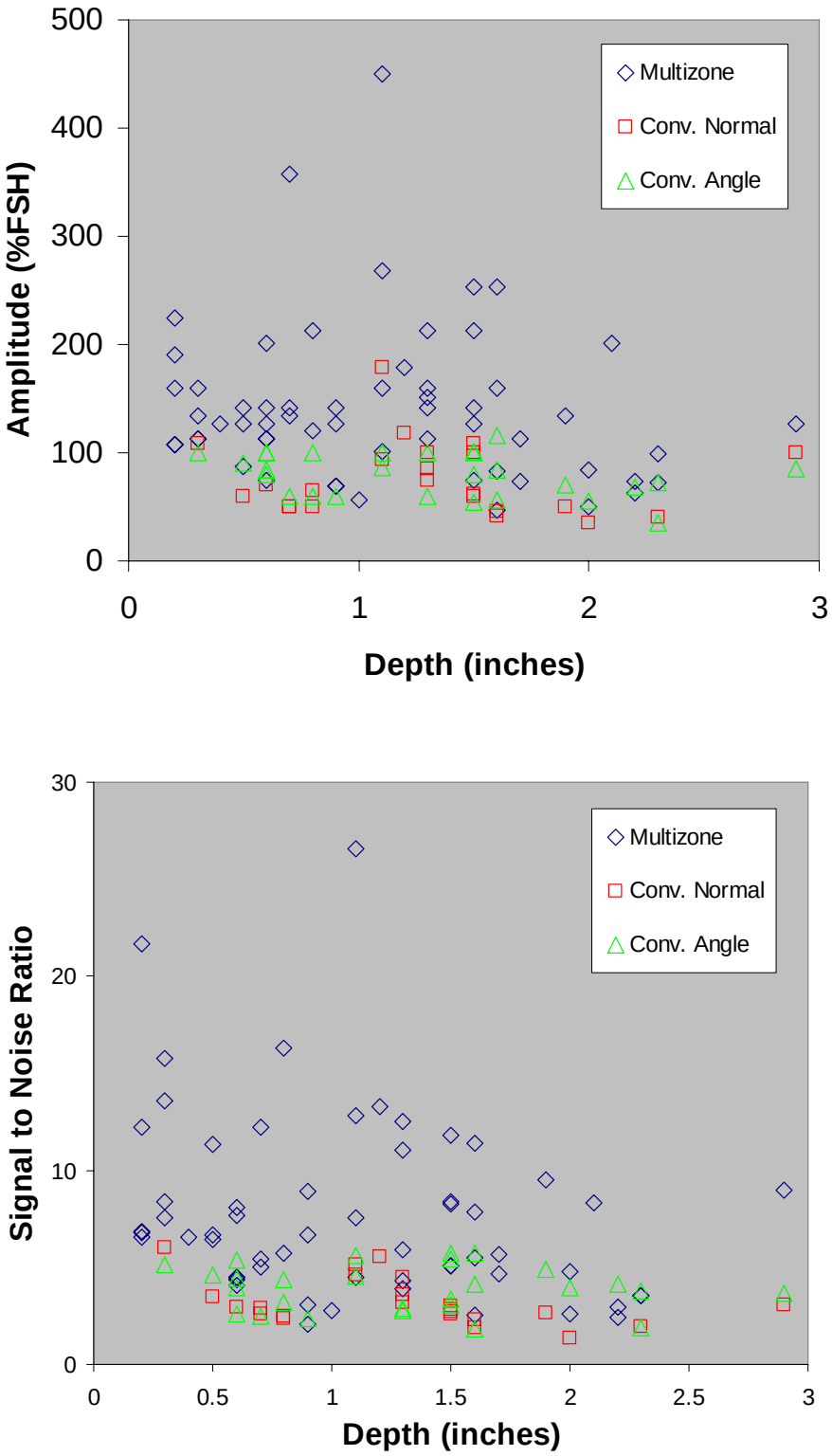


FIGURE 23. AMPLITUDE (TOP) AND SNR (BOTTOM) RESULTS AS A FUNCTION OF DEPTH

3.2 PHASED ARRAY INSPECTION OF THE CBS BILLETS.

As part of the ETC Phase I program, a feasibility study [8, 18, 19, and 20] of phased array ultrasonics was completed. This technology enables a single transducer, made up of discrete elements, to be focused electronically. The variable focusing capability allows zoned inspections to be performed on-the-fly. The original objectives were

- to review the commercially available phased array equipment and identify a source for the evaluation process.
- to evaluate the performance of the phased array transducer relative to conventional and multizone transducers.
- to access feasibility for implementing a phased array approach in a production environment.

The CBS material offered an excellent opportunity for a feasibility demonstration of the phased array approach. While the effort of this program provided a preliminary assessment, it was recognized that advances in system design, transducer design, and data analysis had occurred since the time of the work represented here. Nevertheless, these results provide an indication of the state of the technology in the mid 1990s. At the time of the program (1995), two phased array suppliers were identified with Structural Integrity Associates (SIA) selected to provide hardware and software for the feasibility study. The SIA phased array instrumentation is referred to as the Focussed Array Transducer System (FATS). The system has seven ultrasonic channels and is, therefore, limited to seven separate phased elements. This is sufficient for the simple annular array transducer designed for billet inspection. With advances in computational speed and capability, today's phased array systems typically include 128 channels, which may offer further flexibility in optimizing billet inspection. Figure 24 depicts a conventional single-zone setup versus the phased array multiple-zone setup. The most obvious difference between the two zoned inspection approaches is the requirement for either one transducer (phased array) or multiple transducers located at several positions along the billet, as shown in figure 10.

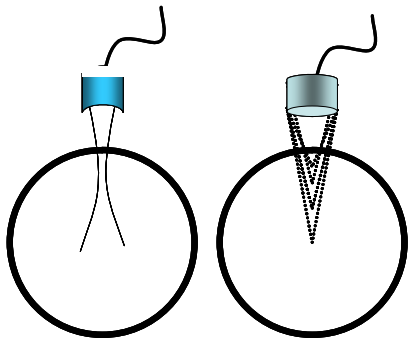


FIGURE 24. COMPARISON OF SINGLE-FOCUS TRANSDUCER (LEFT) AND PHASED ARRAY (RIGHT)
(Note that phased array concept allows inspection at multiple depths using a single transducer.)

Phased array technology involves using transducers with several (~5-7) elements to many (>100) elements. Each element has all the characteristics of a conventional single-element transducer except typically the shape. Conventional immersion transducers are typically circular with a flat, spherically or cylindrically focused face. Phased array transducers typically are configured in linear, annular, or two-dimensional (2D) configurations. Annular array transducers also come in one-dimensional (1D) and 2D forms. Though the focusing capability is axisymmetric for the simpler annular array, it is still considered a 1D array and is the approach evaluated in this program. Figure 25 depicts a simple annular transducer with seven concentric elements. Whereas a 2D annular may have five concentric rings, the rings themselves may be, for example, segmented into four segments for a total of 20 elements. More recent developments [21] have included specialized probes with up to 128 elements arranged as a sectorial annular array. This configuration will permit variable focusing and beam steering unlike the earlier 1D version evaluated in this program that only permitted variable focusing. The transducer was designed to operate at 5 MHz, the same frequency used in the conventional and multizone billet inspection. A 10-MHz center element was selected to provide improved near-surface resolution.

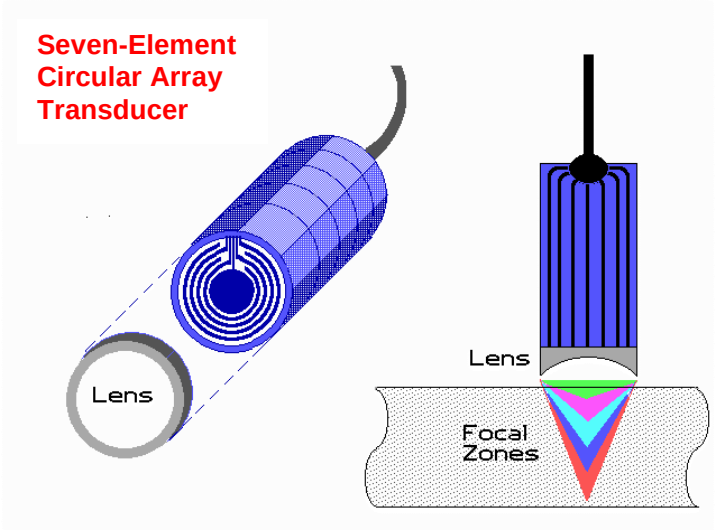


FIGURE 25. SEVEN-ELEMENT ANNULAR ARRAY DEVELOPED FOR THE CBS EVALUATION

Phased array transducers are designed and fabricated similar to conventional transducers based on a desired characteristic resonant frequency and focusing requirements. The discretization of the transducer produces separate elements that respond independently. Controlling the excitation of the electronic delay (phasing) mechanism for the individual elements provides for the variable focusing capability. Typically, at least one dimension of the elements in the array is very small, resulting in a highly divergent beam characteristic for that direction. The phasing and integration of the individual beams from each element produce the resultant beam. The overall beam will have a natural focus like a conventional transducer. For some cases in which a concave lens is mounted on the face of the transducer, the transducer takes on a new focus due to the lens. This is referred to as the geometric focus, which defines where the transducer will focus when all the elements are in phase.

The phasing process is implemented by controlling the timing of pulsing and receiving of each element relative to the other elements. By choosing the timing appropriately, the effective focus is either moved in or out relative to the geometric focus. Fundamentally, there is a maximum of a quarter wavelength limit relative to how much of a phase difference can be introduced between any two elements. For spherical focusing with an annular array transducer, the maximum delay would be between the center element and the outer most element. Note that all the elements are not typically used to create all the focal zones. Where possible, the elements are used to maintain a constant focal length/aperture ratio in an attempt to keep the beam spot size within the focal zones relatively constant. This leads to the observation, which is often confusing, that there is not a direct relationship between the number of elements and the number of focal zones. The phasing of the elements creates the focal zones, so the greater the control of phasing, the greater the number of focal zones. Another aspect of the ultrasonic inspection of contoured surfaces is the use of a mirror with a contour to counteract the distortion introduced by the inspection surface, i.e., the cylindrical surface of the billet. The mirror is designed for a specific curvature to produce a beam profile comparable to that of the beam going through a flat surface. Figure 26 shows the phased array billet inspection arrangement with the curvature-correcting mirror used in the ETC Phase I program.

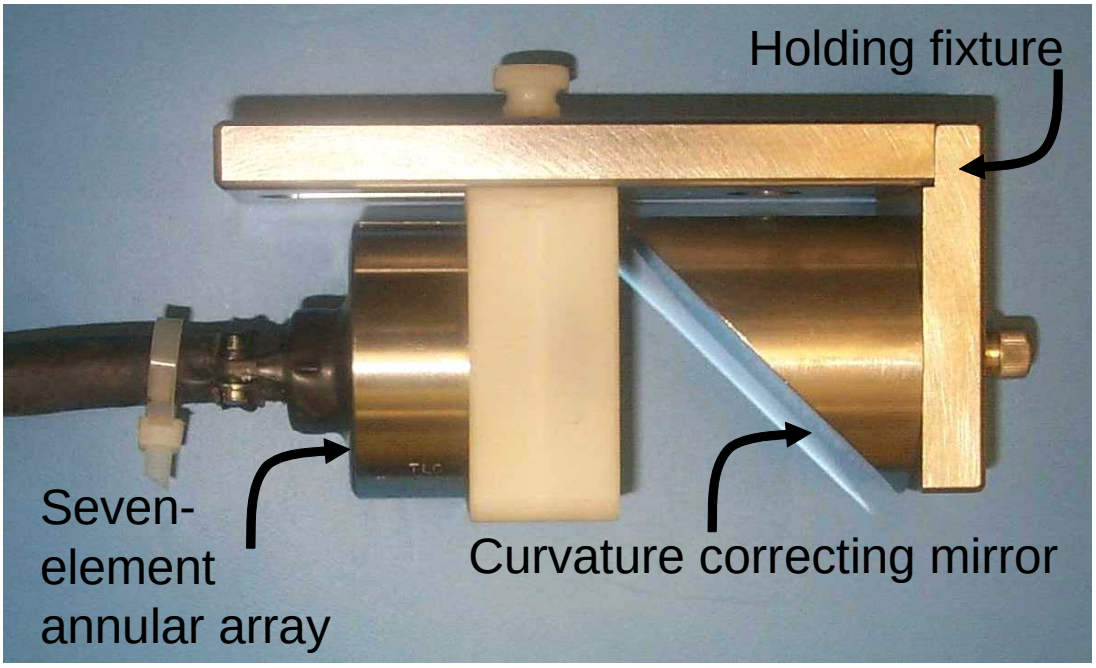


FIGURE 26. SETUP USED IN BILLET INSPECTION
(Note mirror design is optimized for a given billet diameter extending the number of billet sizes for which a single transducer can be used.)

A lens and mirror was designed to produce a zoning arrangement for the 6″ diameter material, as described in table 5. Though the first and second zone do not have a -3 dB overlap, there is a -6 dB overlap and an SNR at this depth of about 25:1. Table 5 lists the zoning scheme and the elements involved in achieving the focal characteristics for each of the zones.

TABLE 5. ZONING ARRANGEMENT FOR PHASED ARRAY INSPECTION OF CBS 6″ DIAMETER BILLET

Zone	-6 dB	-3 dB	Center	+3 dB	+6 dB	Elements
1	0.1	0.2	0.4	0.9	1.2	1
2	1.1	1.2	1.4	2.1	2.25	2-3
3	1.45	1.55	1.9	2.2	2.4	2-4
4	1.9	2.0	2.2	2.5	2.6	2-5
5	2.2	2.3	2.7	3.3	3.5	2-6

To enable C-scan data acquisition using FATS at supplier B, fixturing and cabling were fabricated. The fixturing was to adapt the FATS transducer to the ultrasonic tank bridge. The cabling interfaced with the existing encoders used by multizone for the purpose of data registration. A calibration standard specific to the FATS zoning scheme was also fabricated. The location and size of the zones in FATS are interrelated. This dependency is only a limitation of the FATS analog design and not phased array technology. A design with more control of the time delays promotes an ability to optimize the zoning arrangement. Other instruments are currently available using more flexible designs with digital capability.

The primary interfacing issues were access to the encoder signals to generate C-scan data with position synchronization, hardware interfacing to the FATS transducer fixturing, and cable lengths and grounding. The cabling and grounding issues were not resolved during the first five billet scans (B1BW1, B1AW3, B2W3, B1BW3, and B2W2), therefore, analysis of this data was not possible. B3W1B, B1AW1, and B1AW2 were run next and a rescan was performed for B1BW1 from 36″ to 84″. B1AW1 and B1AW2 had to be run in two separate scans since the billets were too long to permit scanning with the shorter cable lengths and had to be turned end-to-end to complete the scan. Amplitude and SNR were calculated for comparison to the multizone inspection results and are plotted in figure 27 with similar performance found between the two approaches. The data plotted in figure 27 is limited to zones 2 through 5 since zone 1 of the phased array transducer used the 10-MHz center element. A tabulation of the amplitude and SNR for the indications from the phased array inspection is provided in table 6.

This preliminary evaluation suggests that phased array technology could be an alternate solution for the zoned billet inspection requirements, given the data in figure 27, with the following advantages noted:

- Requires only a lens and mirror change for each billet diameter versus potentially a different set of transducers, reducing the overall cost.
- Complexity of the fixturing is reduced significantly over multiple discrete transducers.
- Setup is simpler since only one transducer is involved.

Other factors such as capital equipment costs, system reliability, operator training, and equipment durability are unknown at this time.

TABLE 6. SIGNAL TO NOISE AND AMPLITUDE DATA FROM PHASED ARRAY INSPECTION

Billet ID	Defect ID	SNR	Amplitude (%)	Depth (inches)	Position From Top (inches)
B1AW1	A	4.3	56	0.2	3.3
B1AW1	B	4.06	75	0.6	25.9
B1AW1	C	12.53	179	1.6	66.4
B1AW1	D	5.66	99	1.7	92.7
B1AW1	E	3.07	76	0.6	95.2
B1AW2	A	12.15	253	0.3	42.5
B1AW2	B	5.93	101	0.2	72.0
B1AW2	C	6.31	113	0.8	89.0
B1AW2	D	5.4	94	0.7	98.0
B1AW2	E	6.87	179	1.3	104.0
B1AW2	F	4.5	142	1.1	114.4
B1AW2	X	2.92	61	0.5	98.7
B1AW3	A	3.82	69	0.7	60
B1AW3	B	2.54	86	0.9	63
B1AW3	C	11	357	1.5	79
B1AW3	D	3.78	98	1.1	94.8
B1AW3	E	2.06	47	1.6	106
B1AW3	Y	3.24	99	1.3	77
B1AW3	Z	3.47	90	1.3	81
B1BW1	A	5.08	225	2.2	21.8
B1BW1	B	10.12	179	1.7	28.5
B1BW1	C	6.43	113	0.6	44.8
B1BW1	D	4.22	94	1	49
B1BW1	F	14.47	357	1.1	67.8
B1BW1	G	6.68	142	1.5	81
B1BW1	H	6.18	82	0.4	99.5
B1BW3	A	3.24	94	1.3	22
B1BW3	B	3.45	61	1.1	43.5
B1BW3	C	5.66	73	0.5	66
B1BW3	D	4.36	99	1.5	86
B2W2	B	3.99	66	0.6	14
B2W2	D	2.37	76	0.6	55
B2W2	X	2.04	36	0.55	57
B2W3	A	6.12	80	0.2	20.1
B2W3	B	3.27	160	2.3	27.8
B2W3	C	3.3	58	2	31
B3W1B	A	8.57	357	2	68.8
B3W1B	B	3.8	179	2.2	84.8
B3W1B	C	2.78	142	2.3	102.5
B3W1B	D	2.36	127	1.9	104.3

Note: Not all billets were inspected with the phased array setup.

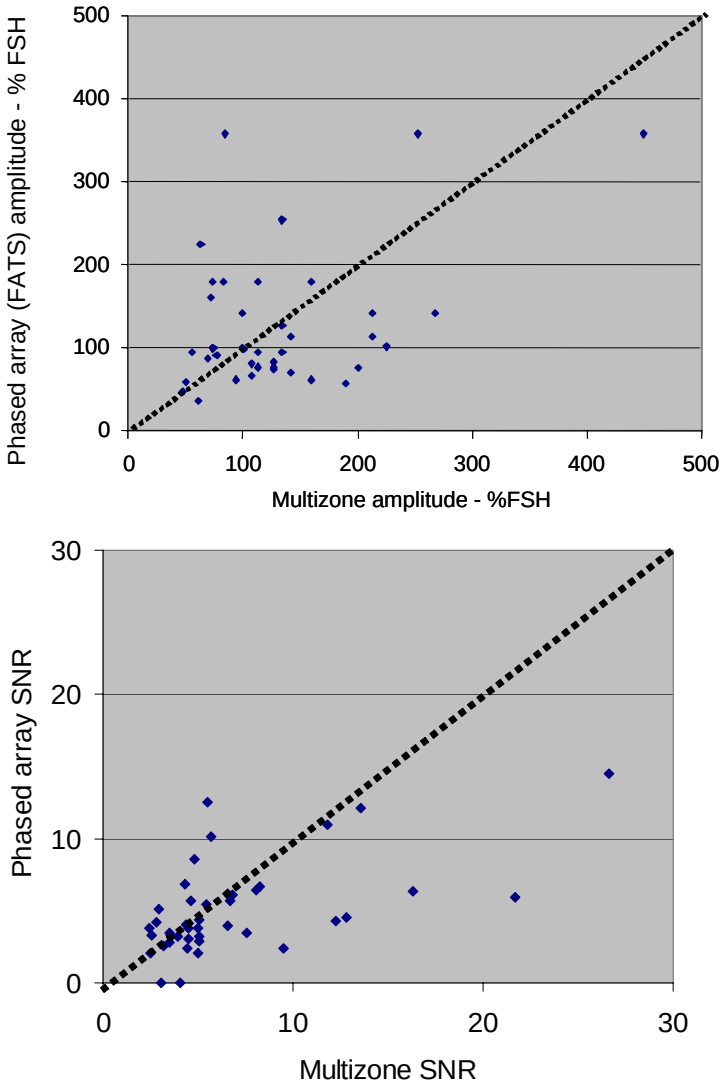


FIGURE 27. COMPARISON OF AMPLITUDE (TOP) AND SNR (BOTTOM) FOR PHASED ARRAY AND MULTIZONE INSPECTION OF CBS BILLETS

3.3 DEFECT CHARACTERIZATION.

As listed in table 4, ten defects were selected for detailed characterization and reconstruction for use in PoD studies. Ultrasonic results from the billet supplier were reviewed to determine the location of the defect. Mults were sectioned from the billets such that the desired indication was positioned in the center of the mult, providing the needed material envelope to begin the ultrasonic characterization. The characterization process included a 5-MHz multizone zone inspection at the depth of the indication. The mult was then sectioned from the billet leaving a 1.0″ envelope of material surrounding the indication where possible. The sample containing the indication was referred to as the 3″ cube. A 5-MHz scout inspection was done on the 3″ cube to guide further sectioning. Only depth information was collected during this process. The 3″ cube was then sectioned so that approximately 0.500″ of material envelope surrounded the indication where possible. The sample containing the indication was referred to as the 1″ cube. The 1″

cube was then ultrasonically characterized with a 25-MHz, F10 transducer focused on the indication. The cube was scanned at a 0.010″ index with a 100-MHz sampling rate, both C-scan and waveform data were collected. The process is depicted in figure 28. After completion of the ultrasonic characterization, the sample was shipped to the metallography team for sectioning, micrograph capture, and microprobe analysis. The results for the first indication are discussed in detail below with the results for all ten indications provided in appendix E.

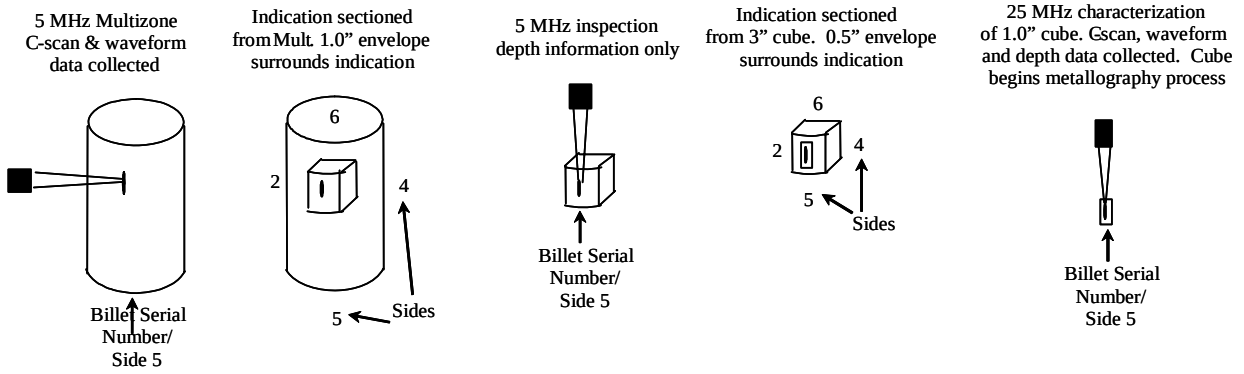


FIGURE 28. PROCESS USED FOR ULTRASONIC CHARACTERIZATION OF THE INDICATIONS

The first of the indications came from billet B3W3. Indication B was sectioned from the billet at the axial position of 51.0″. Initial characterization and sectioning was completed at GE with the results shown in figure 29. The sample was then shipped to ISU for detailed ultrasonic characterization. The results are shown for side 4 in figure 30. After completion of the ultrasonic measurements in the 1″ cube, the samples were shipped to Pratt & Whitney for sectioning, capture of the digital micrographs, and microprobe analysis. For indication B3W3-B, 21 sections were required to polish through the indication. The results for several of the slices are shown in figure 31. Four sections were selected as representative of the defect. The first section shows the initial occurrence of diffusion zone and serves as the section from which other sections are measured. In the third section, taken at 15 mils, the occurrence of voiding is noted with more expansive voiding present in the 60-mil section. The last section occurred at 95 mils and shows the last remnants of diffusion zone for this sample. Note that for the 60-mil section, over 35 micrographs were taken and digitally pasted to generate the montage shown in figure 31. In some of the more extended defects, the number of micrographs required to fully capture the defect in a given section plane exceeded 120, generating copious amounts of metallographic data.

For indication B3W3-B, microprobe measurements were made after the fifth and eleventh sections and are provided in figures 32 and 33 respectively. Full tabulations of the data are provided in appendix E. Note that the concentration is highest in the core and drops rapidly away from the core. Even within the areas where the microstructure is distributed, i.e., area that would typically be classified as diffusion zone, the concentration is already at less than 1 wt% nitrogen. Given the narrow region over which the high nitrogen concentration occurs, the impact of the nitrogen on ultrasonic response is minimal (see related figure and discussion in section 3.4).

Mult inspection parameters:
Transducer- Zone 1, 6″ diameter, 5MHz
Index - 0.010
Data Acquisition Rate - 0.010
Inspection Sensitivity- #2 FBH at 80-90% in Titanium
Inspection Range- 0.2″ to 0.8″
Sampling Rate- 100 MHz

Depth	Axial Length	Amplitude	Signal-to-Noise Ratio
0.8	0.8”	127%	5.7

View is from Side 1, the side which was polished. Sides 5 and 6 represent the axial ends with Side 5 having the serial number. Sides 2 and 4 represent the hoop direction (the circumferential plane)

25 MHz inspection parameters
Transducer- 25 MHz, F10- focal point positioned at indication depth
Index - 0.010
Data Acquisition Rate- 0.010
Inspection sensitivity- #2 FBH at 84% at
Inspection range- C- scan, Between Front and Back/B-scan entire volume
Sampling Rate- 200 MHz

Side	Depth	Axial Length	Amplitude %	Sensitivity, dB
1	0.444″	0.8″	66	60
2	0.496″	0.8″	93	60
3	0.453″	0.8″	76	60
4	0.399″	0.8″	96	60
5	0.460″	0.8″	73	74
6	0.435″	0.8″	79	72

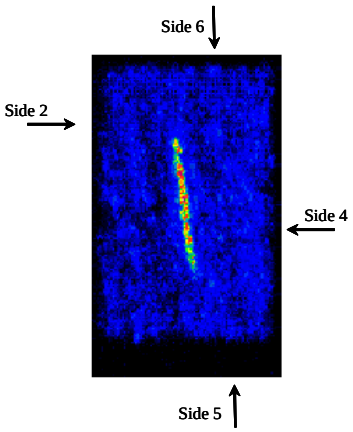


FIGURE 29. ULTRASONIC CHARACTERIZATION FOR B3W3 INDICATION B

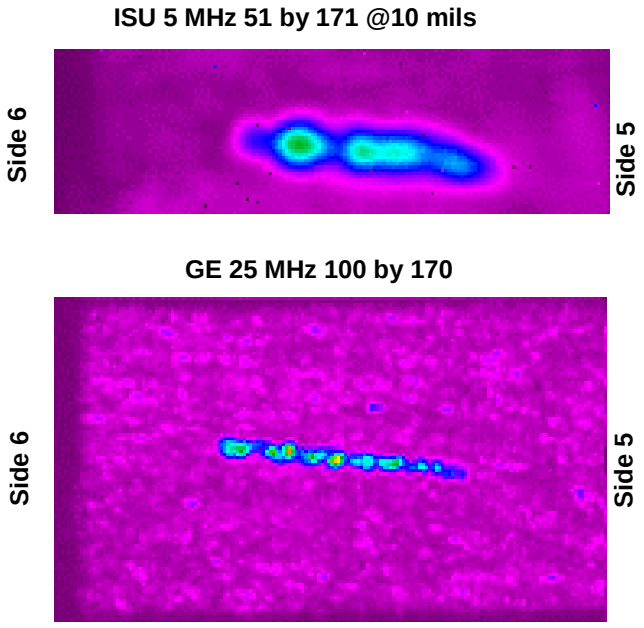


FIGURE 30. ULTRASONIC CHARACTERIZATION AT CUBE STATE PRIOR TO METALLOGRAPHIC SECTIONING OF B3W3 INDICATION B
(Results are shown for side 2 at 5 MHz (top) and 25 MHz (bottom).)

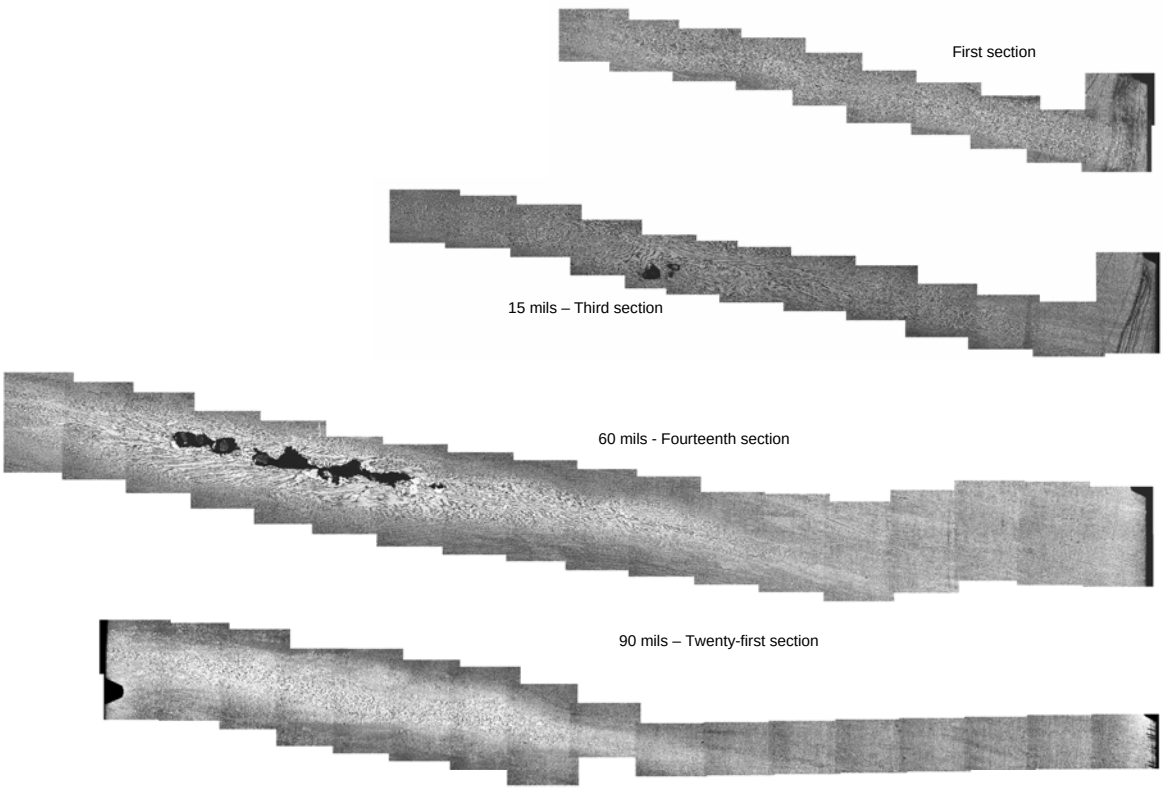


FIGURE 31. SELECTED METALLOGRAPHIC SECTIONS FOR SAMPLE B3W3-B
(The montages shown here were generated from a series of 3″ x 5″ micrographs taken at 100X magnification that were digitally pasted to form the image for the full indication.)

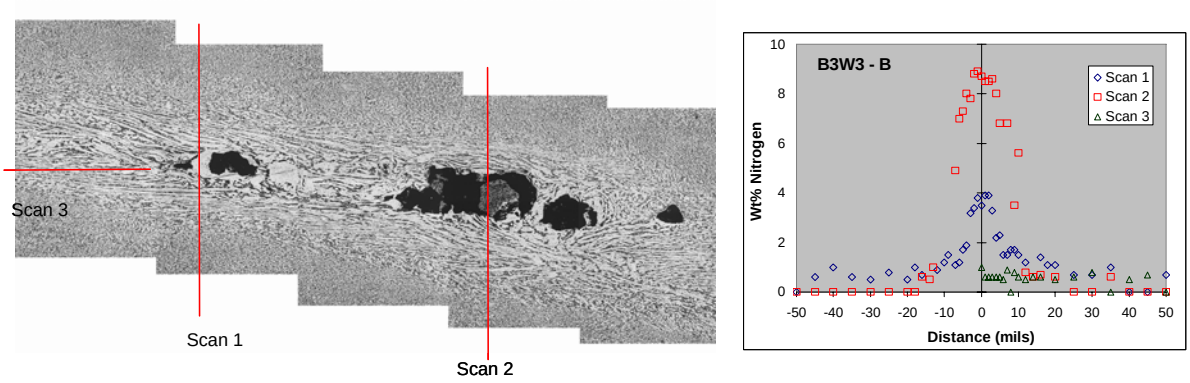


FIGURE 32. MICROPROBE RESULTS FOR SECTION 5
(APPROXIMATELY 20 mils) IN DEFECT B3W3-B
(Three scans were made, as shown on the micrograph. The results are plotted for nitrogen concentration as a function of distance from the core. Note that the longitudinal scan (scan 3) extended away from the indication with nitrogen levels at nominal levels out to 400 mils (data not plotted past 50 mils).)

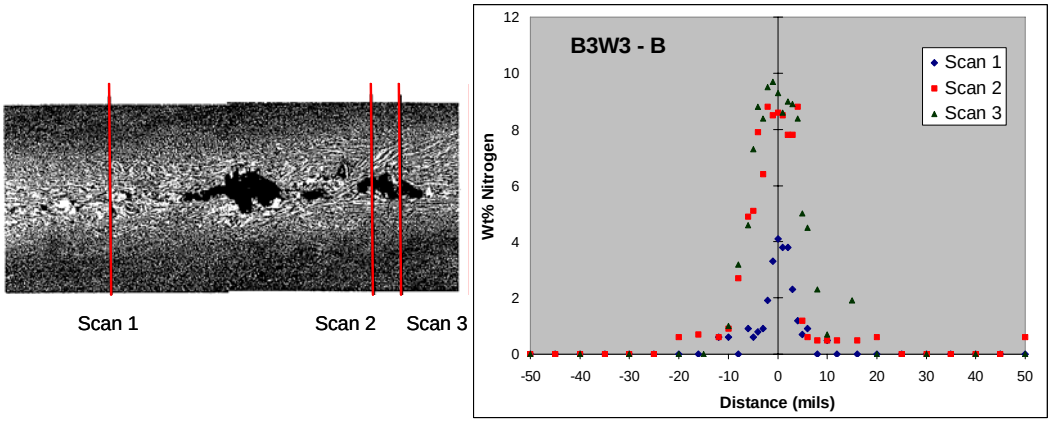


FIGURE 33. MICROPROBE RESULTS FOR SECTION 11 (APPROXIMATELY 65 mils) IN DEFECT B3W3-B
(Three scans were made, as shown on the micrograph. The results are plotted for nitrogen concentration as a function of distance from the center of the core.)

Complete defect characterization results for each of the ten indications is provided in appendix E. Specific highlights for each individual indication are provided in summary form to conclude appendix E. The defect characterization was completed with a dual purpose: (1) to improve the detailed understanding of hard alpha defects for use by metallurgists, life management, design, and inspection personnel and (2) to provide input into PoD calculations and, in particular, for use in model validation, as discussed in the following.

3.4 GENERATION OF GEOMETRICAL DATA FOR USE IN PoD CALCULATIONS.

PoD plays an important role in estimates of engine life, which requires an understanding of the relationship between detectability and flaw size. Many factors impact the detectability of a given flaw including the size, shape, and orientation of the flaw; the chemical composition of the defect; the location in the component (depth); and the geometry/part factors (curvature, surface finish), all of which should be taken into account in the design of the inspection. The efforts of this program were to provide basic knowledge to improve the detection of hard alpha by developing an understanding of the acoustic, physical, and chemical properties of hard alpha and incorporating those into PoD considerations. In meeting these objectives, the following steps were accomplished:

- Quantify the ultrasonic response.
- Quantify the defect descriptors, including the shape and distribution of voids, the general microstructural variations associated with core and diffusion zones, and the relationship of these to chemical composition.
- Develop and verify a model for predicting the ultrasonic response in terms of defect descriptors.
- Use this information to access and improve detection reliability.

In the past, PoD studies normally required statistical analysis of large amounts of experimental data. However, the rare occurrence of naturally occurring hard alpha defects and the difficulty of manufacturing realistic synthetic flaws have made data acquisition very difficult. To get around this obstacle, a new approach has recently emerged using ultrasonic models to accurately calculate the flaw responses. These require, as input parameters, geometrical models containing the spatial and material descriptions of the flaws. By using models in this way, one was able to examine the effect of flaw morphology on the ultrasonic signals in a reasonable time frame and to extract a more extensive knowledge base from the limited naturally occurring flaws. In addition, a variety of inspection scenarios can be simulated rapidly to generate the necessary data for PoD evaluation. The efforts of the ETC Phase I program advanced this new approach with the CBS providing an unprecedented opportunity to gain extensive knowledge on naturally occurring hard alpha defects. As was previously stated, ten of the indications were chosen as representative sample defects for these studies, and various experimental data have been obtained by ultrasonic, metallurgical, and chemical analyses to determine the detailed morphology and composition of these defects.

During the early stages of the CBS, it was assumed that the ultrasonic response of the hard alpha defect came from the whole hard alpha region consisting of diffusion zone, hard alpha nuggets, and the void/crack components. Effort was focused on improving the capability in geometric and ultrasonic modeling for the entire hard alpha defect, including each of the subregions. A number of software building blocks were developed [22 and 23]. Based on metallographic data of real hard alpha defects, solid geometric models of subregions treated initially as if they had uniform acoustic properties were developed. Various methods to determine and extract the flaw boundary on the metallographs were also developed (see appendix F). The ultrasonic response was derived from the Thompson-Gray measurement model framework using the Born Approximation [24]. The Born inclusion model was thoroughly tested using output of the solid models and several data sets of synthetic hard alpha inclusions of known size and properties [22 and 24].

As results of the microprobe/chemical analyses became available during the program, ETC gained a much better understanding of the microstructures of the hard alpha defects. The microprobe/chemical analyses revealed that the nitrogen concentrations are only high in thin layers up to approximately 10 mils around the void components of the hard alpha defects (see figures 32 and 33). At the edges of these regions, there is a sharp transition to much lower levels, characteristic of the diffusion zone. This localized nitrogen concentration led to a profile of acoustic properties that peaks around the void boundary and rapidly decreases to the baseline of the normal titanium moving away from the voids. This has important ultrasonic implications. It is well known that regions of slowly varying acoustic properties produce only weak ultrasonic signals, whereas sharp boundaries produce strong signals. Since rapid changes only occur near the voids, this suggests that the voids and the near-void region in which nitrogen is high, will produce the majority of the ultrasonic response. Based on this finding, a new material model was developed to estimate the acoustic properties throughout the titanium alloys, including the hard alpha regions [25]. The essential feature of that work was the study of the effects of hard alpha layers, i.e., the core and diffusion zones, on the ultrasonic responses in the presence and absence of voids/cracks. The major results of that study are summarized in the following paragraph.

To obtain an accurate benchmark to test the Born inclusion model for such nonuniform property profiles, an exact solution for a spherical-shaped inclusion with varying properties was derived from the classic Ying-Truell result [26]. For a spherical hard alpha inclusion, this new exact solution approximates the nonuniform material profile piecewise by a number of concentric spherical shells of uniform properties. The simulation result showed that the contribution of these thin layers to the total ultrasonic response of the hard alpha defects, compared with those from the void components, is insignificant. Figure 34 compares the peak amplitudes of the inclusion and void, with or without the hard alpha shell, for different inclusion diameters (in terms of FBH numbers). For either inclusion or void, the amplitudes only change slightly with hard alpha shells included. Based on this study, effort was focused only on the void components in the subsequent modeling work. In the geometric model development, this shifted attention from the earlier solid models of full hard alpha regions to the surface models of the void components. However, it should be pointed out that the basic theory of nonuniform rational b-splines (NURBS) developed in the solid model case still hold for the newer surface model (see appendix G).

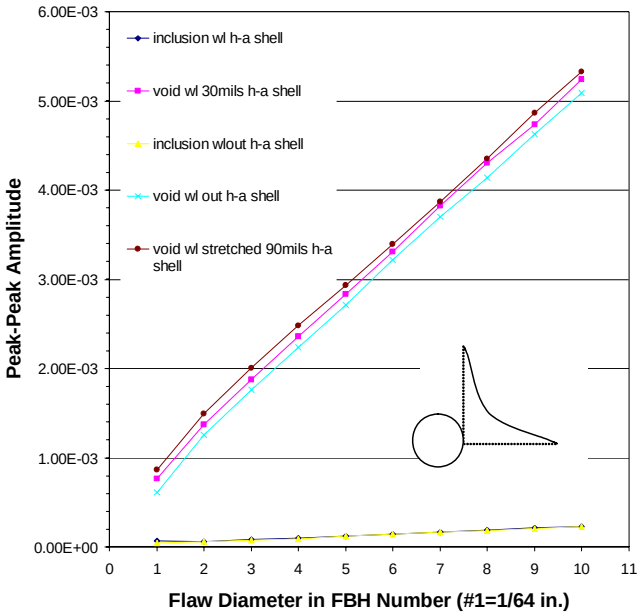


FIGURE 34. PEAK AMPLITUDES OF INCLUSION AND VOID WITH AND WITHOUT THE HARD ALPHA SHELLS FOR DIFFERENT INCLUSION DIAMETERS

3.4.1 Geometrical Modeling.

To generate the necessary flaw surface data for each of the ten hard alpha defects, a multistep process was required. Here, defect B1AW2-X is used as an example to illustrate the various steps. Detailed results of the other nine defects are provided in appendix E. To obtain the necessary information from the hard alpha defects for geometrical reconstruction, the exact locations of the defects in the billets were first identified ultrasonically. As detailed previously, small blocks of 1- to 2-inch dimensions containing these defects were then cut from the billets, followed by both 5-MHz and high-frequency ultrasonic scans taken from each of the six sides.

These scans included volumetric A-scans and C-scans, which will be compared later with the ultrasonic model predictions. Prior to the destructive sectioning, on the two opposite sides of the cube block along the original billet axial direction, microscopic fiducial marks were drilled into the cube block parallel to the sectioning direction. These fiducial marks served as the common alignment reference for later stack up of the metallographs for reconstruction. The sectioning process was carried out by successive polishing of the block surface at small increments from 2 to 10 mils. After each polishing session, the cross sections were photographed through an optical microscope to form the metallographs. Next, the metallographs were realigned by using the fiducial marks and other features on the metallographs. These submetallographs provided the main data bases for building the geometrical models. Figure 35 shows polishes 8-13 of the realigned and reduced cross-section images used to reconstruct defect B1AW2-X, depicting the complicated geometry of the void structures. Figure 36 illustrates the orientation and stack-up sequence of these metallographic images.

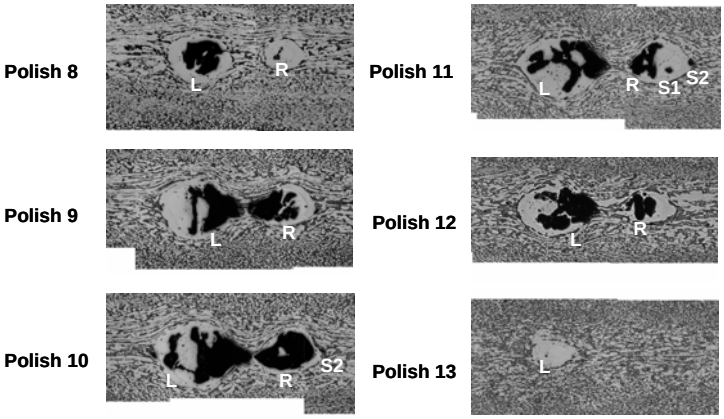


FIGURE 35. POLISHES 8-13 OF THE REALIGNED AND REDUCED CROSS-SECTION IMAGES USED TO RECONSTRUCT DEFECT B1AW2-X
(Each image is of 256 gray-scale level, 1000(H) by 500(V) pixels in size.
The dimension scale is 135 pixels = 10 mils.)

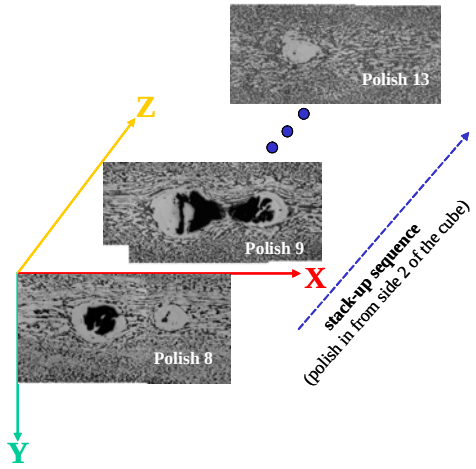


FIGURE 36. STACKING ORIENTATION OF THE METALLOGRAPHS OF HARD ALPHA DEFECT B1AW2-X

The most important step of the process is to identify the void parts and to determine their connectivities, i.e., the blue prints showing how corresponding void cross-section boundaries on adjacent metallographs are connected. The labels associated with each void cross section (L, R, S1, and S2) in figure 36 are the simplest connections among the ten selected hard alpha defects. Figure 37 shows an example of one of the more complicated voiding structures from defect B1BW3-C. The connectivity trees shown in figures 36 and 37 were generated for each of the ten defects.

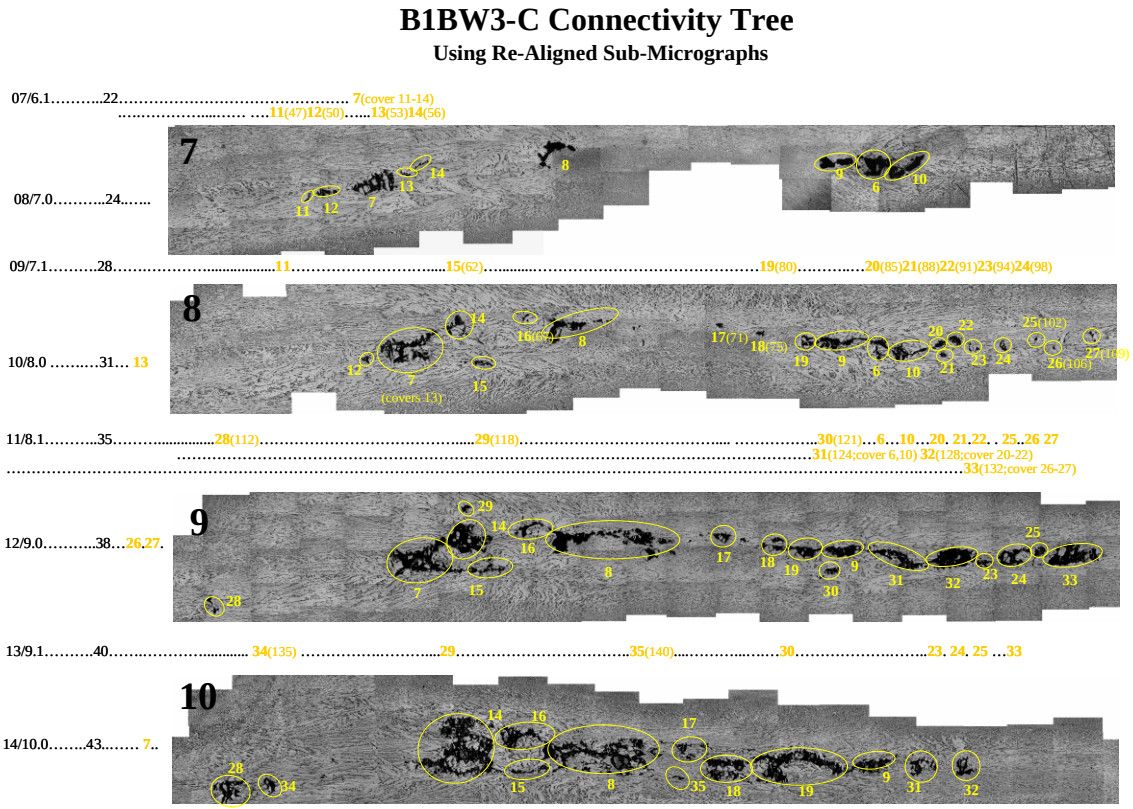


FIGURE 37. EXAMPLE OF MORE COMPLICATED VOID CONNECTIONS
(Results are shown for slices 7 through 10 of indication B1BW3-C. Numbers used to track voids between slices are shown in yellow.)

The other important step is to accurately and efficiently determine the enormous number of boundaries from these void cross sections. To automate this step, several edge detection techniques were applied from image-processing tools, including the regional growth technique discussed in appendix F. However, none of these techniques were found to adequately handle the complexity of the void boundary structures. Therefore, it was decided that tracing the boundary manually by using a screen locator was the most suitable method for this task.

Before the 3D surface models of the void parts could be reconstructed, all cross-section boundary traces of each void part must be parameterized. Using the manually traced data as input, this parameterization involved 2D interpolation of these cross-section boundaries using the NURBS technique. Figure 38 compares several boundary trace projections of the right void

of B1AW2-X, showing both the manually traced and the NURBS interpolated data. It is seen that NURBS works very well in tracking the rather complicated manually traced boundaries. Using the connectivity plan (figure 36) and the parameterized 2D cross-section boundary data (figure 38), the 3D surface model of a void part can then be built by interpolating the corresponding points on all cross-section boundary traces of the same void part. (See appendix F for details.) Three angle views of the 3D surface model for defect B1AW2-X are shown in figures 39 and 40, showing its physical dimensions.

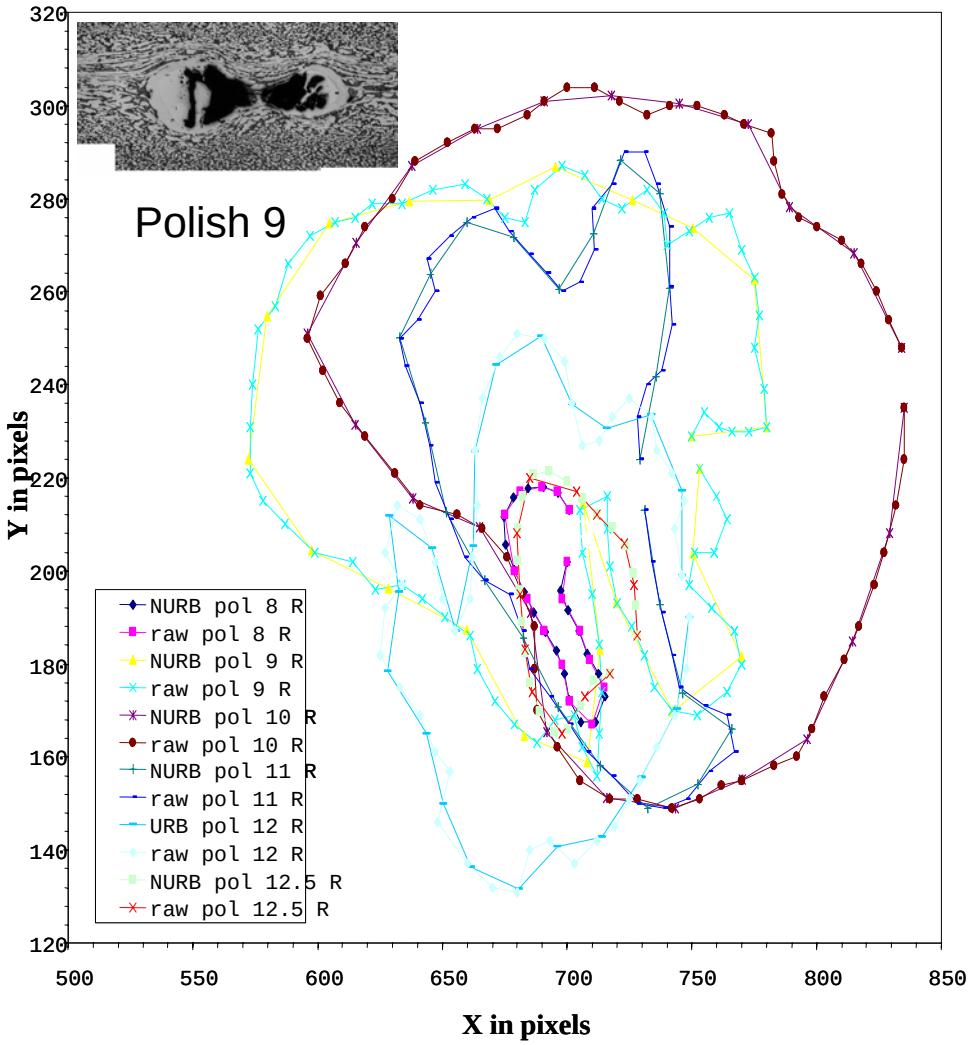


FIGURE 38. RAW VS NURB VOID BOUNDARY TRACE PROJECTION: RIGHT VOID OF B1AW2-X

In this particular model, 3702 spatial coordinate points were used to construct 7388 triangular facets on the discrete defect surface. The size of the defect is about 52 x 18 x 34 mils, with the 52-mil dimension at a slight tilt from the original billet axis. The size of the triangular facets was maintained around one-tenth of the ultrasonic wavelength at the upper quarter of the frequency spectrum. This size ratio was selected to ensure the convergence of the ultrasonic model calculations.

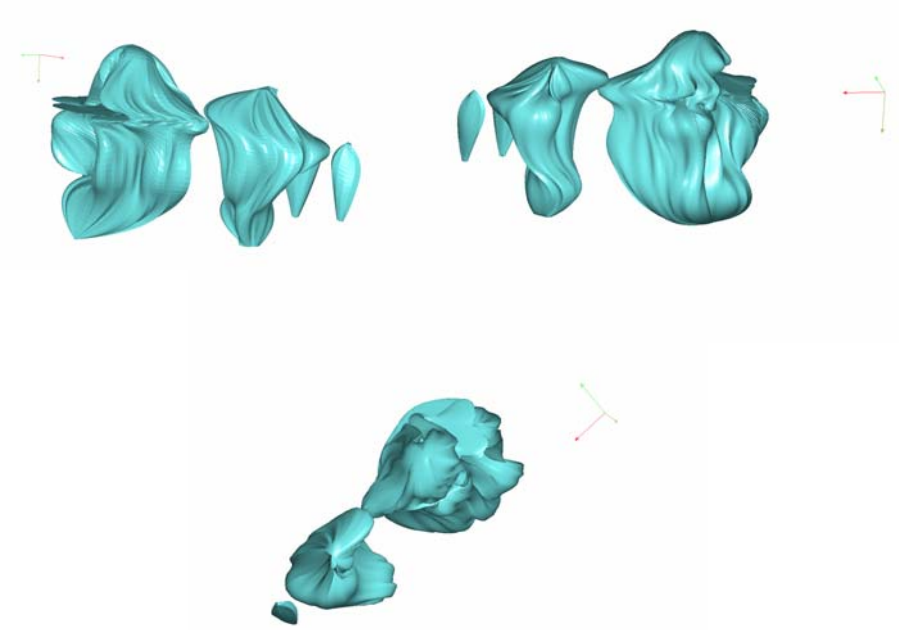


FIGURE 39. THREE ANGLE VIEWS OF THE SURFACE MODEL FOR DEFECT B1AW2-X

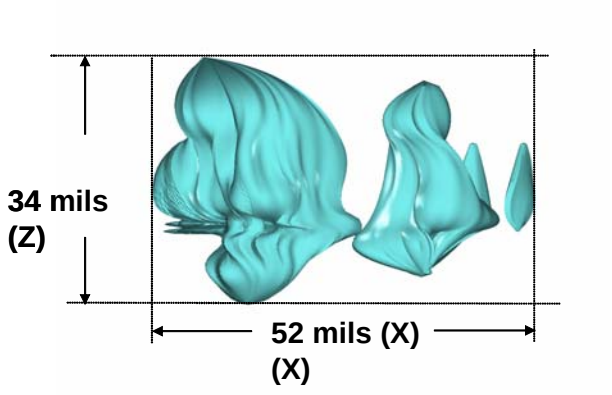


FIGURE 40. ACTUAL DIMENSIONS OF DEFECT B1AW2-X
(The dimension in Y direction is 18 mils.)

To construct a geometric surface of an irregular shape that is representative of a typical hard alpha defect, cross-section boundaries of the defect must be available in adjacent micrographs. When this requirement was not met, supplemental boundary patches were derived from neighboring micrographs. Every identifiable void cross section, shown as a dark area in the micrograph, is numbered on each micrograph for use in the reconstruction. The other situation in which patches are needed is when extreme shape change occurs between two adjacent boundary cross sections. The middle ground patches make the transition of the shape change smoother so that a geometrically feasible model can be constructed. Polish 12.5 in figure 38 depicts one such example. Many other patches were used in much more complicated connective structure of the other hard alpha defect reconstructions (appendix F).

3.4.2 Ultrasonic Modeling.

In this section, the ultrasonic modeling results of defect B1AW2-X are described using a multifacet Kirchhoff model. For details of this and other ultrasonic models, the reader is referred to appendix G.

After the geometrical surface model consisting of multiple triangular facets was created as described above, a global beam tracking routine needs to be performed so that proper coordinate information of the illuminated defect surface can be provided to the ultrasonic models. Given an origin source (beam), the objective was to determine which facets on the surface of the model would be illuminated with how much incident amplitude, the area covered by the source (beam radius), and the direction in which the beam is propagating. This was done by using a forward ray-tracing technique. Figure 41 demonstrates the beam-tracking analysis completed on a void, where the beam coverage (size) of the flaw, as indicated by the central white region, was reduced for purposes of illustration.

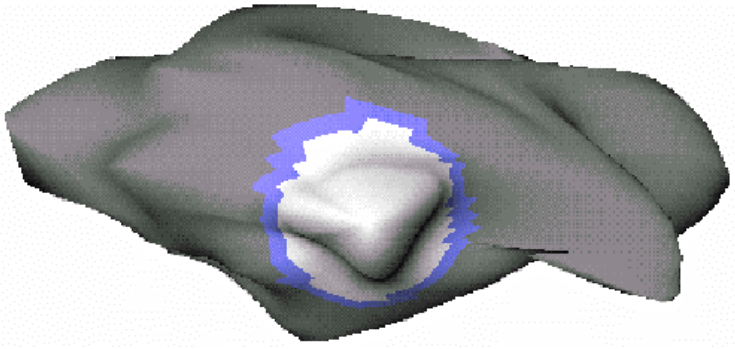


FIGURE 41. EXAMPLE OF FLAW ILLUMINATION BY ULTRASONIC BEAM

The illuminated geometric information then serves as input to the ultrasonic model to calculate the flaw signals. As described previously, the morphology of hard alpha defects is complicated. Exact models capable of predicting the ultrasonic responses of real defects with such complexity are not available. If exact models were available, current technology does not provide sufficient and accurate morphological data. Thus, modeling efforts were focused on the use of approximations to reduce the complexity. An approximate ultrasonic model using the high-frequency Kirchhoff approximation has proven to be successful for modeling hard alpha defects [23]. The Kirchhoff model is particularly suitable for making use of the multifaceted data of the defect surfaces provided by the geometric model. Following previous ultrasonic model development [24 and 27], the new void model was also derived from the Thompson-Gray measurement framework [28] and the Auld's reciprocity formulation [29]. The unique feature of this approach was that radio frequency waveforms (A-scans) were calculated directly and can be compared with the actual measurement on an absolute level. Figure 42 shows the coordinate system defining the orientation of the cube containing the defect, and figure 43 displays the C-scan comparisons between the model and experiment for defect B1AW2-X. It can be seen that the agreement in both peak amplitude and image shape are very good with the largest difference only being 5.7 dB.

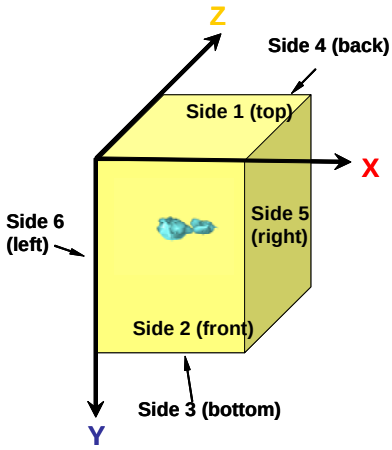


FIGURE 42. BLOCK ORIENTATION FOR EXPERIMENTAL ULTRASONIC MEASUREMENTS
(Sides 5 and 6 are in the billet axial direction. Sides 1 and 3 are in the original direction of billet (beam) inspection.)

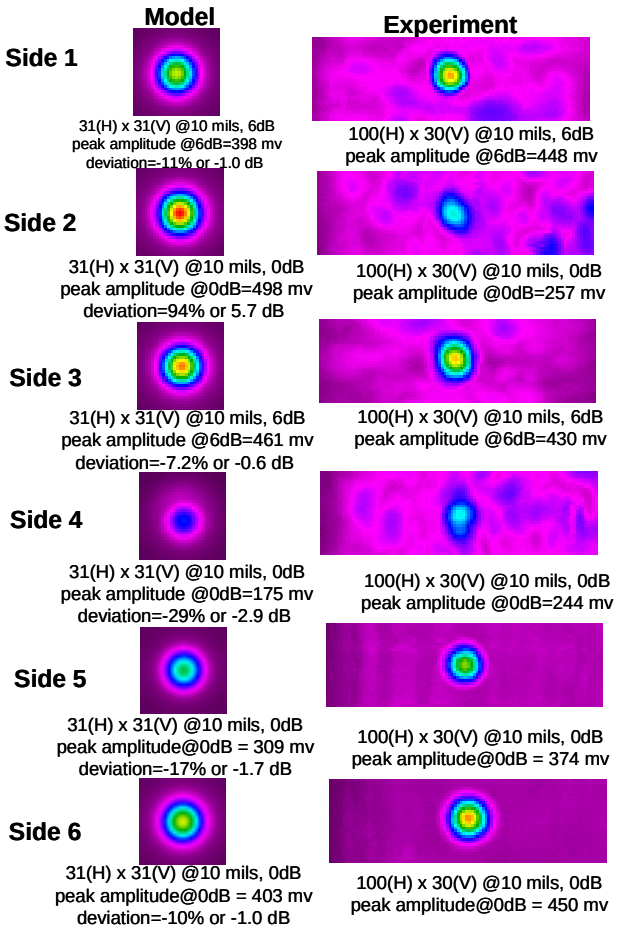


FIGURE 43. COMPARISON OF ULTRASONIC C-SCAN RESULTS, MODEL AND EXPERIMENT

3.4.3 Error Analyses.

As described in section 3.4, the characterization and modeling of each of the hard alpha defects is a multistep process. There are at least five potentially significant error sources that occur in the process.

- Ultrasonic measurement error may occur during ultrasonic data acquisition from the blocks. Even in a carefully controlled laboratory setting, a 10% daily fluctuation (0.8 dB) in the measurement is not unusual.

- The procedure for sectioning and capturing micrographs, material pullout, nonuniform etching, and insufficient light exposure can lead to incorrect interpretation of the cross-section images and lead to micrograph production error.

- Micrograph alignment errors are introduced when spatial registrations of information from successive sections with respect to a common reference cannot be maintained. In some cases, severe misalignments in the raw data of more than one gross size of the defect were experienced, and corrections had to be made in the reconstruction.

- Discretization error of the geometric model arises due to the sparse spacing between the micrographs. Although the spacing of 5 mils is the smallest currently affordable, it implies a resolution in the polishing direction that is 30 times worse than that of the micrograph image. In fact, rapid shape changes in a defect's cross-section boundary were often observed from neighboring micrographs. It is evident that important geometric information on these shape changes has been lost in most cases.

- Ultrasonic model error exists in both theory and numerical implementation. Other than the approximation made in the model, the omission of the hard alpha layer can cause additional deviations.

Geometric and ultrasonic modeling were completed for all ten hard alpha defects selected for detailed analysis, namely, B3W3-B, B1BW3-C, B1BW3-D, B1AW3-E, B1AW3-D, B1AW3-A, B2W2-C, B1AW2-D, and B1AW2-B, of which some results have been presented in references 22, 23, and 27. The shape and size of these hard alpha defects differ widely from each other, ranging from a large elongated cigar shape (B1BW3-C) of size 1404 (axial) by 171 by 59 mils to a small four-piece pancake (B1AW2-X) of size 52 by 18 by 34 mils.

An error analysis of the model results was performed over the five major error sources identified above. Since a statistical flaw rejection is based on peak amplitude thresholding, the main assessment focused on the accuracy of model peak amplitude in the C-scan images. The other important indicator is the degree of matching of the C-scan image shape between the experiment and model. As a first cut, the degree of C-scan matching was determined from the amplitudes at peak position and two sets of four neighboring positions in the scan grid at 40 and 80 mils offset, respectively.

It is interesting to see that the model predictions for inspections from sides 2 and 4, whose planes are parallel to the micrograph planes, seem to have larger errors than those with incidence through the perpendicular sides 1, 3, 5, and 6, as illustrated in figure 44, for the cases of defect B1AW2-X. This was largely due to the lack of information in between the sparse micrograph data and the possible misalignment of the micrographs. The lack of information is particularly problematic, given that the exact starting and ending locations and shapes of a single defect or defect branches were usually unknown, and would have to be deduced from the nearest micrographs. At these defect locations, the construction algorithms of the geometric model tended to conservatively create flat plateaus that cause the ultrasonic model to predict incorrect specular responses. These structural plateaus are clearly depicted in figure 45 from the geometric model of defect B2W2-C. It should be emphasized, however, that these difficulties do not occur for the insonification through side 1, corresponding to the actual (radial) inspection direction in the billet. Indeed, that was one of the motivations in determining the orientation of the polishing direction, as shown in figure 12.

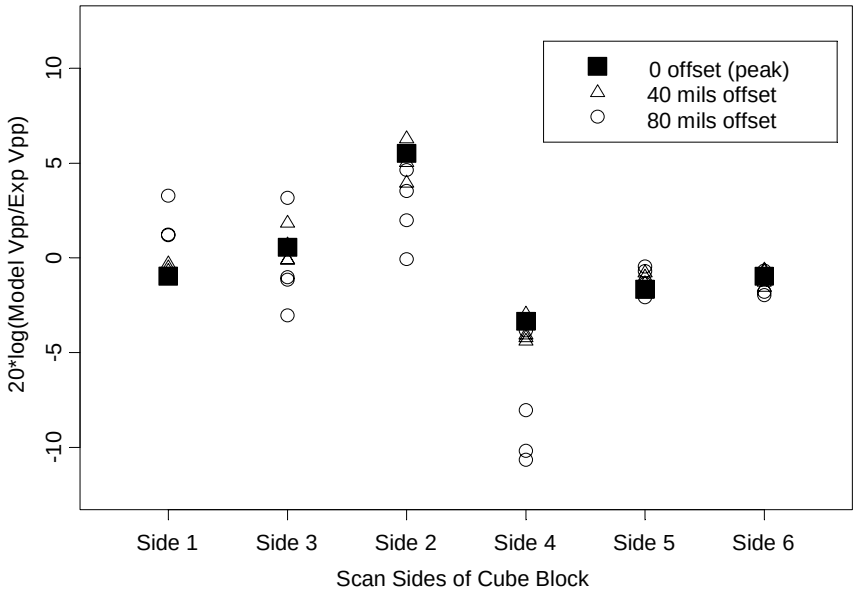


FIGURE 44. DECIBEL AMPLITUDE ERRORS AT 0- (PEAK), 40-, AND 80-mil SCAN OFFSET FOR ALL SIX SIDES OF DEFECT B1AW2-X

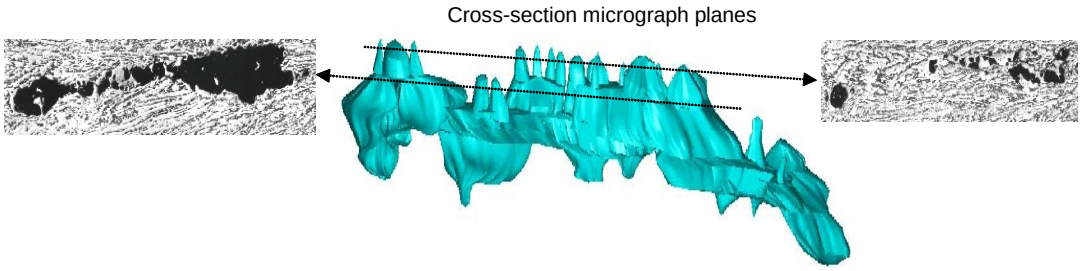


FIGURE 45. STRUCTURAL PLATEAUS IN DEFECT B2W2-C'S GEOMETRIC MODEL

In most cases, the model error increases with the defect cross-section area (figure 46). This appears to be the accumulated effect of the geometric model errors, which in turn originated from the insufficient micrograph data. Similarly, the size of model deviations increases with the scan offset from the peak position, as shown in figure 47. This is an indication of C-scan image mismatch. The boxes in figure 47 indicate the position of the middle 50% of the data, and the line inside the box is the median of the responses. The whiskers show the range of the data, except for one extreme outlier, which is shown as a short horizontal line. When restricting attention to the experimental data in the original billet scan direction, the accuracy of the combined geometric and ultrasonic models is very much in line with variability found in current industrial inspection. This is evident from the upper graph in figure 48, which shows that in the optimal direction, except for one minor exception, the model deviations of the peak amplitudes in the original billet inspection directions are all within ±6 dB bounds. This is typical of ranges of ultrasonic field reproducibility, but twice the described reproducibility range of ±3 dB. In fact, as figure 49 shows, more than 50% of the deviations of the peak are well below 3 dB, well above the expectation. Data is also provided for the nonoptimal direction, i.e., the direction in which more variability exists from the metallographic reconstruction process. Even in this case, agreement is still reasonable, as shown in the lower portion of figure 48.

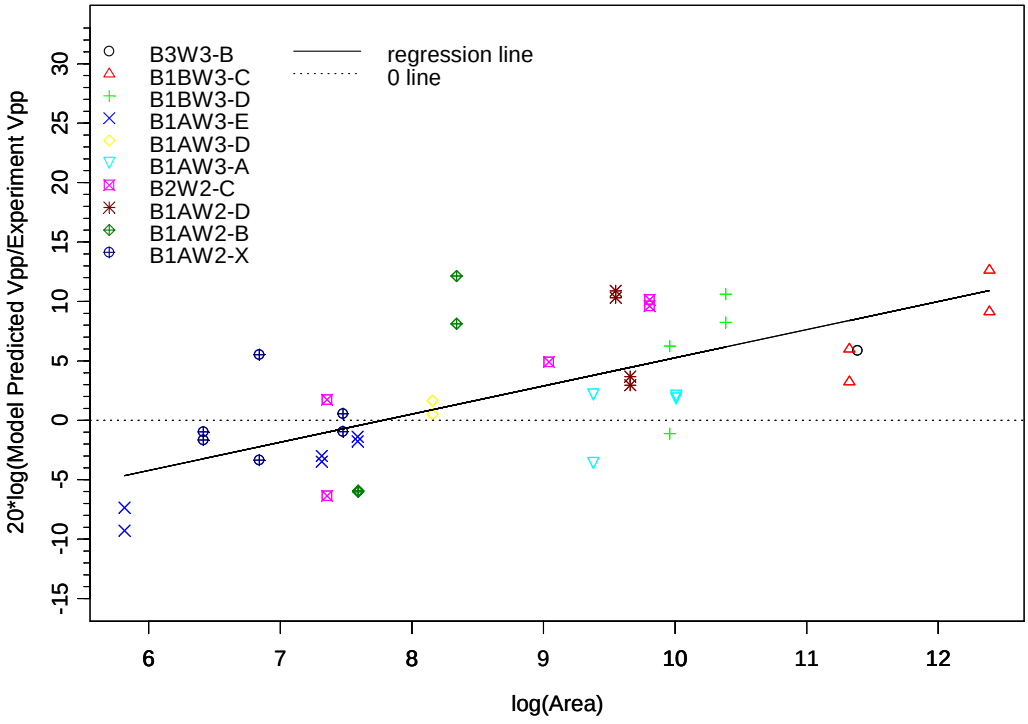


FIGURE 46. COMPARISON BETWEEN MODEL AND EXPERIMENT: dB ERROR OF PEAK AMPLITUDE VS LOG OF PROJECTED FLAW AREA

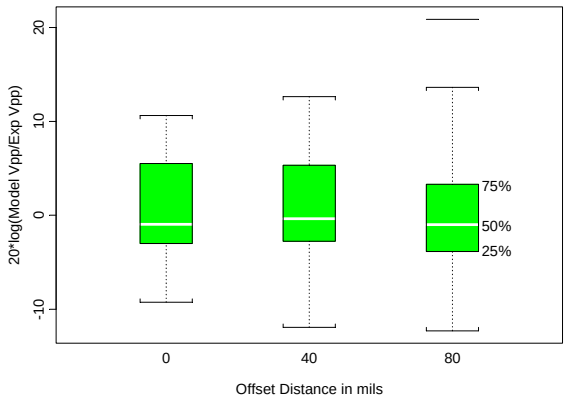


FIGURE 47. DECIBEL MODEL ERRORS VS THE SCAN OFFSETS FOR CASES OF FIVE DEFECTS
(This is a graphical depiction of the errors with 50% of the points falling within the green area.)

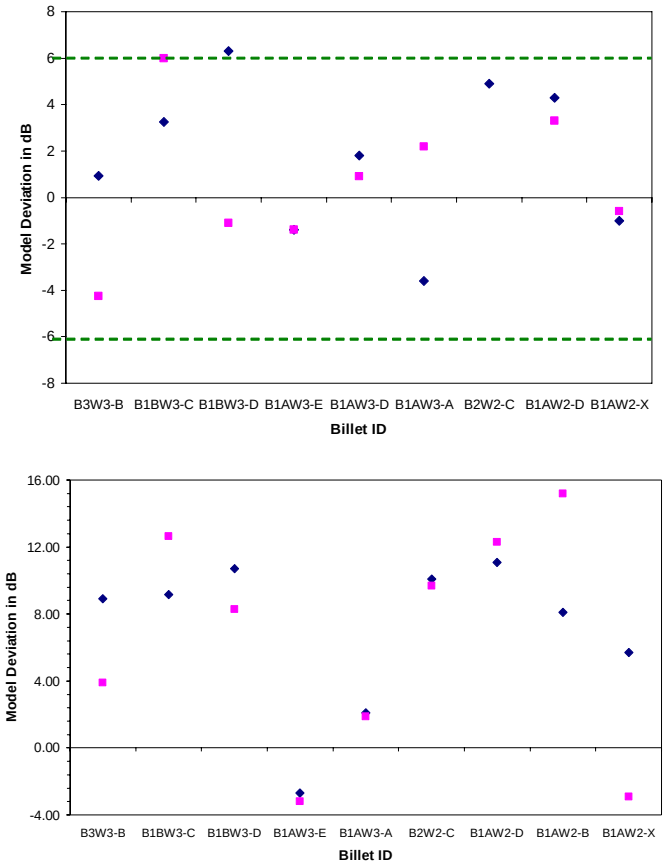


FIGURE 48. DISTRIBUTION OF dB MODEL ERRORS OF PEAK AMPLITUDES IN THE OPTIMAL ORIENTATION
(Original billet scan direction; sides 1 and 3 shown in upper plot.
Distribution of dB model errors of peak amplitudes in the nonoptimal orientation
(orthogonal to original billet scan direction; sides 2 and 4) shown in lower plot.)

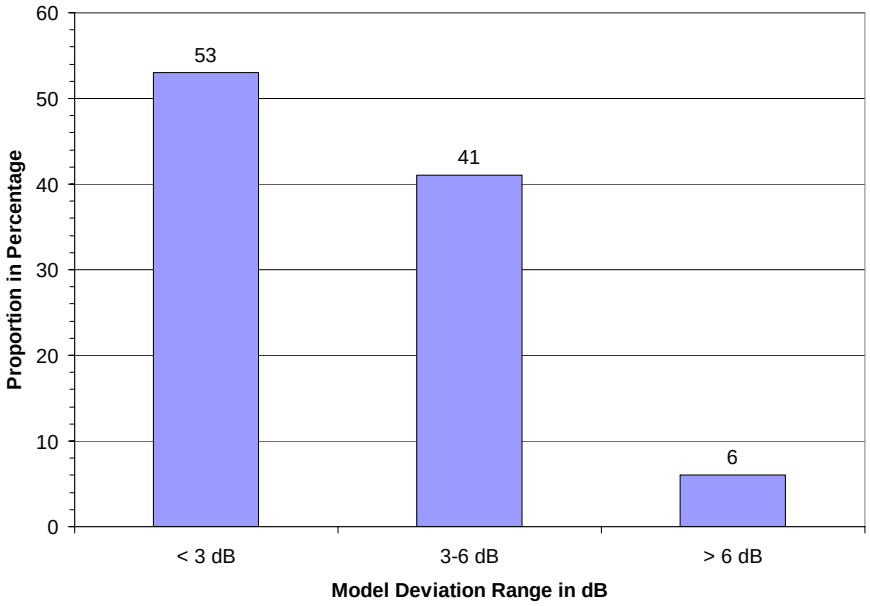


FIGURE 49. SUMMARY OF dB MODEL ERRORS OF PEAK AMPLITUDES IN OPTIMAL ORIENTATION (Original billet scan direction; sides 1 and 3)

3.5 UTILIZATION OF DATA FOR PoD ANALYSIS.

Improving knowledge of PoD was a major motivation for the CBS, as was discussed in section 1.1. The data described in this report significantly expands the information upon which PoD estimates can be made, particularly in light of the fact that the CBS provided the highest fidelity data available defining the responses of naturally occurring hard alpha inclusions. Significant efforts have been made to estimate PoD from this data. However, a number of complexities have been encountered during the analysis, which indicate that traditional techniques are not appropriate for the analysis of this data [30]. Alternate approaches for PoD analysis of the data are being developed. The results of the PoD analysis will be issued in a separate report.

3.6 NOISE ANALYSIS STUDIES.

A key element in the detection of a defect is the SNR, which was the focus of a short study within the CBS program. The purpose of this study was to gain a better understanding of the physical phenomena that control noise levels—information that could be used to guide future efforts to modify processing to reduce noise. An 11″ section of billet, B3W3, was characterized for further sectioning and study [31 and 32]. A multizone transducer (serial no. 015261; 5 MHz, 1″ diameter, focused 1.55″ deep in a 6″ billet at a 3″ water path) and a Sonix scanner with a rotating turntable were used for the initial characterization. The inspection water path was 3″, and three time gates were set, each having a duration of 4 microseconds. These gates were centered 8.2, 16.4, and 24.6 microseconds after the onset of the front surface echo, respectively, so they were centered about 1″, 2″, and 3″ deep in the billet. The C-scan images in figure 50 display the gated-peak noise voltage at each point in the scan for the three time gates. Red is

high voltage, blue/violet is low voltage, with dark red coloration indicating that the voltage takes up 100% of the vertical oscilloscope scale (with no distance amplitude corrections for focusing). Since the third time gate is well beyond the focal zone, all noise values there are well below 100%, and no red colors are seen in the third image. The horizontal axis is a rotation angle from 0º to 360º (or, equivalently, 18.8″ of length along the billet circumference), and the vertical axis is 11″ of travel along the billet axis. The vertical dimension has been stretched so that in the image, the 18.8″ (horizontal) circumferential length and the 11″ (vertical) axial length are about in the proper proportion at the billet surface. Thus, one can imagine that the image simply wraps around the billet circumference without distortion. There is a dark blue feature in each image, which is associated with a mask made of multiple layers of duct tape (trapping some air) that was placed on the outside of the billet. This mask was used to orient the image to the actual billet surface.

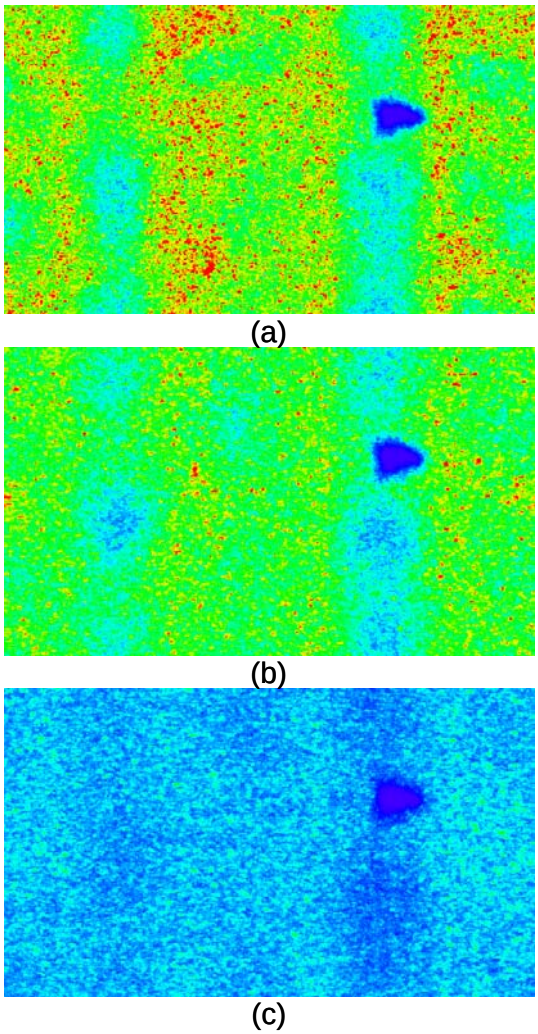


FIGURE 50. C-SCAN IMAGE OF 11″ SECTION OF BILLET B3W3
(Red = high noise; violet = low noise. Gate centered (a) at 1″ deep, (b) 2″ deep, and (c) 3″ deep.)

Noise banding, which had been observed since the application of multizone inspection to titanium billets in the late 1980s and early 1990s, is quite evident. In the top two images, the average noise level in the high-noise regions (red) is about twice that of the low-noise regions (blue). For the top two images, different regions of metal are being inspected as the billet rotates, so the variations seen result from variations of the microstructure with position. Note that the third time gate is centered near the billet axis, so the same central tube of material is being insonified at all inspection angles. Thus, the variations seen in the third image partially result from the dependence on beam propagation direction of the scattering from a fixed metal region. Based on the characterization, a sectioning plan was developed to generate samples from the high- and low-noise regions, as shown in figure 51.

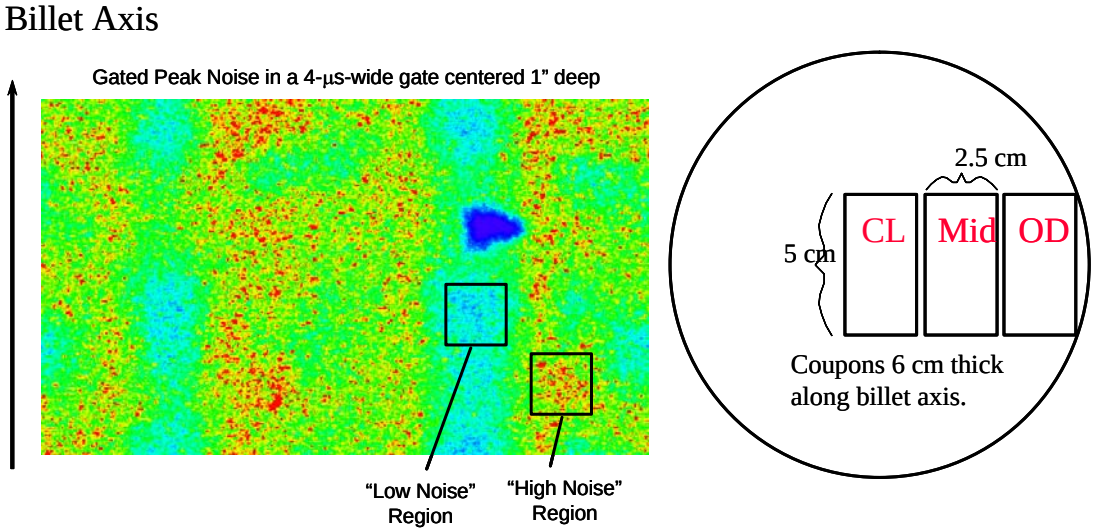


FIGURE 51. SAMPLE SECTIONING PLAN FOR NOISE STUDIES

Measurements made on the noise samples included microstructural analysis, ultrasonic characterization (velocity and backscatter noise), and grain orientation imaging. The results of the macrostructural characterization of the high- and low-noise samples are shown in figure 52. Highly elongated macrograins are seen with orientations that are significantly different in the high- and low-noise regions. More detail is provided by the micrographs in figure 53. For the samples taken from the outside diameter (OD) in both the high- and low-noise regions, micrographs were made under both normal illumination (right-hand image) and under crossed polarizers (left-hand and middle images). Metallographs were made on each of three orthogonal faces of the samples and assembled and shown to give a 3D representation of the structure under different magnification and illumination. As was seen from the macrographs, an elongated structure appears in both the high- and low-noise regions, but with quite different orientations. Generally speaking, the role of the radial and hoop directions seem to be interchanged.

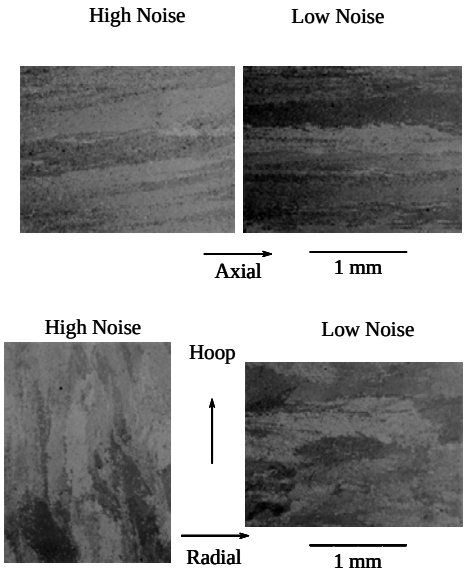


FIGURE 52. MACROSTRUCTURE RESULTS FOR HIGH- AND LOW-NOISE SAMPLES

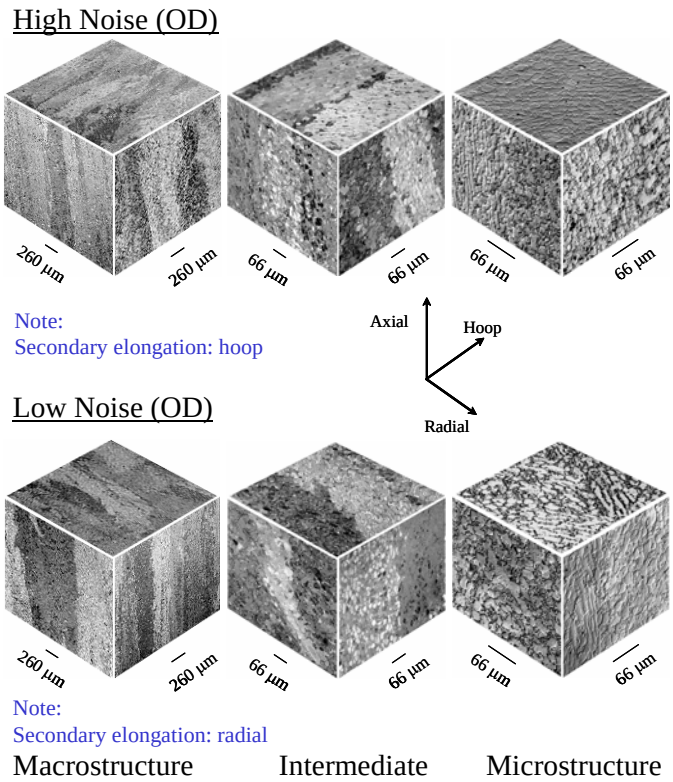


FIGURE 53. MICROSTRUCTURE OF HIGH- AND LOW-NOISE SAMPLES
(For each sample, the left and center images were taken under crossed polarizes to indicate regions of correlated orientation while the right image was taken under normal illumination.)

When ultrasound propagates in the radial direction, as would be the case during a billet inspection, it will be incident on the large faces of the macrostructural elements in the high-noise sample, whereas it will be propagating parallel to the large faces in the low-noise sample. At an intuitive level, it is not surprising that the noise is greater in the former case. It is interesting to note that at a high magnification under normal illumination, these differences are not evident.

Figure 54 shows the results of velocity measurements made on these samples. In the high-noise OD sample, the longitudinal velocity in the hoop direction is the greatest, while in the radial direction, it is the smallest. These roles are reversed in the low-noise OD sample. Because of the anisotropy of the single crystal elastic constants of titanium, such results are generally indicative of preferred orientation. This is consistent with the previous observations. The changes in the orientation of the macrostructures from high- to low-noise regions is presumably a consequence of different deformations that occurred in these regions. Since deformation processing is well known to create texture in titanium, as a result of slip on particular crystallographic planes, the existence of different textures in regions with different deformation-controlled macrostructures is not surprising.

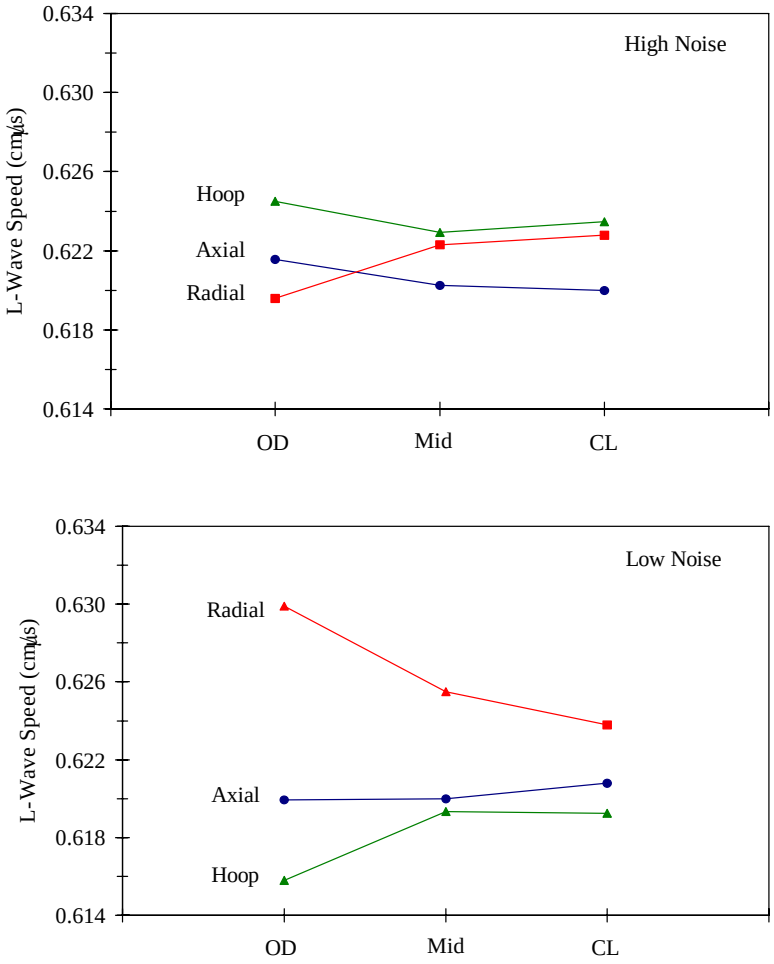


FIGURE 54. VELOCITY RESULTS FOR HIGH- AND LOW-NOISE SAMPLES

Figure 55 presents the results of measurements of attenuation and the backscattering figure of merit (FOM) on these same samples. The FOM is a measure of the material's capacity to create noise and can be considered a material property. A careful discussion of this quantity, and its influence on the inspection of titanium, can be found in reports on the fundamental studies of titanium billet of ETC Phase I. As would be expected, the FOM for radial propagation is greater in the high-noise region than in the low-noise region. As was observed for the velocity, there appears to be a total reversal of the behaviors in the radial and hoop directions for the two samples. The same is observed for the attenuation. This interchange in properties between the radial and hoop directions in the two samples is consistent with the micrographs shown in figure 55.

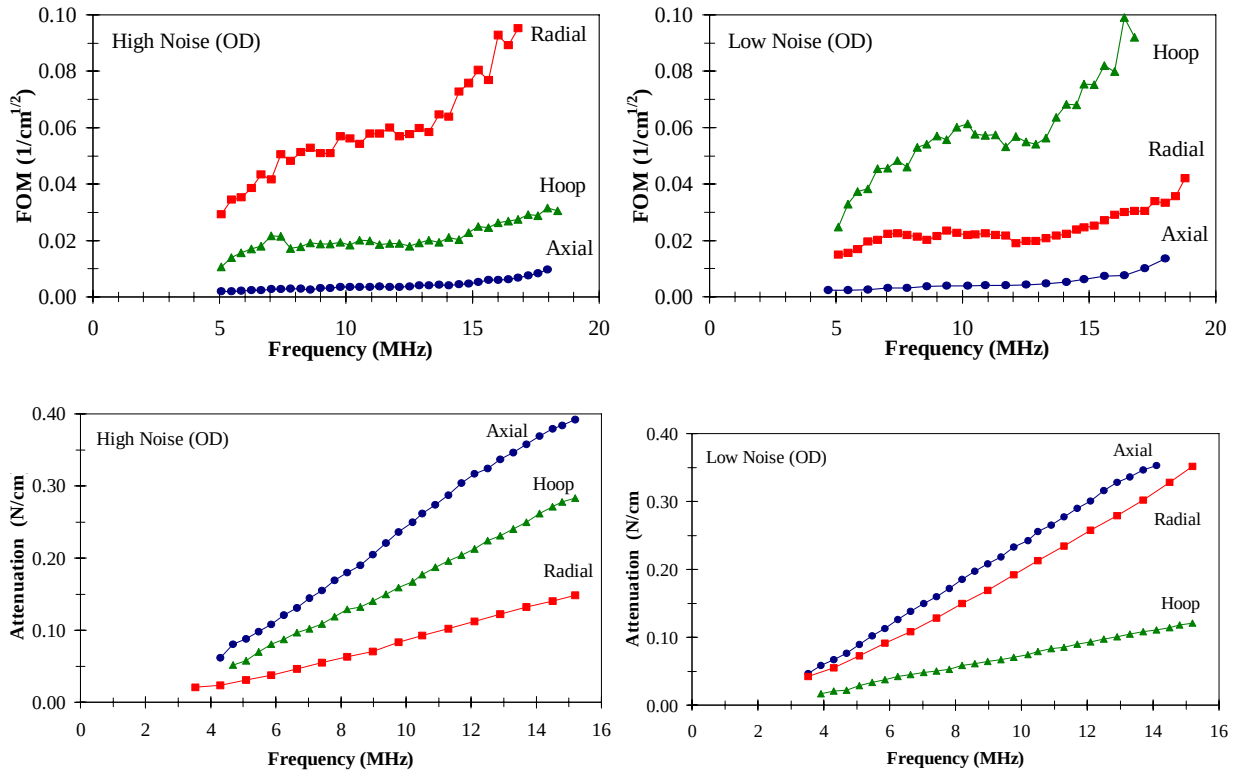


FIGURE 55. ATTENUATION AND FOM RESULTS FOR HIGH- AND LOW-NOISE SAMPLES

It should be noted that figure 55 indicates that regions of high attenuation exhibit low backscattering and vice versa. This is consistent with previous observations made on titanium as a part of the fundamental studies efforts.

The above discussions provide a qualitative explanation of the differences in noise properties in the high- and low-noise regions. As a part of the fundamental studies, a theory was developed to explain the relationship of microstructure to noise, which was conducted to see if that theory would explain the observed noise behavior. The theory will not be described here other than to indicate that its central element is the degree to which the crystallographic orientations of nearby crystallites are correlated. Since the crystallites are elastically anisotropic, orientation

correlations imply correlations in the local elastic properties that control the backscattering. Figure 56 summarizes the steps needed to test the quantitative theory relating microstructure to noise. Using Electron Backscatter Kikuchi Diffraction measurements, as implemented in an orientation-imaging microscope, an image of the variation of crystallite orientations as a function of position is formed. Combining this information with knowledge of the single crystal elastic constants allows images to be made of the local values of the elastic constants. From such images, one can compute a quantity known as the two-point correlation of elastic constants. This serves as an input parameter to the theoretical prediction of the backscattered ultrasonic noise.

Theory Validation

Measure $\langle \delta C_{II}(\mathbf{r}) \delta C_{II}(\mathbf{r'}) \rangle$ using
Orientation Imaging Microscopy (OIM)

1. Electron Backscatter Kikuchi Diffraction (EBSD)
   - Euler angles as a function of position.
2. Calculate C_{II} $I = 1,2,3$
3. Calculate $\langle \delta C_{II}(x,y) \delta C_{II}(x',y') \rangle$
4. Input into theory to predict backscattered noise

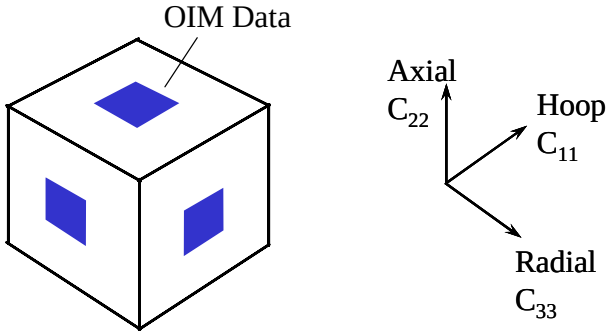


FIGURE 56. STEPS REQUIRED TO VALIDATE THEORY OF NOISE MODELS

Figures 57 and 58 show the results of the orientation imaging for the high- and low-noise samples. The first image shows a pseudocolor map in which changes in color simply indicate changes in orientation, i.e., grain boundaries. The next three maps show the spatial variation of particular elastic constants. The elongated structures that were observed in the macrographs and micrographs are again observed, but now in a way that can provide direct input to theories predicting the noise levels. Figure 59 provides an example of the two-point correlations of elastic constants that are inferred from this data. This has a much greater extent in the axial direction, consistent with the elongation of the macrostructure in that direction.

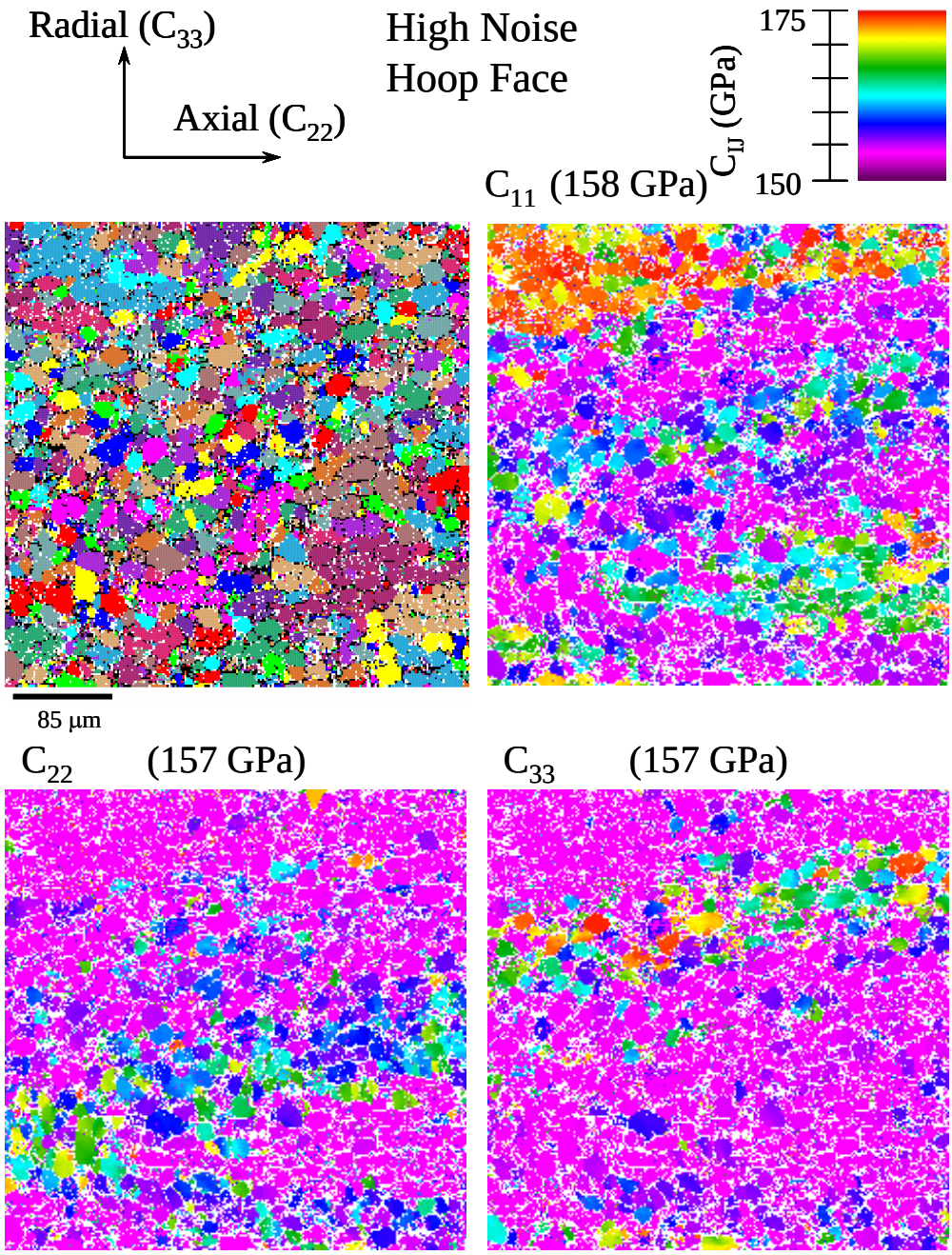


FIGURE 57. ELECTRON BACKSCATTER KIKUCHI DIFFRACTION RESULTS FOR HIGH-NOISE SAMPLES

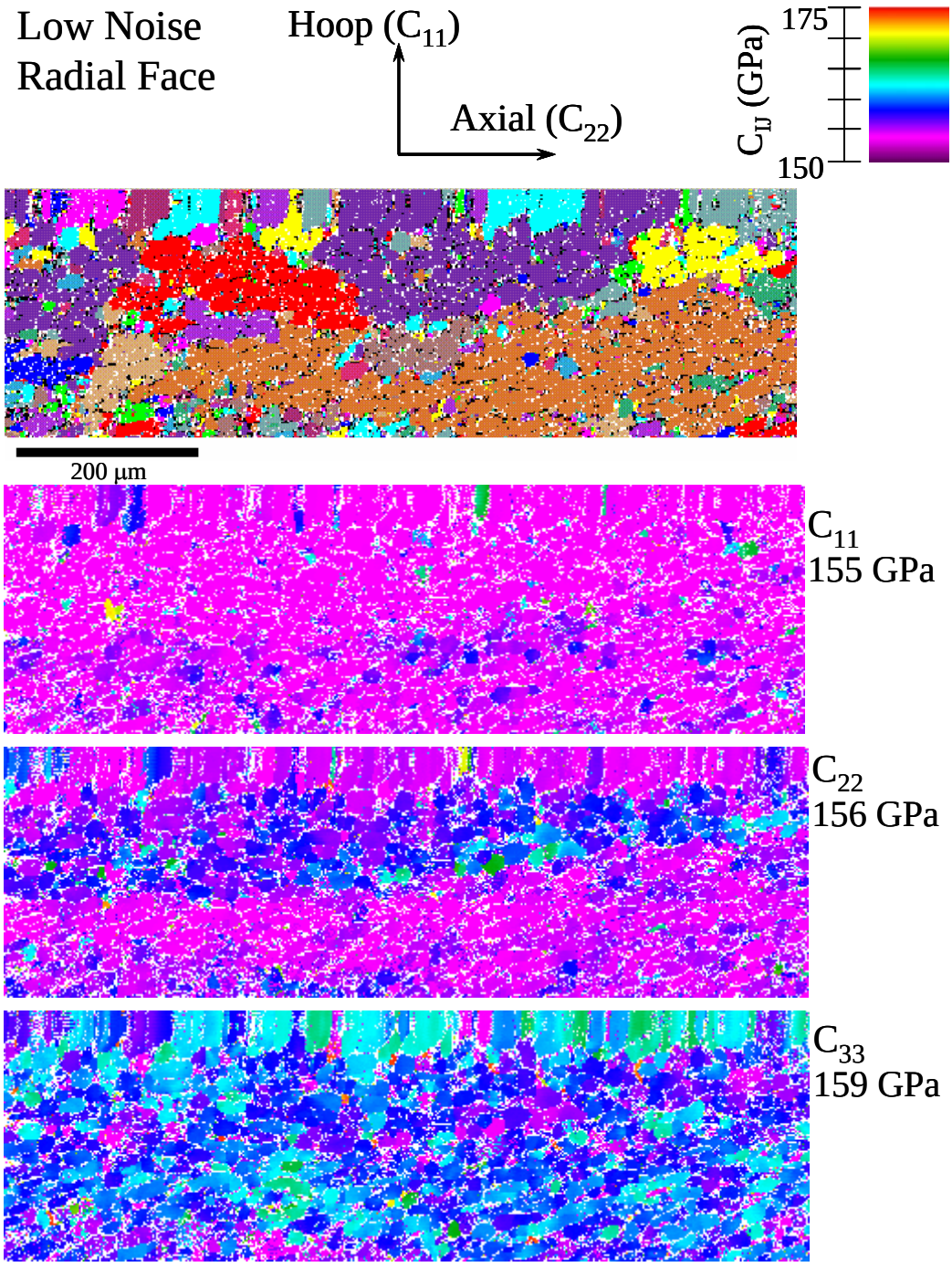


FIGURE 58. ELECTRON BACKSCATTER KIKUCHI DIFFRACTION RESULTS FOR LOW-NOISE SAMPLES

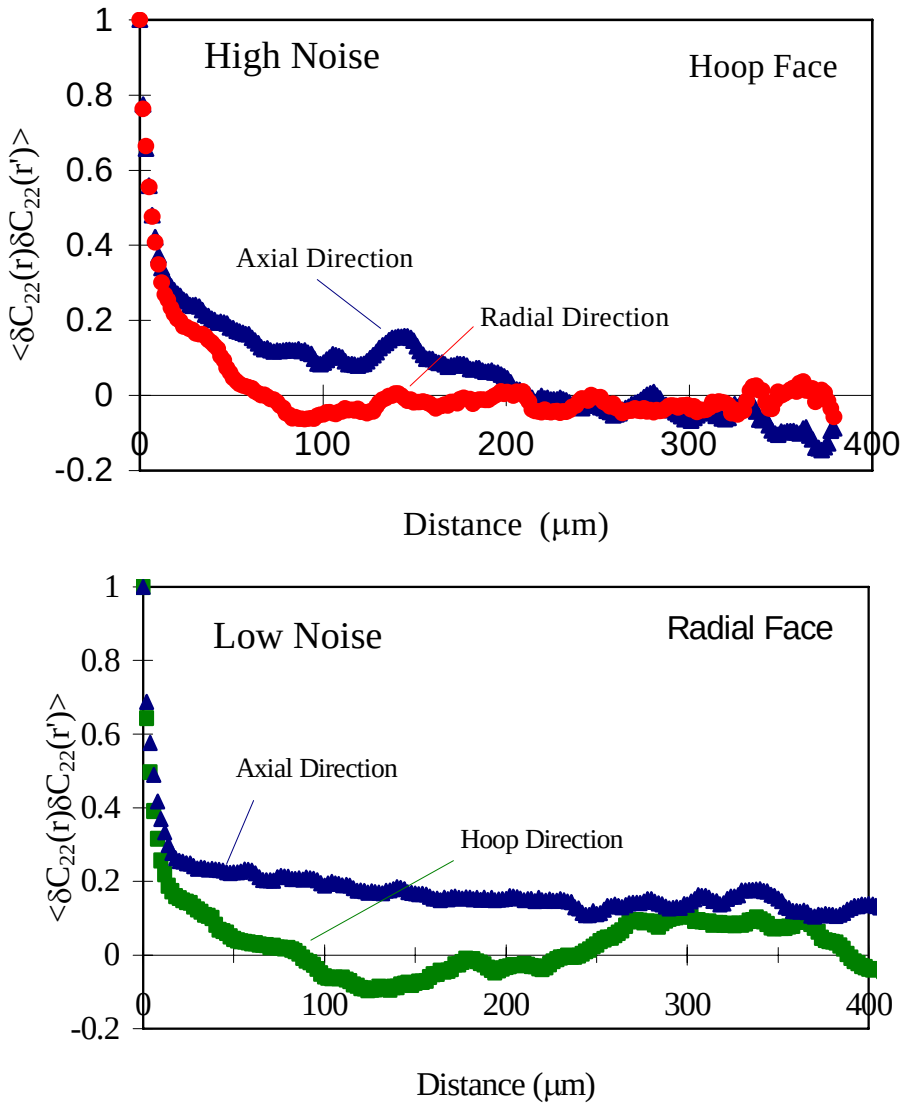


FIGURE 59. TWO-POINT CORRELATION FROM HIGH- AND LOW-NOISE REGIONS OF THE SAMPLES

Figure 60 presents a comparison of theoretical predictions of the backscattering coefficient, based on the orientation-imaging data as discussed above, to the experimental observations that were reported in figure 55. Note here that $\eta^{1/2}$ is identical to the FOM. The agreement between theory and experiment is clearly excellent. This suggests that a good understanding of the relationship of backscattering to micro- and macrostructure is now in hand. Such information will be of significant value in guiding the design of improved alloys with lower backscattered noise. This understanding may also provide insight into the development of improved techniques to detect the microtexture zones that have been associated with dwell time fatigue.

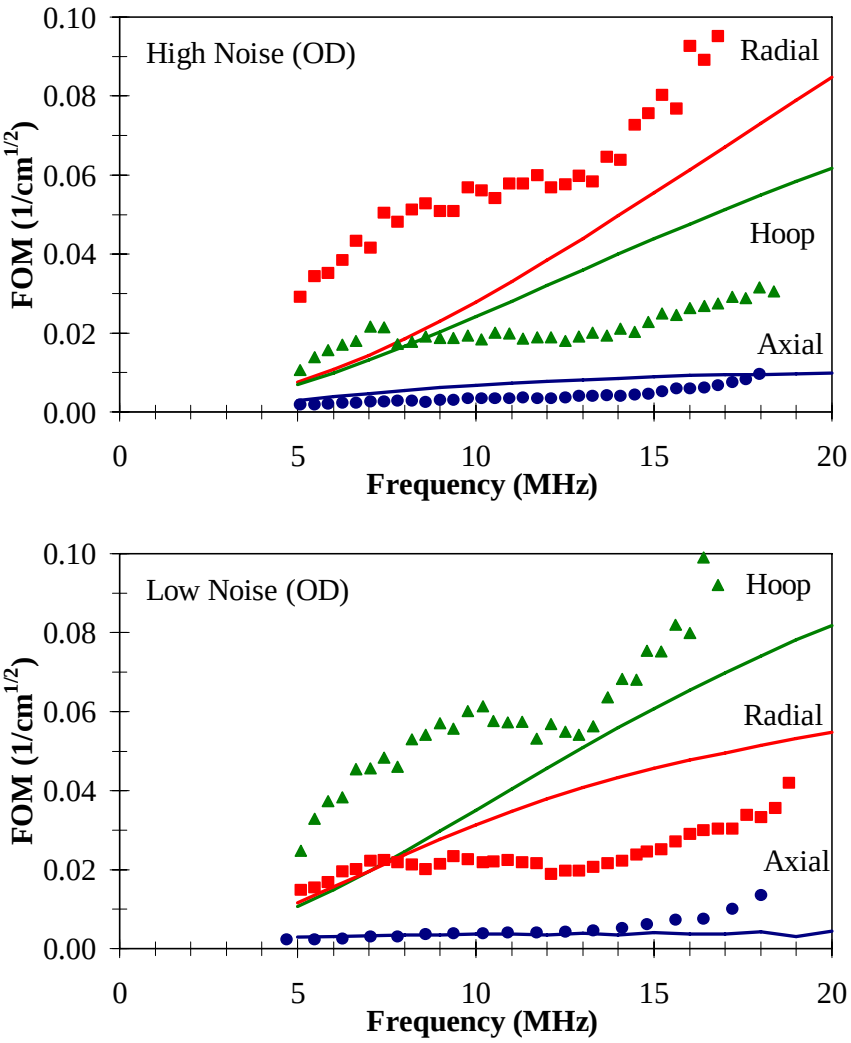


FIGURE 60. COMPARISON OF PREDICTED AND OBSERVED VALUES OF BACKSCATTERING COEFFICIENT

3.7 REPRODUCIBILITY STUDIES USING THE CBS BILLETS.

3.7.1 Reproducibility Studies—Rolls-Royce.

Because of the unique opportunities offered by the CBS billets, Rolls-Royce requested access to a portion of the heat for use in comparison studies of multizone and conventional inspection. The work [33] performed by Rolls-Royce in cooperation with billet supplier A had three objectives:

- Determination of defect detectability differences between conventional inspection (Rolls-Royce procedure) and multizone at the same level of inspection sensitivity

- Assessment of the performance of multizone in normal operation taking advantage of reduced noise level capability

- Assessment of the frequency dependency of suspected type 1 defects related to FBH targets

Three billets were selected that included two billets with the maximum number of indications found by multizone and one billet with indications found by multizone but no indications found using the conventional inspection. Table 7 shows the detections for the three billets selected. The conventional inspection procedure followed RPS 707 (QCTP 6317), which included using a #3 FBH calibration reference set at 80% FSH and distance-amplitude correction. Stop-on-defect was used with an alarm set at 10% above noise, which led to an alarm setting of 35% in the CBS material. A 5-MHz cylindrical focused transducer with an 8″ focal length and dimensions of 1.5″ by 0.75″ was focused at the surface. Back-wall echo was monitored and an index of 50% of the minimum beam width was used.

TABLE 7. BILLETS USED IN ROLLS-ROYCE REPRODUCIBILITY STUDY

Billet Identification	Number of Indications From Sept. 1995 Inspection	
	Conventional Normal	Multizone
B1BW1	3	8
B1BW3	0	4
B3W2	2	8

The three billets were shipped to the billet supplier (supplier A) for inspection. Upon their arrival, the surface was belt polished, which complicated the comparison of the inspection data before and after polishing. The number of detections for each of the inspections is provided in table 8. At this facility, only the amplitude response was used to determine the multizone detections. They did not use the SNR responses. Note that billet B1BW1 was not inspected using multizone in September 1994. Other variations in inspection are provided as footnotes to the table. In their analysis of the data, Rolls-Royce reported a variation between separate multizone inspections. These variations were attributed to difficulties in setup and were similar to that found in a later reproducibility study performed by ETC, as described below.

As part of the Rolls-Royce studies, a comparison was made of multizone when calibrated to a #2 and #3 FBH sensitivity. The first three multizone inspections were performed using a protocol similar to AMS 2826 and were calibrated using a #2 FBH standard. The results are shown in the first three multizone columns of table 8. The last column in table 8 shows the results for the #3 FBH inspection. The inspection was achieved by using the same inspection setup parameters established for a #2 FBH but decreasing the gain for each channel by 7 dB to simulate a #3 FBH sensitivity. The detectability was best, i.e., more indications were found, with the #2 FBH inspection.

TABLE 8. TABULATION OF DETECTIONS IN ROLLS-ROYCE REPRODUCIBILITY STUDY

Billet Identification	Conventional Normal[a] Inspection			Multizone			
	RPS 707 Jan. 1996[b]	Supplier B Sept. 1995	Supplier B Nov. 1994[b]	Supplier A Jan. 1996	Supplier B Sept. 1995	Supplier B Nov. 1994	Supplier A No. 3 Jan. 1996
B1BW1	6	3	5	8	8	NA	4[c]
B1BW3	0	0	0	4	4	4	4
B3W2	5[d]	2	4	6[d]	8	4[e]	6

[a] Conventional inspections used a different transducer and setup, as described above.

[b] Stop-on-defect was used for these two inspection runs.

[c] All eight indications were detected, but only four were above the 35% threshold.

[d] A section of the billet was removed that contained indication H. Indication C was not detected with multizone in the supplier A study but was detected in a prior supplier B September 1995 inspection.

[e] A section of this billet containing three defects was not scanned in November 1994.

The final part of the Rolls-Royce study was a comparison of various frequency cylindrical focused transducers as listed in table 9. Amplitude data for each of the indications are provided in table 10 and plotted in figure 61. For these results, the 5-MHz conventional inspection provided higher amplitudes than the 7.5- and 10-MHz inspections compared to the response from a #2 FBH. Comparable S/N data were not available but may contribute to overall improvements in detection [34 and 35]. The variability between supplier B and supplier A data are also evident in these results as is the improved amplitude when calibrating to a #2 FBH compared to the #3 FBH setup. Various factors contribute to the variability including flaw morphology and depth, transducer, and inspection setup. For these data sets, the surface finish was also different between supplier B and supplier A inspections, i.e., the billets underwent a polishing step that changed the surface condition between the two inspection locations.

TABLE 9. TRANSDUCERS USED IN ROLLS-ROYCE COMPARISON STUDY

Type	Frequency	Focal Length (inches)
Meccasonics	5 MHz	8
Harisonic	7.5 MHz	4
Harisonic	10 MHz	4
Harisonic	10 MHz	12

TABLE 10. AMPLITUDE DATA FROM TRANSDUCER COMPARISON STUDY

	Conventional #3FBH					Multizone		
	Supplier B September 1995	Supplier A January 1996				Supplier B September 1995	Supplier A January 1996	
	#2 FBH (%)	5 MHz (%)	7.5 MHz (%)	10 MHz (%)	10 MHz (%)	#2 FBH (%)	#2 FBH (%)	#3 FBH (%)
B1BW1								
A		81	40		25	63	72	19
B		100	60	30	25	113	152	38
C	70	126	100	112	112	142	114	56
D						56	56	28
E		50	30	30	20	69	55	31
F	179	251	178	251	200	450	322	174
G	100	126	100	95	100	213	219	101
H						127	74	33
B1BW3								
A						113	102	45
B						160	122	68
C						127	73	36
D						74	124	48
B3W2								
A		355	251	200	178	357	287	128
B		200	158	126	126	113	338	151
C						201		
D	80	200	126	80	75	127	154	58
E	74	158	112	65	75	213	184	87
F						160	122	52
G		158	141	80	90	142	260	116
H						253		

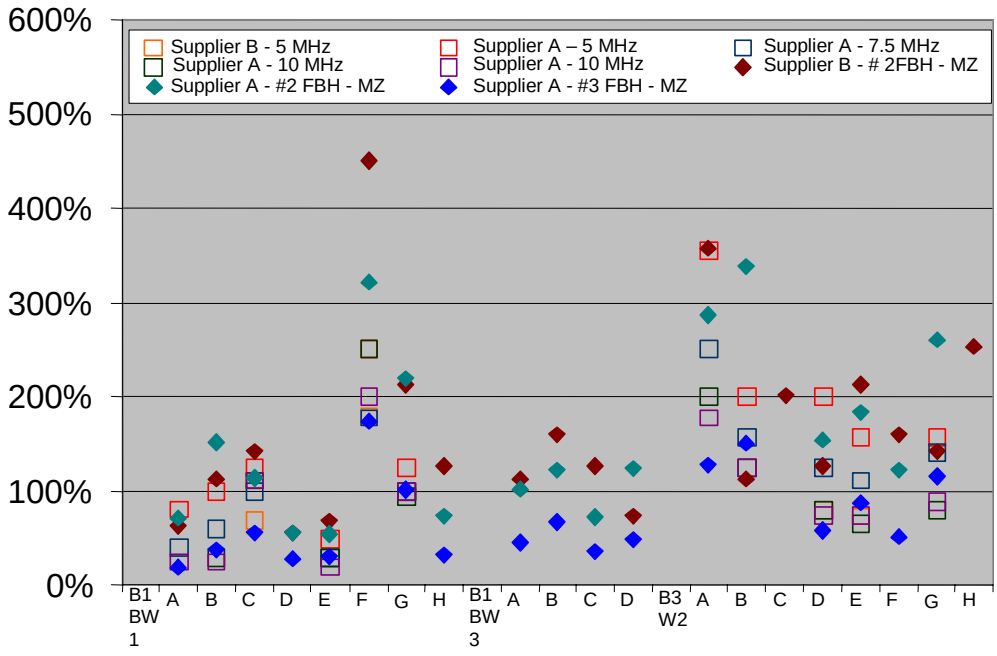


FIGURE 61. AMPLITUDE DATA FOR VARIOUS TRANSDUCERS USED IN THE ROLLS-ROYCE STUDY

Given these results, the following conclusions were found:

- Multizone demonstrated a better level of detectability than RPS 707 conventional ultrasonic inspection.
- Variation in process capability between separate multizone inspections (suppler B compared to suppler A) was noted. Process variation is believed to be attributable to the setup problem.
- At conventional inspection sensitivity, i.e., #3 FBH, multizone demonstrated a better level of detectability than the conventional ultrasonic inspection used in this study. At the same alarm level, the detectability was approximately the same.
- Defect indication response in titanium billet is consistently diminished as transducer frequency is increased from 5 MHz to 10 MHz.

3.7.2 Reproducibility Studies—ETC.

Motivated by the results of the Rolls-Royce study, two billets from the CBS heat were selected, B2W3 131″ long and B1BW1A 72″ long, for use in an ETC study of reproducibility [36]. Note that B1BW1A was cut from billet B1BW1, which was originally 104″ long. Table 11 summarizes the results of previous multizone and conventional inspections for the two billets.

TABLE 11. SUMMARY OF PRIOR ULTRASONIC INSPECTION RESULTS FOR BILLETS SELECTED FOR REPRODUCIBILITY STUDY

Indication	Axial Location (inches)	Depth (inches)	Multizone November 1994		Multizone September 1995		Conventional November 1994		Conventional September 1995	
			Ampl. (%)	SNR	Ampl. (%)	SNR	Normal Ampl. (%)	Angle Ampl. (%)	Normal Ampl. (%)	Angle Ampl. (%)
B1BW1A										
A	21.8	2.2	nt	nt	63	2.96	nr	nr	nr	68
B	28.5	1.7	nt	nt	113	5.67	70	30	nr	nr
C	44.8	0.6	nt	nt	142	8.09	70	>100	70	>100
D	49.0	1.0	nt	nt	56	2.79	nr	nr	nr	nr
E	61.3	0.9	nt	nt	69	3.05	30	>100	nr	nr
F	67.8	1.1	nt	nt	450	26.6	>100	70	179	>100
B2W3										
A	20.1	0.2	>100	6.54	107	6.81	nr	nr	nr	nr
B	27.8	2.3	49	2.9	72	3.54	nr	nr	nr	72
C	31.0	2.0	nr	nr	50	2.59	40**	60**	nr	nr

** Amplitudes reported for indication at correct axial location but at 0.25″ to 0.5″ depth may be a false call.
nt = Not Tested nr = Not Reported

A text matrix that included an inspection at three locations, using five sets of multizone transducers and six sets of conventional transducers with multiple inspectors at each location, is shown in table 12. The multizone inspection followed the GE specification. This included directions to inspect at the calibration gain (#2 FBH) with a repeat, with the gain reduced by 12 dB if saturated indications occurred. The encoder adapter was removed and reattached between operators. The operators were asked to record amplitude and SNRs for rejectable indications along with the noise level. The conventional test matrix was similar to the multizone with the exception that the inspection with multiple transducer sets was to be performed at two locations. The multizone test matrix led to 15 inspection opportunities for each of the 9 indications. The test matrix generated for the conventional inspection differed from the multizone test matrix because the multiple transducer sets were used at two locations, resulting in 21 inspection runs. The conventional transducer set consisted of two transducers, one for normal incidence and one for angle beam inspection. The normal incidence transducers used were 5 MHz cylindrically focused, with element dimensions 1″ by 0.5″ or 1″ by 0.75″. The transducers used for angle beam included both types used for normal beam inspection, as well as a spherically focused, 0.75″ diameter, 5-MHz model. The inspection was in accordance with an engine manufacturer's approved procedure, using approved inspectors and calibration standards. The angle beam

inspection used an offset of 1/6 of the billet radius, producing a refracted longitudinal wave at 45º from the surface normal, as described in figure 9.

TABLE 12. TEST MATRIX USED FOR REPRODUCIBILITY STUDY

Location	Transducer Set	Operators
Multizone Inspection Matrix		
Z	1	A, B, C
Z	2	A, B, C
Z	3	A, B, C
Y	4	D, E, F
X	5	H, I, J
Conventional Inspection Matrix		
W	6	J, K, L
W	7	J, K, L
W	8	J, K, L
V	9	M, N, O
V	10	M, N, O
V	11	M, N, O
U	12	P, Q, R

Instructions were given to evaluate and report all rejectable indications and to re-evaluate any saturated indications at a reduced gain level, reporting the amplitude and gain adjustment. Reports were requested of the noise level, the attenuation difference from the calibration standard, and the applied attenuation correction. Copies of strip chart recordings were requested if used during the conventional inspections (note: strip chart that recording is not a requirement but is used by some suppliers—one of the three suppliers provided strip charts).

The results were derived from the written inspection reports. For the supplier who used strip chart recording, the strip charts were reviewed for consistency with the reports. Any indication reported on either normal incidence, angle beam, or both, which corresponded with a previously reported indication (see table 11), was counted as a find. In four instances, indications were reported that did not correspond to any known indication. Each was reported on only 1 of the 21 inspection runs and had an amplitude of either 10% or 15% above the reported noise level (reject level was 10% above noise). These four indications were recorded as false calls during the conventional inspection and are listed in table 13. Note that these presumed false calls were all reported from the same inspection location.

TABLE 13. SUMMARY OF CONVENTIONAL INDICATIONS RECORDED AS FALSE CALLS IN BILLET B1BW1A

Axial Location (inches)	Depth (inches)	Angle or Normal	Amplitude (%)	Signal Minus Noise (%)
6.25	3.00	angle	40	15
37.5	3.50	normal	50	15
39.25	3.25	normal	50	10
54.25	3.25	normal	50	10

The summary statistics for the multizone inspection data that are presented in table 14 show the reported signal amplitudes and SNR statistics.

TABLE 14. SUMMARY OF STATISTICS OF MULTIZONE REPRODUCIBILITY STUDY

Indication	Rejections	Amplitude Statistics (15 Runs)				S/N Statistics (15 Runs)			
		Min.	Max.	Mean	Std. Dev.	Min.	Max.	Mean	Std. Dev.
B1BW1AA	15	50	92	65.33	12.00	3.3	4.52	3.89	0.413
B1BW1AB	15	58	152	103.07	26.67	4.07	10.88	7.02	1.866
B1BW1AC	15	98	200	138.47	33.54	6.69	12.29	9.42	1.467
B1BW1AD	9	40	77	56.07	13.60	1.91	3.36	2.65	0.346
B1BW1AE	15	44	100	69.67	12.82	2.18	4.16	3.22	0.663
B1BW1AF	15	200	560	349.07	118.68	10.09	45.34	18.42	11.133
B2W3A	15	53	140	77.93	27.42	3.33	9.58	6.36	1.752
B2W3B	15	41	116	67.33	22.88	2.79	5.48	4.09	0.950
B2W3C	11	23	68	42.60	14.74	1.74	4.18	3.16	0.775

The summary statistics for the conventional inspection that are presented in tables 15 and 16 tabulate the amplitude and signal minus noise, respectively. The signal minus noise data are shown to allow comparison with the typical reject criterion of 10% above noise for the conventional inspection. For each of the two tables, statistics of maximum, minimum, mean, and standard deviation are shown for each indication. These were calculated from only the finds information for each indication.

TABLE 15. SUMMARY OF AMPLITUDE STATISTICS FOR CONVENTIONAL INSPECTION

Indication	Finds			Normal Incidence Amplitude				Angle Incidence Amplitude			
	Total	Normal Incidence	Angle Beam	Min. (%)	Max. (%)	Mean (%)	Std. Dev. (%)	Min. (%)	Max. (%)	Mean (%)	Std. Dev. (%)
B1BW1AA	18	7	18	40	65	49	8	35	65	47	10
B1BW1AB	18	17	17	30	90	58	13	30	90	46	19
B1BW1AC	20	20	7	50	134	79	23	30	55	45	11
B1BW1AD	0	0	0								
B1BW1AE	1	1	0	40	40	40	0				
B1BW1AF	21	21	9	113	401	190	83	60	142	88	28
B2W3A	0	0	0								
B2W3B	0	0	0								
B2W3C	9	0	9					30	80	46	14

TABLE 16. SUMMARY OF SIGNAL MINUS NOISE STATISTICS FOR CONVENTIONAL INSPECTION

Indication	Finds			Normal Incidence Signal Minus Noise				Angle Incidence Signal Minus Noise			
	Total	Normal Incidence	Angle Beam	Min. (%)	Max. (%)	Mean (%)	Std. Dev. (%)	Min. (%)	Max. (%)	Mean (%)	Std. Dev. (%)
B1BW1AA	18	7	18	10	30	16	7	10	45	26	10
B1BW1AB	18	17	17	10	70	28	16	10	65	24	18
B1BW1AC	20	20	7	15	89	48	20	10	35	25	11
B1BW1AD	0	0	0								
B1BW1AE	1	1	0	20	20	20	0				
B1BW1AF	21	21	9	85	324	150	63	35	117	66	28
B2W3A	0	0	0								
B2W3B	0	0	0								
B2W3C	9	0	9					10	55	24	13

A review of the data shows that one of the indications (B1BW1A indication F) was rejected on all 21 inspection runs. This was also the highest amplitude indication on both the multizone and conventional tests. Three of the indications were not rejected on any conventional inspection run. The remaining five indications were rejected between runs 1 and 20. The reported amplitudes of indication F found on all runs varied between 113% and 401% in longitudinal mode, showing a degree of variation similar to that observed by the multizone inspection, as shown by the data in table 14.

The fraction of opportunities [36] that resulted in detections, which will be referred to here as percent efficiency for conciseness, are shown in table 17 for both the multizone and conventional inspections conducted in the reproducibility study.

TABLE 17. PERCENT EFFICIENCY OF MULTIZONE INSPECTION DURING REPRODUCIBILITY STUDIES

Billet ID	Indication ID	Opportunities	Detections	Percent Efficiency
B1BW1A	A	15	15	100
	B	15	15	100
	C	15	15	100
	D	15	9	60
	E	15	15	100
	F	15	15	100
B2W3	A	15	15	100
	B	15	15	100
	C	15	11	73
All Indications		135	125	92.5

TABLE 18. PERCENT EFFICIENCY OF CONVENTIONAL INSPECTION DURING REPRODUCIBILITY STUDIES

Billet ID	Indication ID	Opportunities	Detections	Percent Efficiency
B1BW1A	A	21	18	86
	B	21	18	86
	C	21	20	96
	D	21	0	0
	E	21	1	1
	F	21	21	100
B2W3	A	21	0	0
	B	21	0	0
	C	21	0	0
All Indications		189	87	46

Comparison of these results shows that the ratio of the percent efficiency for conventional and multizone inspections during the reproducibility studies was 49.7%; a value that is very close to the ratio of 51.7% during the overall CBS based on the 31 conventional finds and the 60 multizone finds, as shown in figure 19.

The data was analyzed further for statistical comparison. Separate variability comparisons were made of the amplitude for the multizone (figure 62) and conventional (figure 63) inspections. Figure 64 plots all the data on a single graph. Note that similar variability was found between the two methods.

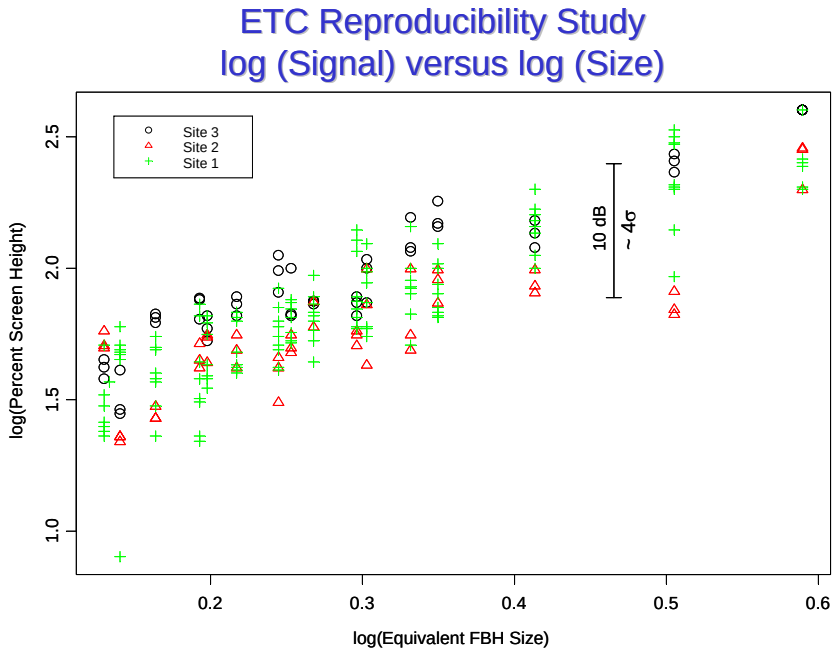


FIGURE 62. VARIABILITY ANALYSIS FOR AMPLITUDE FROM MULTIZONE INSPECTION
(Approximately 10 dB variation was found.)

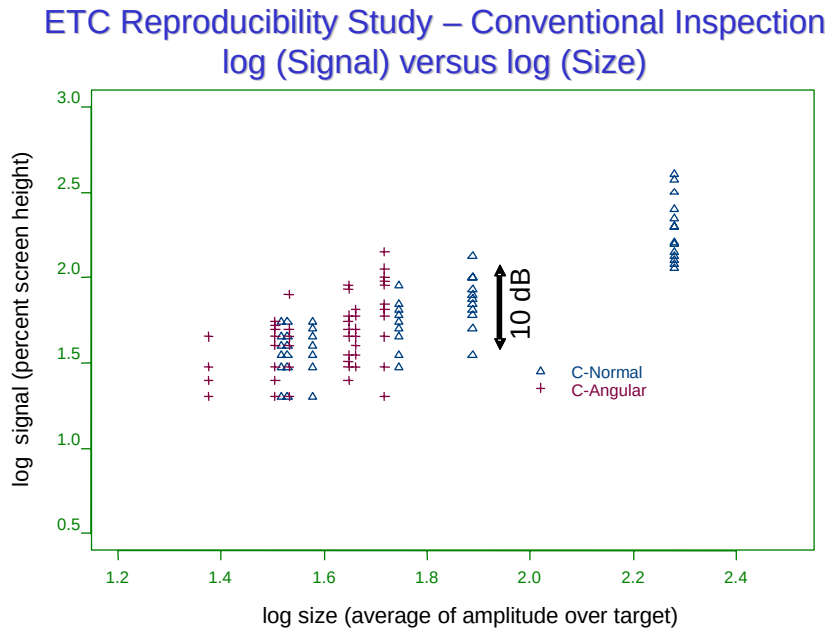


FIGURE 63. VARIABILITY ANALYSIS FOR AMPLITUDE FROM CONVENTIONAL INSPECTION
(Approximately 10 dB variation was found. Data shown for both normal and angular inspection modes.)

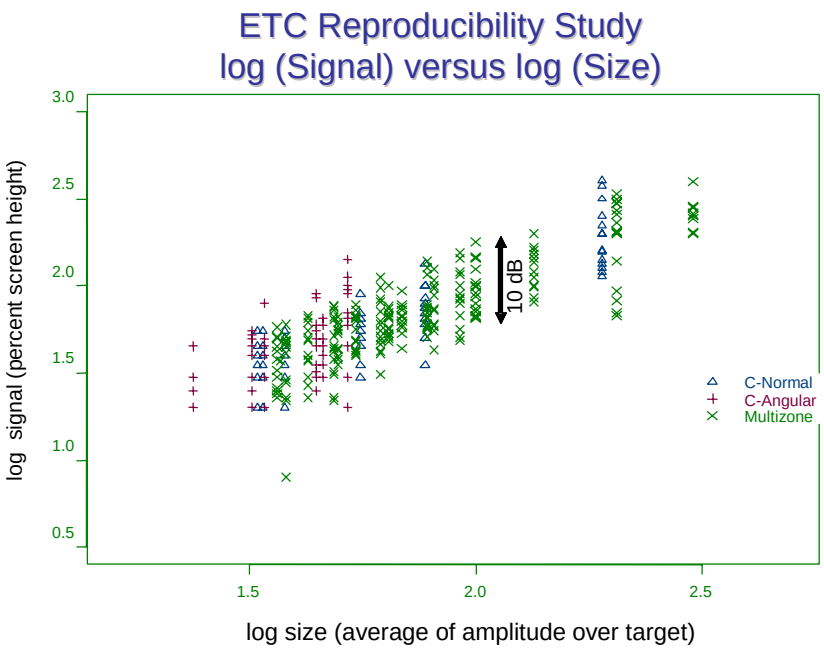


FIGURE 64. COMPARISON OF MULTIZONE AND CONVENTIONAL INSPECTION VARIABILITY

Typical results for a single indication are shown in figure 65. Indication B1BW1A-B was selected and the results were plotted. Each group represents three operators and the same location and using the same transducers.

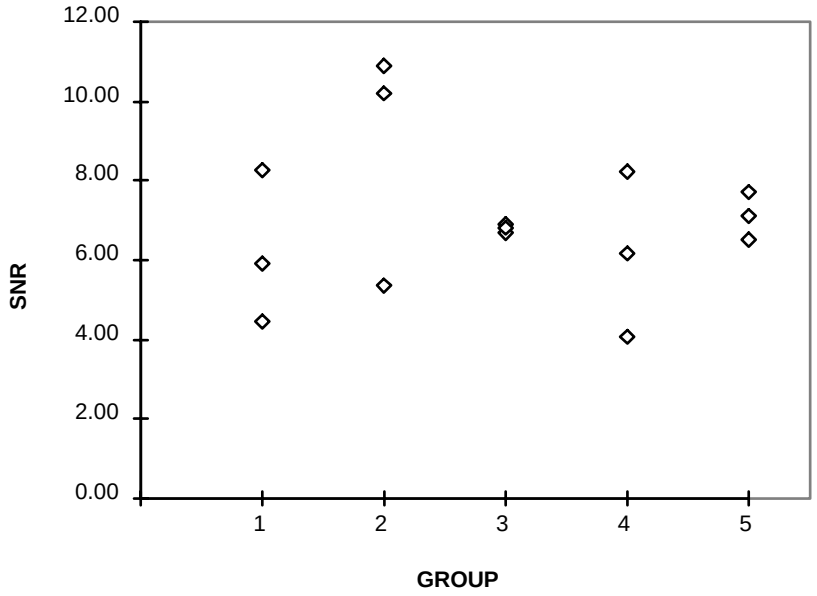


FIGURE 65. REPRODUCIBILITY RESULTS FOR INDICATION B1BW1A-B FROM FIELD STUDIES

Based on these results, a laboratory study was designed to assess the factors that could lead to such variability with a concentration on factors that affect the SNR. The factors evaluated in the laboratory study included transducer, water path, and transducer alignment, as shown in figure 66. Other potential causes not considered included instrumentation, sampling/line spacing, SNR algorithm, and gate position.

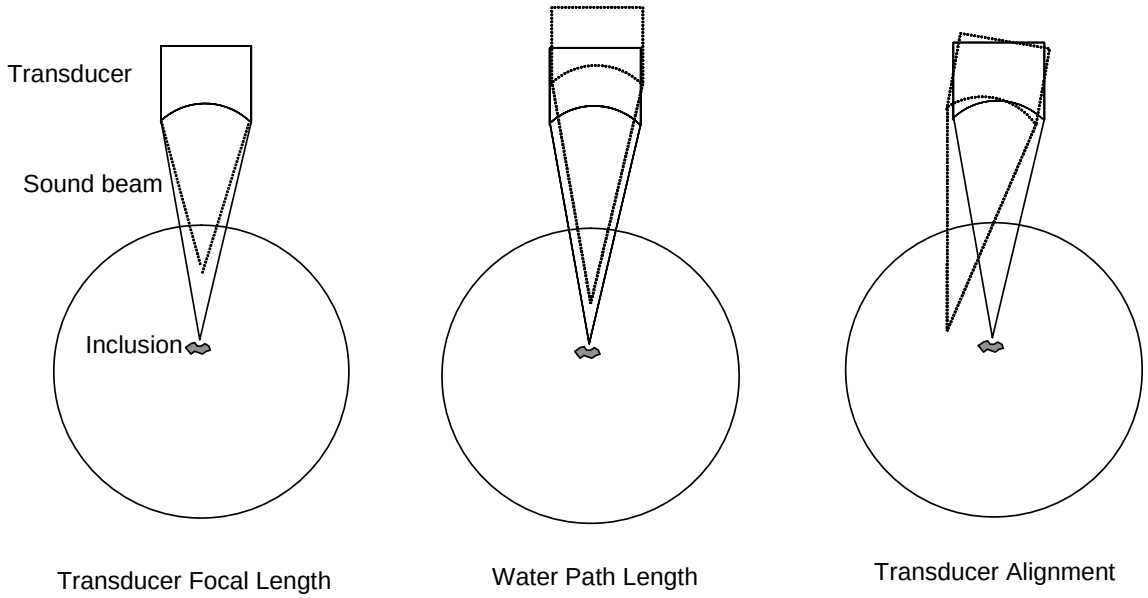


FIGURE 66. FACTORS EVALUATED DURING REPRODUCIBILITY STUDY

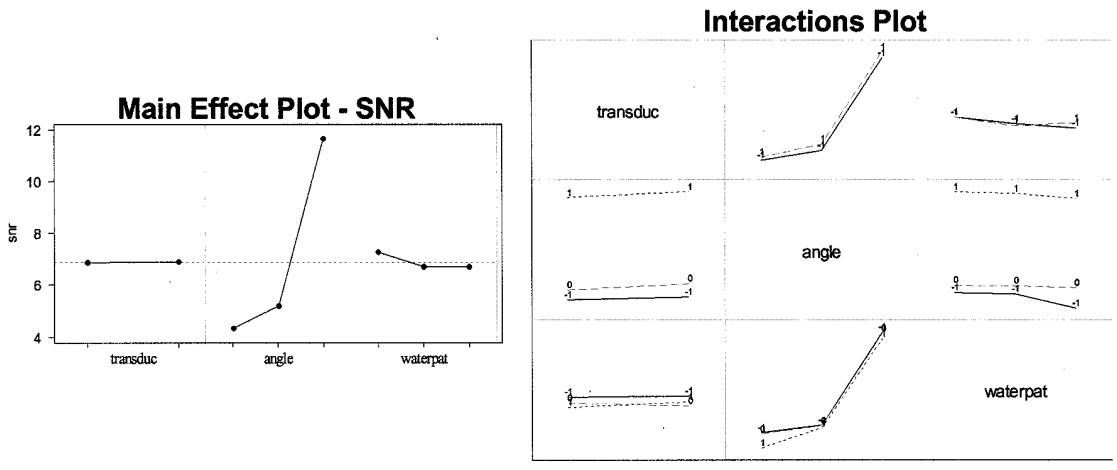
A full factorial study was planned, which included the following:

- Transducer: 2 levels (NDT Systems, Panametrics)
- Water Path: 3 levels (2.6″, 3.0″, and 3.4″)
- Alignment: 3 levels (-1.5º, 0º, and +1.5º)
- 20 runs total (3 x 3 x 2 plus two duplicates)

The results are provided in table 19 with the main effects and interactions plots presented in figure 67. No significant interactions were found between the factors; therefore, each could be evaluated separately.

TABLE 19. RESULTS OF FULL FACTORIAL EXPERIMENT PERFORMED IN LABORATORY ENVIRONMENT

Run	Transducer	Angle	Waterpath	SNR		
1	-1	-1	-1	4.79		
2	-1	0	-1	5.23	transducer:	-1 NDT Systems
3	-1	1	-1	11.79		+1 Panametrics
4	-1	-1	0	4.23		
5	-1	0	0	4.54	angle:	-1 -1.5 degrees
6	-1	1	0	11.71		0 0 degrees
7	-1	-1	1	3.65		+1 +1.5 degrees
8	-1	0	1	4.94		
9	-1	1	1	10.93	waterpath:	-1 2.6 inches
10	1	-1	-1	4.68		0 3.0 inches
11	1	0	-1	5.26		+1 3.4 inches
12	1	1	-1	11.96		
13	1	-1	0	5.03		
14	1	0	0	5.92		
15	1	1	0	11.82		
16	1	-1	1	3.58		
17	1	0	1	5.2		
18	1	1	1	11.89		
19	1	0	0	5.32		
20	1	0	0	5.11		



(a) (b)

FIGURE 67. (a) MAIN EFFECTS PLOT AND (b) INTERACTIONS PLOT

As a final step in the analysis, a comparison was made of the field and laboratory results, as shown in figure 68, indicating that similar variations were found between the two studies.

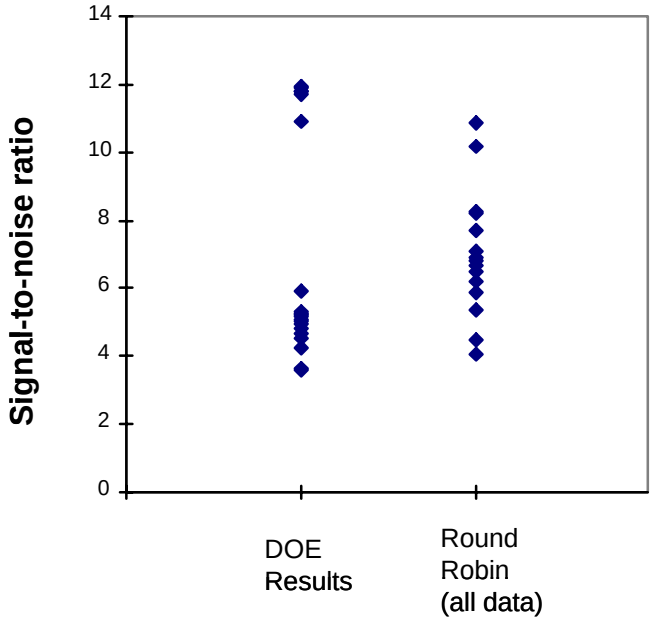


FIGURE 68. COMPARISON OF SNR FOR LABORATORY DESIGN OF EQUIPMENT AND ROUND-ROBIN FIELD STUDY

The following conclusions were reported [36]:

- Variability was found to be similar for the conventional and multizone inspections, even though more indications were found with multizone. The ratio of percentage efficiency for conventional and multizone was 49.7%.
- Primary sources of variability were transducer, transducer alignment, and water path distance, with the greatest contributor believed to be the transducer alignment.
- Factors deemed less significant were instrumentation, sampling, the SNR algorithm as implemented in the multizone software, and gate position (which can affect zone 1).

3.8 MISSES ASSESSMENT.

A critical aspect of any inspection method is an understanding of those defects, which may be missed. In an effort to assess the occurrence of defects that were not detected with the ultrasonic methods described in section 3.1, two separate efforts were undertaken to determine if misses existed. Three mults, approximately 51″ long, were selected for further reduction and subsequent inspection. The mults were shipped to Braeburn Steel for reduction to 1.5″ bar. The bars were hot-rolled, straightened, and centerless ground to a surface finish of 63 root mean square prior to inspection in a typical bar inspection facility. The bars were inspected at 10 MHz at the WestPenn Testlabs using their TestTec bar inspection facility with calibration set at a sensitivity of #1.5 FBH. The three mults selected for the study were B1AW2A, B1AW3A, and B2W2D. Note that the B1AW2A mult contained an indication that was detected during an

earlier inspection. This mult was selected to be compared to an indication-free material. An inspection of the bars did not lead to rejectable indications because of high-noise conditions. This was the case for the bars from all three mults, including B1AW2A, which contained a known indication with 134% FSH and 13.6 SNR, as recorded during the multizone inspection. Given the noise conditions of the bars, using the bars for misses assessment was deemed inconclusive.

The second effort to assess misses involved inspection of mults to a higher sensitivity using phased array inspection. Eleven mults of various lengths were selected and are listed in table 20. An annular array probe with a 10-MHz center element surrounded by a 7.5-MHz operating frequency in the outer rings was used for the evaluation. Seven overlapping zones were used at 0.6″ increments at a sensitivity of #2 FBH. Several of the mults had indications detected during prior inspections, as indicated in the final column of table 20. The presence of all prior indications was confirmed using the phased array method. As an example, figures 69 and 70 show the results for indications B, C, and D of billet segment B3W1BB. Note that indications C and D were found in multiple zones.

TABLE 20. MULTS USED IN THE MISSES ASSESSMENT

Billet Segment ID	Mult Length	Inspection Results
B3W3CA	32″	Confirmed presence of indication D. No new indications.
B3W3C	36″	Confirmed presence of indication C. No new indications.
B3W3A	35″	Confirmed presence of indication A. No new indications.
B2W1C	29″	Confirmed presence of indication D. No new indications.
B2W1CA	36″	No new indications.
B3W1BB	34″	Confirmed presence of indications B, C, and D. No new indications.
B1AW1B	32″	Confirmed presence of indications D and E. No new indications.
B3W2CA	36″	Confirmed presence of indication F. No new indications.
B1BW3CB	14″	One new indication found.
B1BW3C	13″	No new indications.
B1BW3A	12″	No new indications.

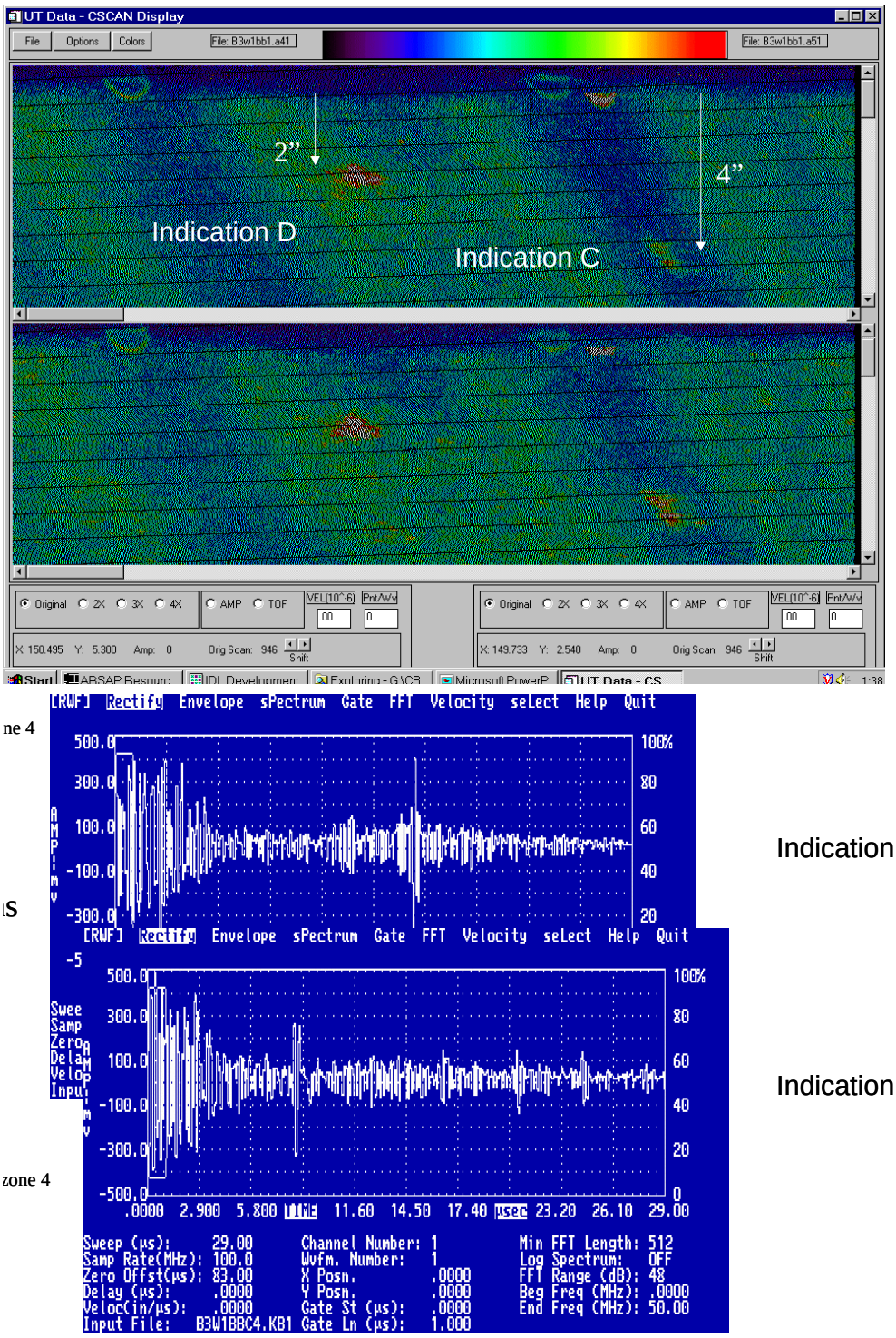


FIGURE 69. C-SCAN OF INDICATIONS D AND C FROM BILLET SEGMENT B3W1BB ALSO DETECTED IN PRIOR INSPECTIONS
(Note that both indications were detected in zones 4 and 5.
Waveforms from zone 4 are also shown for both indications (lower).)

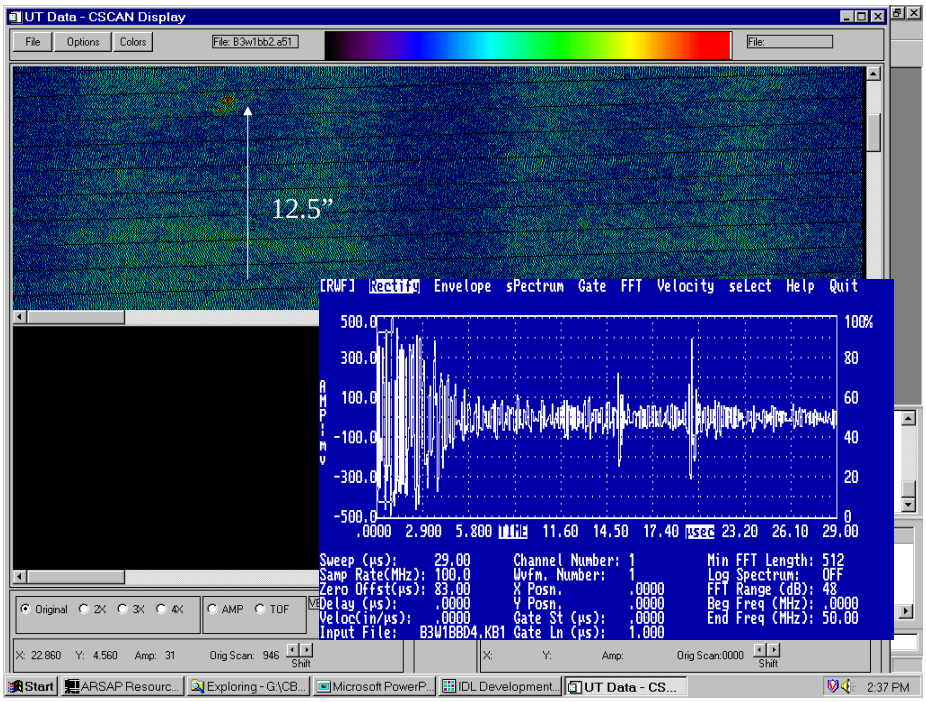
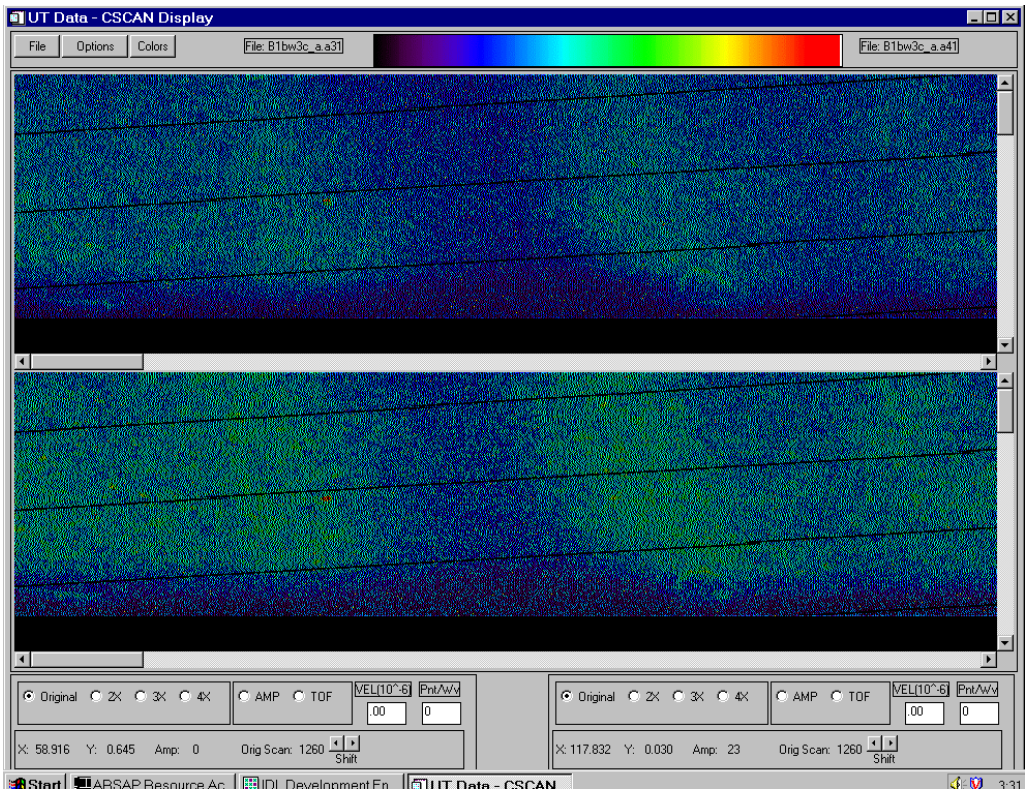


FIGURE 70. C-SCAN AND WAVEFORM RESULTS FOR INDICATION B OF BILLET SEGMENT B3W1BB

As indicated in table 20, only one new indication was identified. The indication was found in billet segment B1BW3CB with an amplitude of 95% of a #2 FBH. Figure 71 shows the C-scan and waveform results taken with the phased array setup. After completion of the high-sensitivity phased array inspection (7.5 MHz), the sample was shipped to the GE Quality Technology Center (QTC) for multizone inspection. The GE-QTC staff reinspected the mult using production multizone probes and probes fabricated by Corporate Research and Development. A 34% amplitude was reported (based on 80% calibration for a #2 FBH), which is not rejectable. An offset of 0.1″ was used both axially and circumferentially. The axial offset resulted in no change. The circumferential offset increased the amplitude to 60%, which is below the reject threshold. These results are indicative of the variability that is present in billet inspection and point to the importance of flaw morphology and inspection setup to the detection of flaws. The sample was also inspected with a higher-frequency (10 MHz) phased array probe. The results from the inspection are shown in figure 72. Given the strong ultrasonic response from multiple inspections, the decision was made to destructively characterize the indication.



B1BW3CB; indication at ~1.2″ depth; ~95% of #2 FBH

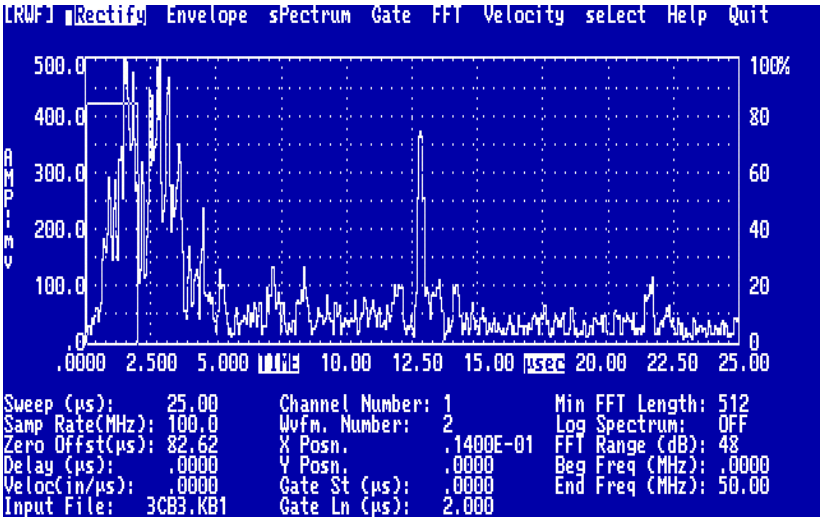
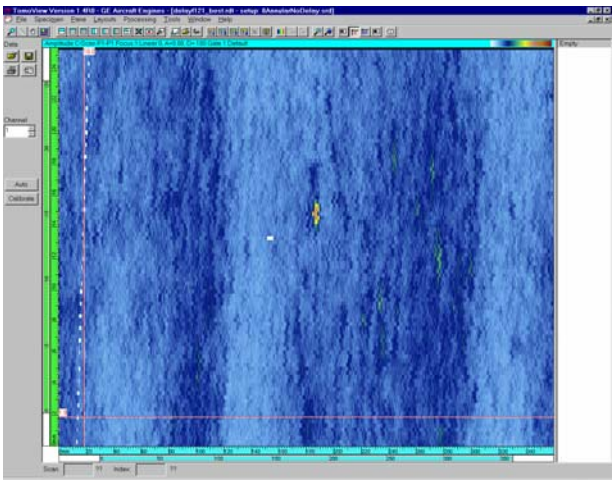


FIGURE 71. C-SCAN AND WAVEFORM RESULTS FOR NEW INDICATION FOUND IN BILLET SEGMENT B1BW3CB



10 MHz phased array inspection results

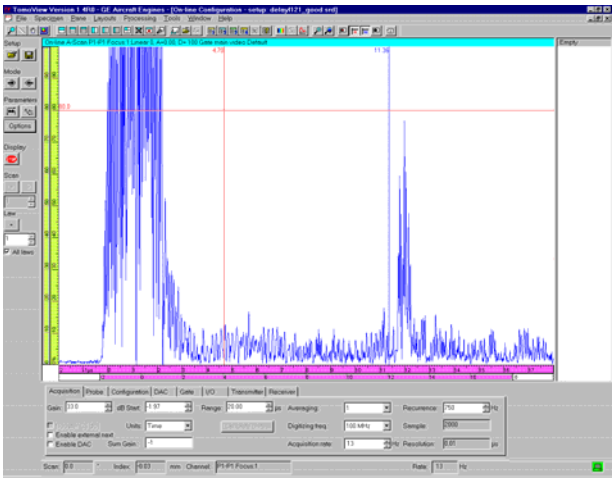


FIGURE 72. C-SCAN AND WAVEFORM RESULTS FOR NEW INDICATION FOUND IN BILLET SEGMENT B1BW3CB USING 10-MHz PHASED ARRAY INSPECTION

3.9 DISPOSITION OF CBS MATERIALS.

Included in the program objectives was the goal to provide reference samples containing naturally occurring hard alpha defects for evaluation of future inspection techniques, validation of PoD and ultrasonic methodologies, and support of technology transfer to titanium billet suppliers. A number of samples remain and are incorporated into the FAA sample library, which is managed by the Airworthiness Assurance Nondestructive Inspection Validation Center (AANC) at Sandia National Laboratories. Table 21 provides a description of the billet materials and indicates those sections that were transitioned for future public domain access. Column 1 contains the original billet ID number. Column 2 contains the indication designator. Column 3 contains the current billet segment ID designator. Columns 4 and 5 provide location information for the indications with inspection amplitude and SNR for each of the three inspection methods contained in columns 6 through 11. Column 12 provides the disposition of the material. Those items that are included in the AANC sample library are indicated.

TABLE 21. LISTING OF SAMPLES REMAINING FROM ORIGINAL BILLET MATERIAL

Original Billet ID	Indication ID	Current Billet Segment ID	Inches From Top	Depth	MZ SNR	MZ Amp (%)	CL SNR	CL Amp (%)	CA SNR	CA Amp (%)	Disposition of Material
B1AW1	A	B1AW1A	3.3	0.2	12.14	190	NA	NA	NA	NA	80″ mult incorporated into sample library with ID B1AW1A
B1AW1	B	B1AW1A	25.9	0.6	4.36	201	NA	NA	2.62	42	80″ mult incorporated into sample library with ID B1AW1A
B1AW1	C	B1AW1A	66.4	1.6	5.47	83	1.91	42	1.85	28	80″ mult incorporated into sample library with ID B1AW1A
B1AW1	D	B1AW1B	92.7	1.7	4.65	73	NA	NA	NA	NA	32″ mult incorporated into sample library with ID B1AW1B
B1AW1	E	B1AW1B	95.2	0.6	4.47	127	NA	NA	4.44	55	32″ mult incorporated into sample library with ID B1AW1B
B1AW2	A	B1AW2A - bar	42.5	0.3	13.59	134	NA	NA	NA	NA	Material from 0″ to 51″ reduced to 1.5″ bar, incorporated into sample library with ID B1AW2A
B1AW2	B	no remaining pieces	72.0	0.2	21.7	225	NA	NA	NA	NA	ETC defect characterization study
B1AW2	C	B1AW2C	89.0	0.8	16.29	213	2.49	65	3.2	>100	14″ mult incorporated into sample library with ID B1AW2C
B1AW2	D	no remaining pieces	98.0	0.7	5.46	134	2.61	50	NA	NA	ETC defect characterization study
B1AW2	E	B1AW2E	104.0	1.3	4.29	160	3.2	>100	2.92	>100	14″ mult incorporated into sample library with ID B1AW2E
B1AW2	F	B1AW2E	114.4	1.1	12.8	268	5.15	94	4.52	86	14″ mult incorporated into sample library with ID B1AW2E
B1AW2	X	no remaining pieces	98.7	0.5	5.05	94	NA	NA	NA	NA	ETC defect characterization study
B1AW3	none	B1AW3A - bar	51								Material from 0″ to 51″ reduced to 2″ bar, incorporated into sample library with ED B1AW3A

TABLE 21. LISTING OF SAMPLES REMAINING FROM ORIGINAL BILLET MATERIAL (Continued)

Original Billet ID	Indication ID	Current Billet Segment ID	Inches From Top	Depth	MZ SNR	MZ Amp (%)	CL SNR	CL Amp (%)	CA SNR	CA Amp (%)	Disposition of Material
B1AW3	A	no remaining pieces	60.0	0.7	5.02	142	2.92	50	2.48	60	ETC defect characterization study
B1AW3	B	B1AW3AA	63.0	0.9	2.05	69	NA	NA	NA	NA	18″ mult incorporated into sample library with ID B1AW3AA
B1AW3	C	B1AW3AB	79.0	1.5	11.79	253	2.69	62	5.7	>100	20″ mult incorporated into sample library with ID B1AW3AB
B1AW3	D	no remaining pieces	94.8	1.1	4.49	101	NA	NA	NA	NA	ETC defect characterization study
B1AW3	E	no remaining pieces	106.0	1.6	2.52	47	NA	NA	NA	NA	ETC defect characterization study
B1AW3	Y	B1AW3AB	77	1.3	5.05	99	NA	NA	NA	NA	20″ mult incorporated into sample library with ID B1AW3AB
B1AW3	Z	B1AW3AB	81	1.3	3.48	77	NA	NA	NA	NA	20″ mult incorporated into sample library with ID B1AW3AB
B1AW3	none	B1AW3AC									14″ mult incorporated into sample library with ID B1AW3AC, remnants after sectioning of indication
B1BW1	A	B1BW1A	21.8	2.2	2.96	63	NA	NA	4.12	68	74″ mult to be incorporated into sample library with ID B1BW1A
B1BW1	B	B1BW1A	28.5	1.7	5.67	113	NA	NA	NA	NA	74″ mult to be incorporated into sample library with ID B1BW1A
B1BW1	C	B1BW1A	44.8	0.6	8.09	142	2.96	70	5.36	>100%	74″ mult to be incorporated into sample library with ID B1BW1A
B1BW1	D	B1BW1A	49.0	1.0	2.79	56	NA	NA	NA	NA	74″ mult to be incorporated into sample library with ID B1BW1A

TABLE 21. LISTING OF SAMPLES REMAINING FROM ORIGINAL BILLET MATERIAL (Continued)

Original Billet ID	Indication ID	Current Billet Segment ID	Inches From Top	Depth	MZ SNR	MZ Amp (%)	CL SNR	CL Amp (%)	CA SNR	CA Amp (%)	Disposition of Material
B1BW1	E	B1BW1A	61.3	0.9	3.05	69	NA	NA	NA	NA	74″ mult to be incorporated into sample library with ID B1BW1A
B1BW1	F	B1BW1A	67.8	1.1	26.6	450	4.6	179	5.6	>100%	74″ mult to be incorporated into sample library with ID B1BW1A
B1BW1	G	B1BW1B	81.0	1.5	8.28	213	2.85	100	3.39	80	HIP to heal sample in 16″ billet segment
B1BW1	H	B1BW1C	99.5	0.4	6.56	127	NA	NA	NA	NA	14″ mult to be incorporated into sample library
B1BW2B	A	B1BW2B	1.1	1.2	13.27	179	5.54	118	NA	NA	86″ mult incorporated into sample library with ID B1BW2B
B1BW2B	B	B1BW2B	17.4	0.3	15.74	160	6.00	108	NA	NA	86″ mult incorporated into sample library with ID B1BW2B
B1BW2B	C	B1BW2B	43.2	0.3	7.55	113	NA	NA	NA	NA	86″ mult incorporated into sample library with ID B1BW2B
B1BW2B	D	B1BW2B	51.2	1.6	11.38	160	2.31	46	4.14	116	86″ mult incorporated into sample library with ID B1BW2B
B1BW2B	E	B1BW2B	65.0	1.5	8.38	142	2.57	108	5.42	101	86″ mult incorporated into sample library with ID B1BW2B
B1BW3	none	B1BW3A									12″ mult incorporated into sample library with ID B1BW3A
B1BW3	A	B1BW3AA	22.0	1.3	3.92	113	NA	NA	NA	NA	Forged to pancake for use in ETC inspection studies
B1BW3	B	B1BW3AB	43.5	1.1	7.56	160	NA	NA	NA	NA	Provided to TRMD for forging study—with 2″ piece incorporated into sample library with ID B1BW3AB

TABLE 21. LISTING OF SAMPLES REMAINING FROM ORIGINAL BILLET MATERIAL (Continued)

Original Billet ID	Indication ID	Current Billet Segment ID	Inches From Top	Depth	MZ SNR	MZ Amp (%)	CL SNR	CL Amp (%)	CA SNR	CA Amp (%)	Disposition of Material
B1BW3	C	no remaining pieces	66.0	0.5	6.67	127	NA	NA	NA	NA	ETC defect characterization study
B1BW3	D	B1BW3CA	86.0	1.5	5.06	74	NA	NA	NA	NA	ETC defect characterization study with 10″ piece incorporated into sample library as B1BW3CA
B1BW3	none	B1BW3CB									14″ mult incorporated into sample library with ID B1BW3CB
B1BW3	none	B1BW3C									13″ mult incorporated into sample library with ID B1BW3C
B2W1	A		10.7	0.5	11.35	142	3.46	60	4.59	90	9″ mult incorporated into sample library with ID B2W1A
B2W1	B		24.5	1.3	11.05	151	3.59	85	2.76	60	attenuation study
B2W1	C	B2W1B	65.0	0.9	6.67	127	NA	NA	22.35	60	Forged to pancake for use in ETC inspection studies
B2W1	D	B2W1C	69.5	0.5	6.46	87	NA	NA	NA	NA	29″ mult incorporated into sample library with ID B2W1C
B2W2	none	B2W1CA									36″ mult incorporated into sample library with ID B2W1CA
B2W2	A		Visible end burst, indication marked as A; ultrasonic inspection not feasible								
B2W2	B	B2W2B	14.0	0.6	6.55	107	NA	NA	NA	NA	10″ mult incorporated into sample library with ID B2W2B

TABLE 21. LISTING OF SAMPLES REMAINING FROM ORIGINAL BILLET MATERIAL (Continued)

Original Billet ID	Indication ID	Current Billet Segment ID	Inches From Top	Depth	MZ SNR	MZ Amp (%)	CL SNR	CL Amp (%)	CA SNR	CA Amp (%)	Disposition of Material
B2W2	C	no remaining pieces	22.4	0.2	4.09	74	NA	NA	NA	NA	ETC defect characterization study
B2W2	D	B2W2C	55.0	0.6	4.46	113	NA	NA	NA	NA	25″ mult incorporated into sample library with ID B2W2C
B2W2	none	B2W2D									Material from 72″ to 123″ reduced to 2″ bar, incorporated into sample library with ID B2W2D
B2W2	X	B2W2C	57	0.55	4.97	61	NA	NA	NA	NA	25″ mult incorporated into sample library with ID B2W2C
B2W3	A	B2W3B	20.1	0.2	6.81	107	NA	NA	3.78	72	18″ mult incorporated into sample library with ID B2W2B
B2W3	B	B2W3B	27.8	2.3	3.54	72	NA	NA	NA	NA	18″ mult incorporated into sample library with ID B2W2B
B2W3	C	B2W3B	31.0	2.0	2.59	50	NA	NA	NA	NA	18″ mult incorporated into sample library with ID B2W2B
B3W1B	A		68.8	2.0	4.8	84	1.36	35	3.96	55	Attenuation study
B3W1B	B	B3W1BB	84.8	2.2	2.45	73	NA	NA	NA	NA	34″ mult incorporated into sample library with ID B3W1BB
B3W1B	C	B3W1BB	102.5	2.3	3.52	99	1.95	40	1.91	35	34″ mult incorporated into sample library with ID B3W1BB
B3W1B	D	B3W1BB	104.3	1.9	9.52	134	2.65	50	4.91	70	34″ mult incorporated into sample library with ID B3W1BB
B3W2	A	B3W2A	1.9	0.7	12.25	357	NA	NA	NA	NA	11″ mult incorporated into sample library with ID B3W2A
B3W2	B	B3W2A	3.3	0.3	8.39	113	NA	NA	5.11	>100	11″ mult incorporated into sample library with ID B3W2A

TABLE 21. LISTING OF SAMPLES REMAINING FROM ORIGINAL BILLET MATERIAL (Continued)

Original Billet ID	Indication ID	Current Billet Segment ID	Inches From Top	Depth	MZ SNR	MZ Amp (%)	CL SNR	CL Amp (%)	CA SNR	CA Amp (%)	Disposition of Material
B3W2	C	B3W2A	8.7	2.1	8.32	201	NA	NA	NA	NA	11″ mult incorporated into sample library with ID B3W2A
B3W2	D		16.9	1.5	5.06	127	3.0	60	3.05	54	Part of B3W2B section to be located
B3W2	E		40.0	1.3	12.53	213	4.47	74	NA	NA	Provided to TRMD for forging study—remnants of length 6″ provided to sample library with ID B3W3CB
B3W2	F	B3W2CA	85.5	0.2	6.83	160	NA	NA	NA	NA	36″ mult incorporated into sample library with ID B3W2CA
B3W2	G	B3W2CB	113.0	1.3	5.88	142	NA	NA	5.74	84	Provided to TRMD for forging study—remnants of length 2″, 5″, 4.5″, and 11″ pieces incorporated into sample library with ID B3W2CB
B3W3	A		12.3	0.6	7.65	113	NA	NA	3.96	80	35″ mult incorporated into sample library with ID B3W3A
B3W3	B	no remaining pieces	51.0	0.8	5.74	120	2.39	50	4.37	60	ETC defect characterization study
B3W3	C	B3W3C	67.6	2.9	8.99	127	3.08	>100	3.67	85	36″ mult incorporated into sample library with ID B3W3C
B3W3	D	B3W3CA	109.6	0.9	8.93	142	NA	NA	NA	NA	32″ mult incorporated into sample library with ID B3W3CA
B3W3	none	B3W3CB									6″ mult incorporated into sample library with ID B3W3CB

Among the samples that are included in the library is the hot isostatic press (HIP)-to-heal sample. In an effort to evaluate the effect or reducing and eliminating the cracks and voids normally associated with hard alpha inclusions on detectability of hard alpha, an indication was selected and a mult removed from the billet. Indication B1BW1-G was selected, and a 16″ section was removed. The details of the inspection are provided in table 22, and the results are shown in figure 73. The indication was detected using all three methods during the field inspection. After sectioning, the mult was inspected using the multizone system at GE prior to and after the HIPping process. No indications were found after the HIPping process. These results point to the enhanced detectability of hard alpha in the presence of cracks and voiding. The sample also provides an excellent resource for the evaluation of future inspection improvements.

TABLE 22. INSPECTION AMPLITUDES AND SNR FOR INDICATION B1BW1-G USED IN HIP-TO-HEAL SAMPLE

Inspection location	MZ Amplitude and SNR	Conventional Normal Amplitude and SNR	Conventional Angle and SNR
Field inspection	213% - 8.3 SNR	100% - 2.9 SNR	80% - 3.4 SNR
Laboratory inspection	125% - 7.4 SNR		
After HIPping	No indication detected		

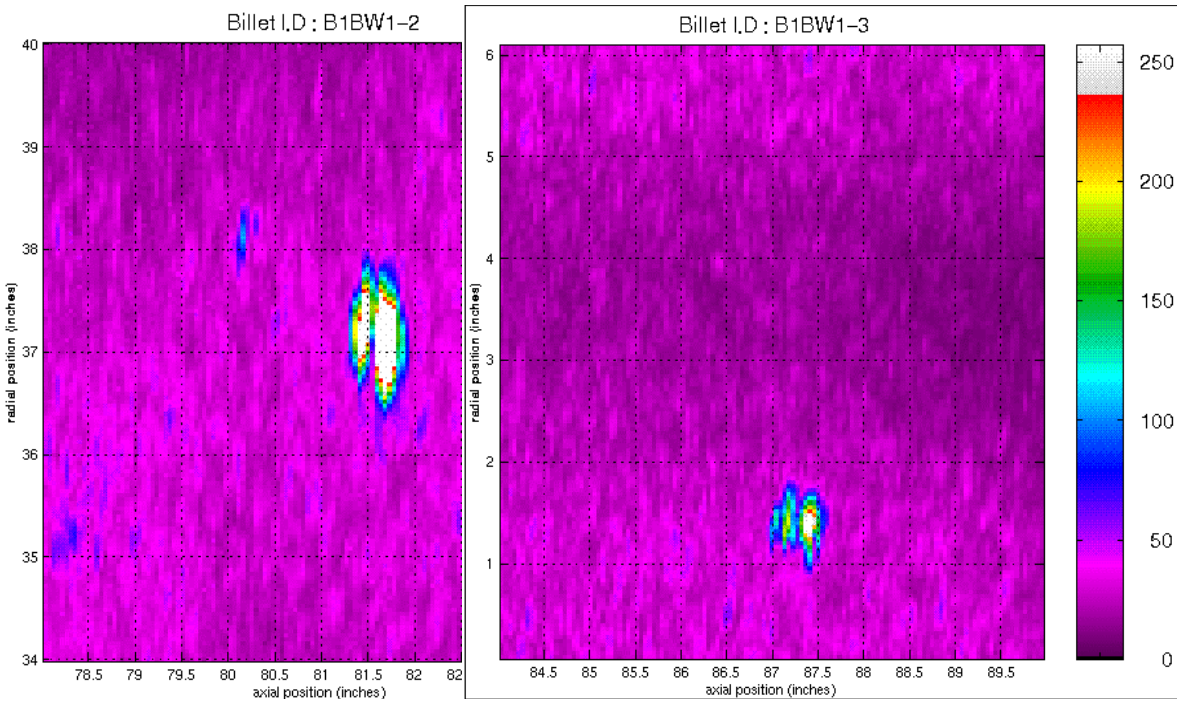


FIGURE 73. C-SCAN RESULTS FOR INDICATION B1BW1-G USED IN HIP-TO-HEAL SAMPLE
(Note: the indication was detectable in zones 2 and 3 during the original field inspection.)

4. CONCLUSIONS.

Hard alpha defects are defined as an interstitially stabilized alpha phase region of substantially higher hardness than surrounding material, arising from very high local nitrogen, oxygen, or carbon concentrations that produce the high hardness, often brittle, alpha phase. Defects may occur because of the inadvertent use of burned sponge or contaminated raw stock, improperly processed electrodes, or vacuum leaks. If hard alpha defects are found, the entire heat in which any hard alpha defect occurs will be downgraded from premium quality and is no longer acceptable for use in critical rotating components. The occurrence of hard alpha defects is rare and detailed study has not been possible. In 1995, the existence of a contaminated heat of material was made known to the Engine Titanium Consortium. The heat was purchased and inspected using multizone and conventional inspection methods. Sixty indications were detected using the multizone method with four misses, compared to 30 detections with conventional inspection. Ten of the defects were selected for detailed characterization. Metallographic characterization of the defects was accomplished using optical microscopy at 5-mil intervals. The optical micrographs were digitally recorded for subsequent reconstruction leading to solid models representing the cracking and voiding of the ten defects. The Contaminated Billet Study (CBS) material offers an unprecedented opportunity to evaluate naturally occurring hard alpha defects and understand the factors related to their detectability. The following primary conclusions were found:

- More than twice as many indications were found with multizone inspection than with the dual probe (longitudinal and angle inspection) conventional inspection. Detection occurred over the full depth of the billet for both methods. Conventional inspection detection was not correlated to the multizone amplitudes, i.e., the conventional misses occurred over the range of amplitudes.

- Phased array inspection was demonstrated to have similar capability to the multizone results with the advantage of simpler fixturing.

- In chemical analysis studies of the defects, the nitrogen concentration was found to drop to less than 1% within 10 mils from the defect center (center of the voiding). The implications of these results are that the nugget and diffusion zone contribute little to the detection of the defect. Ultrasonic response is dominated by the presence of cracks and voiding.

- Defect characterization of ten defects provided detailed hard alpha defect data for metallurgists, life management, design, and inspection personnel. The data also provided input for probability of detection (PoD) calculations and was used in model validation.

- Of the ten hard alpha defects selected for metallographic sectioning, seven were not detected by conventional inspection. All of the missed defects had hard alpha core areas in the 15,000 to 100,000-square-mil range.

- Using the solid model results, the sizes of the defects were tabulated and used in subsequent PoD calculations. The preliminary results indicated inconsistencies between PoD calculations generated from prior data and the recent CBS characterization.

- Several reproducibility studies were performed using a subset of the billets. Variability of up to 10 dB was found for both methods. Inspection setup and transducer alignment were identified as key contributors to the variability.

5. REFERENCES.

1. FAA Advisory Circular 33.15-1, "Manufacturing Process of Premium Quality Titanium Alloy Rotating Engine Components," September 22, 1998.

2. "United Airlines Flight 232 McDonnell Douglas DC-10-10 Sioux Gateway Airport, Sioux City, Iowa," July 19, 1989, NTSB Report Number, AAR-90-06, November 1, 1990.

3. J.R. Costa, R.E. Gonzalez, R.E. Guyotte, D.P. Salvano, T. Swift, and R.J. Koenig (chair), "Titanium Rotating Components Review Team Report," Federal Aviation Administration, Aircraft Certification Service, Engine and Propeller Directorate, Boston, MA, December 14, 1990.

4. FAA Advisory Circular AC 33.14-1, "Damage Tolerance for High Energy Turbine Engine Rotors," January 8, 2001.

5. Howard, P., Copley, D., and Gilmore, R., "Transducer Design for High Sensitivity Ultrasonic Inspection of Titanium," in *Rev. of Prog. in QNDE, Vol.16A*, D.O. Thompson and D.E. Chimenti, eds., Plenum, New York, 1997, pp. 893-900.

6. Gray, T.A., "Application of Measurement Models to Specification of Ultrasonic Inspections," in *Rev. of Prog. in QNDE, Vol.16B*, D.O. Thompson and D.E. Chimenti, eds., Plenum, New York, 1997, pp. 2061-2068.

7. Thompson, R.B., Margetan, F.J., Yalda, I., Chiou, C.-P., and Panetta, P.D., "Coupling Microstructure Outputs of Process Models to Ultrasonic Inspectability Predictions," in *Rev. of Prog. in QNDE, Vol.17B*, D.O. Thompson and D.E. Chimenti, eds., Plenum, New York, 1998, pp. 1847-1853.

8. Umbach, J.A. and Roberts, R.A., "Ultrasonic Phased Array Transducers-Model and Experiment," presented at *ASNT Fall Conference*, October 1997.

9. K. Smith and L. Brasche, "Successful Implementation of FAA Research Addressing the Disk Inspection Initiative," in *Proceedings of the 5th Annual FAA/NASA/DOD Aging Aircraft Conference*, on CD, 2003.

10. Filkins, R.J., Fulton, J.P., Patton, T.C. and Young, J.D., "Recent Advances and Implementations of Flexible Eddy Current Probe Technology," in *Rev. of Prog. in QNDE*, Vol.17B, D.O. Thompson and D.E. Chimenti, eds., Plenum, New York, 1998, pp. 1809-1816.

11. Amos, J.M. and Chao, J.C., "Optimization of a Wide-Field Eddy Current Probe Using a Boundary Element Method Based Model," in *Rev. of Prog. in QNDE, Vol.17A*, D.O. Thompson and D.E. Chimenti, eds., Plenum, New York, 1998, pp. 275-282.

12. Chao, J.C., Nakagawa, N., Raulerson, D.A., and Moulder, J.C., "Boundary Element Method Based Probe Design Model Validation," in *Rev. of Prog. in QNDE, Vol.16A*, D.O. Thompson and D.E. Chimenti, eds., Plenum, New York, 1997, pp. 967-972.

13. Meeker, W.Q., Chan, V., Thompson, R.B., and Chiou, C.-P., "A Methodology for Predicting Probability of Detection for Ultrasonic Testing," in *Rev. of Prog. in QNDE, Vol.20B*, D.O. Thompson and D.E. Chimenti, eds., AIP, Melville, NY, 2001, pp. 1972-1978.

14. "A Methodology for the Assessment of the Capability of Inspection Systems for Detection of Subsurface Flaws in Engine Components," FAA Report DOT/FAA/AR-01/96, September 2002.

15. G.R. Leverant, R.C. McClung, Y.-T. Wu, H.R. Millwater, D.S. Riha, M.P. Enright, G.G. Chell, K.S. Chan, P.C. McKeighan, M. Gorelik, C. Fischer, D. Lehmann, K. Green, J. Bartos, N. Howard, and S. Srivatsa, "Turbine Rotor Material Design," FAA Report DOT/FAA/AR-00/64, December 2000.

16. S. Srivatsa, "Turbine Rotor Material Design—Task 2, Effect of Forging on Defect Morphology," Southwest Research Institute, December 11, 2002.

17. W.W. Bogan, "Metallurgical Evaluation: RMI 2XVAR Ti64 Heat 883588 Hard Alpha," Internal ETC Letter Report, April 27, 1995.

18. Smith, K.D., "Zoned Ultrasonic Inspection of Titanium Billet Using Phased Array Transducers," *Engine Titanium Consortium Open Forum Proceedings*, February 1995.

19. Mucciardi, T., "Phased Array Inspection of Titanium Billets," *Engine Titanium Consortium Open Forum Proceedings*, May 1996.

20. Umbach, J. and Roberts, R. "Focussed Array Transducer for Billet Inspection: Model and Experiment," *Engine Titanium Consortium Open Forum Proceedings*, November 1997.

21. Lacroix, B., Lupien, V., Duffy, T., Kinney, A., Khandelwal, P., and Wasan, H.S., "Phased-Array Ultrasonic System for Inspection of Titanium Billets," *Review of Progress*

in Quantitative Nondestructive Evaluation, D.O. Thompson and D.E. Chimenti, eds., Vol. 21A, p. 861, 2002.

22. B. Boyd, C.-P. Chiou, R.B. Thompson, and J. Oliver, "Development of Geometrical Models of Hard Alpha Inclusions for Ultrasonic Analysis in Titanium Alloys," *Review of Progress in Quantitative Nondestructive Evaluation*, D.O. Thompson and D.E. Chimenti, eds., Vol. 17A, 1998, pp. 823-830.

23. C.-P. Chiou, B. Boyd, R.B. Thompson, and J. Oliver, "Geometrical and Ultrasonic Modeling of Hard Alpha Defect Components in Titanium Alloys," *Review of Progress in Quantitative Nondestructive Evaluation*, D.O. Thompson and D.E. Chimenti, eds., Vol. 18B, 1999, pp. 1829-1836.

24. C.-P. Chiou, F.J. Margetan, and R. B. Thompson, "Modeling of Ultrasonic Signals from Weak Inclusions," *Review of Progress in Quantitative Nondestructive Evaluation*, D.O. Thompson and D.E. Chimenti, eds., Vol. 15A, 1996, pp. 49-55.

25. C.-P. Chiou and R.B. Thompson, "A Comparative Study of Ultrasonic Models for Hard Alpha Defects in Titanium Alloys," Presented in *Review of Progress in Quantitative Nondestructive Evaluation*, July 30, 1999.

26. C.F. Ying and R. Truell, "Scattering of a Plane Longitudinal Wave by a Spherical Obstacle in an Isotropically Elastic Solid," *Journal of Applied Physics*, Vol. 27, No. 9, 1956, pp. 1086-1097.

27. C.-P. Chiou, F.J. Margetan, R.B. Thompson, and Brian Boyd, "Development of Ultrasonic Model for Hard Alpha Inclusions in Titanium Alloys," *Review of Progress in Quantitative Nondestructive Evaluation*, D.O. Thompson and D.E. Chimenti, eds., Vol. 16B, p. 1529, 1997.

28. R.B. Thompson and T.A. Gray, "A Model Relating Ultrasonic Scattering Measurements Through Liquid-Solid Interfaces to Unbounded Medium Scattering Amplitudes," *Journal of Acoustical Society of America*, 74 (4), 1983, pp. 1279-1290.

29. B.A. Auld, "General Electromechanical Reciprocity Relations Applied to the Calculation of Elastic Wave Scattering Coefficients," *Wave Motion*, 1, 1979, pp. 3-10.

30. Thompson, R.B., Meeker, W.Q., Chiou, C.-P., Brasche, L., Burkel, D., and Sturges, D.J., "Issues in the Determination of Default POD for Hard Alpha Inclusions in Titanium Rotating Components for Aircraft Engines," *Review of Progress in Quantitative Nondestructive Evaluation*, Vol. 23B, D.O. Thompson and D.E. Chimenti, eds., AIP, NY, p. 1587-1594, 2004.

31. P.D. Panetta, R.B. Thompson, and F.J. Margetan, "Use of Electron Backscatter Diffraction in Understanding Texture and the Mechanisms of Backscattered Noise

Generation in Titanium Alloys," in *Rev. of Prog. in QNDE*, Vol. 17A, D.O. Thompson and D.E. Chimenti, eds., Plenum, New York, 1998, p. 89-96.

32. Panetta, P.D., Thompson, R.B., Margetan, F.J., and Yalda, I., "Ultrasonic Microstructural Characterization and Modeling of Attenuation in Ti-17 and Ti-6Al-4V Alloys," *Nondestructive Evaluation and Materials Properties*, O. Buck and P. Liaw, eds., TMS, Warrendale, OH, 1998.

33. Gooding, C. and Biddulph, J., "Ultrasonic Inspection of Titanium Alloy Billet From RMI Contaminated Heat #883588," *Engine Titanium Consortium Open Forum Proceedings*, May 1996.

34. Margetan, F.J., Yalda, I.M., and Thompson, R.B., "Estimating Ultrasonic Signal-to-Noise Ratios for Inspections of Cylindrical Billets," *Review of Progress in Quantitative Nondestructive Evaluation*, D.O. Thompson and D.E. Chimenti, eds., Vol. 13B, p. 1737, 1994.

35. Howard, P.J. and Gilmore, R.S., "Ultrasonic C-Scan Imaging for Hard Alpha Flaw Detection and Characterization," *Review of Progress in Quantitative Nondestructive Evaluation*, D.O. Thompson and D.E. Chimenti, eds., Vol. 13B, p. 763, 1994.

36. Copley, D., "Billet Inspection Reproducibility Study: ETC Open Forum Proceedings," Houston, Texas, 1997.

APPENDIX A—LITERATURE SURVEY COMPLETED BY ALLIEDSIGNAL IN PHASE I: ENGINE TITANIUM CONSORTIUM PROGRAM

A REVIEW OF THE ORIGIN AND CHARACTER OF INGOT DEFECTS THAT MAY OCCUR IN AEROSPACE TITANIUM ALLOYS AND NDE METHODS FOR THEIR DETECTION

James A. Hall, Janet Wade, Lloyd Schaefer, Andy Kinney
Materials and Process Engineering
and
Valerie Peters
Component Investigation
AlliedSignal Engines
June 1997 updated February 2003

1. ABSTRACT

In support of the Federal Aviation Administration's (FAA) Engine Titanium Consortium (ETC), this paper discusses the origin and characteristics of titanium melt related defects, provides a brief synopsis of experiments conducted to date relating to the evaluation and/or control of melt related defects, the potential nondestructive evaluation (NDE) methods for detecting such defects, and contains literature search references pertaining to these subjects. The report is divided into three sections:

Section 1 of this report contains discussions of Type I defects, high-density inclusions, Type II defects, ingot porosity, and alloy segregation with their definitions, causes and characteristics. Brief synopses of several published experiments relating to sources of nitride inclusions, defect removal, nitride seed development, effect of defects on fatigue properties, and alpha segregation are also included. Forging or conversion related defects are not included in this report.

Section 2 addresses surface and volumetric NDE methods appropriate for detecting and characterizing titanium melt related defects. Image and signal analysis techniques for these methods are identified and discussed as well as various means of measuring NDE methods probability of detection (POD).

Section 3 comments on the utility of the literature review and recommendations for future work.

2. ACKNOWLEDGMENT

This material is based upon work performed as a part of the Engine Titanium Consortium operated by Iowa State University for the FAA New England Engine and Propeller Directorate and the FAA Technical Center under Grant Number 94-G-048.

3. INTRODUCTION

As a part of the Fundamental Studies in Titanium Task of the ETC, a literature review was undertaken. The literature review had the following purposes:

- Provide the latest information about the formation of various defect types
- Detail any known preventative measures for these types of defects

- Provide information regarding the effect of microstructure and macrostructure of the parent material on detectability

- Catalog data on the material properties

- Provide background information on NDE methods developed by other researchers appropriate to titanium inspection

The intent is to provide data for the formulation of approaches to the various defect detection problems in various material forms. The available literature was reviewed from the NERAC and NOTICE databases. Additional information was also gathered from other available sources such as the following: non-proprietary information solicited from members of the ETC, various domestic producers of titanium, and the Jet Engine Titanium Quality Committee; QNDE proceedings; and other open literature journals. The synopses provided below are only a sampling and should not be interpreted as being complete, nor inclusive of all key work.

4. INGOT DEFECTS, DEFINITION, ORIGINS and CHARACTERISTICS

4.1 TYPE I DEFECTS [A-1 to A-5]

Type I defects are also known as high interstitial defects (HID), interstitial rich inclusions or low density inclusions (LDI). They are recognized as alpha rich particles interstitially stabilized with nitrogen, oxygen or carbon, or some combinations of these. Their metal alloy content may range from very nearly all titanium to nominal alloy content of the host heat or even of a different alloy.

The embryo form of these defects have a much higher melting point than titanium or Ti alloys and must be consumed by dissolution into the melt. Depending on the relative size and densities of Type I defects, large heavy defects may survive multiple vacuum arc remelt (VAR) processing and smaller lighter defects may survive cold hearth melting (CHM). The defects are substantially harder than the surrounding matrix and may impair fatigue resistance and ductility. The defects are difficult to detect unless associated with voids or cracking from thermo-mechanical working. The term LDI arose from this void association, however, the alpha-rich phase itself is not of "low density." Of course, creation of a defect during melting as described below, will negate some, or all, of the dissolution opportunities offered by melting.

4.2 SOURCES OF TYPE I DEFECTS

4.2.1 BURNED SPONGE, REACTOR VESSEL BURNING [A-2 and A-5]

Type I defects, originating from this source are attributed to the entry of air into the reaction vessel or vacuum distillation chamber during sponge production. If in a confined volume, air reacts with the titanium sponge, which consumes oxygen ($O_{2)}$ first, and then the nitrogen ($N_{2)}$. Nitrogen rich defects resist dissolution in the liquid titanium.

Visual Appearance: Regions of high nitrogen content titanium, when removed from the reactor vessel appear much like the titanium metal, only much more friable. It seldom is golden in color

as the near stoichiometric TiN intermetallic would be and therefore it is not easy to visually separate them from the normal particles.

Metallurgical Characteristics: the metallic alloy content will be considerably less than that of the host alloy and the hardness will be significantly higher. Voids may be associated with the larger variety of these defects.

Location in Ingot: Large defects are heavier than the liquid and will tend to concentrate in the bottom 1/3 of the ingot. Smaller (if not dissolved) defects, may be more uniformly distributed. Defects in this family reflect an out-of-control process and may appear in all heats incorporating the culprit sponge lot, and have a size distribution only slightly different than that of the sponge, reduced slightly in size by melting dissolution.

4.2.2 BURNED SPONGE, OTHER [A-5]

Type I defects are attributed to burned sponge caused by the following:

- Fires or flashing which may occur during extraction of sponge from the reactor or vacuum distillation chamber
- Downstream processes, such as crushing the chip to sponge
- Drying, in the case of leached sponge
- Sponge may experience combustion during blending and compacting of the electrode

Visual Appearance: In most cases the burned sponge is discolored and visually separable. The refractory particle is brittle and easily crushed. As these causes will affect entire lots of sponge production, a visual examination of selected samples of each lot is often used as a quality control process and finding of HID embryos will disqualify the entire lot from rotor grade applications. However this inspection is ineffective in screening out down stream defect sources from events, such as combustion during the blending operation.

4.2.3 BURNED BULK SCRAP [A-5]

- Torch cutting. Type I defects may be attributed to torch cutting in preparation of bulk scrap for fabrication. Part of the process detail involves combustion of titanium and in the tight confines of the cutting zone, nitrogen combustion is possible. Furthermore, residual organic material may contribute to carbon stabilization in this region.
- Infoliated ends of mill scrap may contain high O_2 and/or N_2 levels and should be avoided for rotor grade material as they are not easily cleaned.

Metallurgical characteristics: The defect will have normal metallic alloy content of the scrap source. It is unlikely to have cracks or voids unless associated with conversion or forging operations. Size varies but shape will likely be irregular.

4.2.4 BURNED CHIPS AND TURNINGS [A-5].

Burned chips and turnings may be another source of HID formers. If burned in a restricted volume, they may become highly contaminated with nitrogen (or carbon in the case of machining chips burned during the machining operation itself or prior to the cleaning step in the chip processing line), therefore they are refractory. The shape and size of chip (high surface to volume ratio) leads to rapid dissolution during melting and are less likely to be serious HID sources in multiple melted ingot, e.g., double or triple VAR, fabricated from electrodes contaminated by them.

4.2.5 INADEQUATE SHIELDING OF WELDS DURING ELECTRODE FABRICATION [A-2 and A-5]

Type I defects may be attributed to inadequate shielding of welds during electrode fabrication which can result in nitrogen rich weld metal. Defects may be attributed to the use of metal-inert gas (MIG) welding, if the welding process is not shielded well enough to exclude contamination. Welding of sponge electrodes with plasma torches produces a wide gradient of metallic content as the host being welded contains sponge particles, pure metallic additions, and master alloy particles. The use of chamber welding and specially shielded weld enclosures is necessary to assure absence of contaminated welds.

Visual Appearance: They are sometimes discolored with the characteristic gold color of TiN. Visual inspection of the welds after the electrode is fabricated often will reveal indications of poor shielding although this is not fool proof as over welding contaminated welds will destroy the visual evidence.

Metallurgical Characteristics: HIDs from this source may contain metallic alloying elements in the range from unalloyed titanium to that of the host alloy. It will be harder than the host alloy because of the interstitial content. Any cracking associated with the HID will come from deformation processing at either billet or forging stages. However, this type of defect may survive the melting and conversion processes without developing cracks.

Location in Ingot: This type of HID will be heavier than the liquid titanium and tend to sink to the bottom of the liquid pool. In multiple melting operations, each melt ingot will concentrate the HIDs in the bottom 1/3 of its length. Each melt will reduce the HID size depending on the pool depth, the alloy melting temperature, and the practice for electrode inversion between melts. It is a good practice to disallow welding in preparation of the final melt electrode because any HID embryo will have only one chance to dissolve.

4.2.6 VAR FURNACE LEAKS [A-2, A-4, and A-5]

Type I defects attributed to air leaks are most commonly associated with leaks in sliding seals (the ram feed through in most VAR furnace designs). This rarely occurs. Such condition is evidenced by a pressure increase in the furnace, unless a rapid increase in leak rate is also experienced. This may be dampened by high pumping capacity.

Visual Appearance: The defect will be rather large and may appear associated with a hole in the remaining wafer after hot top which may appear much like a torch cut surface.

Metallurgical Characteristics: The defect will be harder than the matrix and have the metallic composition of the host ingot with a higher alpha content when occurring in alpha-beta alloys. The defect is unlikely to have cracks or voids except those associated with deformation processing. They may be large.

Location in Ingot: The defect will be localized near the top of the ingot produced when the leak occurred but may survive subsequent melting and wind up in the next ingot at a position depending on the electrode inversion practice used.

4.2.7 INEFFECTIVE HOUSEKEEPING [A-5]

Type I defects are often attributed to splatter and other melt condensate deposits within the furnace enclosure (furnace head and ancillary devices and chambers). These will be finely divided and will oxidize (nitride) when such hot particles are exposed to air - this is generally associated with opening the furnace and exposing the virgin alloy splatter to the atmosphere. Subsequent melting may see these particles fall in the molten pool and survive by rapidly sinking to the bottom or sides - most common when the pool is shallow such as at the arc strike or in the hot top operation. This sort of defect may occur in VAR as well as CHM operations.

Metallurgical Characteristics: The origin of the source may have come from another heat of material, therefore the metallic composition could be anything. In this case the HID will be harder than the matrix, and due to the possibility of inter-alloy mixing, there may be a very different microstructure. The defect is unlikely to have voids or cracks associated with them. They are likely to be regularly shaped but not exclusively. They are likely to be smaller than the first 6 HIDs described above.

Location in Ingot: The defects tend to be concentrated near the top or the bottom of the final melt because of the shallow pool existing in these locations. For the deeper pool situations in steady state melting, their survival is problematic and limited to the regions near the ingot surface. With some alloys the final melt is performed entirely with a shallow pool to avoid melt segregation and, in this case, these defects may occur anywhere in the ingot. The defect is not likely to be as refractory as the other HID’s and is not likely to survive multiple melting.

4.2.8 RESIDUAL BURNED MATERIAL FROM FIRST INGOT SURFACE[A-5]

Recent experience has shown that residual magnesium or sodium in the sponge will vaporize during the first melt of a sponge electrode. The condensate from this vaporization forms on the crucible surface and is effectively transferred to the ingot surface as it subsequently fills the crucible. When the crucible is stripped from this first melt ingot, which will become an electrode for the next VAR, under certain conditions these metal deposits will ignite and burn with enough heat released to oxidize the rather porous ingot surface forming oxide and nitride rich titanium.

These areas are refractory and may not melt during the subsequent two or three VAR steps.

Metallurgical Characteristics: These particles start out rather large and pancake shaped and may be free of initial voids. Their composition may be near that of the base alloy. But they may also be rich in the high vapor pressure alloying elements such as aluminum. They may have almost any size or shape as these features will be modulated some by subsequent melts. Depending on both the size and initial interstitial content, these defects may or may not crack during deformation processing so we cannot count on having cracks or voids to aid UT detection. They will be oxygen and nitrogen stabilized but not stabilized with carbon.

Location in Ingot: These defects are most likely to find their way to the bottom part of each subsequent melt if they are refractory enough to survive the liquid metal exposure and the thermal shock of transfer across the arc zone. If the electrode inversion practice is such that the bottom of the first melt becomes the top of the second and inversion occurs again to make the third VAR ingot, it is possible that part of the final electrode will melt through the HID containing material during the hot-topping operation. Therefore, such defects will have no deep pool into which to sink. Accordingly, there is a possibility that the hot-topped region may contain hard alpha defects. Generally speaking, this material is all lost in top cropping for other reasons so we seldom, if ever find such defects near the top of the billet made of rotor grade triple VAR ingot.

Prevention: Take precautions to avoid the environment conducive to the burning described above. With the anticipation that not always will the operation be able to avoid ignition of the inevitable deposit (even vacuum distilled sponge contains sufficient volatile residuals to cause a light case of this problem) by observing the crucible stripping operation operators can identify the potential problem areas and take measure to eliminate them from the process stream.

4.3 HIGH DENSITY INCLUSIONS [A-2, A-3, and A-5]

High-density inclusions include refractory metals (W, Mo, Ta, and Nb) or refractory metal carbides. The main sources of these defects are scrap and poor housekeeping. Carbide and tungsten particles have often been traced to machine turnings cut with carbide tools and non-consumable welding electrodes, respectively. Refractory metals have higher melting points and densities than titanium and tend to sink to the liquid-metal interface at the bottom of the molten pool and to a lesser extent on the outer 25% of the radius.

Another source of high-density inclusions is ineffective housekeeping associated with equipment repair, such as TIG welding. Without proper house cleaning, inadvertent inclusion of a Thoriated Tungsten welding electrode scrap may result. Similarly, even very small tungsten metal pieces, such as incandescent light bulb filaments have been shown to survive multiple VAR of titanium alloys [A-6]

Master alloy additions of refractory metals, such as Molybdenum, are formulated to reduce the melting point so that they will completely dissolve or melt, but there is history of these sorts of particles surviving. Recent, known, events have been attributed to use of coarse master alloy particles in formulating the ingot. The key to avoiding such occurrences is to make sure that the alloy additions are small enough particle size to assure dissolution in multiply melted material.

4.4 TYPE II DEFECTS [A-2, A-3, and A-5]

Type II defects are also known as soft alpha segregates. These defects are found in alloys containing aluminum. Type II defects are often called High Aluminum Defects (HAD) because of the significantly higher than normal aluminum content they exhibit. Another name often used to describe this sort of defect is “chicken tracks” which reflects their appearance in billet slices.

Cause: Type II alpha defects are associated with ingot pipe and void formation. As shrinkage pipe forms in a hot titanium alloy ingot, aluminum (or any other relatively volatile alloying element at the high temperature involved) evaporates rapidly from the hottest surfaces of the void, filling it with metallic vapor which condenses on cooler surfaces of the void as the ingot cools. As a result, the interior surface of the void will be coated with aluminum and/or other volatile elements, and just below the surface, the microstructure will be slightly depleted in these elements. Subsequent forging of the ingot or intermediate mill product, in the production of billet and bar, will cause the voids to close, but the temperature and time combination is insufficient to result in serious homogenization.

Visual Appearance: Areas enriched or depleted with aluminum will often be found to outline portions of the original void/pipe surface and appear as Type II segregation. The result of forging the voids closed is a rather irregularly shaped zone of aluminum rich alloy (the name of chicken tracks is descriptive here) often with an alpha lean zone immediately adjacent. They appear as light and dark etching zones, respectively, in the macrostructure of product.

Metallurgical Characteristics: The aluminum content of the defect is usually somewhat higher than that of the matrix and the vanadium content may be lower in Ti Al-V alloys. However, it is not uncommon to find an associated area which is slightly lower in aluminum content and higher in vanadium that the matrix. The defect is a form of localized alpha segregation but, unlike a Type I defects, is quite ductile with a hardness usually not much greater than that of the matrix. The segregates tend to be relatively long, thin and very irregular. Small defects do not seem to have a pronounced effect on mechanical properties of annealed alloys.

Detection: When these defects are anodized, some develop a characteristic blue color. However, areas depleted in aluminum tend to etch lighter on anodizing. These areas and have

been incorrectly referred to as beta segregation. They present only a small difference in elastic properties so UT inspection is not likely to detect Type II defects, especially the smaller ones.

Prevention: Good hot topping practices that minimize the area removed during billet cropping for macroexamination. A good billet slice inspection and cropping practice will virtually eliminate these defects associated with healed pipe. However, it is possible to create them with aggressive billet conversion practice and these are difficult to detect. The best practice is to avoid their creation by process control in the mill.

4.5 INGOT POROSITY

There are two primary types of ingot porosity: gas porosity and shrinkage porosity.
Gas porosity in VAR ingots has often been found associated with residual chloride salts in the sponge. Salts have essentially no solubility in the solid metal but form vapor bubbles in the liquid phase which have been found to account for the following defects:

- Unhealed pipe in billet
- Blisters observed in Ti-8Mn sheet
- Weld porosity
- Porosity in blended elemental powder metallurgy products

Gas porosity in Plasma Arc Melted (PAM) ingots is usually associated with entrapped inert gas used in the melting operations. Subsequent VAR ought to remove these, and PAM + VAR ingot, produced normally, will be free of gas porosity.

Shrinkage porosity can be found throughout the ingot and in the pipe section. Porosity in the pipe section results from metal shrinkage and is also associated with creation of Type II defects. They can be largely avoided by good hot topping practices. High melt rates have been found to produce more ingot porosity than slow rates (better melt degassing occurs at the slow rates and the shallower pools experience less shrinkage on freezing).

Shrinkage porosity is unlikely to survive ingot conversion practices and should not be confused with strain induced porosity created during the conversion process itself. The latter often results in “clean” porosity which is often seen during UT inspection of the billet when sophisticated means, like multi-zone inspection, are applied.

4.6 ALLOY SEGREGATION [A-2, A-5, and A-7]

Alloy segregation can be influenced by several factors including, primarily, the alloying elements added and their amounts; solidification conditions, including temperature gradients; power interruptions or other perturbations of steady state conditions; hot topping procedure; and the homogeneity of the starting material.

Segregation is most conveniently discussed in terms of the general categories of macrosegregation and microsegregation.

Macrosegregation is generally characterized by alloying element composition differences measurable over a long range such as top to bottom, or center to outside of the ingot, or its primary converted products, such as billet. The causes for this can be lumped generally into three categories:

- Inhomogeneity of starting material or electrode so that the composition of the last to melt dominates the composition of the top of the VAR ingot

- Effects of directional solidification, given homogeneous electrodes, in which the melting point suppressers will concentrate in the liquid and be richest in the last to solidify, which means that the top of the VAR ingot and the centerline will likely be rich in these elements. The opposite is true of melting point raisers.

- Vaporization and re-condensation, on crucible walls, of high vapor pressure elements, such as aluminum. As the ingot lengthens when more electrode is consumed, these elements will be entrapped in the ingot surface creating an aluminum rich zone at the ingot surface. During conversion, these are lost due to intermediate conditioning, but remelted electrodes are then inhomogeneous as the greatest amount of condensate is seen towards the end of the melt (top of the crucible). This occurs because there is much more time for the vaporization/condensation cycle to occur. These are often avoided by proper electrode formulation compensation or electrode inversion practices and, in the last case, splash ring avoidance or remelt procedures.

Microsegregation, as distinguished from inclusions with refractory characteristics, usually results from liquid/solid partitioning during solidification much as for the macrosegregation. Its manifestation will be localized in areas where concentrations of partitioned melting point suppressers in the liquid, at the liquid-solid interface, is subjected to accelerated solidification, such as a rapid reduction in heat input. Also, where the solidification conditions favor the formation of a dendritic liquid/solid interface there is a micro partitioning of liquid formers. The interdendritic zones, being the last to solidify, will entrap extraordinarily high amounts of melting point suppressers that are mostly beta forming elements. The manifestation of this is a local area with its beta transus temperature much lower than its immediate surroundings. Near transus heat treatments will expose these areas as very lean or absent of primary alpha after a subtransus thermal exposure and are called beta flecks. The controls which can minimize the occurrence of such segregation include avoidance of power interruptions or abrupt negative changes in power level, maintenance of high thermal gradients in the liquid at the solid/liquid interface, and adherence to the Tiller [A-8] model for the conditions that favor the formation of planar interfaces. These include, establishing high temperature gradients in the liquid, low interface velocity, and effectively removing the build up of solute in the liquid at the interface.

There are some other liquid phase formers which segregate but do not form beta flecks because subsequent solid state transformations result in discrete precipitates. The most common amongst these is silicon, which can, if large amounts are in the alloy and the proper solidification conditions are not present, result in bands of higher than normal concentration of discrete silicide precipitates. There is considerable controversy regarding the impact these bands have on properties, but there is no disagreement that there is no harm in avoiding them and this is the safe thing to do.

The beta flecks, in an alpha-beta heat treated microstructure, can reduce the fatigue properties due to microstructural discontinuities which produce elastic property discontinuities as was found in low cycle fatigue testing of the high strength alloy Ti-5Al-2Sn-2Zr-4Cr-4Mo (Ti-17) alloy.

4.7 SYNOPSES OF EXPERIMENTAL WORK

This section contains synopses of several articles which were associated with or related to defect removal, sources of nitride inclusions, nitride seed development, and the effect of defects on fatigue properties.

4.7.1 NITRIDE INCLUSIONS IN TITANIUM INGOTS: A STUDY OF POSSIBLE SOURCES IN THE PRODUCTION OF MAGNESIUM-REDUCED SPONGE (1973) [A-1]

Purpose: The objective of this experiment was to demonstrate how impurities may be introduced into titanium sponge during manufacture by the magnesium reduction process and to determine under what conditions they contribute to the formation of defect-forming impurity clusters that persist through the ingot melting cycle.

Conclusions: When contaminated by an air leak during the distillation cycle or when made from air contaminated magnesium, a large variation in nitrogen content was found in the magnesium-reduced titanium sponge. TiN and Ti_2N were found in the highest-nitrogen regions. The observed nitrides were not in the form of hard, high-density particles. However, the friable pieces, powder pockets or loose powder may be compressed during electrode pressing and subsequently sintered, during melting, from the heat of the arc to produce higher-density particles. These higher density particles can survive arc melting.

Color and texture are not reliable criteria for spotting these sort of defects during sponge inspection. During both the reduction cycle and the distillation cycle, air-burned and nitrided sponge may change its color and texture. The sponge particles act as nuclei for sponge growth and may be found partially or completely clad by newly formed sponge.

It is not clear that HIDs with these physical characteristics have been unambiguously identified in any multiple melted VAR heat but the possibility for their existence, none-the-less exists [A-5].

4.7.2 ALPHA SEGREGATION IN TITANIUM ALLOYS [A-9]

Purpose: An experiment was conducted by creating an artificial “pipe” to show that Type II (alpha segregation) defects form in pipe cavities and is a result of non-uniform evaporation and redeposition of relatively volatile alloying elements such as aluminum.

Experiment/Conclusions: An ultrasonically sound Ti-6Al-4V square billet was heated to 1700°F and the corners were severely pressed in such a way as to deliberately create center bursts which would be detectable by UT inspection. After the internally cracked billet was, cooled and conditioned followed by UT verification of the internal cracking, the piece was reheated to

2050°F for six hours and forged to heal the internal cracks. Ultrasonic inspection showed no remaining defects and slices cut from areas previously showing sonic indications showed the characteristics of Type II alpha segregation.

4.7.3 REMOVAL OF DEFECTS FROM TITANIUM ALLOYS WITH ELECTRON BEAM COLD HEARTH REFINING [A-2]

Purpose: An experiment was conducted to evaluate the EBCHM process for removal of defect particles from liquid titanium to prevent inclusion formation in ingots.

Experiment/Conclusions: Various materials including carbide tool chips, nitrided sponge, and flame-cut titanium scrap were used as seed in sub-scale EBCHR experiments.

All of the tungsten carbide tool bit seeds were located in the hearth skull using x-ray inspection after melting of a tungsten carbide tool bit seeded electrode which was fabricated from Ti-6Al-4V scrap. The hearth skull was then remelted several times to show the dissolution rate of HDI's to be roughly 20 microns/sec.

An ingot was produced which contained Type I defects and was then used as melt stock for EBCHM. The material was melted twice in the hearth and cast into an ingot. One defect was detected in the ingot and was attributed to a large transient in the process in which a piece of the electrode fell into the front end of the hearth at the same time that a high voltage arc extinguished the electron beams. The large flow of metal washed over the piece of electrode in the hearth and carried the defect over the lip into the ingot mold. Hearth and baffle design modifications have since been incorporated into production equipment to avoid this sort of occurrence [A-6].

To understand the behavior of HID's, an experiment was run by seeding Ti-6Al-4V bars with cutting slag and nitrided sponge. Though HID's are sometimes believed to be less dense than the liquid surrounding them, their density is actually greater than the liquid and they sink. The analysis is still in progress, however, the seeds that were located were all beneath the surface of the liquid down to the solid-liquid interface. It was shown that HID's settle rapidly to the solid-liquid interface and then process to dissolve at a rate determined by the temperature at that interface.

EBCHM and PCHM have been sufficiently well developed that now they have been incorporated into the permitted processes for producing rotor grade billet for certain OEMs. Substantiating this has been a record of hard alpha inclusions, found in rotor grade billet made from ingots the incorporate these cold hearth melting methods, is equivalent to triple VAR. There is no doubt that this process is matter-of-fact and approaching maturity [A-6].

4.7.4 DEVELOPMENT OF SEEDS FOR REPRODUCIBLE LDI'S IN TITANIUM MELTING TESTS [A-10]

Purpose: The paper discussed the manufacture and evaluation of artificial HID formers (seeds).

Experiment/Conclusions: Sponge particles were nitrided in a furnace containing flowing nitrogen at partial pressure less than one atmosphere to produce a uniform gold color with an of average 12 to 15% nitrogen. The particles were crushed and 200 of the particles were dispersed uniformly throughout the sponge compacts and triple VAR melted. The ingots were processed to an inspectable product and UT inspection to a #2 FBH detected 9 HID's. Although larger, the defects exhibited a similar microstructural appearance, nitrogen content, and microhardness value to that of a natural HID.

While these seeds do help with experiments designed to understand the survivability of nitrogen stabilized sponge in the VAR process, they are clearly not realistic in that they are purely sponge source, have been crushed to irregular shapes, and probably do not contain the internal porosity generally associated with actual burned sponge. As a result, their apparent density will be higher than actual defects and the lack of internal porosity reduces their detectability. Also the nitrogen content is higher, therefore their refractory nature will be more severe than any of the actual burned sponge. Any conclusions drawn by use of such nitrided and crushed sponge will clearly indicate survivability in VAR processes much greater than expected for realistic defects but fails to address the near neutral density particle that has a greater chance of surviving a cold hearth melt by virtue of their not sinking to the skull [A-5].

4.7.5 ELECTRON BEAM MELTED IN-SPEC TITANIUM REMELT ELECTRODES [A-4]

Purpose: This paper discussed a recycle system to incorporate both alloy and oxygen correction during the Electron Beam (EB) melt instead of during the first Vacuum Arc Remitting (VAR) melt. Electrodes whose chemistries have been fully correct during the EB melt are called "in-spec" electrodes and require only one consumable VAR melt to meet specification requirements. EB melting, commonly called EBCHM (Electron Beam Cold Hearth Melting) is used as a method for consolidating titanium machine turnings into electrodes suitable for consumable VAR. The residence time of the large water-cooled copper hearth used in EB melting effectively removes high-density contaminants, such as carbide tool bits and refractory metals. The water cooled copper hearth of the EBCHM process affords the molten titanium additional exposure to the effects of furnace vacuum electron beam superheat and this additional residence time may help reduce or eliminate Type I defects. In a US Bureau of Mines study A-5] entitled, "Type I defects: their causes and methods of elimination," skull melting was identified as a melting process capable of dissolving Type I defects.

Conclusions: The first attempts at EB melting an aggregate blend of machine turnings, sponge, 85-15 Al-V master alloy, and aluminum were less than completely successful. When the initial "in-spec" electrodes were EBCH melted, using a series of conventional master alloy particles crushed to various sizes including the standard size range, master alloy segregation occurred. To solve this segregation problem, a master alloy lot, in which the geometry of the individual particles more closely matched the geometry of the machine turning scrap, was used. By blending components selected for both size and geometrical consistency, segregation during feeding was eliminated. This indicates that to get homogeneous ingots, the master alloy cannot all sink into the skull at the early stages of melting. Increasing the surface-to-volume ratio of the master alloy particles, as was done, helps to accomplish this objective [A-5]. Although not addressed by the authors, EBCHM processes will tend to vaporize volatile elements such as

aluminum so enriched feed materials will be necessary to achieve in-specification chemistry. Furthermore, the final resting point for the vaporized metal creates a situation with condensate that will need attention in order to avoid introduction of additional defects and/or local zones of chemical inhomogeneity [A-6].

4.7.6 MELTING OF NITRIDE SEEDED Ti 6-4 ALLOY INGOTS [A-11]

Purpose: Purpose of the paper is to evaluate the capability of the ISM (Induction Slag Melting) and CVAR (Consumable Electrode Vacuum Arc Melting) processes as a method of dissolving hard alpha defects introduced by contaminated input materials. Two parallel experiments were performed. One experiment used titanium sponge manufactured in a small-scale laboratory facility while the other used commercially available sponge. Non-contaminated control ingots and contaminated ingots were made from each set of sponge material using both melting processes.

Conclusions: Alpha formers were somewhat more readily dissolved during the ISM process than during the CVAR process. This was believed to be a result of a somewhat longer residence time in the molten state and the induction stirring furnaces which may serve to buoy up nitride particles and increase their residence time in the melt as compared to the CVAR process. During CVAR melting high nitrogen areas in the consumable electrode appear to sinter to high density either in the electrode behind the arc or during melting and passage through the arc. The particles fragment during passage through the arc or in the molten pool to result in more, but smaller, defects, which are believed to be more difficult to dissolve in the molten pool due to their high sintered densities.

The ISM process will also generate a bit more superheat and a few degrees of temperature is very effective in dissolving refractory particles. Temperature is much more important than time, as the amount of dissolution is related to the square root of time, while it is related to an exponential with temperature [A-5]. The statement regarding the concurrent sintering and fragmentation of nitrided particles during passage through the arc in a VAR process is a bit puzzling and not totally consistent with observations of nitrided sponge related HIDs [A-5].

Smaller seeds that have a higher surface to volume ratio also dissolve more rapidly. It is not clear that the nitrogen content, and therefore melting temperature, will be affected by any of the processes described. Therefore, fragmentation will be nothing but helpful no matter what went on before [A-5].

Neither induction slag or even the more scaleable induction skull process, which is based on the former, is currently scaleable to production size heats [A-5].

4.7.7 UTILIZATION OF ELECTRON BEAM MELTING IN THE PRODUCTION OF DEFECT FREE TI-6AL-4V INGOTS [A-3]

Purpose: The purpose of this experiment was to produce a defect-free, “in-spec EB/VAR” titanium alloy ingot.

Experiment/Conclusions: Prior to producing a "in-spec EB/VAR" ingot three experiments were conducted to evaluate the removal of dense particles during EB melting, removal of Type I defects during EB melting, and composition control of EB cast product.

During the first experiment, dense particles (tungsten and tungsten carbide tool bits) were successfully removed (excluding nitrides) from the ingot through entrapment in the hearth. The second experiment involved contaminating the input materials with infoliated billet-end crops, which have extensive oxyacetylene flame cut residual metallic drool, characteristic of surface titanium nitrides. Sonic inspection of the EB cast product to a #3 FBH defect confirmed sonic indications in only one of the three ingots that were cast. It was believed that continued efforts were required on furnace design and melt control software to provide adequate residence time and/or temperatures to guarantee Type I defect dissolution. In the third experiment, compositional control of the EB cast product, was accomplished by controlling the mixing and blending practice through the use of computer models.

A production quantity "in-spec" first stage EBCHM electrode was completed in 1985. No Type I or HDI defects were detected through sonic testing to a #2 FBH defect. The input material consisted of a large portion of scrap. The compositional variations for aluminum, vanadium and oxygen were within the range expected for a single melt process. Oxygen variability, however, was higher and attributed to a greater tendency for freezing segregation due to the sampling technique and appreciable variability in oxygen analytical techniques.

4.7.8 STANDARDIZING DEFECTS FOR TITANIUM SEEDING EXPERIMENTS [A-12]

Purpose: The purpose of this paper is to discuss a process which was developed to generate sponge particles with predictable nitrogen levels between zero and 15% and to establish a seeding procedure.

Experiment/results: Sponge particles were nitrided at various temperatures (1400°F-2300°F) for five minutes in a $95Ar\text{-}5N_2$ atmosphere. The particles were subsequently crushed which allowed the weight and nitrogen content of both the brittle surface material and the more ductile core to be determined. The higher the temperature, the greater the nitrogen content of the particle. It was found that the bulk nitrogen content of the ductile core decreased to zero as the upper nitriding temperature (2300°F) was reached.

Many experiments have used seeding densities varying from one defect in 20 pounds to one defect in 5 pounds. Recent trials have used the higher density to affect a more stringent test. To avoid agglomeration possibilities, the following HID seed mix was recommended:

Particle Size	Amount
0.25 inch diameter Ti-15N seeds	one per five pounds
0.25 inch diameter Ti-2N seeds	one per five pounds
0.25 inch diameter Ti-8N seeds	one per five pounds
0.12 - 0.25 inch diameter production, burned sponge particles,	one particle per fifty pounds

2 inch by down torch cut sheet stock (Ti-6-2-4-2 or Ti 6-2-4-6) representing flame cut cobbles or Feed stock A	one particle per 250 pounds

The following HDI seed mix was also recommended in the interest of establishing a common standard for all seeding efforts:

Particle Size	Amount
3/8″ /+ 1/4″ mesh	37%
1/4″ /+ 8″ mesh	25%
8″ /+ 14″ mesh	15%
14″ /+ 20″ mesh	10%
20″ /+ 40″ mesh	8%
40″ /+ 60″ mesh	5%
one whole WC tool bit at midpoint of melt, 0.04″ diameter Mo wire, 1/4″ to 1/2″ long	one particle per 125 pounds
one piece of angular Mo 1/4″ diameter	one particle per 250 pounds
one piece of angular Ta 1/4″ diameter	one particle per 250 pounds
one piece of 0.03″ diameter W wire, (1/4″ to 1/2″ long)	one particle per 250 pounds
one piece of angular W 1/4″ diameter	one particle per 250 pounds

4.7.9 TEST MELTING OF TIN AND WC SEEDED Ti-6-4 AND RESULTING INGOT STRUCTURES - A PROGRESS REPORT [A-13]

Purpose: The purpose of this experiment is to evaluate the advantages of EBCHR for improved cleanliness of Ti-6-4 in comparison with conventionally processed VAR materials and to examine the capability of EBCHR for the production of in-specification chemistry of the Ti-6-4 alloy.

Experiment/Conclusions: Test melts of TiN and WC seeded and un-seeded Ti-6-4 were produced by EBCHR, by double VAR, and by the combination of EBCHR and VAR. The EBCHR test melts produced two unseeded and one seeded ingot, in which the seeded and one unseeded ingot were further VAR processed to produce two EBCHR-VAR ingots. One seeded ingot was produced by double VAR. The unseeded EBCHR, un-seeded EBCHR-VAR, seeded EBCHR-VAR, and seeded double VAR ingots were forged into bar. Defects were detected by x-ray in only the double VAR bars. Microscopic skull analysis of the seeded ingot melted by EBCHR showed both WC and TiN particles in the liquid-solid interface.

4.7.10 THE ROLE OF MELT RELATED DEFECTS IN FATIGUE FAILURES OF Ti-6Al-4V [A-14]

Purpose: The purpose of the study was to quantify the reduction of fatigue life caused by high interstitial defects (HID) and high density inclusions in titanium nitride and tungsten carbide seeded double vacuum-arc remelted titanium alloy Ti 6Al-4V.

Experiment: Two lots of material, one triple VAR and one seeded double VAR, were tested. The seeded melt electrode contained compacts of master alloy, elemental aluminum, aluminum-vanadium master alloy, 5% recycled Ti 6-4 scrap, 1.8% nitrided titanium sponge (about 40 each 3 to 6 mm sized seeds/kg), and 0.079% tungsten carbide tool bit inserts (about 0.02 seeds/kg). The 16-inch diameter seeded ingot was beta forged to 8-inch diameter, and the top 1/8th of the ingot was alpha/beta forged to 3-inch diameter according to conventional practices. The 3-inch unseeded triple vacuum melted material was solution heat treated and overaged.

Conclusions: Fatigue testing of the seeded and unseeded materials showed that both high interstitial defects and high density inclusions defects can reduce fatigue life by an order of magnitude.

5. REFERENCES

A-1. Henry, J.L., Hill, S.D., Schaller, J.L., and Campbell, T.T., "Nitride Inclusions in Titanium Ingots: A Study of Possible Sources in the Production of Magnesium-Reduced Sponge," in *Metallurgical Science and Heat Treatment*, 1973, Vol. 4, No. 8, pp. 1859-1864.

A-2. Entrekin, C.H., "The Removal of High Density Inclusions by Hearth Refining Process," in edited *Electron Beam Melting and Refining State of the Art 1985*, by R.A. Bakish, Bakish Materials Corporation, Englewood, NJ, 1985, pp. 40-47.

A-3. Ostheimer, M., and Seagle, S.R., "Utilization of Electron Beam Melting in the Production of Defect Free Ti-6Al-4V Ingots," *Proceedings of the Sixth World Conference on Titanium*, Cannes, June 6-9, 1988, pp. 579-582.

A-4. Herman, W.E. and Forsberg, V.K., "Electron Beam Melted "In-Spec" Titanium Remelt Electrodes," *Proceedings of Titanium 1986 Conference*, October, 1986, Vol. II, pp. 904-917.

A-5. Bellot, J.P., Edie, C., and Mitchell, A., "The Formation and Removal of "Hard-Alpha" Material During the Melting of Titanium Alloys," *Eighth World Conference on Titanium* in Birmingham, England, Institute of Materials Abstract, pp. 22-16, October 1995.

A-6. Grala, E.M., "Characterization of Alpha Segregation in Ti-6Al-4V Alloy," TRW Equipment Laboratories, September 1968, Report ER-7224-2, NERAC Number USG 7702 AD-845 805/1 D7.

A-7. Private communication, Jim Hall, Honeywell Engine Systems.

A-8. Tiller, W.A., et al., Vol. 1, Acta Met, p. 439, 1953.

A-9. Bomberg, H.B., "Alpha Segregation in Titanium Alloys," *Proceedings of Titanium 80, Science and Technology*, May 19-22, 1980, Vol. 3, pp. 2197-2202.

A-10. Poulsen, E.R. and Parris, W.M., "Development of Seeds for Reproducible LDI's in Titanium Melting Tests," *Electron Beam Melting and Refining State of the Art 1986*, Bakish, R.A., 1986, pp. 347-353.

A-11. Paige, J.I., and Redden, T.K., "Melting of Nitride Seeded Ti-6A1-4V Alloy Ingots," *Journal of Metals*, March 1988, Vol. 40, No. 3, pp. 26-28.

A-12. Paige, J.I. and Redden, T.K., "Melting of Nitrate Seeded Ti-gAl-4V Alloy Ingots," *Journal of Metals*, March 1988, Vol. 40, No. 3, pp. 26-28.

A-13. Malley, D. and Belchak, M., "Standardizing Defects for Titanium Seeding Experiments," *Electron Beam Melting and Refining State of the Art 1990*, Bakish, R.A., 1990, pp. 224-231.

A-14. Clark, K.R., Dillar, A.B., Hendrix, J.K., Tien, J.K., and Denda, T., "The Role of Melt Related Defects in Fatigue Failures of Ti-6A1-4V," edited by Fores, F. H. and Caplan, I. L., eds., in *Proceedings of the Seventh World Conference on Titanium*, 1992, pp. 2867-2871.

APPENDIX B—DEFECT CHARACTERIZATION PROTOCOL

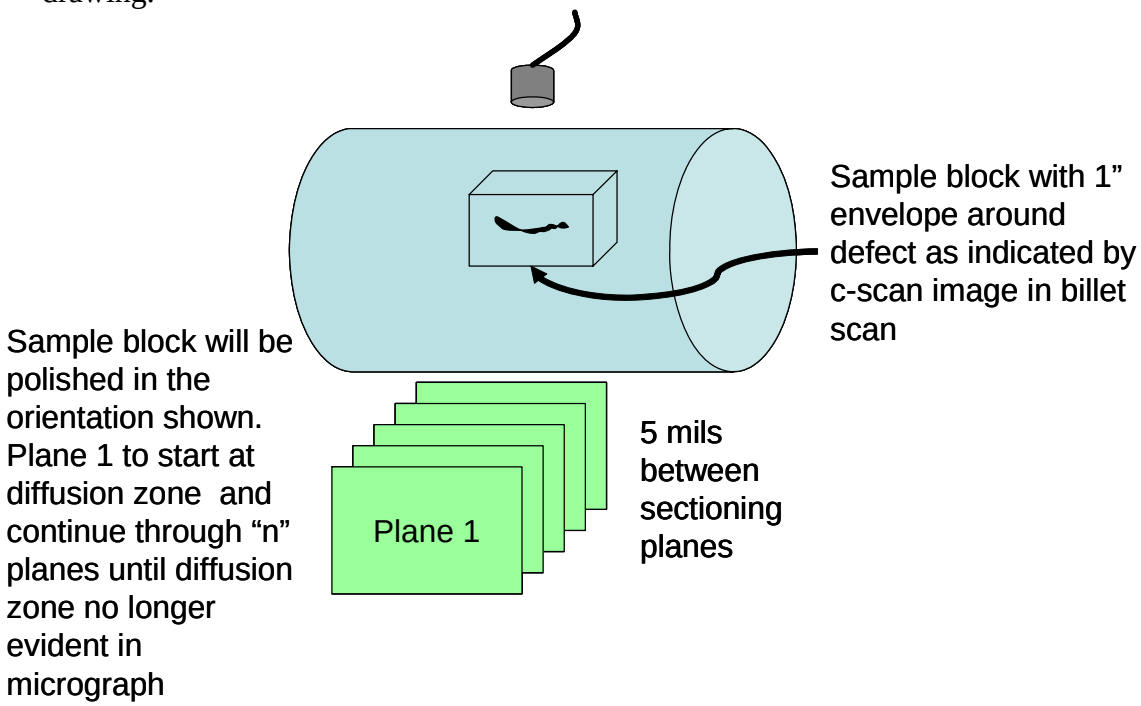
CBS ULTRASONIC AND METALLOGRAPHY PROCEDURE

Scope:

This procedure is intended to describe the ultrasonic process used to locate indications within the 2- to 3-inch cubes sectioned from billets. The locations will be defined on three planes to provide a detailed geometric representation of the indication. Waveform and C-scan data will also be collected from these evaluations. This data will be analyzed for ultrasonic content and used to further reduce the sample block so that approximately 0.5″ of material will surround the defect. The sectioned sample block will again be ultrasonically inspected using higher-resolution transducers so that the location of the indication is accurately defined prior to the metallography. C-scan data will be recorded for later comparison to model calculations. A three-dimensional (3D) metallographic analysis will be done on these indications. This process involves gathering digital micrographs from the serial slices then stacking those images through a software program to create a 3D representation of the indication.

Billet Sectioning:

1. The indication will be sectioned from the billet so that approximately a 1″ envelope of material surrounds the indication. Due to the depth of some of the indications, a 1″ envelope may not be possible from the inspection surface side and this will be noted. The sample removal and metallographic section approach is depicted in the following drawing.



2. During the sectioning, the orientation of the indication with respect to the original billet axis will be controlled by placing a large chamfer on the left corner of the curved surface tangent to the axial face containing the serial number of the billet.

3. The six machined surfaces of each cube shall be finished so that the roughness is no greater than 16 microinches.

4. An etching operation will be done on the cube at this stage to determine if the diffusion zone is present. If the diffusion zone is detected, the two remaining sections of the billet should be analyzed to determine the size of the diffusion zone.

Note: Etchant will be ammonium bifluoride 10% with water.

Ultrasonic Evaluation:

Initial ultrasonic evaluations on the sectioned block will be performed on the Sonix system at GEQTC. The various transducers that will be used are listed below. The particular instrument parameters will be noted as they are developed during the evaluation. However, the beam diameter sensitivity will be (0.5)(3db) for all of these evaluations.

1. RF waveforms will be collected at ISU from six sides of the 2- to 3-inch cubes using a 5-MHz, F8, 6.0″ focal length transducer. This data will be compared against the conventional 5-MHz billet data and the 3D model.

2. The data from the scans described in the preceding step will be reviewed to determine in which plane the specimen will be serial sectioned. Note: the sectioning plane will be perpendicular to the direction of sound.

3. After the serial section plane has been determined, the material envelope surrounding the indication will be reduced to 0.450″. Again, the machine surfaces will have a surface roughness of 16 microinches.

4. The orientation will be maintained by use of an EDM to machine two holes of different diameters through the side that will be serial sectioned. The holes shall be placed so that they are close to the axial face that contained the billet serial number. The larger of the two holes will be on the side where the 2- to 3-inch cube was chamfered.

5. These pieces will be returned to ultrasonic where they will be evaluated using a 25-MHz, F10. RF waveforms will be collected from the original radial surface (billet curved surface) to compare flat surface data to the curved. Also, the depth of the indication, from the sectioning surface, will again be verified prior to metallography. C-scans will be done from all six sides using the 25-MHz, F10 transducer.

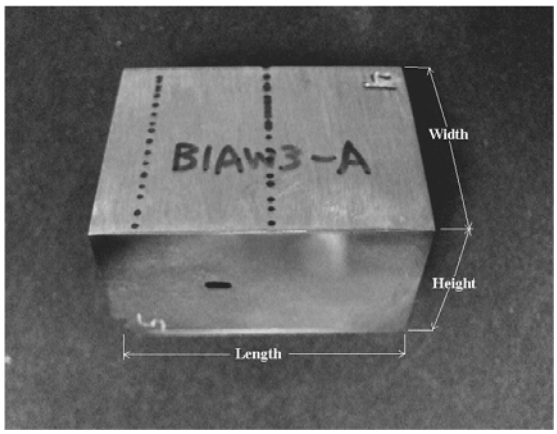
6. All ultrasonic parameters will be recorded in inspection log book.

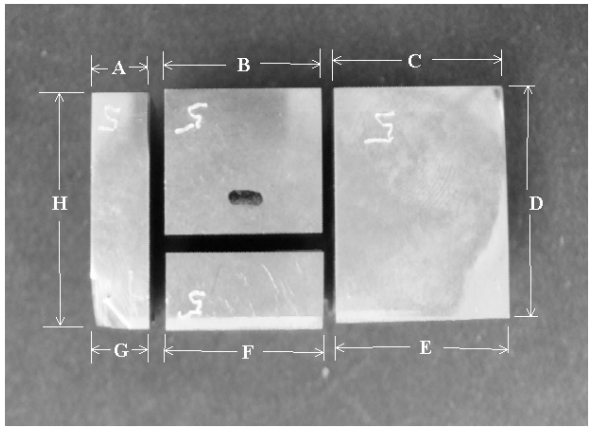
X-ray CT:

1. One specimen will be evaluated with this method. If the data collected form this evaluation provides good information, a decision will be made as to whether this process will be used on subsequent specimens.

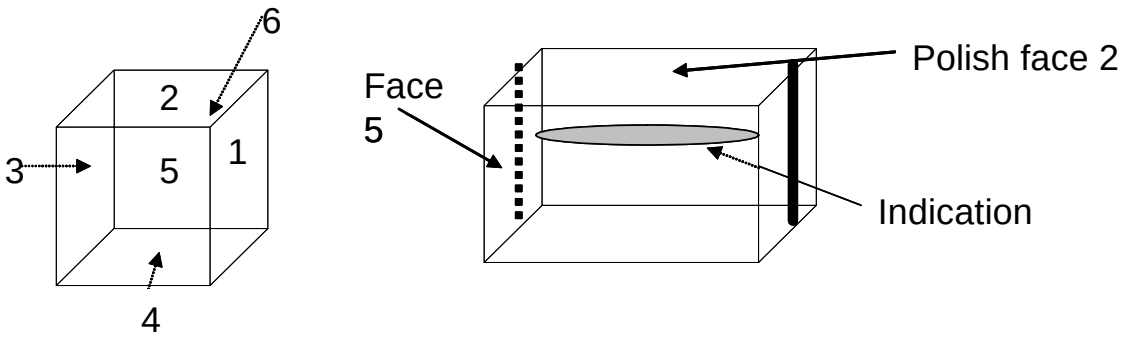
Metallography Process Preparation and Serial Sectioning for 3-D Modeling:

Initial preparation and documentation: Before and after any cutting or grinding is performed on the sample provided for review, it is imperative that dimensions be clearly documented. Photodocumentation of the sample with cut locations outlined will aid greatly at report time, and is crucial for tracking material removal before the final working sample is defined. Important data that needs to be recorded includes length, width, height, and orientation of the sample from a larger piece, if applicable. The indication being documented will eventually have to be traced back to the original billet or forging. All subsequent sections cutoff of the sample in the course of getting closer to the indication, as well as the material loss due to cutoff blade thickness, must be measured and recorded. Below is a typical example.





Fiducial marks: Information on the actual location of the indication of interest can come from x-ray or UT techniques. Once you are confident that you have cut down the sample as close to the indication as reasonably possible (approx. 50 mils away to allow for human error), fiducial or reference marks can be cut into the sample. The fiducial marks are required to be able to accurately orient the flaw with respect to the disk or billet surfaces. Also, without the fiducial marks for reference, a solid model of the flaw cannot be reconstructed since orientation from slice to slice is critical. Two fiducial marks should be made on opposite ends of the sample, perpendicular to the face to be polished and parallel to each other. To ensure parallelism and perpendicularity, these marks should be made in a machine shop. Below is an example of fiducial mark locations cut into a sample. The reference cube diagram is added to keep orientation clear to the reader. Making the marks as close to the indication as possible (this will be an estimation) will minimize the number of images taken later.



Sample mounting: Once the reference marks are cut, the sample is ready to be mounted in Bakelite for serial polishing. Again, remember to track the face that is being polished and the orientation of the sample in relation to the original piece. Once the sample is mounted, lightly polish the sample with 600-grit paper to remove any mounting flash or burrs. Measure the thickness of the mount in the completed state. This number will be the starting measurement to which all future material removal measurements will be related.

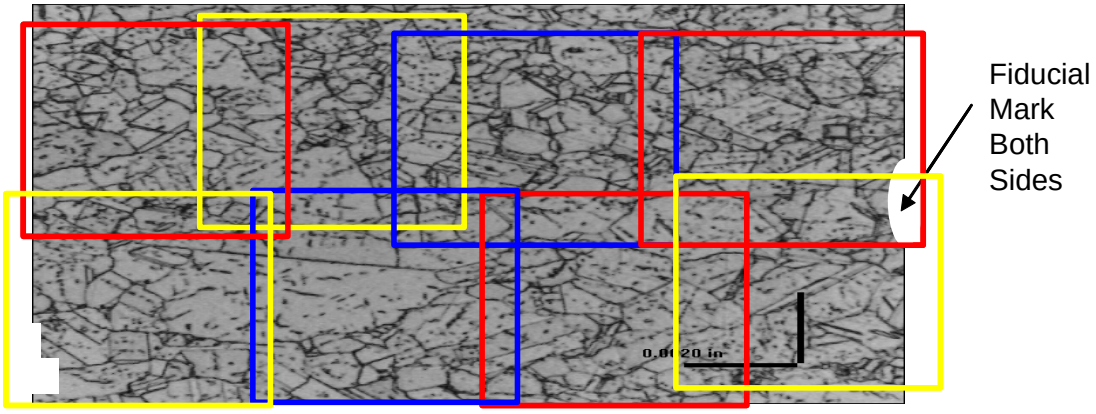
Serial polishing: All polishes in this procedure are done with an automated polishing system holding the samples in a rigid fixture or "rack". The preferred rack is one that holds the sample with a pinching action rather than a setscrew. This system is necessary to maintain reproducibility from polish to polish. Before starting the polish procedure, you must decide on how much material will be removed on each polishing step. The first few polishes performed in the safe zone will define the steps to use to produce the same material removal rate with each polish. An example of typical polishing steps follows:

Abrasive	Time	Pressure	Lubricant	Speed
120-grit SiC	20 sec.	200 Newtons	Water	300 rpm
240-grit SiC	20 sec.	200 Newtons	Water	300 rpm
240-grit SiC	20 sec.	200 Newtons	Water	300 rpm
320-grit SiC	20 sec.	200 Newtons	Water	300 rpm
320-grit SiC	20 sec.	200 Newtons	Water	300 rpm
400-grit SiC	20 sec.	200 Newtons	Water	150 rpm
400-grit SiC	20 sec.	200 Newtons	Water	150 rpm
600-grit SiC	20 sec.	200 Newtons	Water	150 rpm
2400-grit SiC	20 sec.	200 Newtons	Water	150 rpm

The logical progression of papers in this procedure is common to all sample preparation in metallography. This combination was defined by trial and error to produce a 0.005-inch removal rate when performed with fresh SiC paper and the same "dummy" samples. A dummy is a sample of like material and size as the sample of interest, used to balance a rack when autopolishing. The final polish and etching of the sample is dependent on material properties. Material removal in the final polishing step is immeasurable and therefore neglected when searching for the right combination of papers and times.

Documentation of indication: Once the sample has been prepared for review, documentation of the indication can be performed. Do not measure the material removal until after documentation as the micrometer or caliper used will scratch the polished/etched surface of the sample. Since image documentation of the entire indication from fiducial mark to fiducial mark will require a number of images to be linked together, the microscope must have enough travel to view both fiducial marks without moving the sample on the microscope stage. Align the sample so that it can be traversed from mark to mark in the x direction without moving the y-direction control. This will greatly help the operator who will be creating the photomontage from the individual images.

Once it's verified that all images can be taken without moving the sample, the imaging process can start. The first image is taken at an extreme edge of the area to be documented. Subsequent images must be taken with a small percent of overlap (approximately 5%) from one image to the next. The diagram below shows typical overlapping images in a montage.



This pictorial representation purposely shows that the overlap in images does not have to be precisely the same from location to location, but it must include both fiducial marks (squared notch on left and elliptical notch on right) and all areas of interest. Note the asymmetric shape of the fiducial mark on the left, which distinguishes the orientation of the image uniquely to facilitate later reconstruction. Image capturing was performed on an inverted Reichert Metallograph using a digital camera and image capturing software. The images were taken at 480 by 640 resolution at a magnification suitable to capture the details of the indication. The magnification and resolution that is determined, as appropriate for the job, must be documented and used through the entire sample analysis and for any other samples that could be compared with each other.

After imaging is complete, measure and record the thickness of the micro. Subtracting the new thickness measurement from the previous measurement. At each slice (step), evaluate for detection of diffusion zone. Continue with this process until diffusion zone is detected. At this position, normally 0.040″ to 0.050″ from the indication, begin finer steps. The size of the finer steps will be determined based on the size of the indication and the direction of the polishing in reference to the indication.

After each polishing step, etch and photograph. During the step polishing, it may be necessary to verify the location of the indication periodically to avoid the possibility of polishing through it. Etchant will be ammonium bifluoride 10% with water. Gray levels must be kept consistent at each step for the normal structure and the defect in all photos. Digitize each image (image analysis) along with photo. Digitized images will be compiled into a 3D representation of the indication. The EDM holes will provide the mark to maintain the registration of the digitized images.

Microprobe and microstructure characterization:

1. All microprobe work will be done at Pratt & Whitney.
   Microprobe will be done at 4 stages:
   a. In the diffusion zone
   b. Beginning of the indication
   c. Middle of the indication
   d. End of the indication
   Note: Microprobe data collection was reduced to one slice for most samples.

2. Rayleigh wave and grain orientation images will be performed on the same slice that the microprobe data was collected for selected samples.

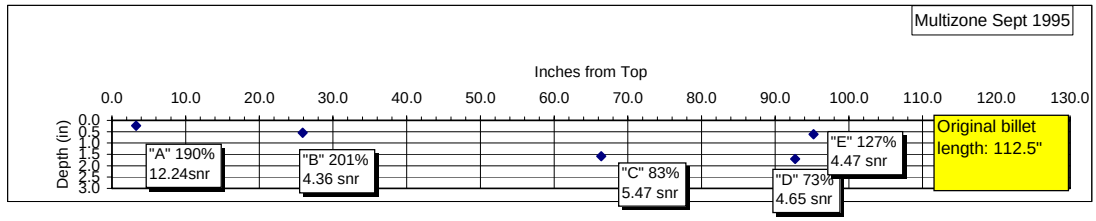
APPENDIX C—INSPECTION RESULTS FOR CONTAMINATED BILLET

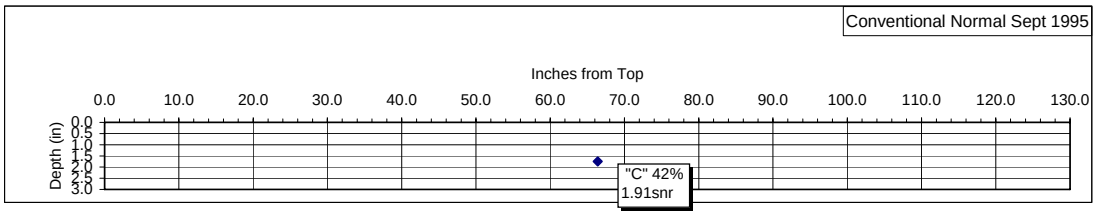
The 12 Contaminated Billet Study billets were inspected for the initial customer in November 1994, and the results were provided to the Engine Titanium Consortium as part of the purchase. In the initial inspection, precautions were not taken to prevent saturation of the ultrasonic signal. To enable capture of digital data using approved multizone and conventional inspection methods, and to ensure that saturation of the signals did not occur, the complete heat was reinspected in September 1995. The results were summarized for each of the billets. The billet ID is provided in the upper left corner of each sheet. Indications were identified alphabetically with the left most indication beginning with A, as shown in the first column. The second column lists the distance from the end of the billet. Indication depths are provided in the next six columns for each of the inspection times (September 1995 and November 1994) and inspection methods (conventional normal, conventional longitudinal, and multizone). Graphical representations, referred to as billet maps, provide the amplitude response and signal-to-noise ratio for each of the indications. Not all billets were tested with all methods in the 1994 inspection, as noted on specific billet maps. Other notes are also included on individual maps.

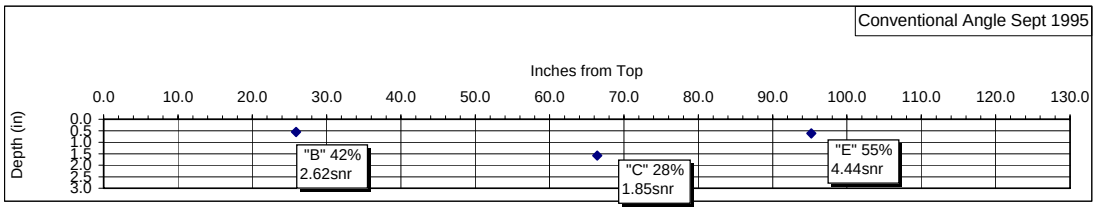
B1AW1

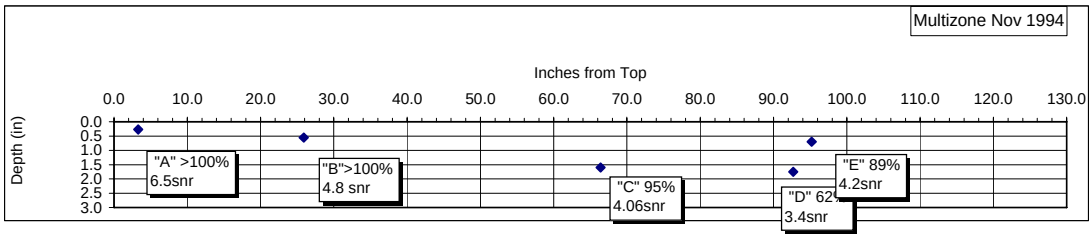
		September 1995 Inspection			November 1994 Inspection		
Stamped I.D.	Inches from top	Multizone Depth	Conv. Normal Depth	Conv. Angle Depth	Multizone Depth	Conv. Normal Depth	Conv. Angle Depth
A	3.3	0.2			0.3		
B	25.9	0.6		0.6	0.6	0.5	0.5
C	66.4	1.6	1.8	1.6	1.6		
D	92.7	1.7			1.8		
E	95.2	0.6		0.6	0.7	0.5	0.5

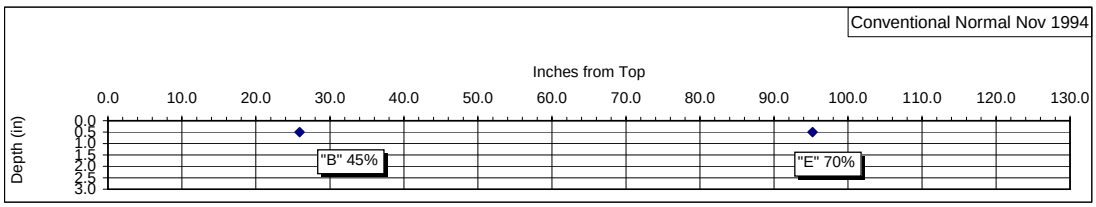
Additional indication reported on Nov 1994 Multizone, 12" from top, 0.94" deep, amplitude 53%, 2.11 SNR (not rejectable)

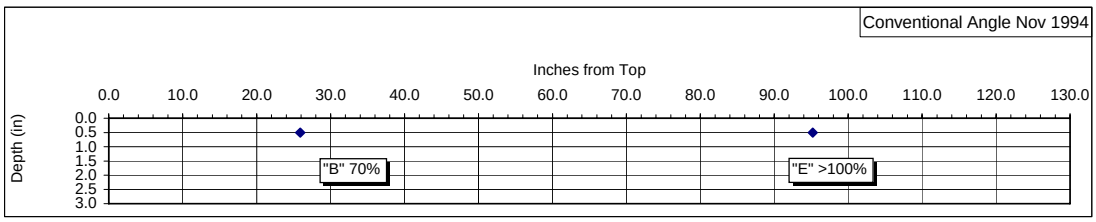






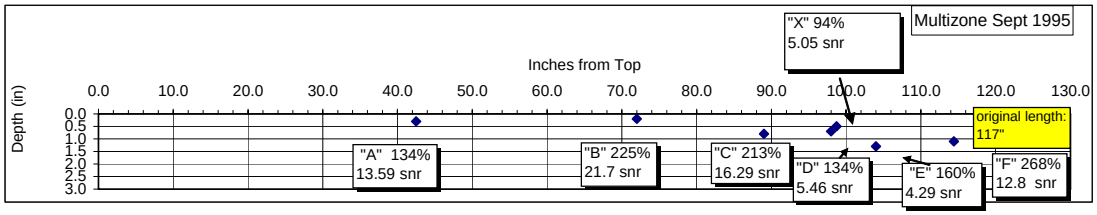


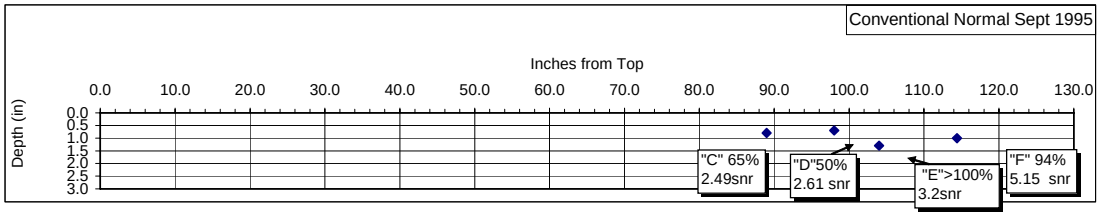


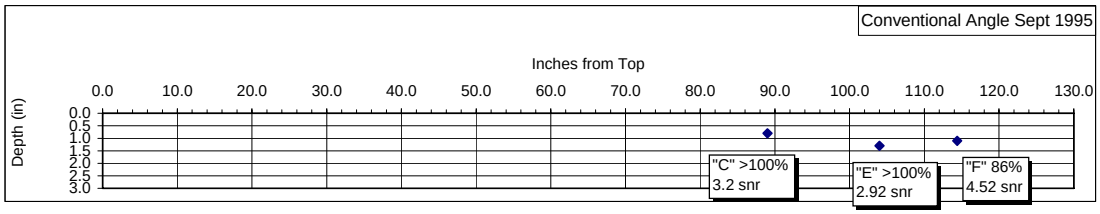


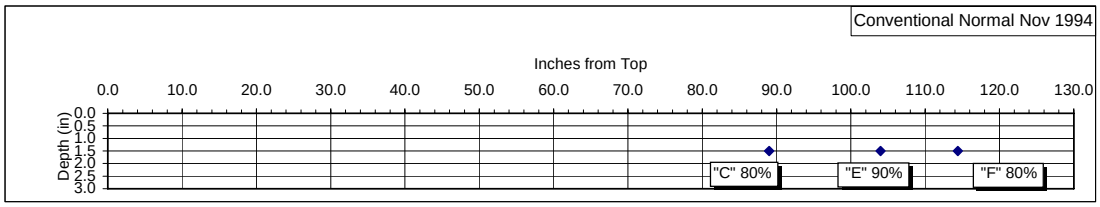
B1AW2

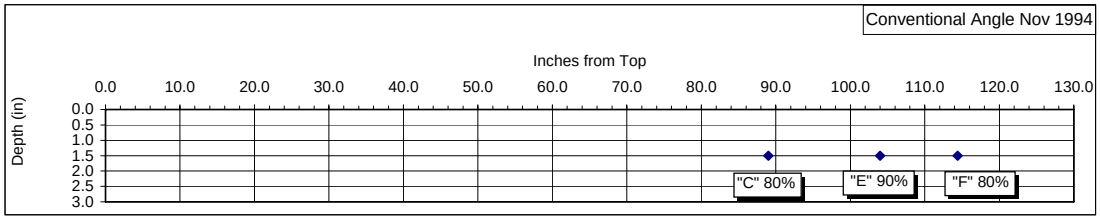
		September 1995 Inspection			November 1994 Inspection		
Stamped I.D.	Inches from top	Multizone Depth	Conv. Normal Depth	Conv. Angle Depth	Multizone Depth	Conv. Normal Depth	Conv. Angle Depth
A	42.5	0.3			NOT TESTED		
B	72.0	0.2					
C	89.0	0.8	0.8	0.8		1.5	1.5
D	98.0	0.7	0.7				
E	104.0	1.3	1.3	1.3		1.5	1.5
F	114.4	1.1	1.0	1.1		1.5	1.5
(x)	98.7	0.5					





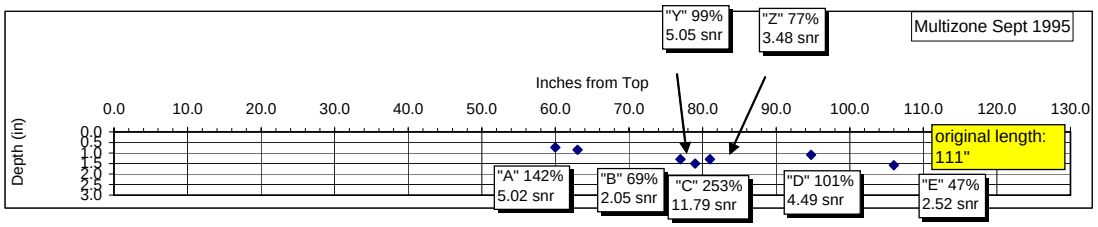


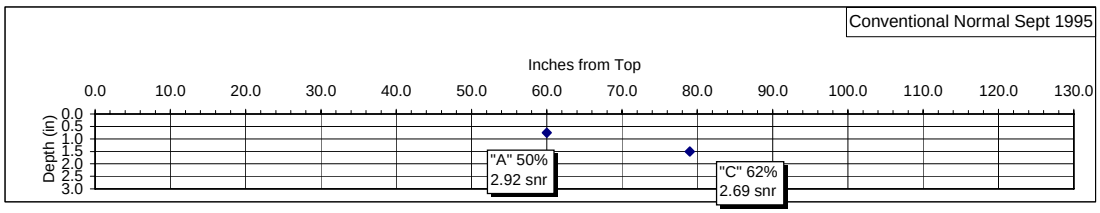


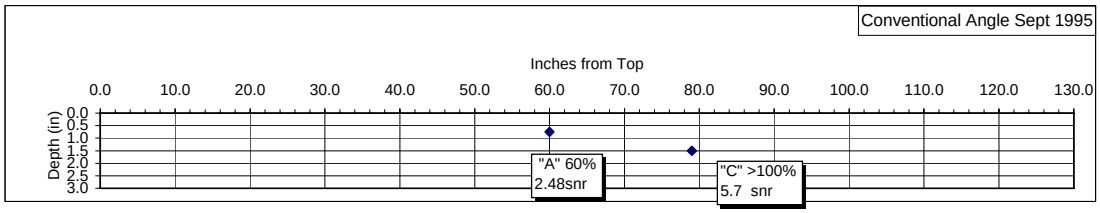


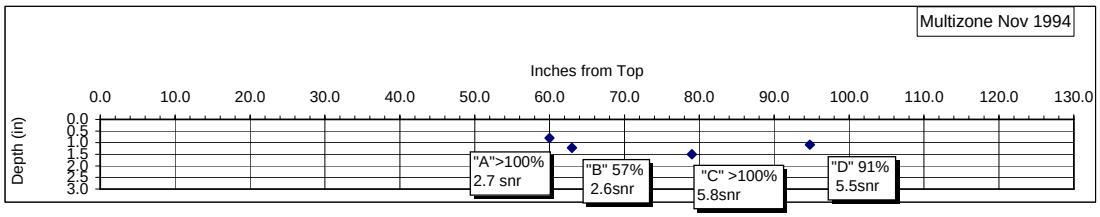
B1AW3

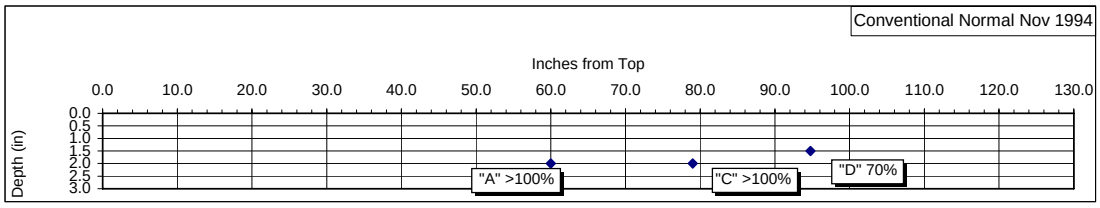
		September 1995 Inspection			November 1994 Inspection		
Stamped I.D.	Inches from top	Multizone Depth	Conv. Normal Depth	Conv. Angle Depth	Multizone Depth	Conv. Normal Depth	Conv. Angle Depth
A	60.0	0.7	0.8	0.8	0.8	2.0	2.0
B	63.0	0.9			1.2		
C	79.0	1.5	1.5	1.5	1.5	2.0	2.0
D	94.8	1.1			1.1	1.5	
E	106.0	1.6					
(y)	77	1.3					
(z)	81	1.3					

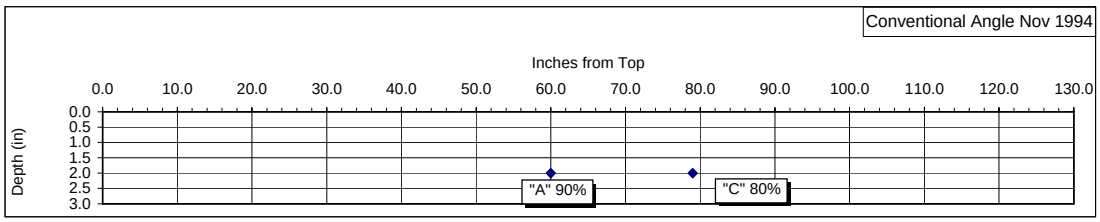






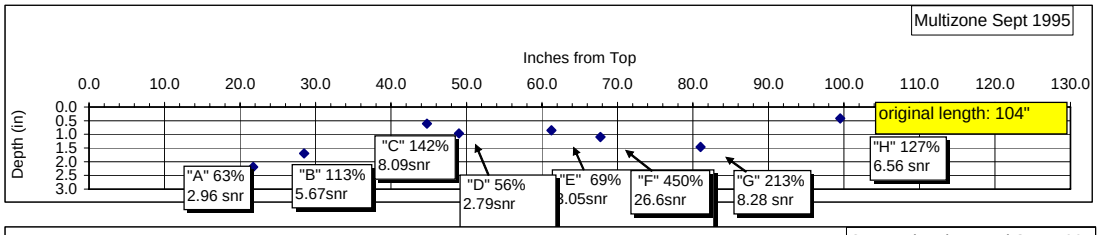


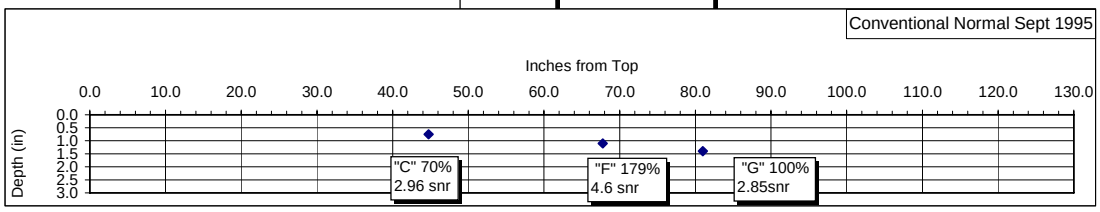


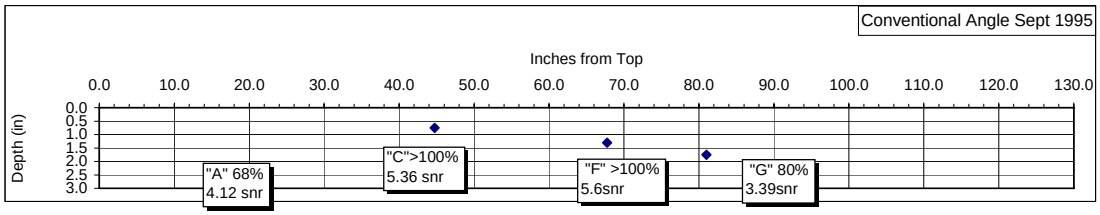


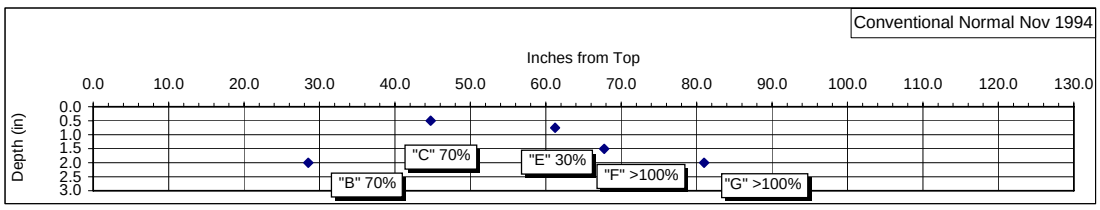
B1BW1

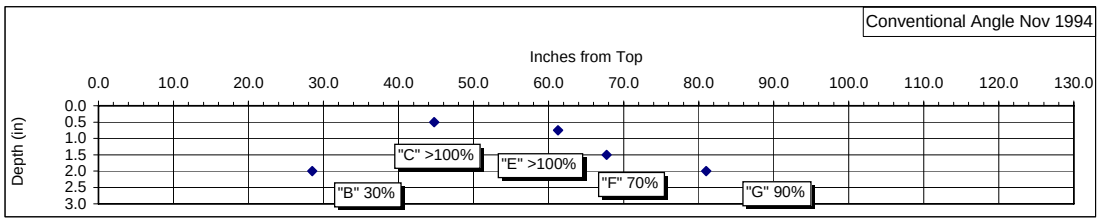
		September 1995 Inspection			November 1994 Inspection		
Stamped I.D.	Inches from top	Multizone Depth	Conv. Normal Depth	Conv. Angle Depth	Multizone Depth	Conv. Normal Depth	Conv. Angle Depth
A	21.8	2.2		2.5	not tested		
B	28.5	1.7				2.0	2.0
C	44.8	0.6	0.75	0.8		0.5	0.5
D	49.0	1.0					
E	61.3	0.9				0.8	0.8
F	67.8	1.1	1.1	1.3		1.5	1.5
G	81.0	1.5	1.4	1.8		2.0	2.0
H	99.5	0.4					







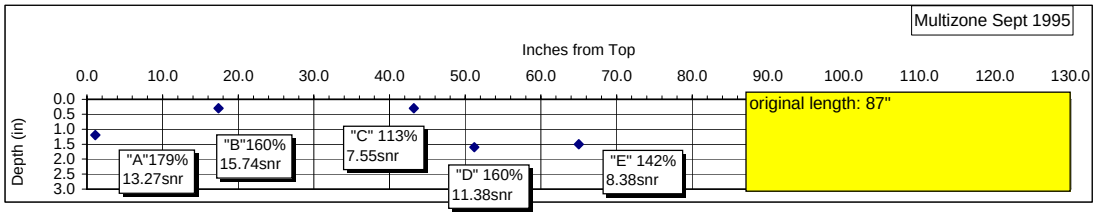


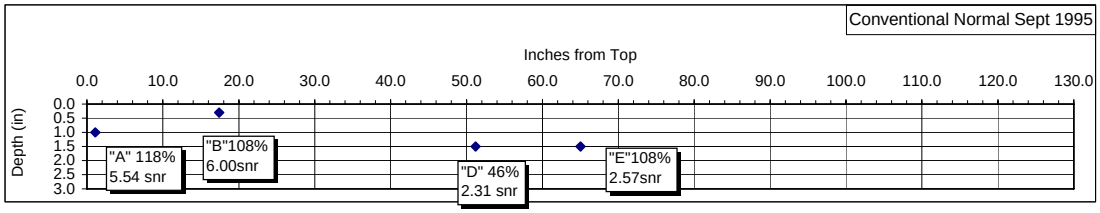


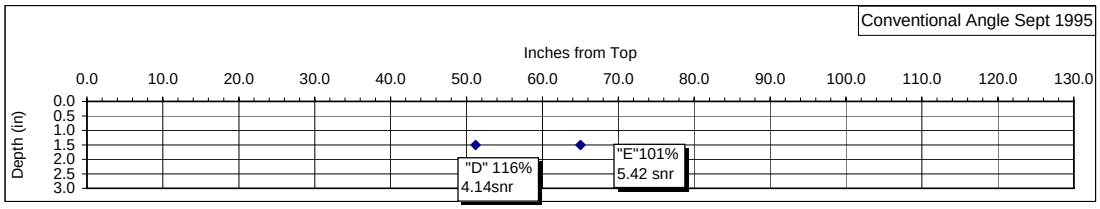
B1BW2B

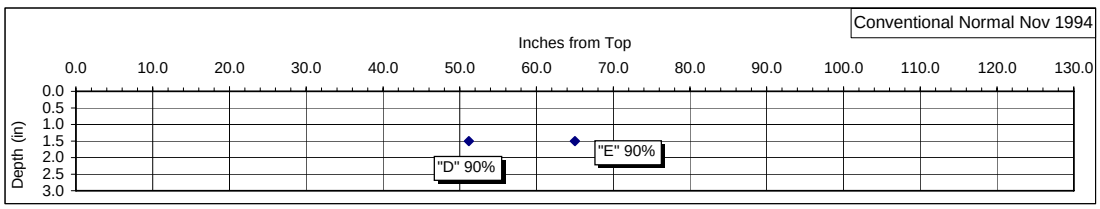
		September 1995 Inspection			November 1994 Inspection		
Stamped I.D.	Inches from top	Multizone Depth	Conv. Normal Depth	Conv. Angle Depth	Multizone Depth	Conv. Normal Depth	Conv. Angle Depth
A	1.1	1.2	1.0		NOT TESTED		
B	17.4	0.3	0.3				
C	43.2	0.3					
D	51.2	1.6	1.5	1.5		1.5	1.5
E	65.0	1.5	1.5	1.5		1.5	1.5

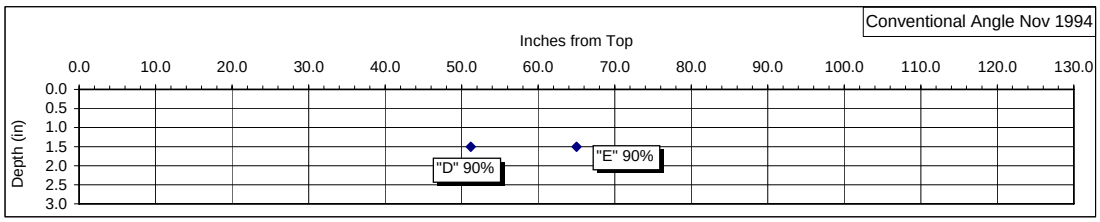
0 TO 14.5" SECTION REMOVED BETWEEN INSPECTIONS









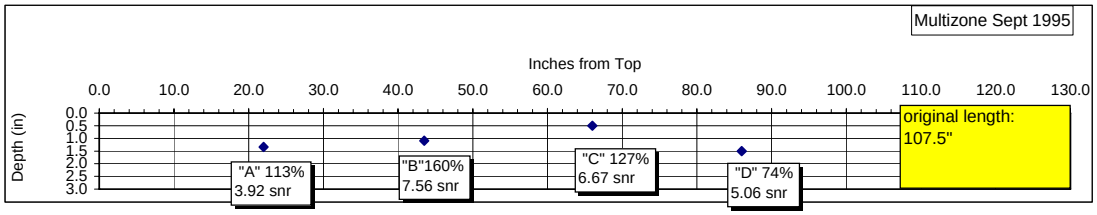


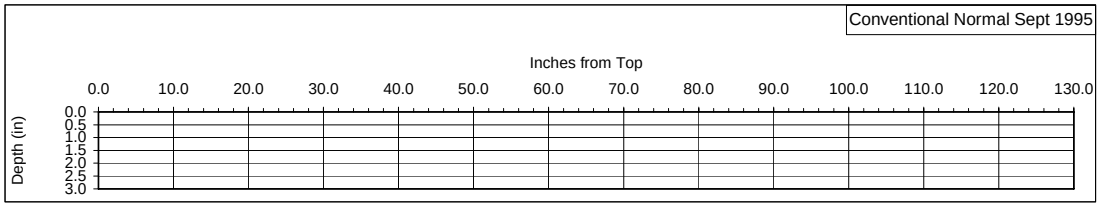
B1BW3

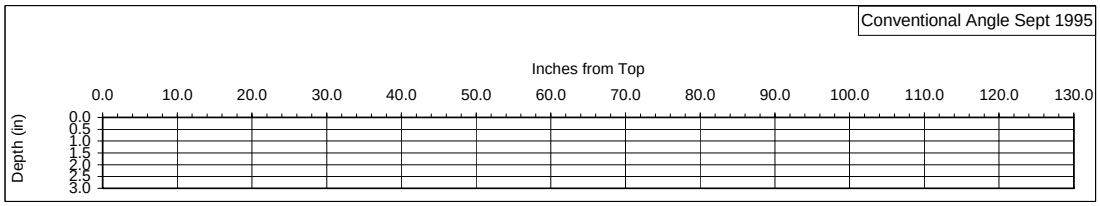
		September 1995 Inspection			November 1994 Inspection		
Stamped I.D.	Inches from top	Multizone Depth	Conv. Normal Depth	Conv. Angle Depth	Multizone Depth	Conv. Normal Depth	Conv. Angle Depth
A	22.0	1.3			1.3		
B	43.5	1.1			1.0		
C	66.0	0.5			0.4		
D	86.0	1.5			1.5		

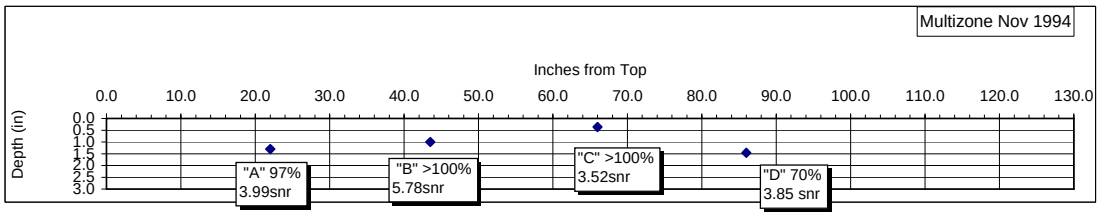
Addtional Multizone 31% amplitude, 1.85 snr reported in Nov '95 test.

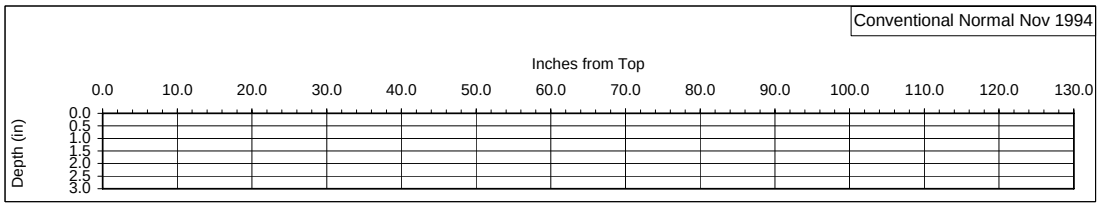
2 indications 19% & 30%, long & shear not marked to cut. No other conv. ind. See RMI11/9/94 report

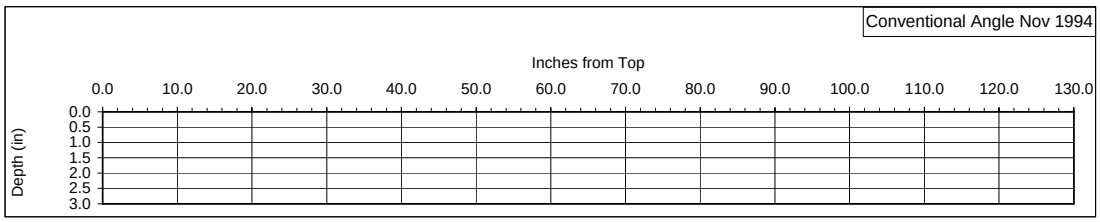








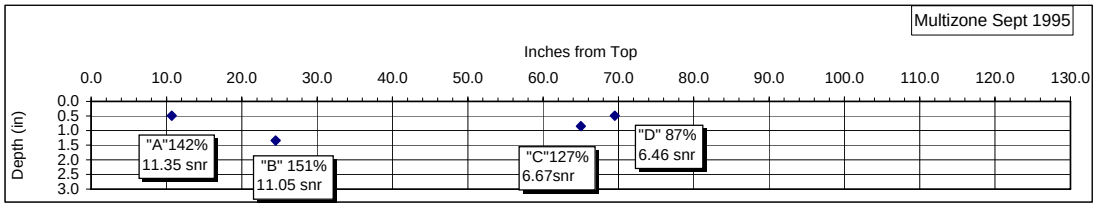


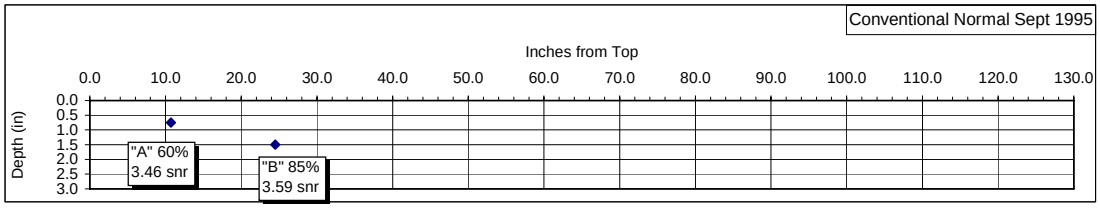


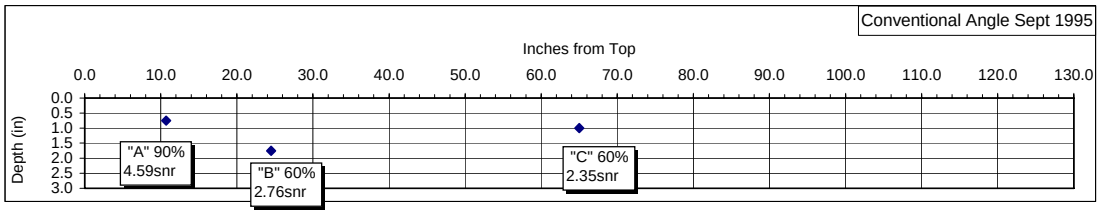
B2W1

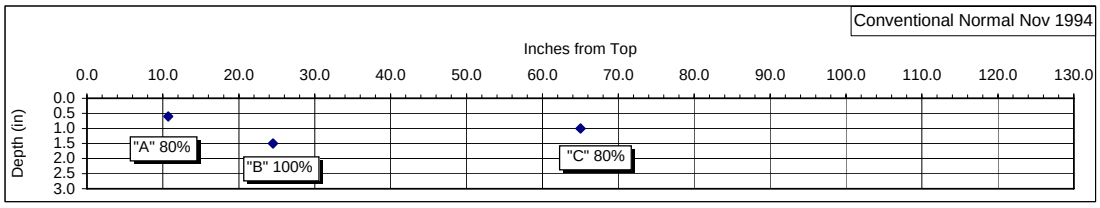
		September 1995 Inspection			November 1994 Inspection		
Stamped I.D.	Inches from top	Multizone Depth	Conv. Normal Depth	Conv. Angle Depth	Multizone Depth	Conv. Normal Depth	Conv. Angle Depth
A	10.7	0.5	0.8	0.8	NOT TESTED	0.6	0.6
B	24.5	1.3	1.5	1.8		1.5	1.5
C	65.0	0.9		1.0		1.0	1.0
D	69.5	0.5					

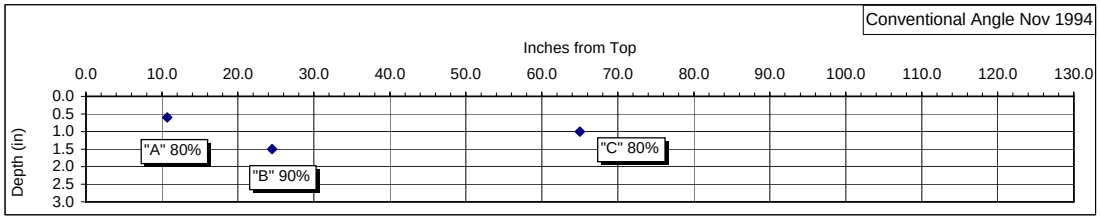
original length: 133"





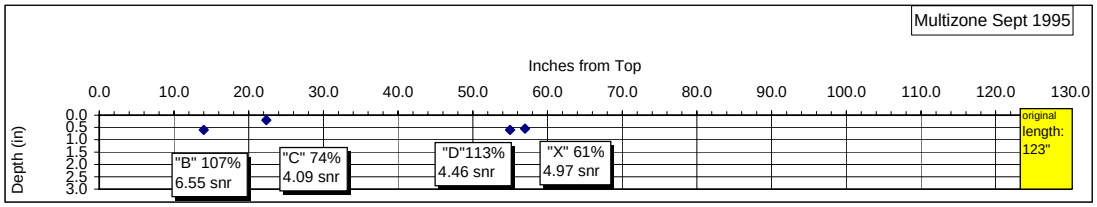


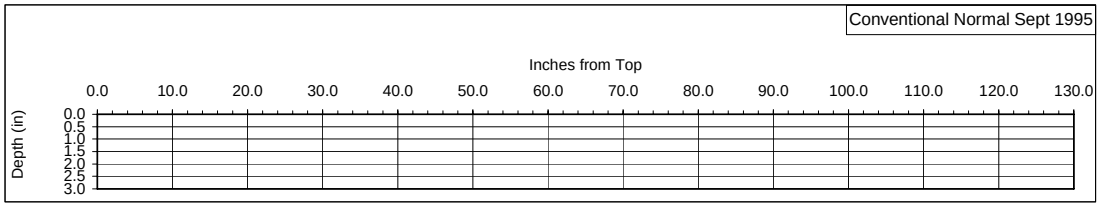


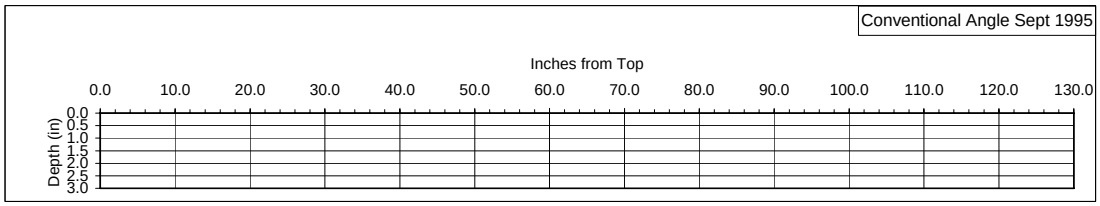


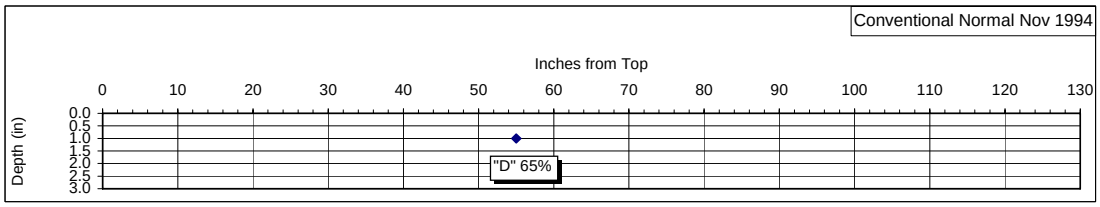
B2W2

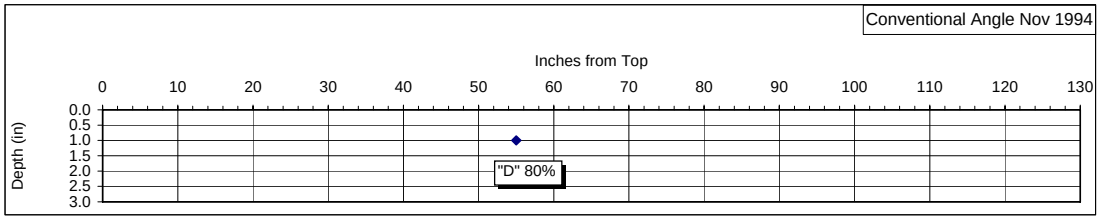
		September 1995 Inspection			November 1994 Inspection		
Stamped I.D.	Inches from top	Multizone Depth	Conv. Normal Depth	Conv. Angle Depth	Multizone Depth	Conv. Normal Depth	Conv. Angle Depth
A	Visible end burst - indications marked "A"						
B	14.0	0.6			Not tested		
C	22.4	0.2					
D	55.0	0.6				1.0	1.0
(X)	57	0.55					









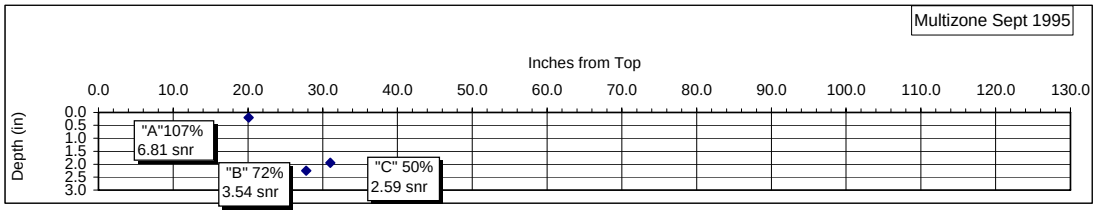


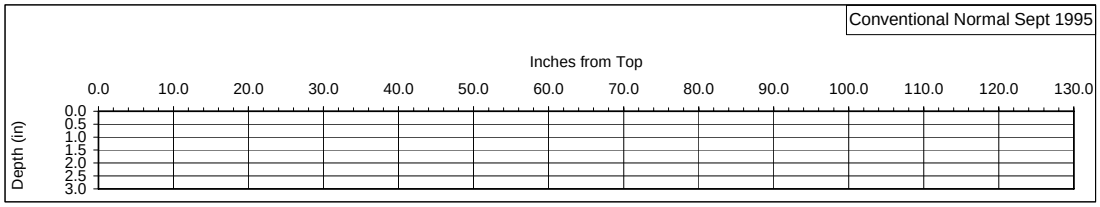
B2W3

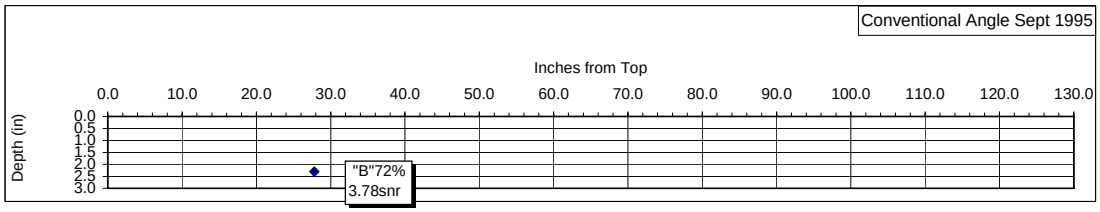
		September 1995 Inspection			November 1994 Inspection		
Stamped I.D.	Inches from top	Multizone Depth	Conv. Normal Depth	Conv. Angle Depth	Multizone Depth	Conv. Normal Depth	Conv. Angle Depth
A	20.1	0.2			0.3		
B	27.8	2.3		2.3	2.3		
C	31.0	2.0			2.0	0.3	0.3

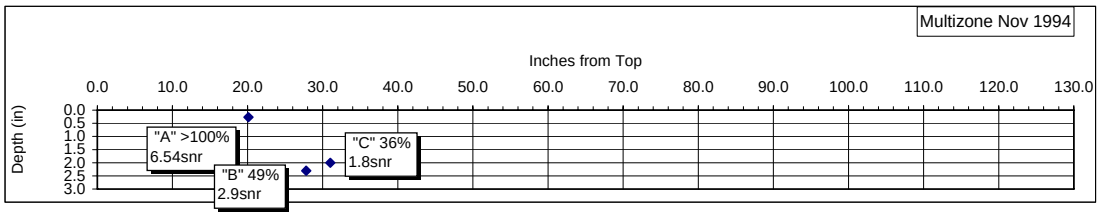
Note: indication B mis-reported as C Nov 94, C not reported.
Billet map shows corrections determined from raw data

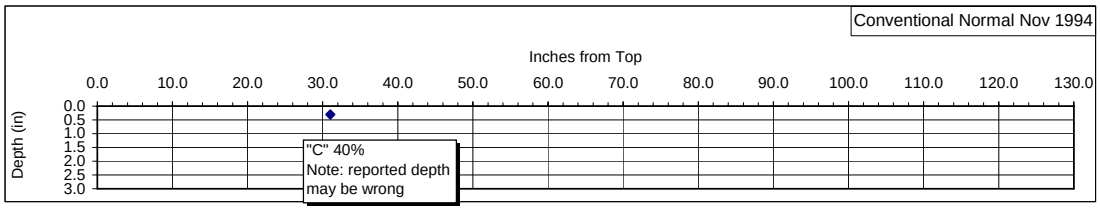
original length: 131"

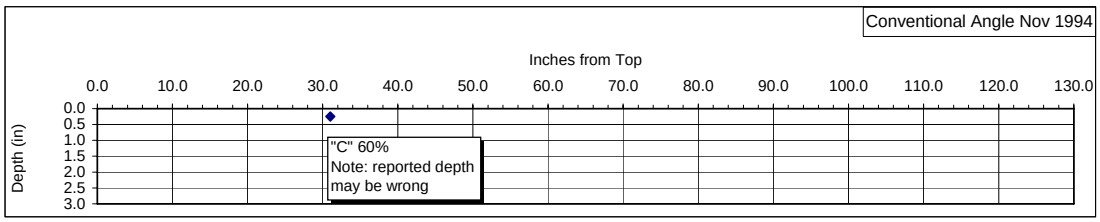










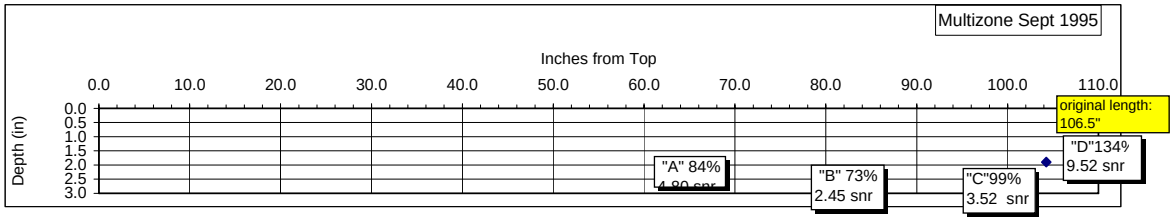


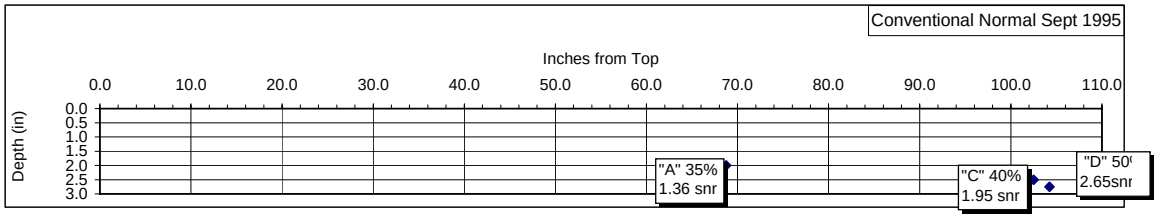
B3W1B

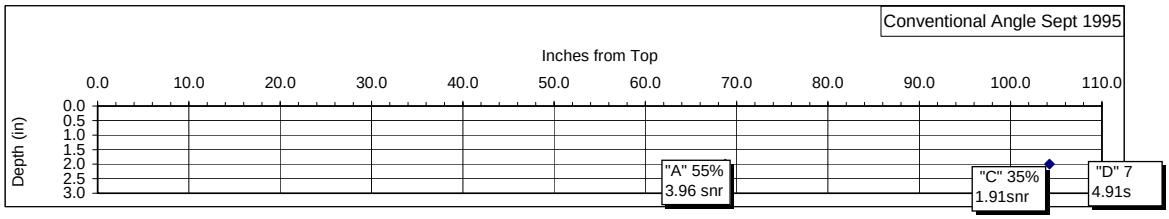
		September 1995 Inspection			November 1994 Inspection		
Stamped I.D.	Inches from top	Multizone Depth	Conv. Normal Depth	Conv. Angle Depth	Multizone Depth	Conv. Normal Depth	Conv. Angle Depth
A	68.8	2.0	2.0	2.0	Test not run	2.0	2.0
B	84.8	2.2					
C	102.5	2.3	2.5	2.3		3.0	
D	104.3	1.9	2.8	2.0		3.0	

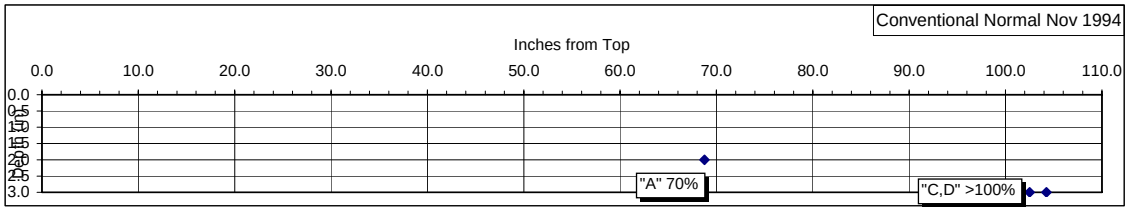
0 - 11.5" section removed between tests

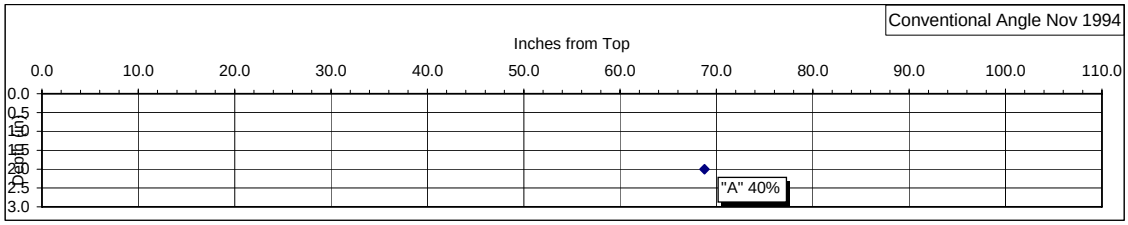
C,D reported as same ind. conv./norm







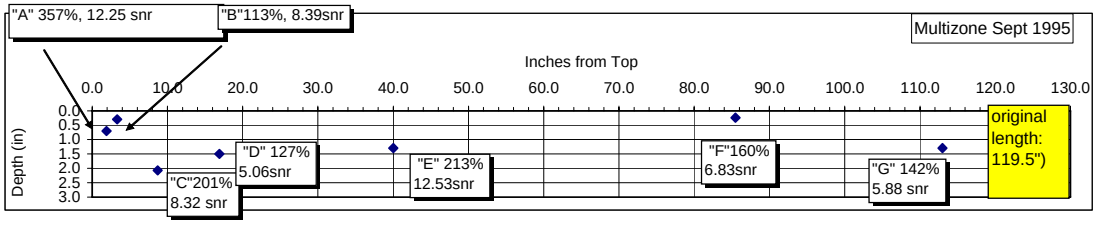


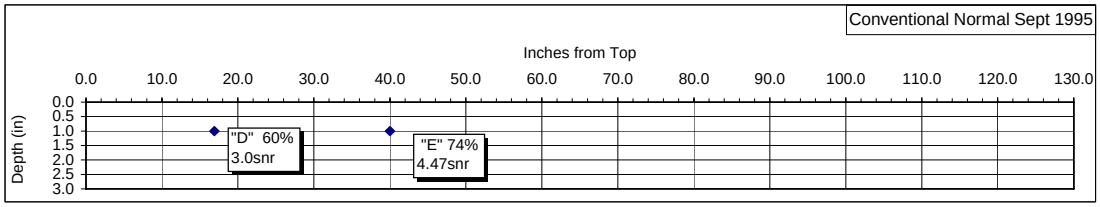


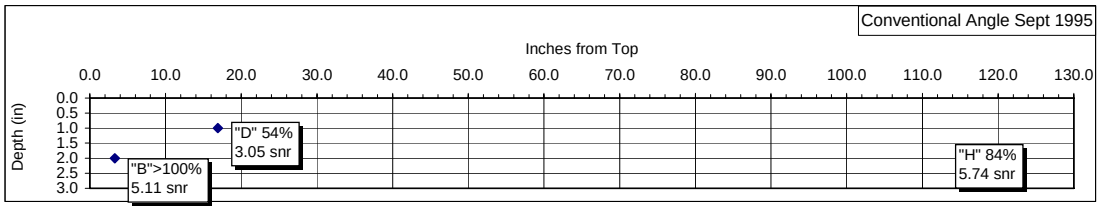
B3W2

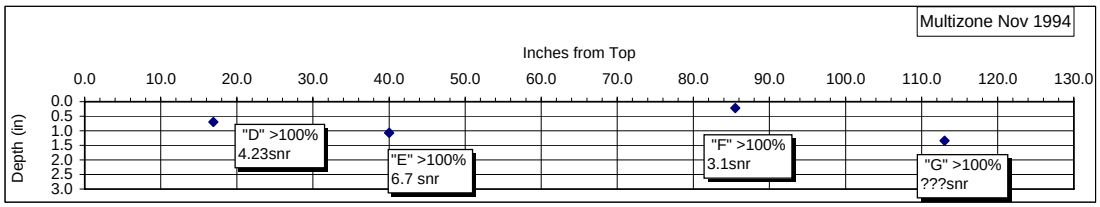
		September 1995 Inspection			November 1994 Inspection		
Stamped I.D.	Inches from top	Multizone Depth	Conv. Normal Depth	Conv. Angle Depth	Multizone Depth	Conv. Normal Depth	Conv. Angle Depth
A	1.9	0.7				2.0	2.0
B	3.3	0.3		2.0			
C	8.7	2.1					
D	16.9	1.5	1.0	1.0	0.7	1.0	1.0
E	40.0	1.3	1.0		1.1	1.0	1.0
F	85.5	0.2			0.2		
G	113.0	1.3			1.3	1.5	1.5

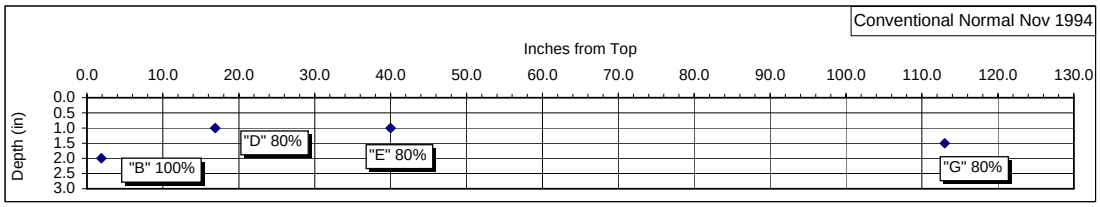
"A","B","C" are in region 0 - 5.5" marked "no test, visible hole" on 12/5/94 RMI report. "C" appears at 3.5" from end on C-scan inconsistent with RMI report). Additional MZ indication at 5", 56%, SNR 2.3 (not rejectable) on RMI

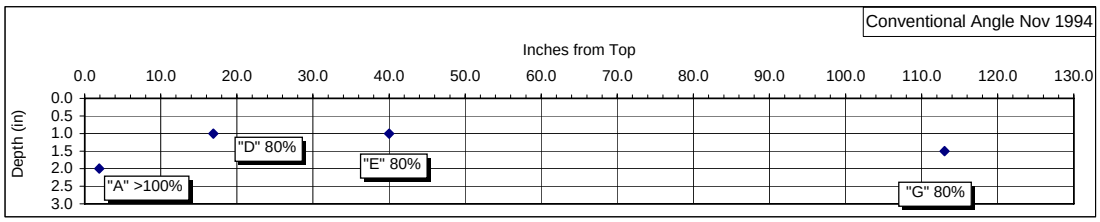






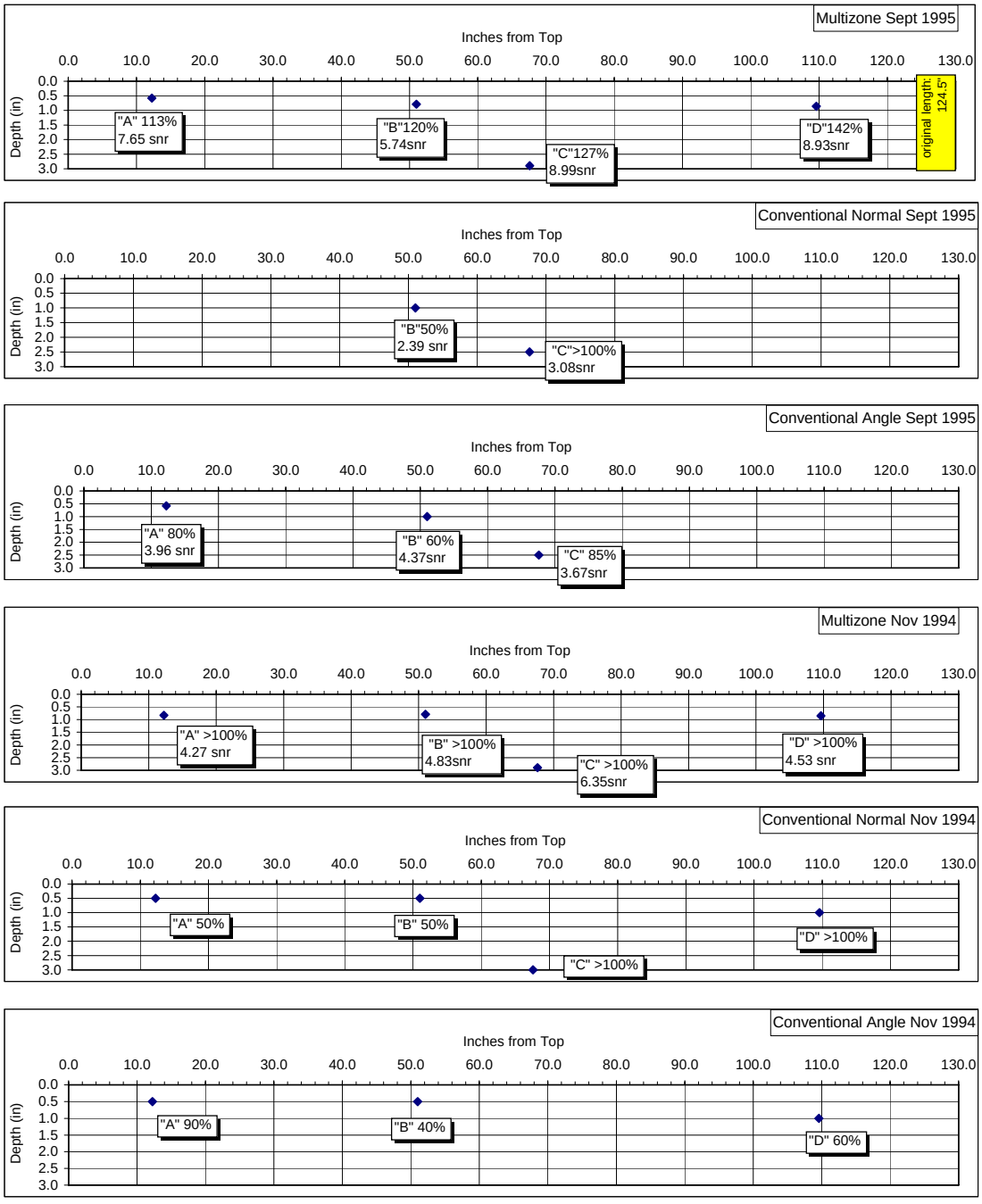






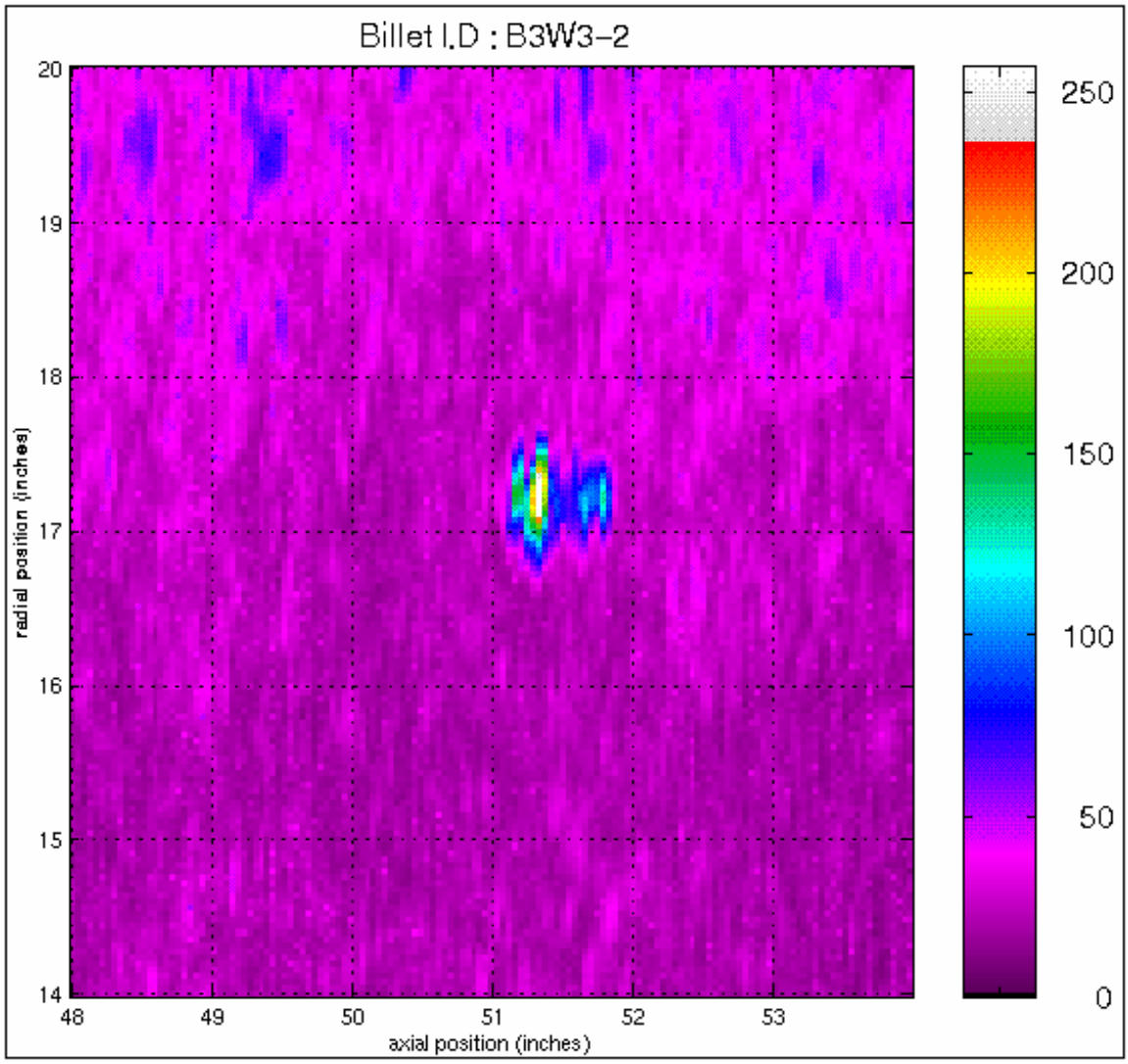
B3W3

		September 1995 Inspection			November 1994 Inspection		
Stamped I.D.	Inches from top	Multizone Depth	Conv. Normal Depth	Conv. Angle Depth	Multizone Depth	Conv. Normal Depth	Conv. Angle Depth
A	12.3	0.6		0.6	0.8	0.5	0.5
B	51.0	0.8	1.0	1.0	0.8	0.5	0.5
C	67.6	2.9	2.5	2.5	2.9	3.0	
D	109.6	0.9			0.9	1.0	1.0



APPENDIX D—ULTRASONIC C-SCAN RESULTS FOR INDICATIONS SELECTED FOR USE IN PROBABILITY OF DETECTION STUDIES

Ten indications were selected for detailed characterization, including ultrasonic measurements, metallographic cutup, microprobe analysis, and three-dimensional reconstruction. Selection of the ten indications was based on review of the inspection data generated at the billet supplier in September 1995. Consideration was given to the location within the billet, inspection methods which resulted in a detection, and character of the C-scan image. The C-scan images and detection information for the ten indications are provided below. The billet ID and indication ID are listed (e.g., B3W3-B) along with the zone in which the indication was found. Inches from top indicates axial location of the defect within the billet. The amplitude, signal-to-noise ratio, and depth are tabulated from the billet maps (see appendix C of this report). Axial and radial lengths were estimated using the pixel size from the indication size C-scan images.



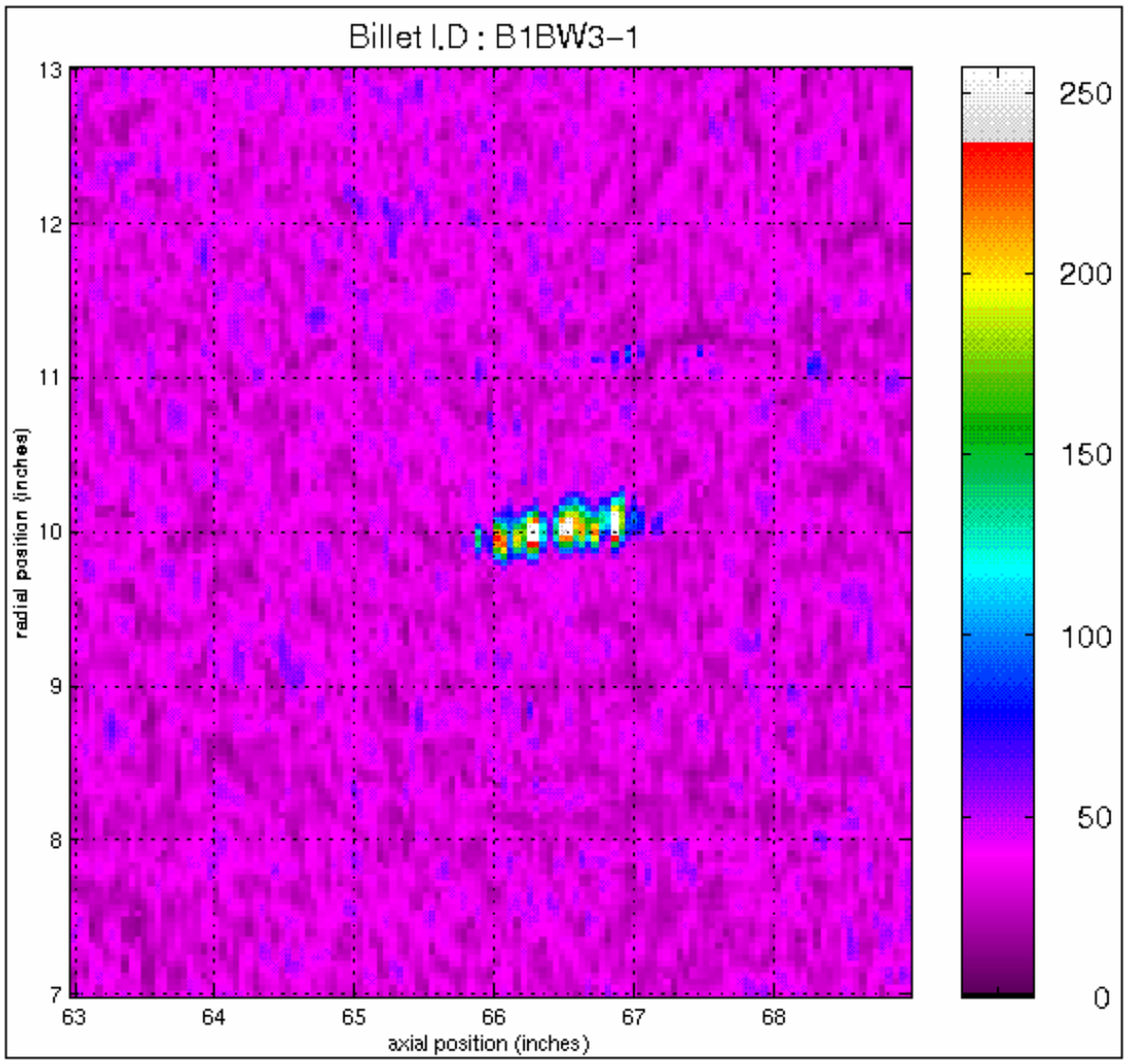
Billet ID: B3W3 - B

Zone: 1

Inches from top: 51

	Amplitude (%)	S/N	depth (in)	axial length (in)	radial length (in)
Multizone	**120**	**5.74**	**0.8**	**0.7152**	**0.2160**
Conv. Longitudinal	**50**	**2.39**	**1.0**		
Conv. Angle	**60%**	**4.37**	**1.0**		

Billet Length: 124.5



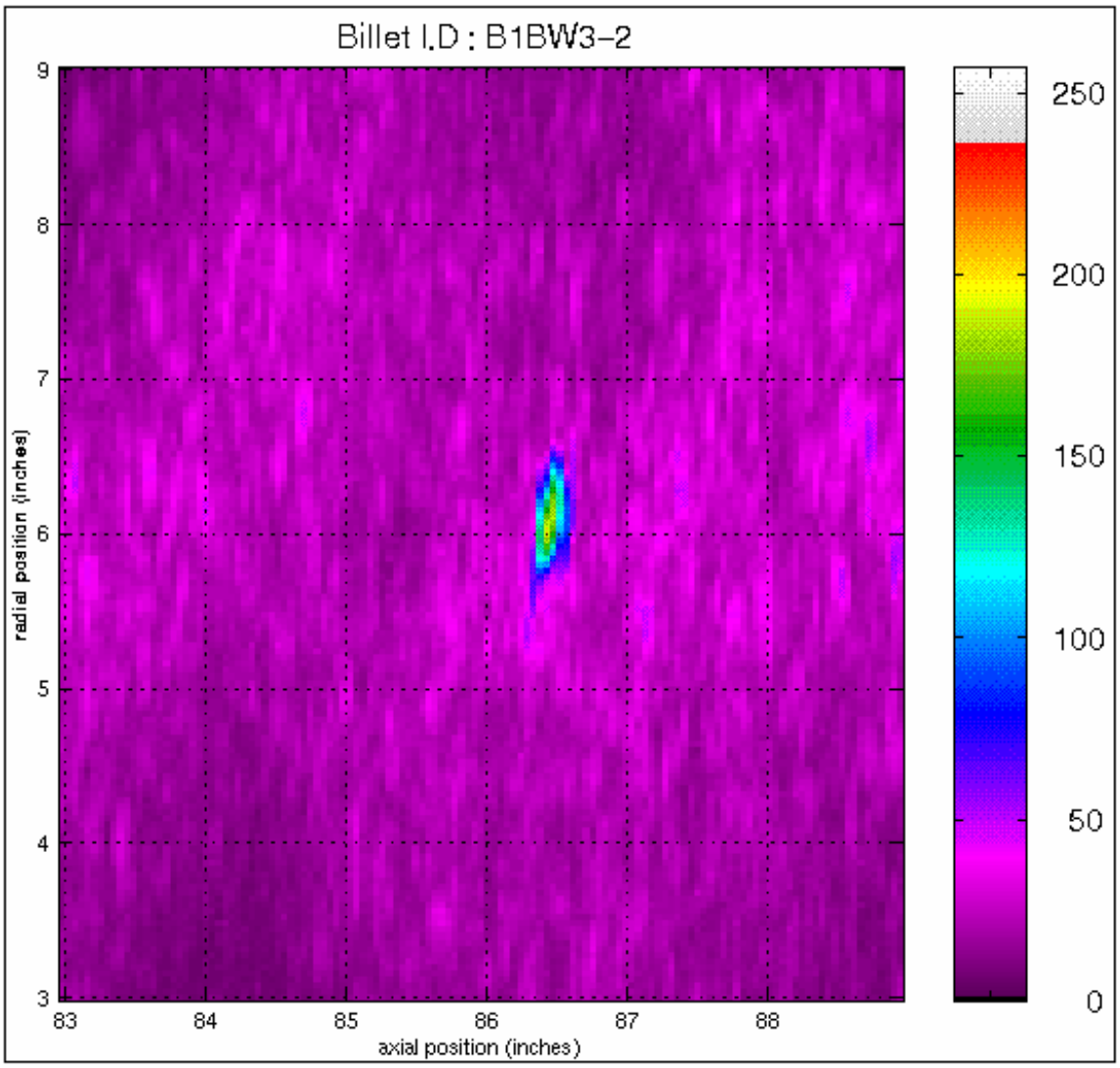
Billet ID: B1BW3 - C

Zone: 1

Inches from top: 66

	Amplitude (%)	S/N	depth (in)	axial length (in)	radial length (in)
Multizone	**127%**	**6.67**	**0.5**	**1.4474**	**0.2301**
Conv. Longitudinal	**%**				
Conv. Angle	**%**				

Billet Length: 107.5



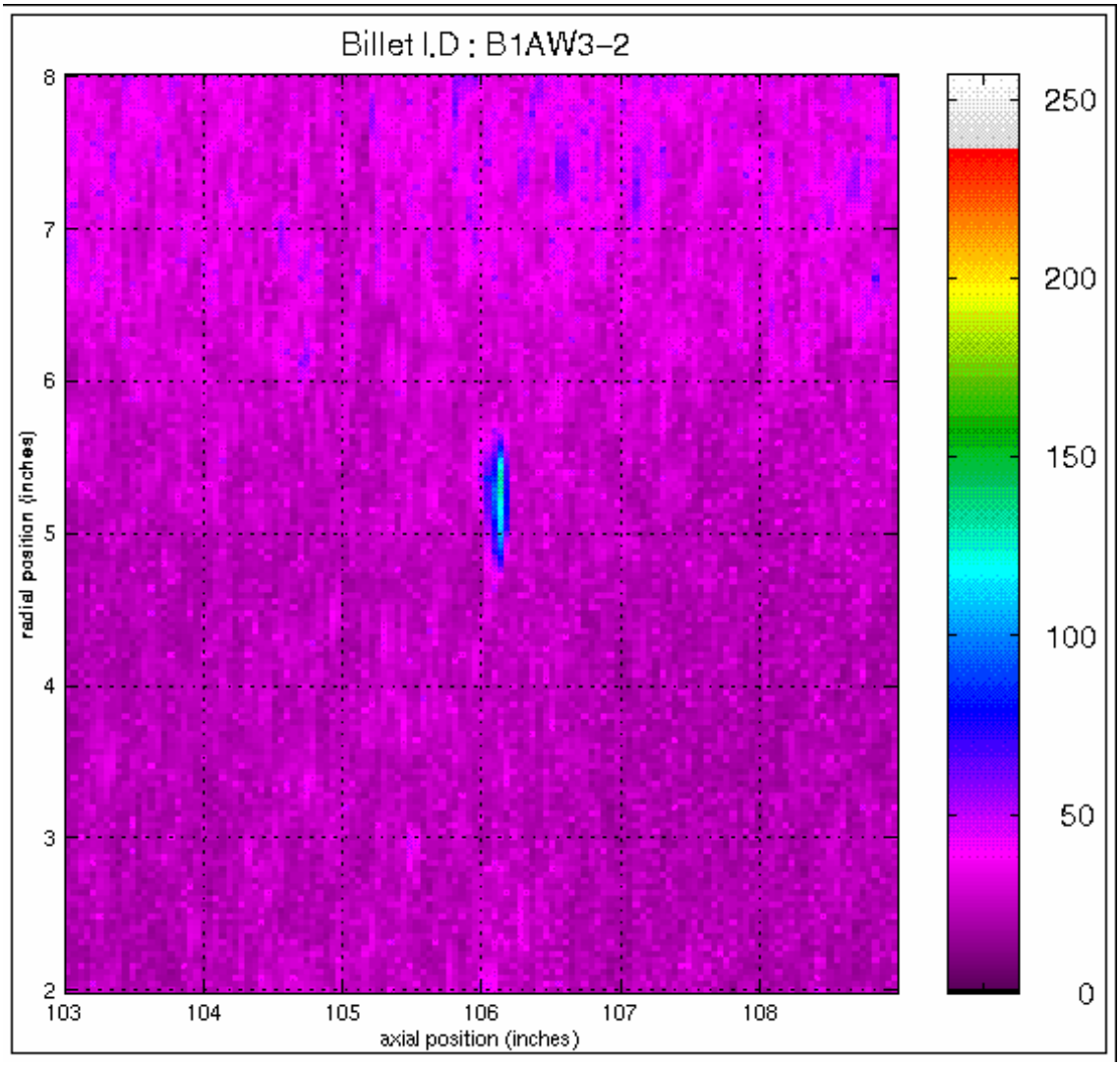
Billet ID: B1BW3 - D

Zone: 2

Inches from top: 86.0

	Amplitude (%)	S/N	depth (in)	axial length (in)	radial length (in)
Multizone	**74%**	**5.06**	**1.5**	**0.3268**	**0.2577**
Conv. Longitudinal	**%**				
Conv. Angle	**%**				

Billet Length: 107.5



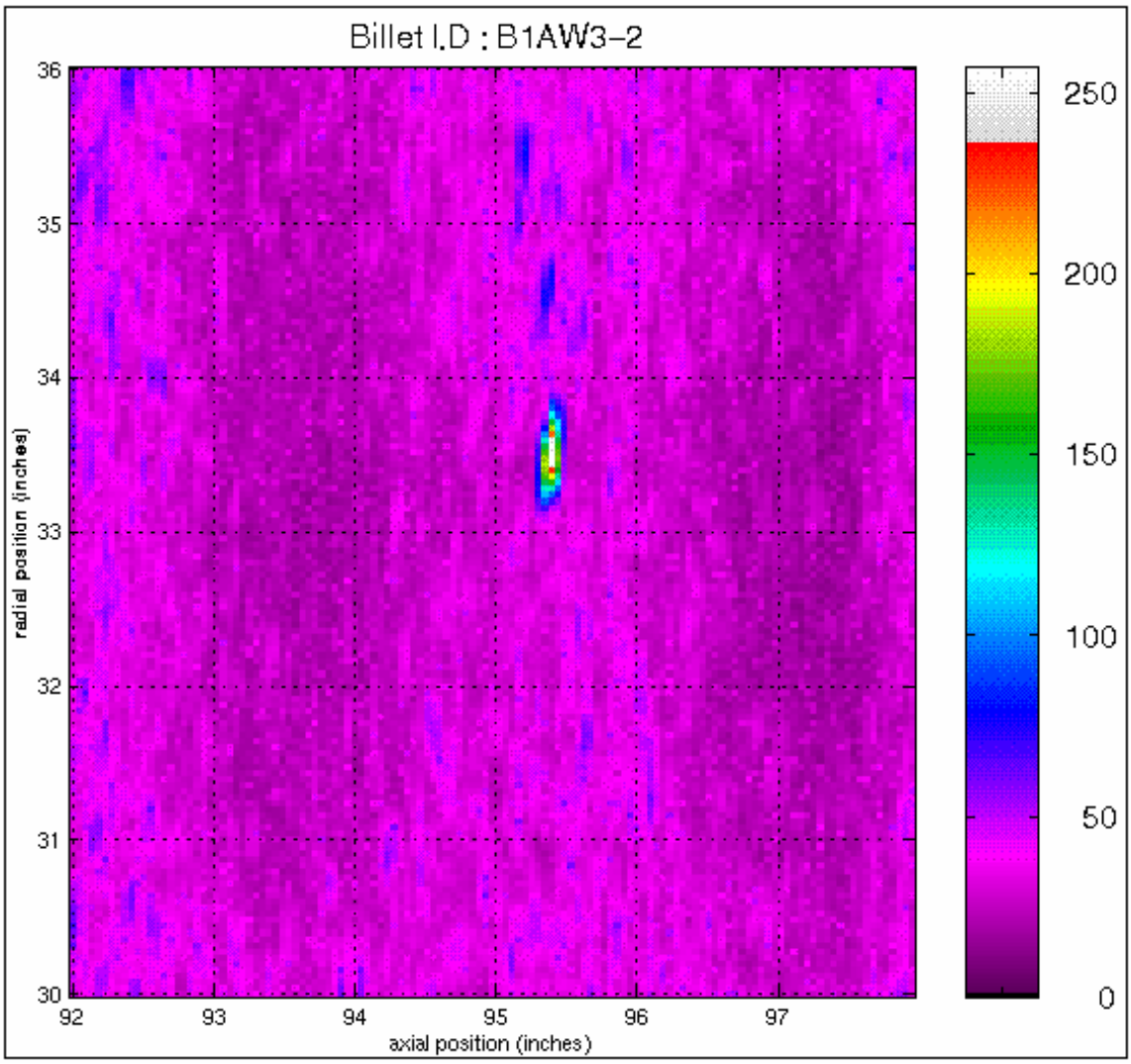
Billet ID: B1AW3-E

Zone: 2

Inches from top: 105

	Amplitude (%)	S/N	depth (in)	axial length (in)	radial length (in)
Multizone	**47**	**2.52**	**1.6**	**.1860**	**.4123**
Conv. Longitudinal					
Conv. Angle					

Billet length: 111



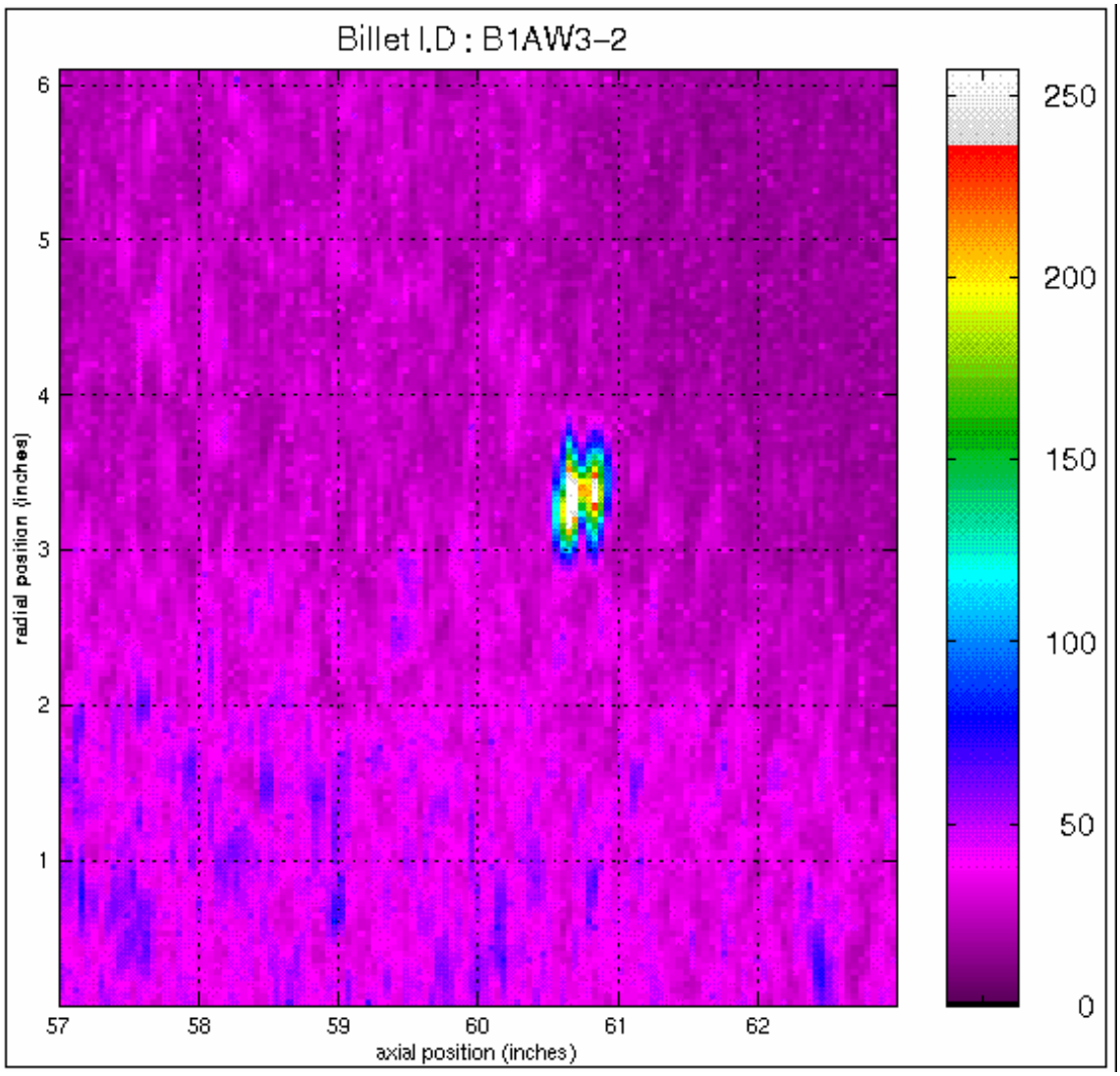
Billet ID: B1AW3-D

Zone: 2

Inches from top: 94.4

	Amplitude (%)	S/N	depth (in)	axial length (in)	radial length (in)
Multizone	**101**	**4.49**	**1.1**	**0.2326**	**0.2215**
Conv. Longitudinal					
Conv. Angle					

Billet length: 111



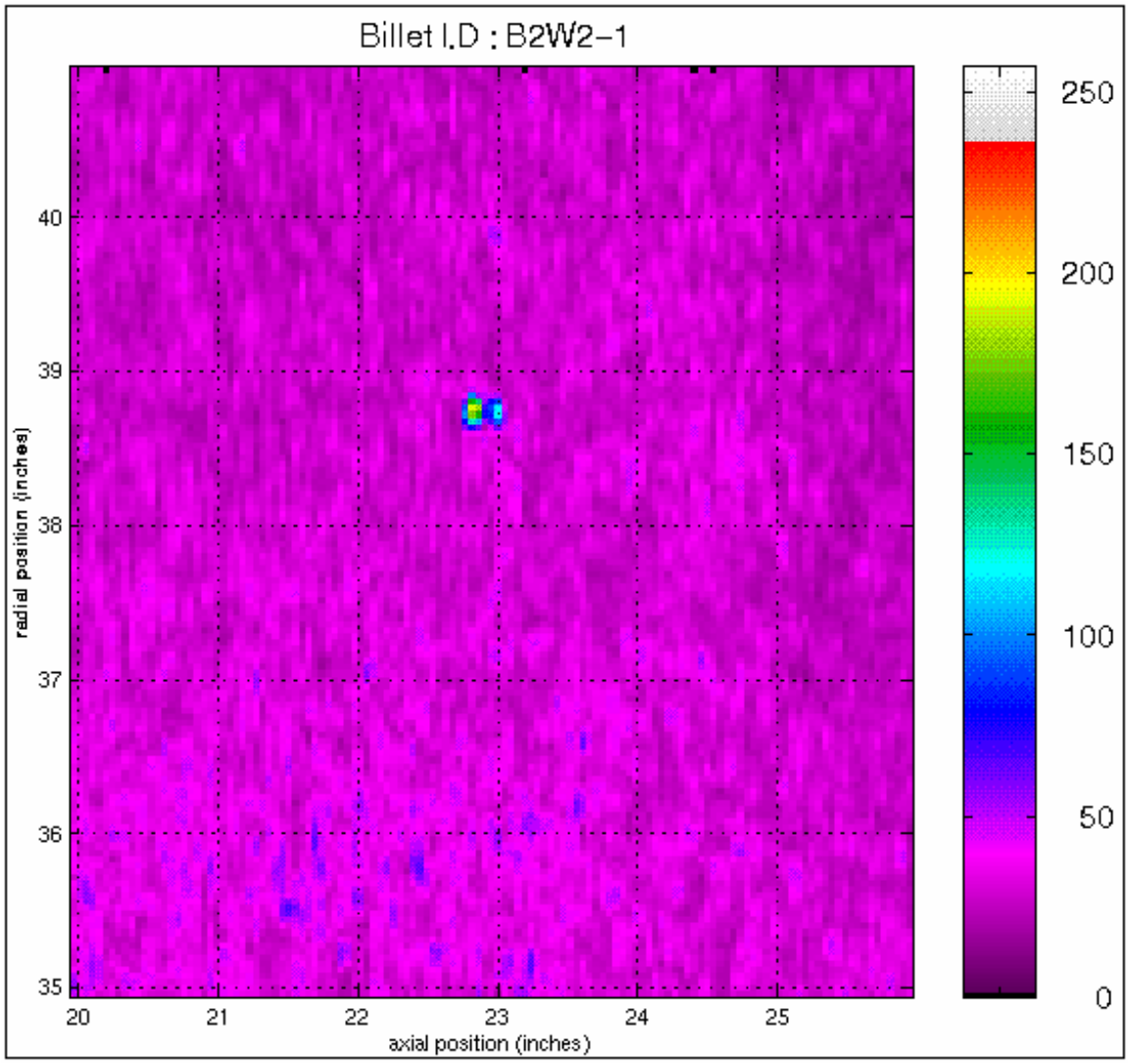
Billet ID: B1AW3-A

Zone: 2

Inches from top: 60.0

	Amplitude (%)	S/N	depth (in)	axial length (in)	radial length (in)
Multizone	**142%**	**5.02**	**0.7**	**0.4186**	**0.3387**
Conv. Longitudinal	**50%**	**2.92**	**0.8**		
Conv. Angle	**60%**	**2.48**	**0.8**		

Billet length: 111



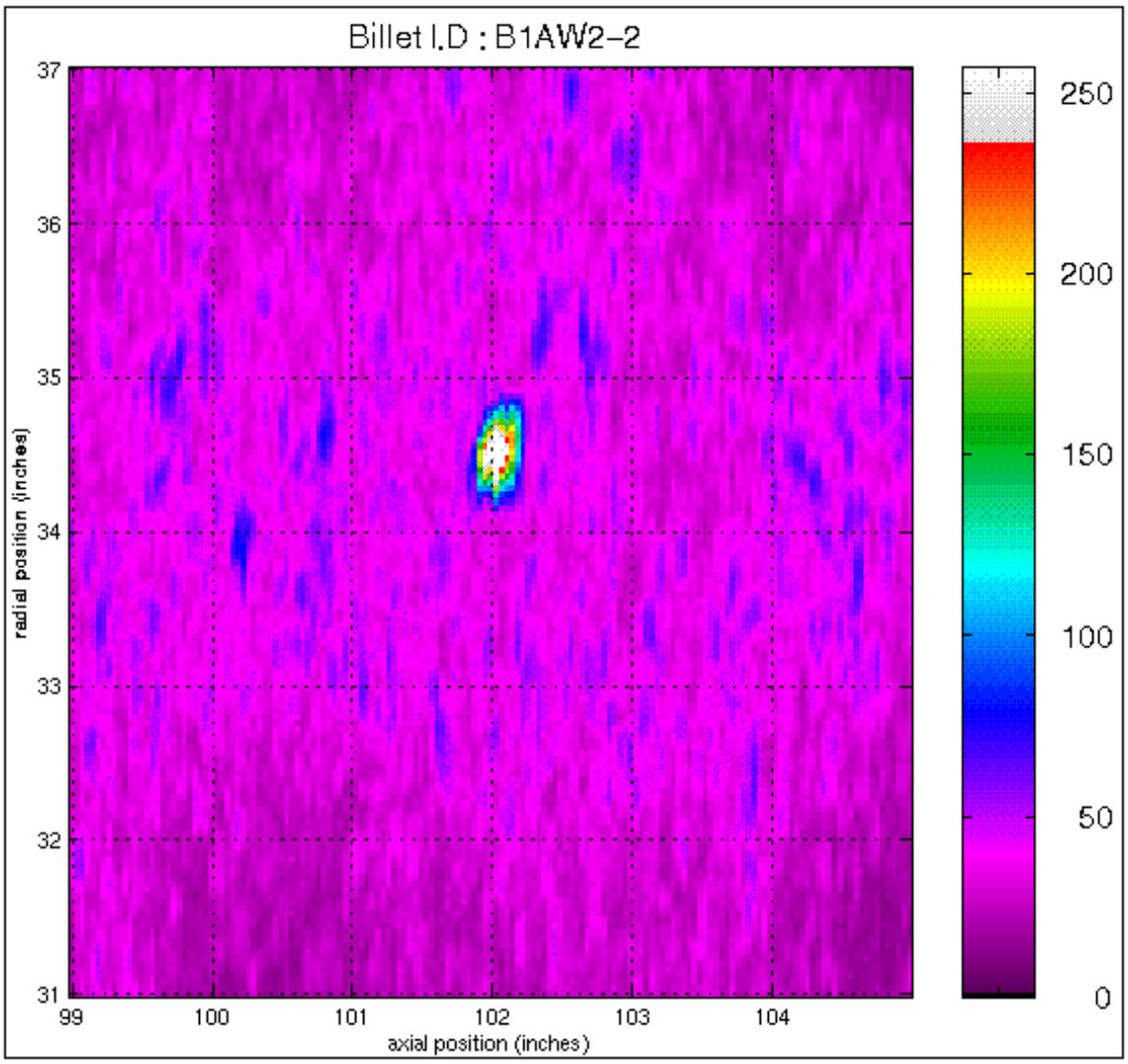
Billet ID: B2W2 - C

Zone: 1

Inches from top: 22.4

	Amplitude (%)	S/N	depth (in)	axial length (in)	radial length (in)
Multizone	**74%**	**4.09**	**0.2**	**0.3273**	**0.1031**
Conv. Longitudinal	**%**				
Conv. Angle	**%**				

Billet Length: 123



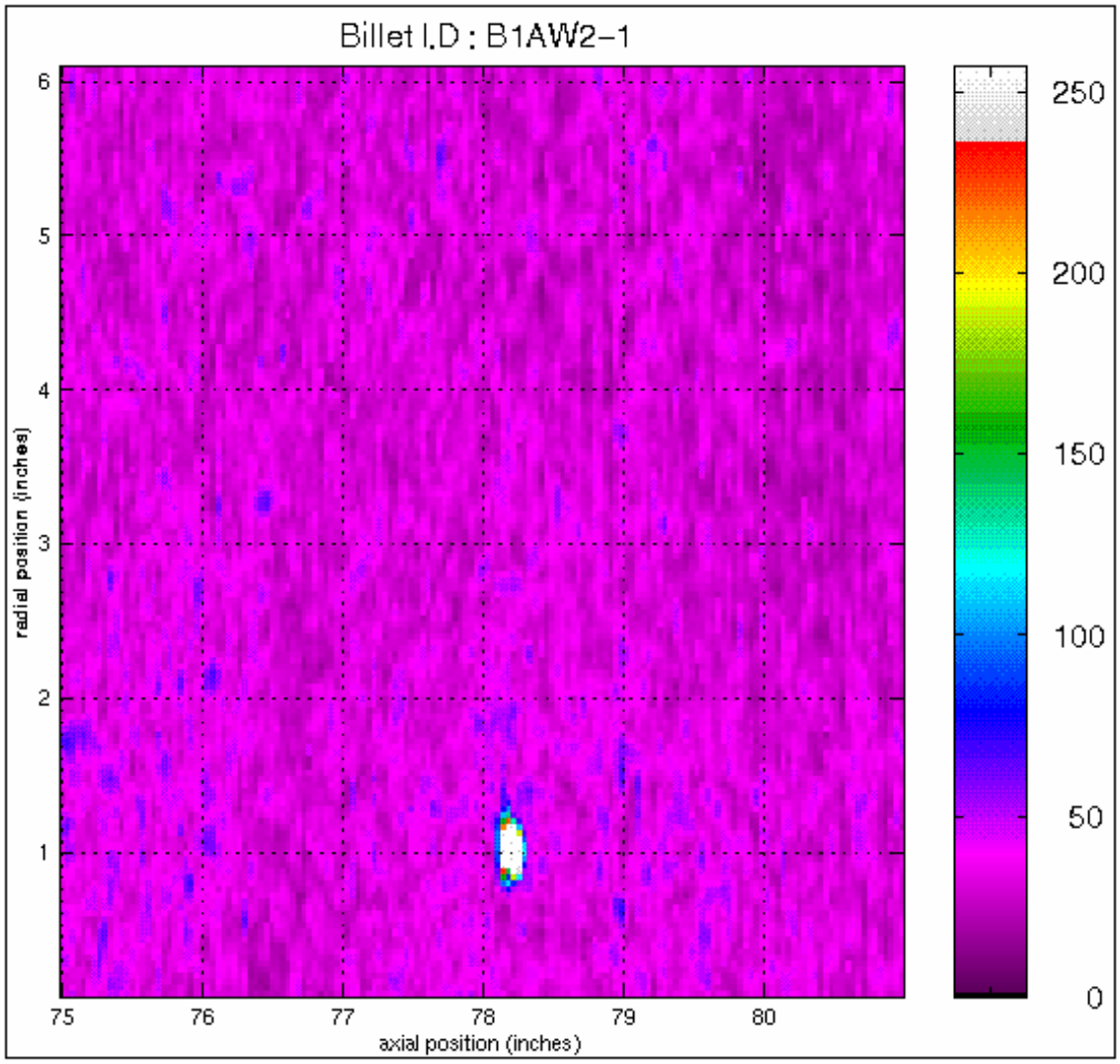
Billet ID: B1AW2 - D

Zone: 2

Inches from top: 98.0

	Amplitude (%)	S/N	depth (in)	axial length (in)	radial length (in)
Multizone	**134%**	**5.46**	**0.7**	**0.4217**	**0.2681**
Conv. Longitudinal	**50%**	**2.61**			
Conv. Angle	**%**				

Billet Length: 117



Billet ID: B1AW2 - B
Zone: 1
Inches from top:

	Amplitude (%)	S/N	depth (in)	axial length (in)	radial length (in)
Multizone	**225%**	**21.7**	**0.2**	**0.2300**	**0.4188**
Conv. Longitudinal	**%**				
Conv. Angle	**%**				

Billet Length: 117

APPENDIX E—DEFECT CHARACTERIZATION DATA

Ten defects were selected for detailed characterization to provide improved understanding of hard alpha defects and to support probability of detection studies. Substantive amounts of data were generated for each of the defects and are provided in appendix E. The following categories of data are provided:

- Defect location: Location of the mult as removed from the original billet.

- Billet inspection: Inspection results from billet supplier including C-scan image. Tabulation of inspection results from repeat inspection performed at General Electric (GE).

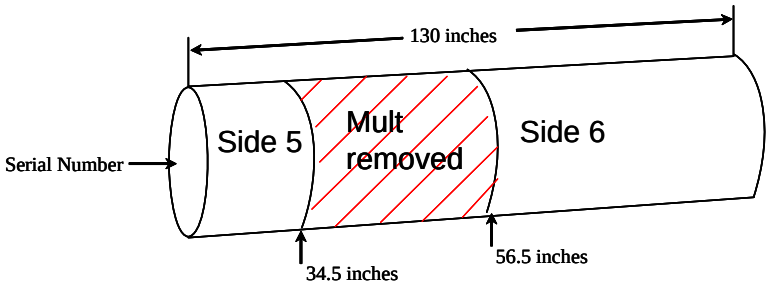
- Cube inspection: Tabulation of 25-MHz inspection results including C-scan image performed at GE. Comparison of 5-MHz experimental results to model predictions performed by Iowa State University.

- Solid model results: Generation of solid models of the voiding was necessary for use in model prediction. A summary of geometric models parameters is provided along with connectivity trees for each of the sections used to reconstruct the defect. Full details of the process are provided in appendix F. Several views of the final solid model used in the model calculations are provided, including final dimensions for the void.

- Microprobe analysis: Electron microprobe measurements were made to provide nitrogen profiles for each of the defects. Concentration was determined for the base alloy elements (titanium (Ti), aluminum (Al), and vanadium (V)) as well as the contaminants (carbon (C) and nitrogen (N)). Micrographs showing the location of the scans are provided along with a tabulation of the concentrations. A graph is provided of the nitrogen profiles.

Indication: B3W3 – B

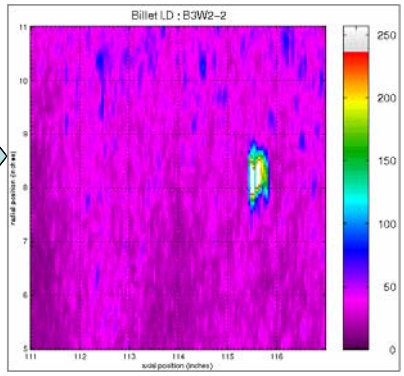
Original billet length: 130”



Billet inspection:

	Amplitude (%)	S/N	depth (in)	axial length (in)	radial length (in)
Multizone	120%	5.74	0.8	0.7573	0.2434
Conv. Longitudinal	50	2.39	1.0		
Conv. Angle	60%	4.37	1.0		

Zone 1



Mult inspection parameters:

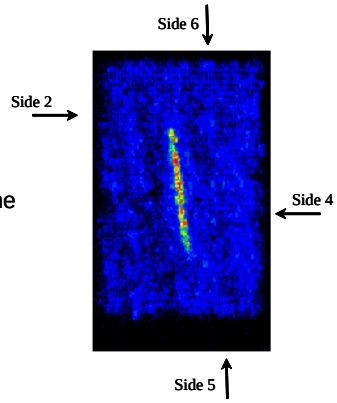
Transducer - Zone 1, 6” diameter, 5MHz
Index - 0.010
Data Acquisition Rate - 0.010
Inspection Sensitivity - #2 FBH at 80-90% in Titanium
Inspection Range - 0.2” to 0.8”
Sampling Rate - 100 MHz

Depth	Axial Length	Amplitude	Signal-to-Noise Ratio
0.8	0.8”	127%	5.7

25 MHz inspection parameters:

Transducer - 25 MHz, F10 - focal point positioned at indication depth
Index - 0.010
Data Acquisition Rate - 0.010
Inspection sensitivity - #2FBH at 84% at 48dB
Inspection range - C-scan , Between Front and Back / B-scan entire volume
Sampling Rate - 200 MHz

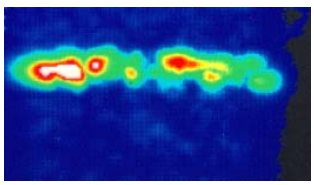
Side	Depth	Axial Length	Amplitude %	Sensitivity, dB
1	0.444”	0.8”	66	60
2	0.496”	0.8”	93	60
3	0.453	0.8	76	60
4	0.399”	0.8”	96	60
5	0.460”	0.8”	73	74
6	0.435”	0.8”	79	72



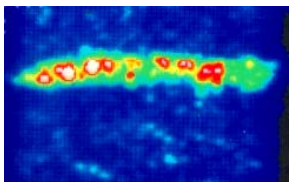
View is from Side 1(side which was polished). Sides 5 and 6 represent the axial ends as shown above. Sides 2 and 4 represent the hoop direction (circumferential plane.)

UT characterization of cube:

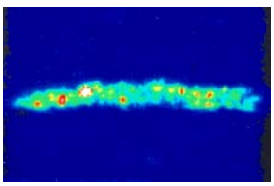
UT measurements completed using multiple frequencies



5MHz



10MHz

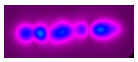


20MHz

B3W3-B 5 MHz C-scan image comparisons:

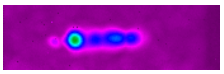
Side 1

Model



Attenuation=10dB
peak amplitude =411 mv
deviation=-39% or -4.25 dB

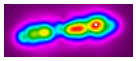
Experiment



Attenuation= 10 dB
peak amplitude= 670mv

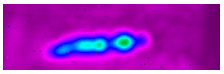
Side 2

Model



Attenuation=10dB
peak amplitude= 1012mv
deviation=56% or 3.89 dB

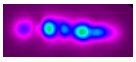
Experiment



Attenuation=10dB
peak amplitude= 647mv

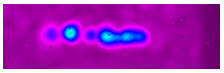
Side 3

Model



Attenuation=8dB
peak amplitude=614 mv
Deviation=11% or 0.92 dB

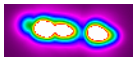
Experiment



Attenuation=8dB
peak amplitude= 552mv

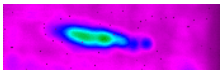
Side 4

Model



Attenuation=8dB
peak amplitude=1845 mv
deviation=179% or 8.90 dB

Experiment



Attenuation=8dB
peak amplitude= 662mv

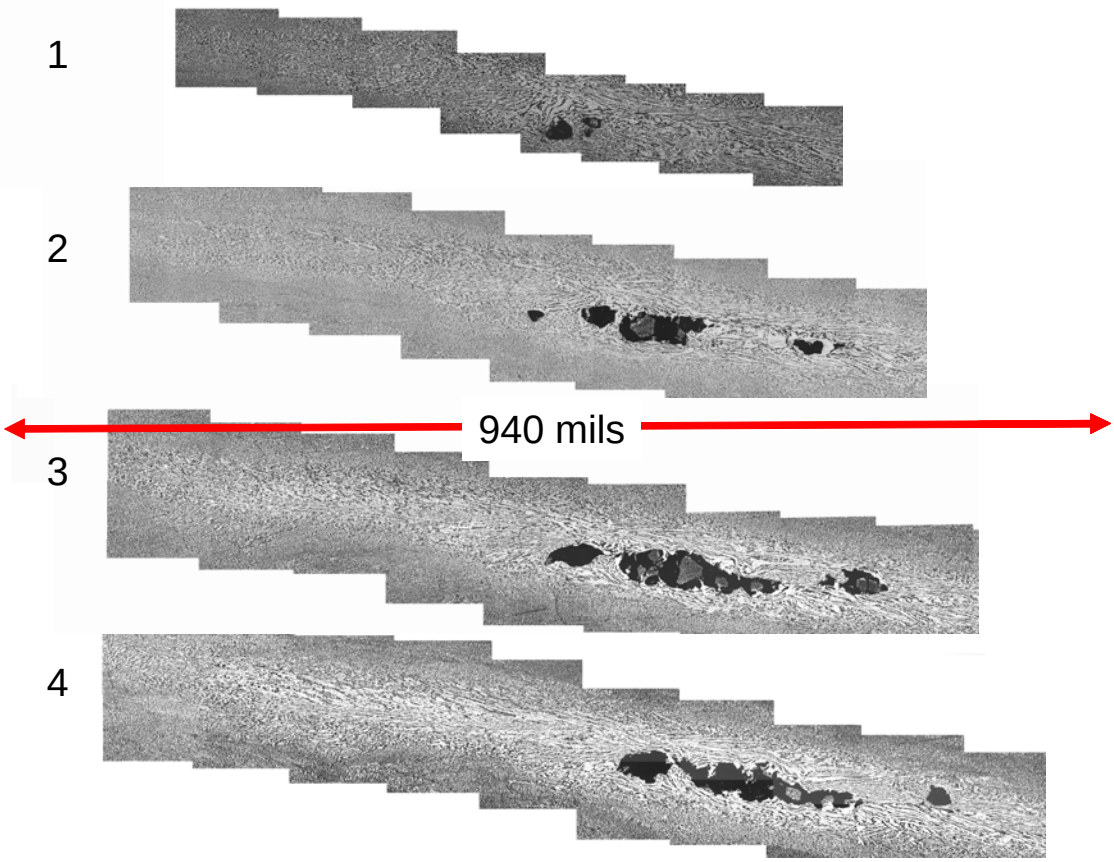
Experiment image: 171(H) x 51(V) @10 mils

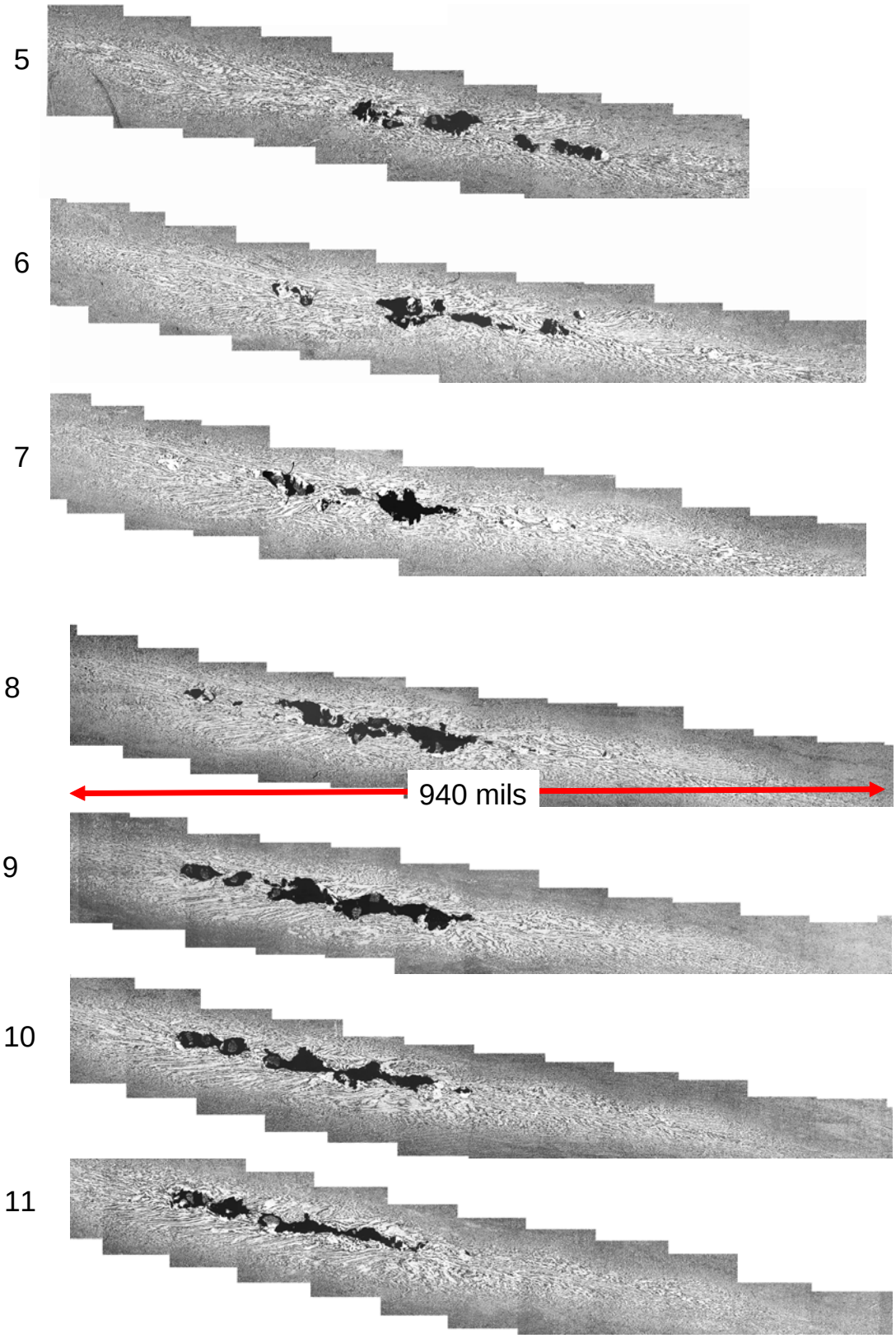
Model image: 101(H) x 41(V) @10 mils

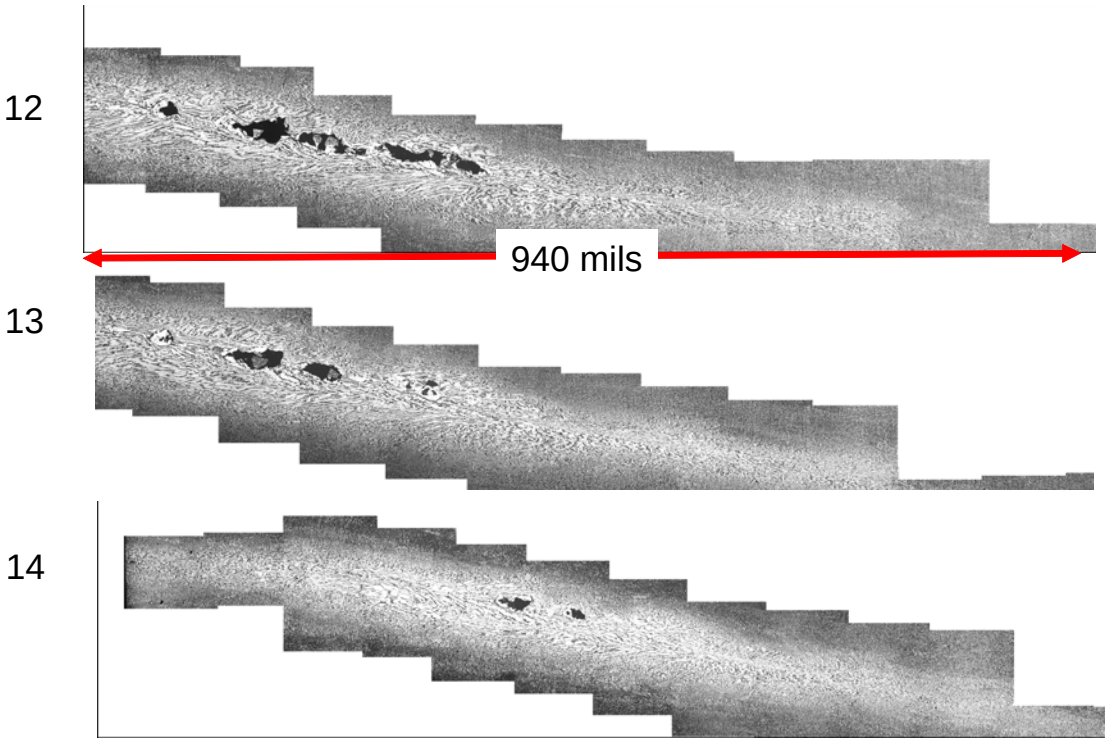


Experiment 255 = 1000mv

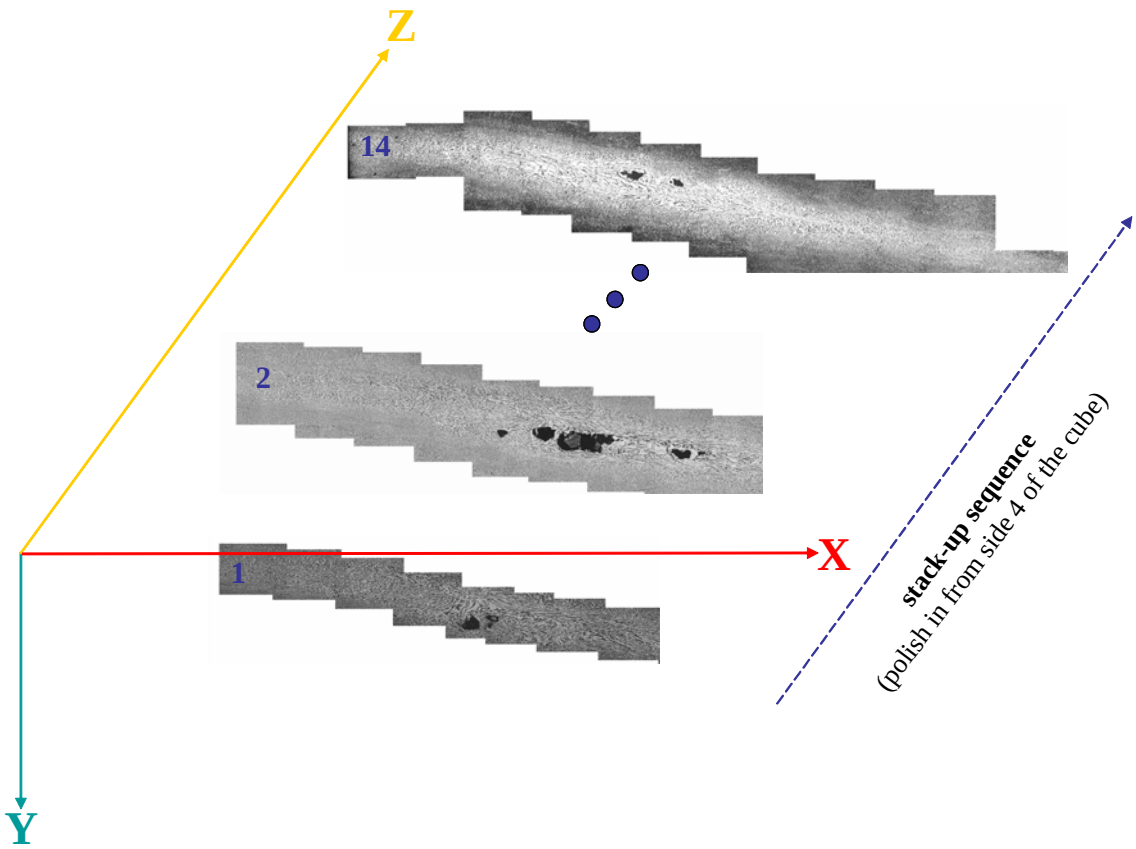
B3W3-B

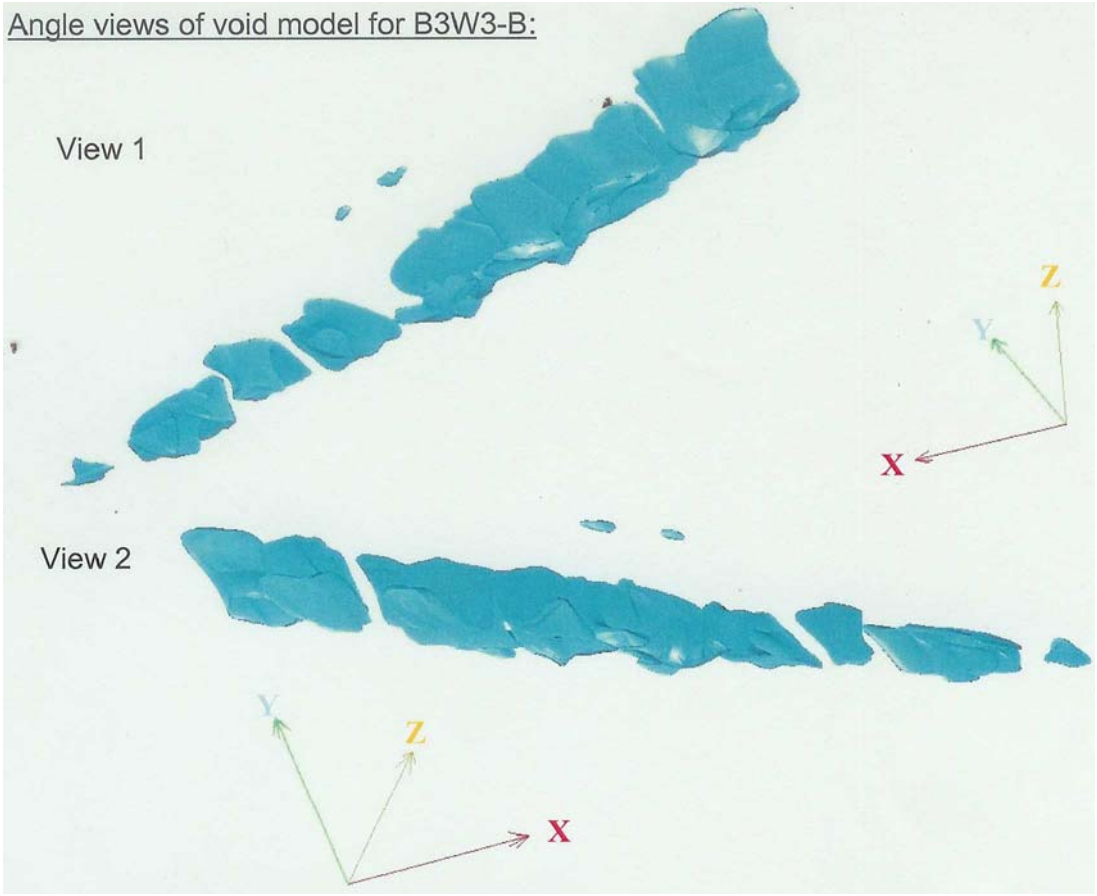



5
6
7
8
940 mils
9
10
11

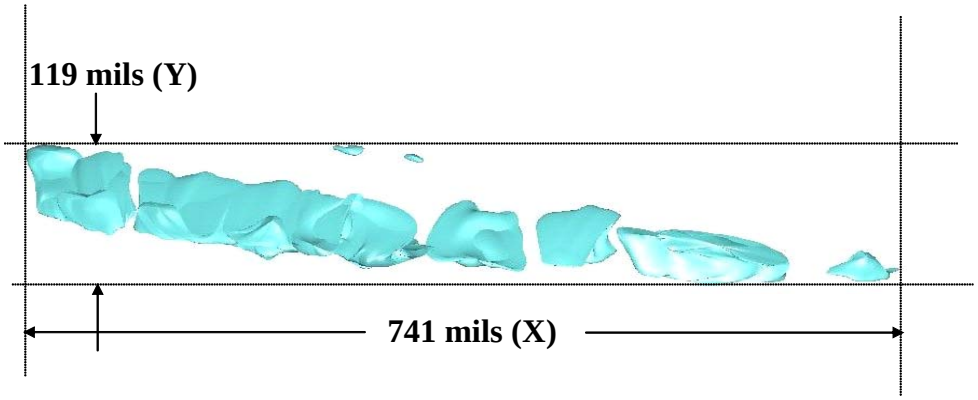


Orientation of Sub-Micrographs (B3W3-B)





Dimensions of B3W3-B

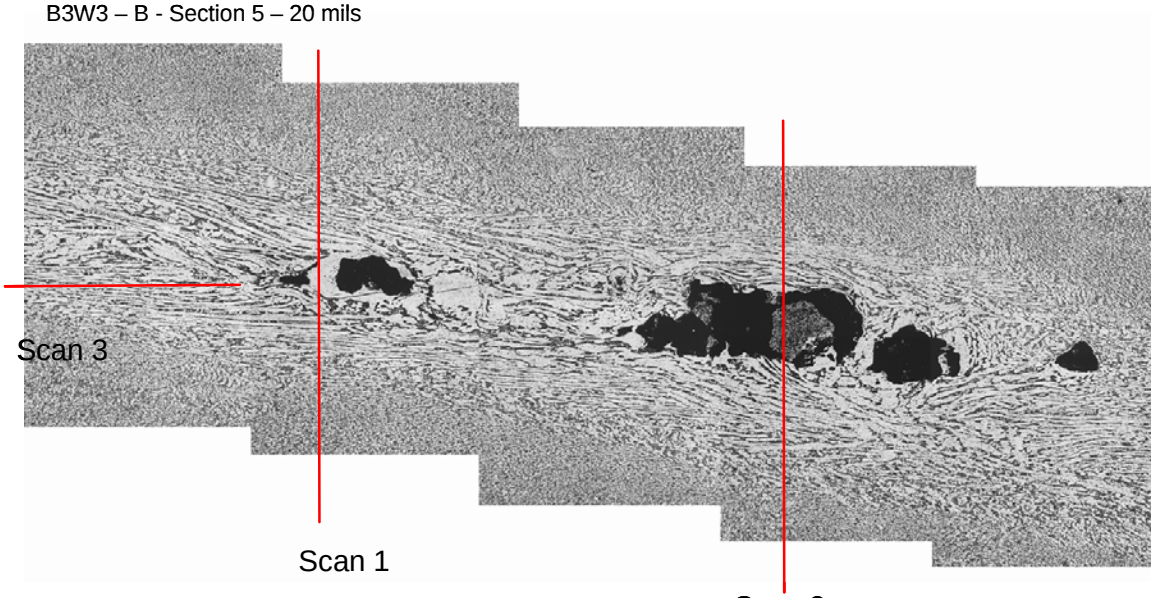


	min.	max.	size
X	298.78	1040.05	741.27
Y	154.24	273.50	119.25
Z	3.18	83.79	80.60

Unit: mils

Microprobe analysis:

B3W3 – B - Section 5 – 20 mils



B3W3 - INDICATION B - TRANSVERSE PROFILE No. 1
ELECTRON MICROPROBE COMPOSITION MEASUREMENTS
Scanned perpendicular to long axis of defect with "zero" located at defect core.

	Weight %					
Distance (mils)	Ti	Al	V	C	O	N
50	91	7.2	1.7	< 0.2	< 0.2	0.7
45	90	6.7	2.2	< 0.2	0.7*	< 0.5
40	85	7.3	1.6	< 0.2	< 0.2	< 0.5
35	85	7.2	1.7	< 0.2	< 0.2	1.0
30	89	6.9	2	0.6	0.4*	0.7
25	88	6.9	2	0.3	< 0.2	0.7
20	88	6.3	2.6	0.8	< 0.2	1.1
18	89	6.3	1.9	0.6	< 0.2	1.1
16	87	5.1	6.1	1.1	0.7*	1.4
12	89	5.6	2.2	0.9	< 0.2	1.2
10	88	5.5	2.1	1.1	< 0.2	1.5
9	90	5.4	2.3	0.9	< 0.2	1.7
8	89	5.4	2.1	1.1	< 0.2	1.7
7	90	5.5	2	1.3	< 0.2	1.5
6	90	4.9	1.7	1.0	< 0.2	1.5
5	91	4.5	1.7	1.2	< 0.2	2.3
4	91	3.6	1.9	1.9	< 0.2	2.2
3	91	2.4	1.7	1.8	< 0.2	3.3
2	91	0.5	1.7	1.4	< 0.2	3.9
1	92	0.2	2	1.7	< 0.2	3.9
0	91	0.3	1.9	1.3	< 0.2	3.5
-1	93	0.3	1.9	1.8	< 0.2	3.8
-2	94	0.3	1.9	1.6	< 0.2	3.4
-3	93	0.4	2.2	1.3	< 0.2	3.2
-4	92	2.9	1.8	2.1	0.8*	1.9
-5	88	4.2	1.8	1.6	< 0.2	1.7
-6	90	5.2	1.9	0.9	< 0.2	1.2
-7	89	5.4	2.5	0.9	< 0.2	1.1
-9	89	5	1.9	1.2	< 0.2	1.5
-10	90	5.7	2	1.0	< 0.2	1.2
-12	92	5.5	1.8	1.0	< 0.2	0.9
-16	91	6.5	1.9	0.8	< 0.2	0.7
-18	90	6.6	2	0.7	< 0.2	1.0
-20	90	6.6	1.9	0.8	< 0.2	0.5
-25	90	7	1.8	0.6	< 0.2	0.8
-30	90	7	1.9	0.4	< 0.2	0.5
-35	90	5.7	2	< 0.2	0.3	0.6
-40	91	7.2	1.9	< 0.2	< 0.2	1.0
-45	91	6.6	1.9	< 0.2	< 0.2	0.6
-50	91	6.8	1.6	< 0.2	< 0.2	< 0.5

* Occasional points of elevated oxygen concentration likely from contamination on specimen surface, and do not represent actual variations in composition.

B3W3 - INDICATION B - TRANSVERSE PROFILE No. 2
ELECTRON MICROPROBE COMPOSITION MEASUREMENTS
Scanned perpendicular to long axis of defect with "zero" located at defect core.

	Weight %					
Distance (mils)	Ti	Al	V	C	O	N
50	90	7.0	1.7	< 0.2	< 0.2	< 0.5
45	89	7.0	1.8	< 0.2	< 0.2	< 0.5
40	90	6.8	2.0	0.2	< 0.2	< 0.5
35	91	6.9	2.0	< 0.2	< 0.2	0.6
30	89	6.5	2.1	< 0.2	< 0.2	< 0.5
25	89	6.3	2.0	0.2	< 0.2	< 0.5
20	88	6.0	2.1	0.2	< 0.2	0.6
16	90	5.6	2.2	0.3	< 0.2	0.7
14	89	5.6	2.1	0.4	< 0.2	0.6
12	88	5.5	2.5	0.5	< 0.2	0.8
10	84	0.7	2.1	1.7	2.4*	5.6
9	83	0.1	0.9	1.0	< 0.2	3.5
7	84	0.1	1.5	0.5	< 0.2	6.8
5	85	0.2	1.9	0.9	< 0.2	6.8
4	86	0.1	2.0	0.7	< 0.2	8.0
3	83	0.4	1.6	0.8	< 0.2	8.6
2	87	0.1	1.9	0.7	< 0.2	8.5
1	86	0.1	1.9	0.8	< 0.2	8.5
0	84	0.2	4.1	0.7	< 0.2	8.7
-1	86	0.1	1.9	0.9	< 0.2	8.9
-2	86	0.1	1.5	1.0	< 0.2	8.8
-3	85	0.1	1.4	1.3	< 0.2	7.8
-4	86	0.1	1.7	1.7	< 0.2	8.0
-5	86	0.1	2.0	2.0	< 0.2	7.3
-6	84	0.2	2.0	3.5	< 0.2	7.0
-7	78	1.6	5.6	8.1	3.7*	4.9
-13	91	5.4	2.1	0.9	< 0.2	1.0
-14	91	5.4	2.3	0.7	< 0.2	0.5
-16	93	5.4	2.2	0.4	< 0.2	0.6
-18	92	5.8	2.2	0.4	< 0.2	< 0.5
-20	93	6.1	1.9	0.2	< 0.2	< 0.5
-25	92	6.6	1.9	< 0.2	< 0.2	< 0.5
-30	94	6.9	1.7	< 0.2	< 0.2	< 0.5
-35	94	6.8	1.4	< 0.2	< 0.2	< 0.5
-40	90	7.1	1.8	< 0.2	< 0.2	< 0.5
-45	91	7.2	1.7	< 0.2	< 0.2	< 0.5
-50	92	7.1	1.6	< 0.2	< 0.2	< 0.5

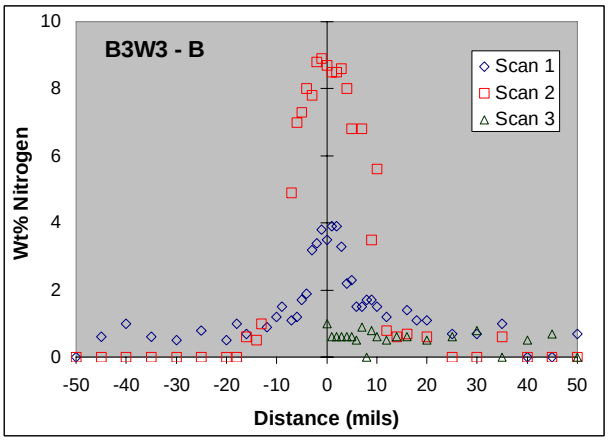
Note: Shaded points were located in the visible core of the defect.

* Occasional points of elevated oxygen concentration likely from contamination on specimen surface, and do not represent actual variations in composition.

B3W3 - INDICATION B - LONGITUDINAL PROFILE
ELECTRON MICROPROBE COMPOSITION MEASUREMENTS
Scanned parallel to long axis of defect with "zero" located at one end of defect core.

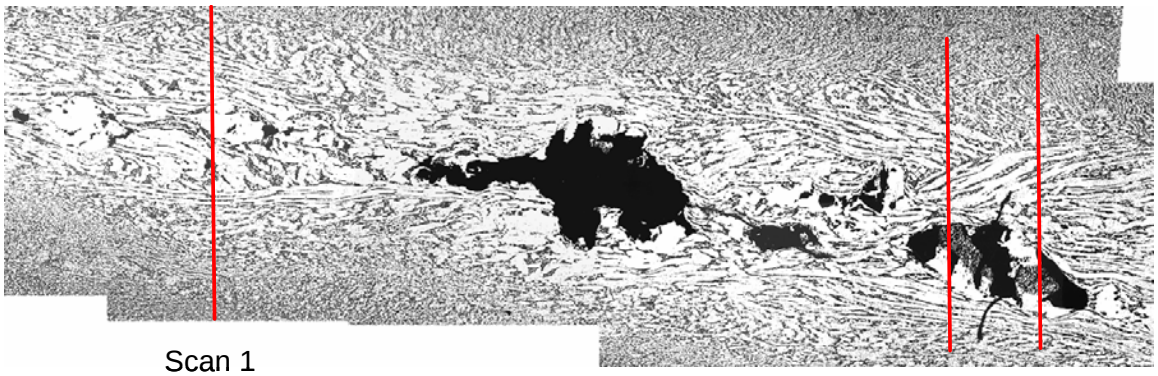
	Weight %					
Distance (mils)	Ti	Al	V	C	O	N
0	89	5.6	1.9	1.1	< 0.2	1.0
1	89	5.3	2.1	1.2	0.3	0.6
2	88	5.5	2.2	0.9	< 0.2	0.6
3	90	5.1	2.1	0.6	< 0.2	0.6
4	90	5.3	2.2	0.7	0.3	0.6
5	90	5.5	2.2	0.4	< 0.2	0.6
6	90	5.4	2.1	0.4	< 0.2	0.5
7	89	5.4	2.1	0.3	< 0.2	0.9
8	90	5.6	2.0	0.6	0.6*	< 0.5
9	90	5.5	2.0	0.4	< 0.2	0.8
10	90	5.5	2.1	0.4	< 0.2	0.6
12	91	5.2	2.1	0.4	< 0.2	0.5
14	91	5.2	2.1	0.3	< 0.2	0.6
16	90	5.6	2.2	< 0.2	< 0.2	0.6
20	90	5.5	2.3	< 0.2	< 0.2	0.5
25	89	5.5	2.2	< 0.2	< 0.2	0.6
30	91	5.9	2.1	< 0.2	< 0.2	0.8
35	91	6.0	2.0	< 0.2	< 0.2	< 0.5
40	90	6.1	2.2	< 0.2	< 0.2	0.5
45	90	6.1	2.1	< 0.2	< 0.2	0.7
50	90	6.2	2.2	< 0.2	< 0.2	< 0.5
60	90	6.1	2.2	< 0.2	< 0.2	< 0.5
70	90	6.4	2.1	< 0.2	0.3	< 0.5
80	90	6.2	1.9	< 0.2	< 0.2	< 0.5
100	91	6.4	2.0	< 0.2	0.4*	0.6
125	91	6.9	2.0	< 0.2	< 0.2	< 0.5
150	90	6.9	2.1	< 0.2	< 0.2	< 0.5
175	90	7.1	1.8	< 0.2	< 0.2	< 0.5
200	91	7.0	2.2	< 0.2	< 0.2	< 0.5
225	91	7.2	2.0	< 0.2	< 0.2	< 0.5
250	91	7.1	1.9	< 0.2	< 0.2	< 0.5
275	90	7.1	1.8	< 0.2	< 0.2	< 0.5
300	91	7.1	1.8	< 0.2	< 0.2	< 0.5
350	91	7.2	1.8	< 0.2	< 0.2	< 0.5
400	91	7.1	1.7	< 0.2	< 0.2	< 0.5

* Occasional points of elevated oxygen concentration likely from contamination on specimen surface, and do not represent actual variations in composition.



Microprobe analysis:

B3W3 – B - Section 11 – 45 mils



DEFECT B3W3-B - METALLOGRAPHIC SECTION No. 11 -
TRANSVERSE PROFILE No. 1
ELECTRON MICROPROBE COMPOSITION MEASUREMENTS
Scanned perpendicular to long axis of defect with "zero" located at defect core.

	Weight %				
Distance (mils)	Ti	Al	V	C	N
50	87	7.4	1.9	0.2	< 0.5
45	88	7.3	1.8	< 0.2	< 0.5
40	88	7.1	1.8	0.2	< 0.5
35	90	7.2	1.9	0.2	< 0.5
30	93	7.0	1.8	0.2	< 0.5
25	92	6.9	2.2	0.2	< 0.5
20	92	6.8	1.8	0.2	< 0.5
16	93	6.5	2.0	0.2	< 0.5
12	91	6.5	2.2	0.2	< 0.5
10	93	5.8	1.8	0.2	0.5
8	93	6.1	2.1	0.2	< 0.5
6	93	6.1	2.4	0.2	0.9
5	92	5.8	2.3	0.2	0.7
4	93	4.8	1.7	0.2	1.2
3	93	1.9	1.9	0.8	2.3
2	94	0.2	2.1	0.5	3.8
1	93	0.2	2.1	0.8	3.8
0	94	0.3	2.0	1.3	4.1
-1	95	1.0	1.9	0.6	3.3
-2	93	3.6	1.8	1.1	1.9
-3	93	5.5	2.2	0.3	0.9
-4	92	6.2	2.6	0.2	0.8
-5	92	6.3	2.5	0.2	0.6
-6	92	6.2	2.2	0.2	0.9
-8	91	6.1	2.2	0.2	< 0.5
-10	90	5.8	1.8	0.3	0.6
-12	91	5.8	2.0	0.4	0.6
-16	93	6.7	2.2	0.3	< 0.5
-20	94	6.6	2.2	0.3	< 0.5
-25	93	6.9	2.2	0.3	< 0.5
-30	94	7.0	2.0	0.5	< 0.5
-35	92	6.8	1.9	0.6	< 0.5
-40	92	6.8	1.9	0.3	< 0.5
-45	95	7.3	1.9	0.3	< 0.5
-50	95	7.3	1.8	0.2	< 0.5

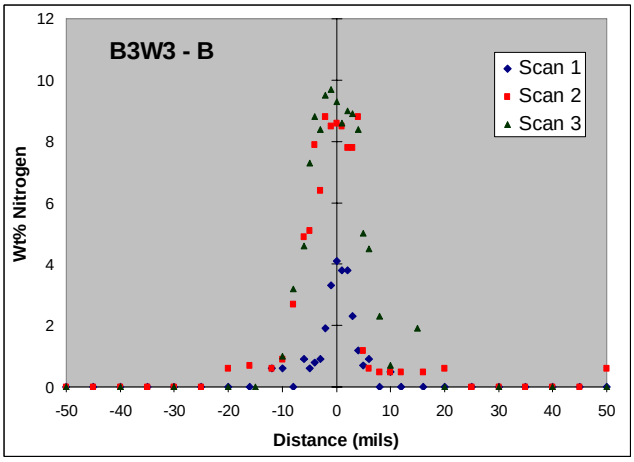
DEFECT B3W3-B - METALLOGRAPHIC SECTION No. 11 -
TRANSVERSE PROFILE No. 2
ELECTRON MICROPROBE COMPOSITION MEASUREMENTS
Scanned perpendicular to long axis of defect with "zero" located at defect core.

	Weight %				
Distance (mils)	Ti	Al	V	C	N
50	86	7.1	1.7	0.2	0.6
45	93	7.2	1.9	0.2	< 0.5
40	91	6.9	2.0	0.3	< 0.5
35	93	7.0	1.9	0.4	< 0.5
30	91	6.8	2.1	0.5	< 0.5
25	92	6.8	1.9	0.4	< 0.5
20	88	6.3	2.0	0.5	0.6
16	92	6.0	2.2	0.4	0.5
12	90	5.8	2.1	0.6	0.5
10	92	5.9	2.2	0.4	0.5
8	92	6.1	2.3	0.5	0.5
6	93	6.0	2.2	0.4	0.6
5	92	5.8	2.6	0.4	1.2
4	90	0.1	1.8	0.5	8.8
3	87	0.1	2.0	1.2	7.8
2	89	< 0.1	0.8	1.6	7.8
1	90	0.1	2.0	0.6	8.5
0	91	< 0.1	0.8	0.8	8.6
-1	91	< 0.1	1.0	0.4	8.5
-2	90	0.1	1.9	0.2	8.8
-3	91	0.2	2.5	0.4	6.4
-4	88	0.1	1.6	1.4	7.9
-5	93	0.5	2.2	0.4	5.1
-6	93	0.5	2.2	0.4	4.9
-8	93	3.1	1.7	0.9	2.7
-10	92	6.1	2.3	0.3	0.9
-12	92	6.1	2.4	0.2	0.6
-16	90	6.1	2.4	0.4	0.7
-20	90	5.8	2.0	0.3	0.6
-25	92	6.5	2.1	0.2	< 0.5
-30	91	6.9	2.0	0.3	< 0.5
-35	92	7.1	2.0	0.4	< 0.5
-40	91	7.2	1.9	0.2	< 0.5
-45	92	7.3	2.0	0.2	< 0.5
-50	93	7.3	1.8	0.2	< 0.5

Note: Shaded points were located in the visible core of the defect.

DEFECT B3W3-B - METALLOGRAPHIC SECTION No. 11 -
TRANSVERSE PROFILE No. 3
ELECTRON MICROPROBE COMPOSITION MEASUREMENTS
Scanned perpendicular to long axis of defect with "zero" located at defect core.

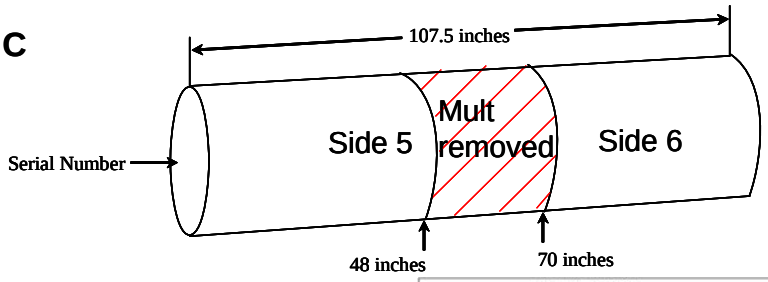
	Weight %				
Distance (mils)	Ti	Al	V	C	N
50	90	7.1	2.0	0.3	< 0.5
40	93	6.8	2.1	0.3	< 0.5
30	93	6.5	2.0	0.4	< 0.5
20	92	6.1	2.1	0.4	< 0.5
15	93	3.2	2.0	1.1	1.9
10	93	5.5	2.1	0.5	0.7
8	93	4.0	1.9	0.9	2.3
6	86	1.0	2.3	0.7	4.5
5	88	0.6	5.4	1.2	5.0
4	91	0.1	1.6	0.6	8.4
3	89	0.1	1.9	0.4	8.9
2	88	0.1	1.9	0.6	9.0
1	88	0.1	2.2	0.6	8.6
0	90	0.1	2.1	0.5	9.3
-1	89	0.1	2.0	0.4	9.7
-2	88	0.1	2.3	0.5	9.5
-3	87	0.2	3.2	0.4	8.4
-4	88	0.1	1.6	0.5	8.8
-5	92	0.2	1.9	0.8	7.3
-6	94	0.2	2.1	0.4	4.6
-8	96	0.7	2.0	0.5	3.2
-10	94	5.3	2.1	0.4	1.0
-15	90	6.3	2.2	0.2	< 0.5
-20	93	6.9	1.8	0.2	< 0.5
-30	92	7.2	1.6	0.2	< 0.5
-40	88	7.2	1.7	0.2	< 0.5
-50	92	7.4	1.7	0.2	< 0.5



Note: Shaded points were located in the visible core of the defect.

Indication: B1BW3 – C

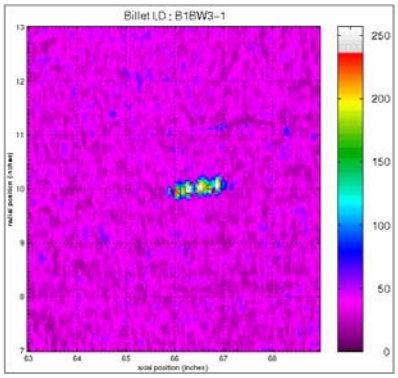
Original billet length: 107.5”



Billet inspection:

	Amplitude (%)	S/N	depth (in)	axial length (in)	radial length (in)
Multizone	127%	6.67	0.5	1.4474	0.2301
Conv. Longitudinal	%				
Conv. Angle	%				

Zone 1



Mult inspection parameters:

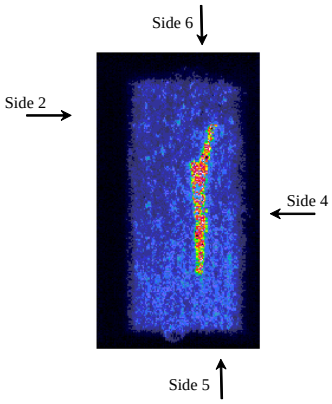
Transducer - Zone 1, 6” diameter, 5MHz
Index - 0.010
Data Acquisition Rate - 0.010
Inspection Sensitivity - #2 FBH at 80-90% in Titanium
Inspection Range - 0.2” to 0.8”
Sampling Rate - 100 MHz

Depth	Axial Length	Amplitude	Signal-to-Noise Ratio
0.5”	1.5”	127%	6.7

25 MHz inspection parameters

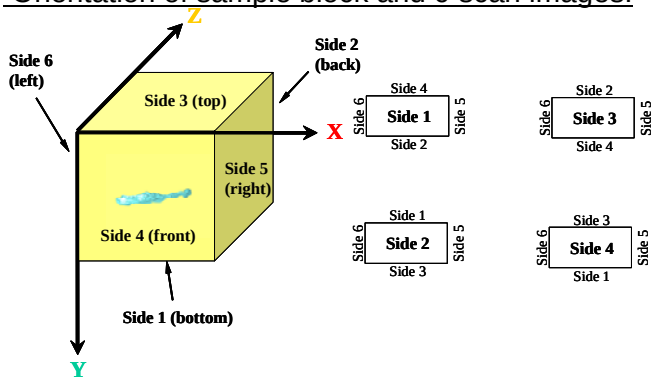
Transducer - 25 MHz, F10 - focal point positioned at indication depth
Index - 0.010
Data Acquisition Rate - 0.010
Inspection sensitivity - #1 FBH at 83% - 56 dB #2FBH at 84% at 48dB
Inspection range - C-scan , Between Front and Back / B-scan entire volume
Sampling Rate - 200 MHz

Side	Depth	Axial Length	Amplitude %	Sensitivity, dB
1	0.304”	1.5”	70	65
2	0.465”	1.5”	89	65
3	0.447”	1.5”	81	65
4	0.448”	1.5”	56	56
5	0.595”	1.5”	51	69
6	0.493”	1.5”	90	67



View is from Side 1(side which was polished). Sides 5 and 6 represent the axial ends as shown above. Sides 2 and 4 represent the hoop direction (circumferential plane.)

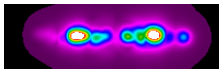
Orientation of sample block and c-scan images:



B1BW3-C 5 MHz C-scan image comparisons:

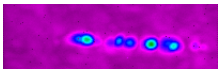
Side 1

Model



Attenuation=6dB
peak amplitude =1316 mv
deviation=100% or 6.01 dB

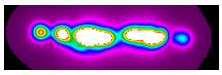
Experiment



Attenuation= 6 dB
peak amplitude= 659mv

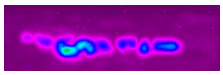
Side 2

Model



Attenuation=14dB
peak amplitude= 2675mv
deviation=329% or 12.64 dB

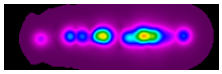
Experiment



Attenuation=14dB
peak amplitude= 624mv

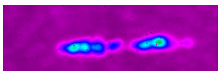
Side 3

Model



Attenuation=8dB
peak amplitude=902 mv
Deviation=45% or 3.26 dB

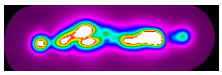
Experiment



Attenuation=8dB
peak amplitude= 620mv

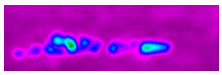
Side 4

Model



Attenuation=12dB
peak amplitude=1901 mv
deviation=187% or 9.15 dB

Experiment

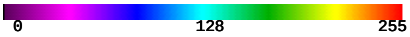


Attenuation=12dB
peak amplitude= 663mv

Experiment image: 201(H) x 61(V) @10 mils

Model image: 201(H) x 61(V) @10 mils

Multizone Color Code



Experiment 255 = 1000mv

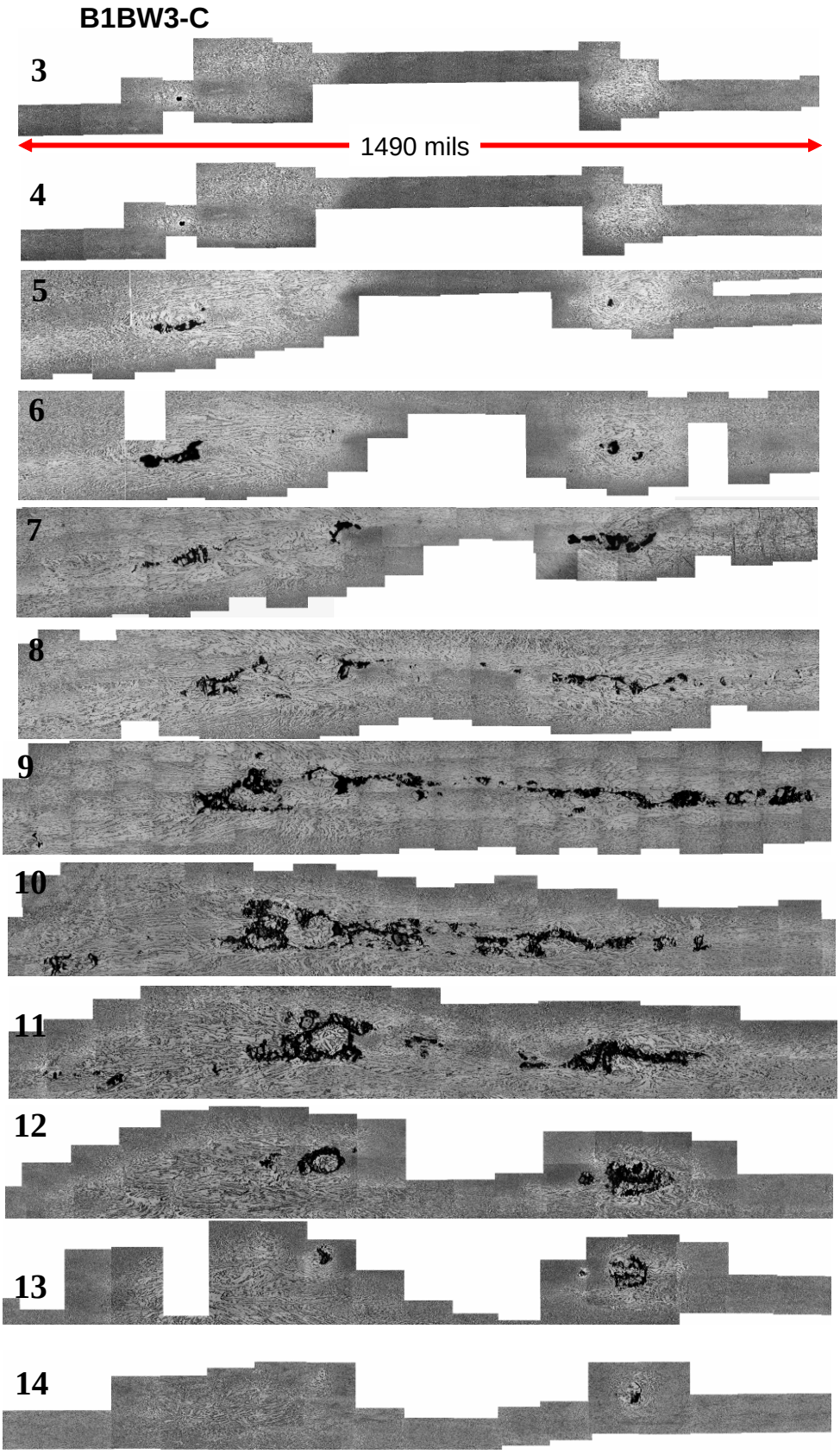
B1BW3-C 3D Solid Model Parameters:

Sub-Micrograph

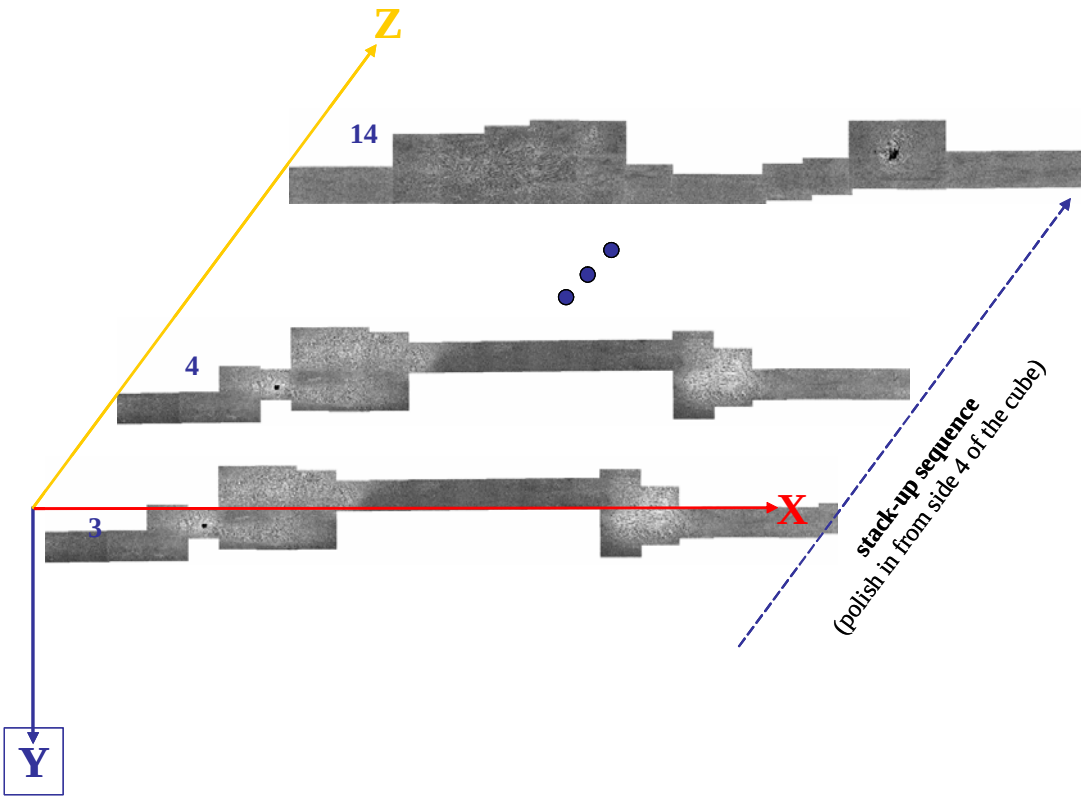
size - 12300(H) by 1700(V) pixels
color - 256 gray-scale of size
scale – 82.6 pixels =10 mils

Geometric Model

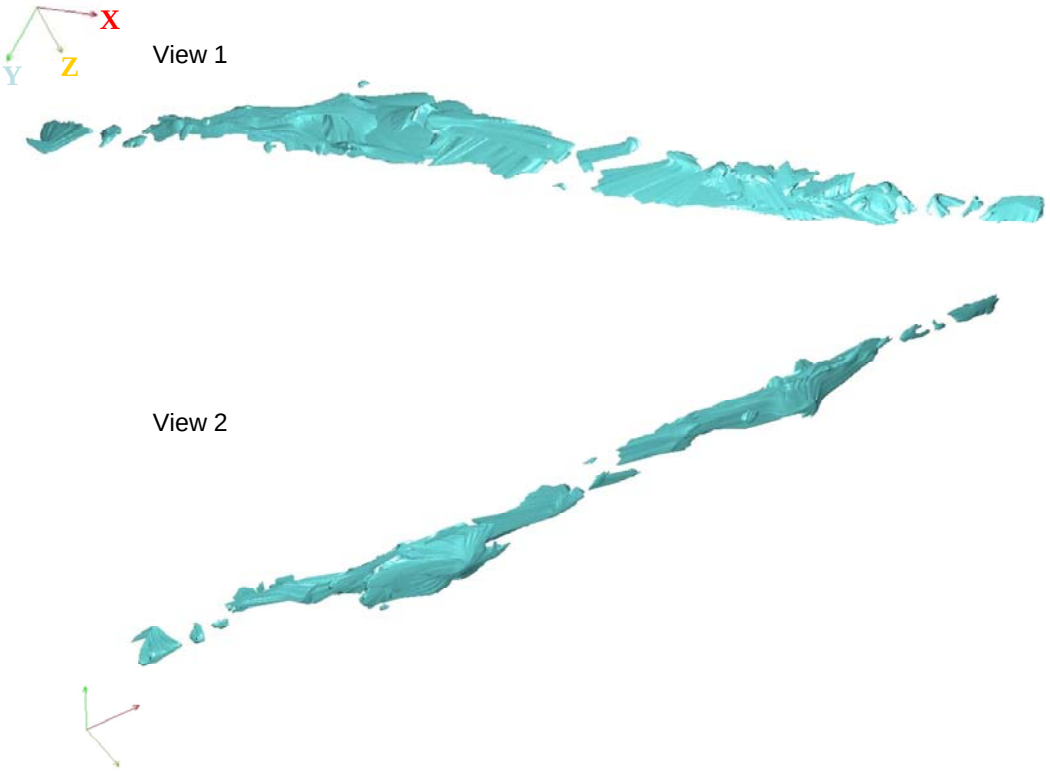
13 void flaw part (with branches)
42 geometric model parts
23 micrograph planes (including 8 patches)
168 void cross-section boundary traces
(model part 7, 8 and 9 use 7;
14, 29 and 39 use 6;
6, 10, 15, 18, 19, 34, 38 use 5;
16, 17, 23, 24, 25, 31, 32 use 4;
the rest use 3 each)


B1BW3-C
3
1490 mils
4
5
6
7
8
9
10
11
12
13
14

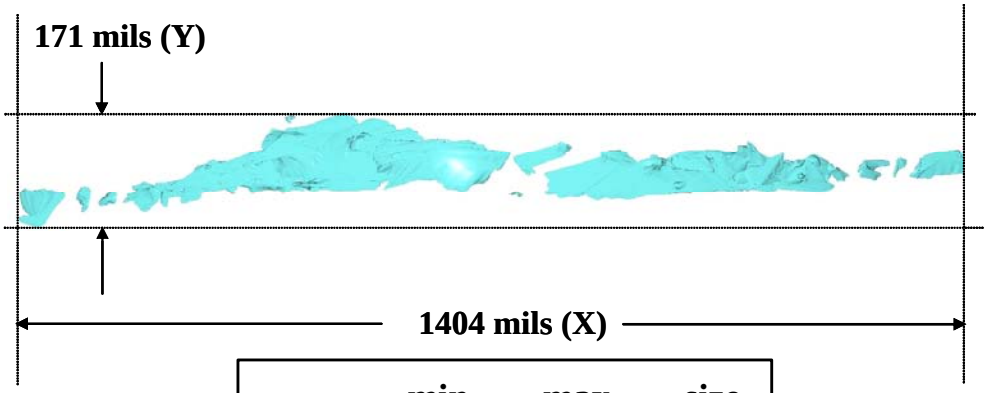
Orientation of Sub-Micrographs (B1BW3-C):



Angle views of void model for B1BW3-C:



Dimensions of B1BW3-C:

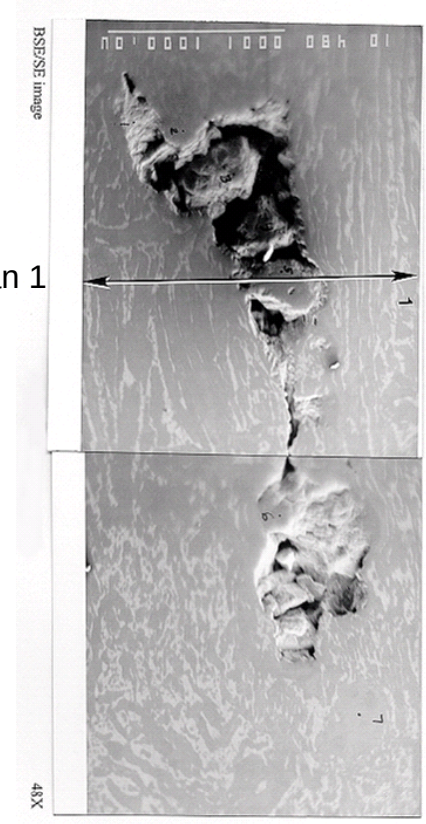


	min.	max.	size
X	55	1459	1404
Y	19	190	171
Z	9	68	59

Unit: mils

Microprobe analysis:

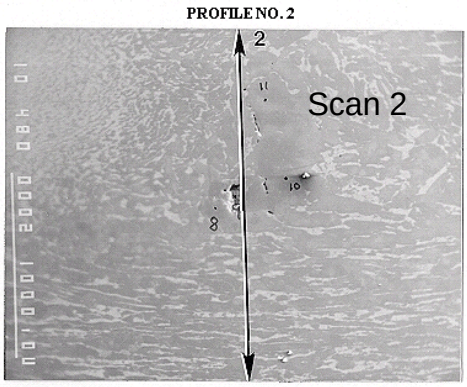
B1BW3 – C - Section 6 – 20 mils



			W %		
Distance (mils)	Ti	Al	V	C	N
40	90	6.2	2.1	< 0.2	0.6
30	92	6.3	2.2	< 0.2	0.8
25	91	6.2	2.1	0.2	0.8
20	92	5.9	2.1	< 0.2	0.5
16	89	5.9	2.2	< 0.2	1.3
14	93	4.8	2	< 0.2	0.9
12	92	5.3	2.2	< 0.2	1.2
10	90	5.2	2	0.3	1.6
8	92	2.6	1.8	< 0.2	1.5
6	91	0.2	2.2	0.4	5.2
5	91	0.2	2.4	0.3	5.4
4	89	0.6	2.2	0.3	5.0
3	89	0.4	2.4	0.4	7.7
2	89	0.1	1.6	0.4	8.7
1	89	< 0.1	1.2	0.6	9.7
0	90	< 0.1	1	< 0.2	8.4
-1	86	0.2	1.5	1.1	8.4
-2	87	0.4	3.2	0.9	8.6
-3	88	0.1	1.2	0.4	8.6
-4	88	0.2	2.3	0.3	7.4
-5	88	0.4	2.4	0.3	5.4
-6	89	0.3	2.1	1.8	6.8
-8	79	1.9	1.3	0.9	2.9
-10	88	5.2	2.2	< 0.2	1.7
-12	90	5.6	2.3	< 0.2	1.5
-14	90	5.5	2.1	< 0.2	1.0
-16	93	5.7	1.8	< 0.2	0.6
-20	92	6.3	2.1	< 0.2	0.5
-25	92	6.3	1.9	< 0.2	< 0.5
-30	92	6.8	2	< 0.2	1.0
-40	91	7	2	< 0.2	0.5

Microprobe analysis:

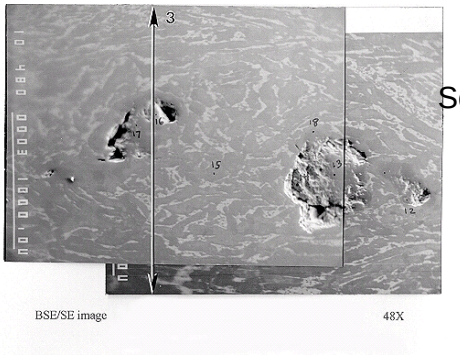
B1BW3 – C - Section 6 – 20 mils



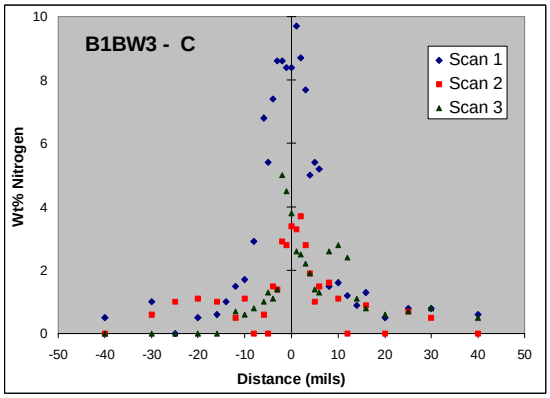
			W %		
Distance (mils)	Ti	Al	V	C	N
40	91	7	2.1	< 0.2	< 0.5
30	90	6.8	1.9	< 0.2	0.5
25	90	6.6	2.3	< 0.2	0.7
20	91	6.3	2.1	< 0.2	< 0.5
16	92	6.4	2.3	< 0.2	0.9
12	92	6.1	2.3	< 0.2	< 0.5
10	90	5.2	2	< 0.2	1.1
8	92	5.3	2	0.3	1.6
6	91	5.6	2.1	< 0.2	1.5
5	91	5.6	2.2	0.2	1.0
4	91	4.6	1.9	0.2	1.9
3	92	2.7	1.8	< 0.2	2.8
2	93	1.4	1.8	0.3	3.7
1	92	0.8	2.1	0.6	3.3
0	94	0.2	1.9	0.5	3.4
-1	93	0.2	2	0.4	2.8
-2	92	0.3	1.7	0.2	2.9
-3	90	5.9	2.7	0.3	1.4
-4	90	5.7	2.6	0.2	1.5
-5	91	6	2.4	< 0.2	< 0.5
-6	90	6	2.1	< 0.2	0.6
-8	92	6.1	1.3	< 0.2	< 0.5
-10	90	6.1	2.2	< 0.2	1.1
-12	92	6.3	2.3	< 0.2	0.5
-16	89	6.1	1.8	< 0.2	1.0
-20	91	6	2.1	< 0.2	1.1
-25	90	6	1.9	< 0.2	1.0
-30	92	5.8	2	< 0.2	0.6
-40	90	7.1	2	< 0.2	< 0.5

Microprobe analysis:

B1BW3 – C - Section 6 – 20 mils



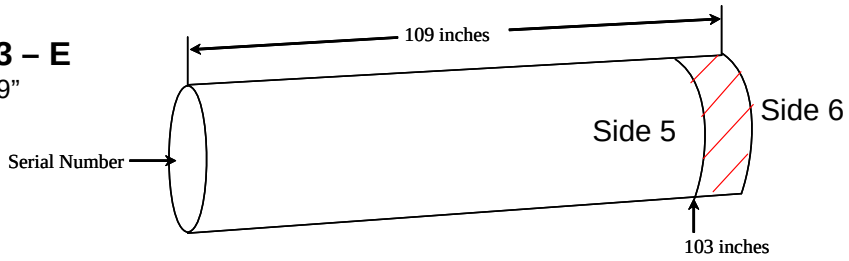
Scan 3



	W %				
Distance (mils)	Ti	Al	V	C	N
40	92	5.7	2.3	< 0.2	0.5
30	92	6.1	2.3	0.2	0.8
25	92	6.3	2.1	0.2	0.7
20	89	6.3	2.1	0.2	0.6
16	88	6.4	2.2	0.2	0.8
14	86	6.1	2.4	0.3	1.1
12	88	4.8	1.9	0.4	2.4
10	91	1.3	1.5	0.3	2.8
8	93	3	2.1	0.3	2.6
6	89	6.3	3	0.3	1.3
5	92	5	2.2	0.4	1.4
4	89	3.8	2.1	0.5	1.9
3	92	3.4	2.2	0.3	2.2
2	88	2.7	2.1	0.4	2.5
1	88	1.2	2.1	0.8	2.6
0	93	0.2	2.4	0.7	3.8
-1	93	0.2	2.2	0.5	4.5
-2	91	0.3	3.1	0.9	5.0
-3	93	0.5	1.5	0.8	1.4
-4	92	2.1	1.7	0.7	1.1
-5	93	5.8	2.2	0.3	1.3
-6	88	6.3	2.3	0.2	1.0
-8	91	6.7	2.4	0.3	0.8
-10	90	6.6	2.1	0.3	0.6
-12	91	6.7	2.2	< 0.2	0.7
-16	91	6.8	2.2	< 0.2	< 0.5
-20	91	7	2.3	< 0.2	< 0.5
-25	89	7.1	2.1	< 0.2	< 0.5
-30	91	7.2	2.2	< 0.2	< 0.5
-40	88	7.5	2.1	< 0.2	< 0.5

Indication: B1AW3 – E

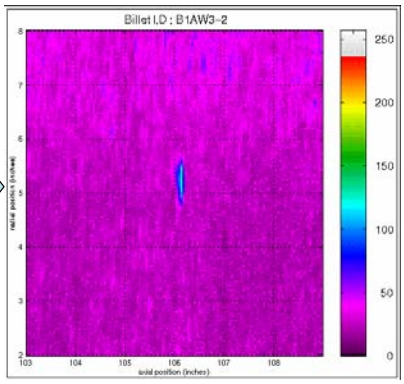
Original billet length: 109”



Billet inspection:

	Amplitude (%)	S/N	depth (in)	axial length (in)	radial length (in)
Multizone	47	2.52	1.6	.1860	.4123
Conv. Longitudinal					
Conv. Angle					

Zone 3



Mult inspection parameters:

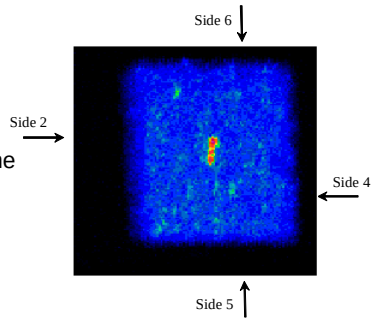
Transducer - Zone 3, 6” diameter, 5MHz
Index - 0.010
Data Acquisition Rate - 0.010
Inspection Sensitivity - #2 FBH at 80-90% in Titanium
Inspection Range - 1.7” - 2.6”
Sampling Rate - 100 MHz

Depth	Axial Length	Amplitude	Signal-to-Noise Ratio
1.725”	0.283”	47%	2.52

25 MHz inspection parameters

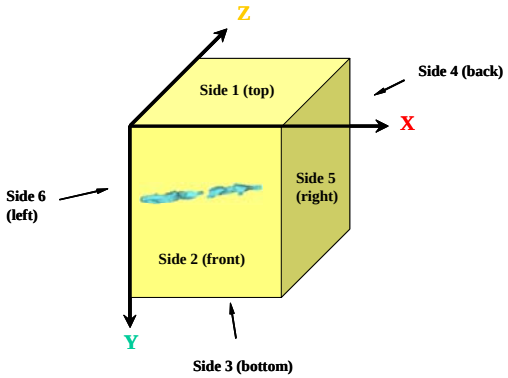
Transducer - 25 MHz, F10 - focal point positioned at indication depth
Index - 0.010
Data Acquisition Rate - 0.010
Inspection sensitivity - #1 FBH at 83% - 56 dB #2FBH at 84% at 48dB
Inspection range - C-scan , Between Front and Back / B-scan entire volume
Sampling Rate - 200 MHz

Side	Depth	Axial Length	Amplitude %	Sensitivity, dB
1	406.6”	0.283	80	75
2	520.3”	0.283	25	79
3	386.0”	0.283	86	67
4	525.1”	0.283	19	79
5	519.1”	0.283	83	68
6	500.4”	0.283	82	66



View is from Side 1(side which was polished). Sides 5 and 6 represent the axial ends as shown above. Sides 2 and 4 represent the hoop direction (circumferential plane.)

Orientation of sample block and c-scan images:



B1AW3-E 5 MHz C-scan image comparisons:

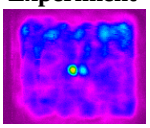
Side 1

Model



41(H) x 31(V) @10 mils, 14dB
peak amplitude @14dB=94 mv
deviation=-15% or -1.4 dB

Experiment



150(H) x 120(V) @10 mils, 14dB
peak amplitude @14dB=110 mv

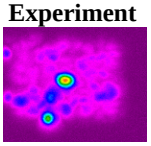
Side 2

Model



41(H) x 31(V) @10 mils, 16dB
peak amplitude @16dB=83 mv
deviation=-27% or -2.7 dB

Experiment



150(H) x 120(V) @10 mils, 16dB
peak amplitude @16dB=113 mv

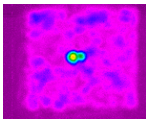
Side 3

Model



41(H) x 31(V) @10 mils, 14dB
peak amplitude @14dB=89 mv
deviation=-14% or -1.4 dB

Experiment



150(H) x 120(V) @10 mils, 14dB
peak amplitude @14dB=104 mv

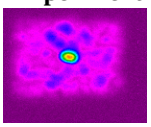
Side 4

Model



41(H) x 31(V) @10 mils, 16dB
peak amplitude @16dB=77 mv
deviation=-31% or -3.2 dB

Experiment



150(H) x 120(V) @10 mils, 16dB
peak amplitude @0dB=112 mv

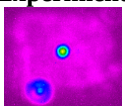
Side 5

Model



41(H) x 31(V) @10 mils, 2dB
peak amplitude@2dB = 36 mv
deviation=-63% or -8.6 dB

Experiment



120(H) x 100(V) @10 mils, 2dB
peak amplitude@2dB = 97 mv

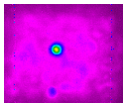
Side 6

Model

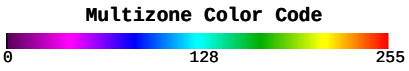


41(H) x 31(V) @10 mils, 0dB
peak amplitude@0dB = 45 mv
deviation=-51% or -6.1 dB

Experiment



100(H) x 30(V) @10 mils, 0dB
peak amplitude@0dB = 92 mv

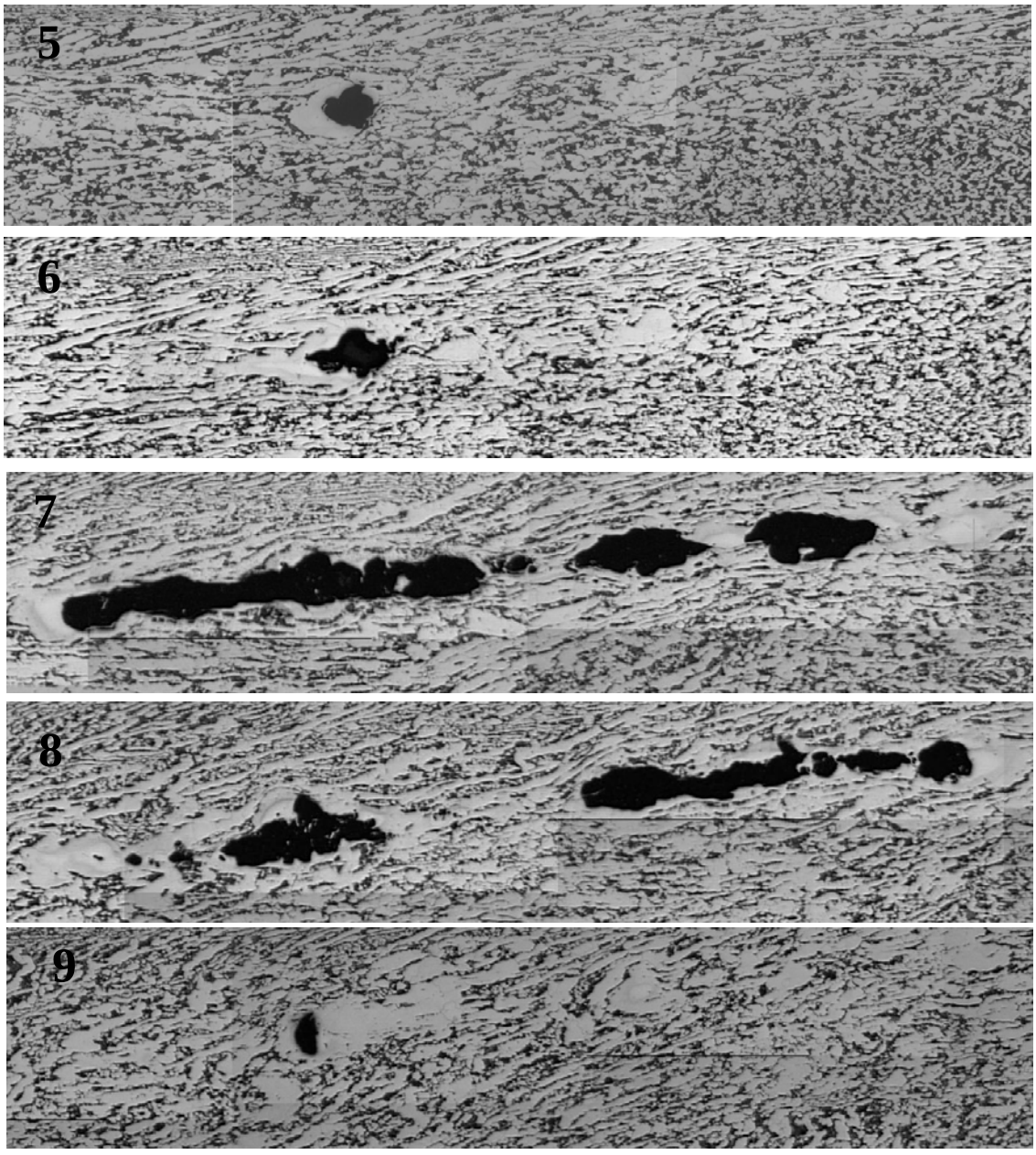


Experiment 255 = 125mv

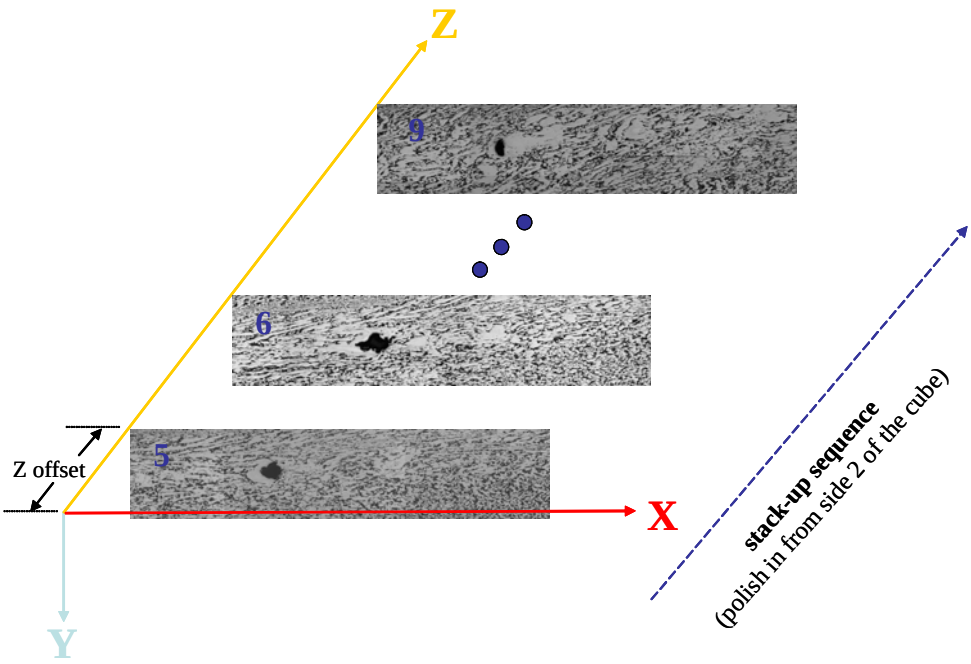
B1AW3-E 3D Solid Model Parameters:

Geometric Model
- 2 void part
  - (with branches)
- 8 geometric model parts
- 13 micrograph planes
  - (including 8 patches)
- 35 void cross-section boundary traces
  - (model part 1 uses 8 traces,
    2, 3 &8 use 5,
    and the rest use 3 each)

B1AW3-E

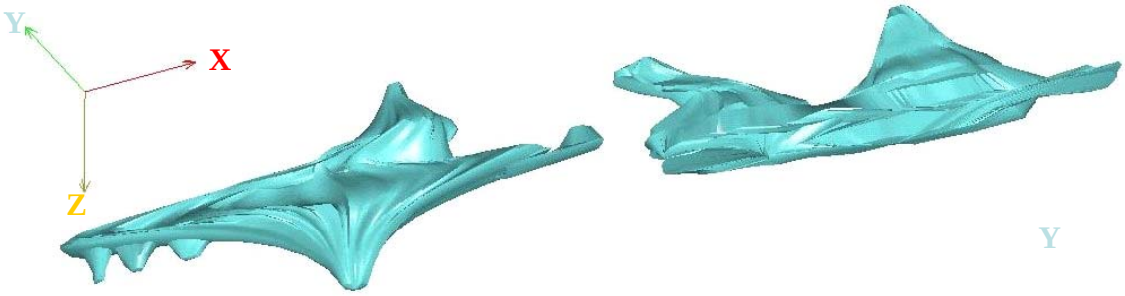


Orientation of Sub-Micrographs (B1AW3-E):

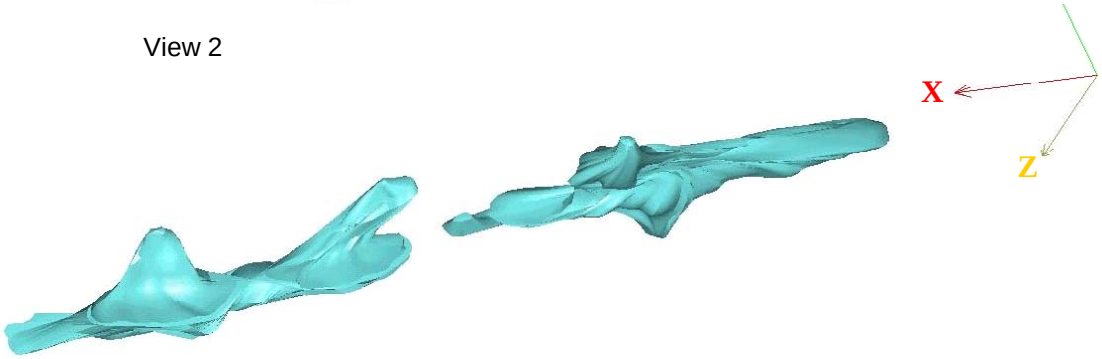


Angle views of void model for B1AW3-E:

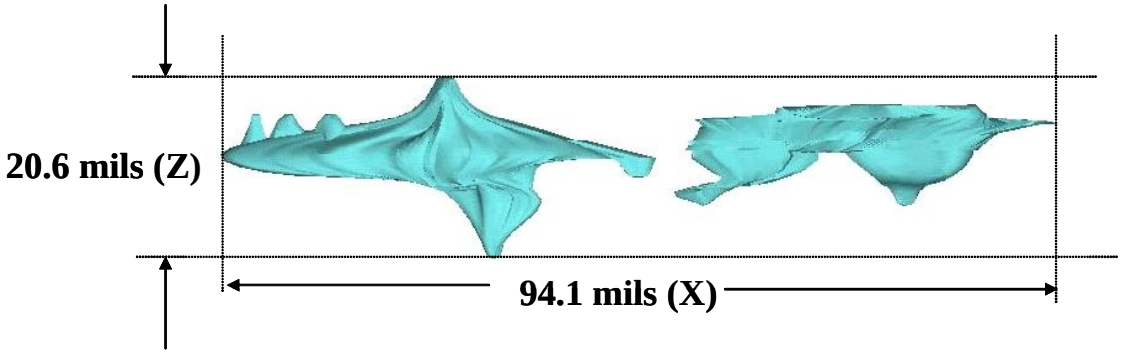
View 1



View 2



Dimensions of B1AW3-E:

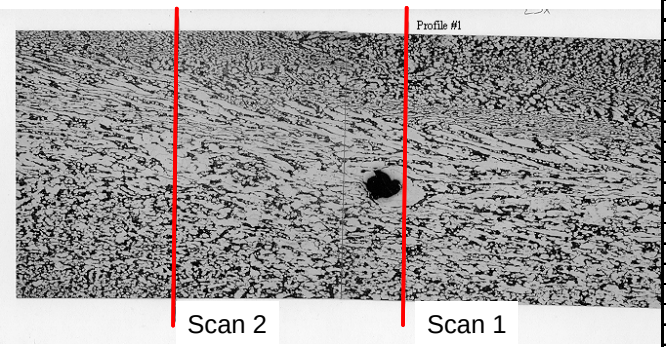


	min.	max.	size
X	5.49	99.57	94.08
Y	2.47	18.23	15.76
Z	16.70	37.30	20.60

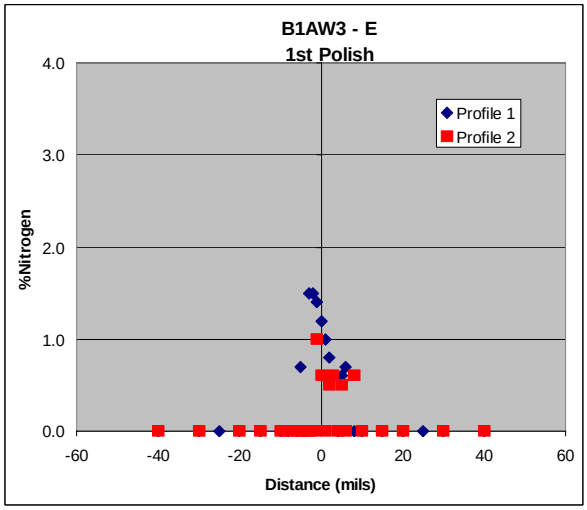
Unit: mils

Microprobe analysis:

B1AW3 – E - Section 5 – 20 mils



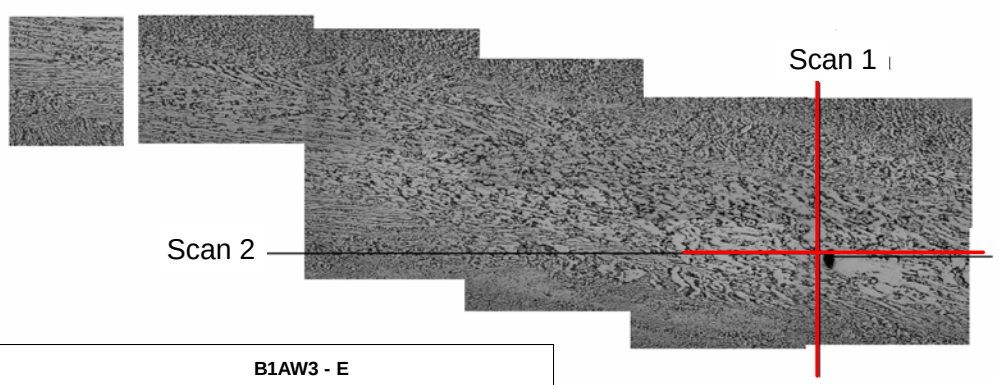
Profile #1 - Section 5					
			W %		
Distance (mils)	Ti	Al	V	C	N
40	91	7.5	1.6	< 0.2	< 0.5
30	89	7.5	1.8	< 0.2	< 0.5
25	90	7.5	2.2	< 0.2	< 0.5
20	90	7.2	1.8	< 0.2	< 0.5
15	90	7.2	2	< 0.2	< 0.5
10	92	6.7	1.8	< 0.2	< 0.5
8	92	6.3	2.1	< 0.2	< 0.5
6	92	6.3	2.4	< 0.2	0.7
5	91	5.9	2.3	< 0.2	0.6
4	92	5.3	1.7	< 0.2	< 0.5
3	93	5.6	1.9	< 0.2	0.6
2	92	5	2.1	< 0.2	0.8
1	95	4.3	2.1	0.2	1.0
0	94	3.4	1.5	0.2	1.2
-1	94	2.3	1.9	0.3	1.4
-2	96	1.7	1.8	0.7	1.5
-3	95	2.2	2.2	0.3	1.5
-4	94	4.8	2.6	< 0.2	< 0.5
-5	92	5.6	2.5	< 0.2	0.7
-6	93	5.9	2.2	< 0.2	< 0.5
-8	91	6.6	2.2	< 0.2	< 0.5
-10	93	6.8	1.8	< 0.2	< 0.5
-15	92	6.8	2	< 0.2	< 0.5
-20	92	7.1	2.2	< 0.2	< 0.5
-25	93	7.1	2.2	< 0.2	< 0.5
-30	93	7	2	< 0.2	< 0.5
-40	92	7.3	1.9	< 0.2	< 0.5

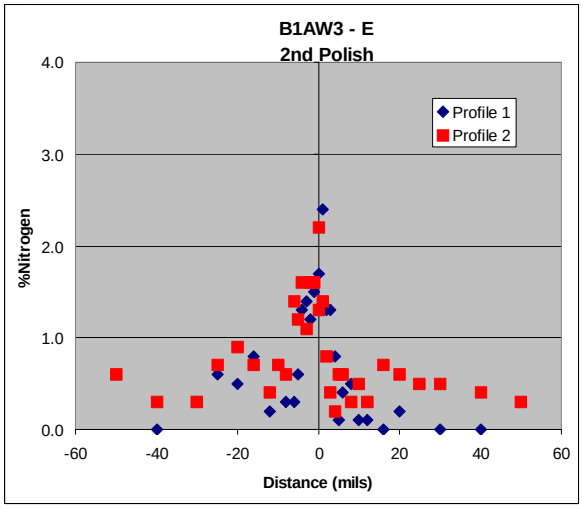


Profile #2 - Section 5					
			W %		
Distance (mils)	Ti	Al	V	C	N
40	86	7.1	1.7	< 0.2	< 0.5
30	93	7.2	1.9	< 0.2	< 0.5
20	91	6.9	2	< 0.2	< 0.5
15	93	7	1.9	< 0.2	< 0.5
10	91	6.8	2.1	< 0.2	< 0.5
8	92	6.8	1.9	< 0.2	0.6
6	88	6.3	2	< 0.2	< 0.5
5	92	6	2.2	< 0.2	0.5
4	90	5.8	2.1	< 0.2	< 0.5
3	92	5.9	2.2	0.2	0.6
2	92	6.1	2.3	0.3	0.5
1	93	6	2.2	0.3	< 0.5
0	92	5.8	2.6	0.3	0.6
-1	90	0.1	1.8	< 0.2	1.0
-2	87	0.1	2	< 0.2	< 0.5
-3	89	< 0.1	0.8	< 0.2	< 0.5
-4	90	0.1	2	< 0.2	< 0.5
-5	91	< 0.1	0.8	< 0.2	< 0.5
-6	91	< 0.1	1	< 0.2	< 0.5
-8	90	0.1	1.9	< 0.2	< 0.5
-10	91	0.2	2.5	< 0.2	< 0.5
-15	88	0.1	1.6	< 0.2	< 0.5
-20	93	0.5	2.2	< 0.2	< 0.5
-30	93	0.5	2.2	< 0.2	< 0.5
-40	93	3.1	1.7	< 0.2	< 0.5

Microprobe analysis:

B1AW3 – E - Section 10 – 31 mils





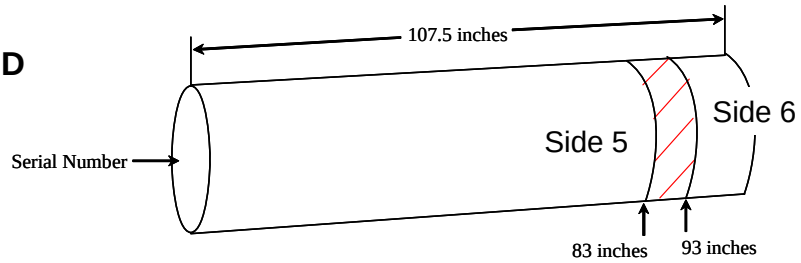
Profile #1 - Section 10					
			W %		
Distance (mils)	Ti	Al	V	C	N
40	91	7.2	2	< 0.2	< 0.5
30	89	7.2	1.7	< 0.2	< 0.5
20	91	7.2	1.6	< 0.2	< 0.5
16	89	7	1.8	< 0.2	< 0.5
12	90	7.1	1.7	< 0.2	< 0.5
10	90	7	1.7	< 0.2	< 0.5
8	90	6.8	1.7	< 0.2	0.5
6	89	6.7	1.8	< 0.2	< 0.5
5	89	6.3	2	0.2	< 0.5
4	89	6	1.9	0.3	0.8
3	89	5.7	2	0.4	1.3
2	89	4.8	2.1	0.5	1.3
1	91	3.5	1.8	0.6	2.4
0	91	3.2	1.8	0.7	1.7
-1	92	3.6	1.5	0.8	1.5
-2	92	4.4	1.8	0.5	1.2
-3	91	4.2	1.6	0.4	1.4
-4	89	5.4	1.9	0.2	1.3
-5	91	6	1.9	< 0.2	0.6
-6	88	6.2	1.9	< 0.2	< 0.5
-8	92	6.3	1.6	0.2	< 0.5
-10	89	6.4	1.9	< 0.2	0.7
-12	92	6.7	1.9	< 0.2	< 0.5
-16	89	6.8	1.8	< 0.2	0.8
-20	91	6.8	1.8	< 0.2	0.5
-25	89	7	1.9	< 0.2	0.6
-30	88	7.1	1.8	< 0.2	< 0.5
-40	88	7.1	1.8	< 0.2	< 0.5

Profile #2 - Section 10 →					
			W %		
Distance (mils)	Ti	Al	V	C	N
0	90	3.3	1.7	1.0	2.2
1	89	4.4	1.9	1.0	1.4
2	88	5.3	1.9	0.5	0.8
3	90	6	2.1	0.3	< 0.5
4	87	5.2	4.7	0.4	< 0.5
5	89	6.2	1.9	0.3	0.6
6	89	6.3	1.9	< 0.2	0.6
8	90	6.3	1.9	< 0.2	< 0.5
10	87	6.3	1.8	0.4	0.5
12	90	6.2	1.8	0.4	< 0.5
16	88	6.4	1.9	< 0.2	0.7
20	90	6.4	2	< 0.2	0.6
25	90	6.5	2	< 0.2	0.5
30	91	6.6	2	< 0.2	0.5
40	90	6.5	1.8	< 0.2	< 0.5
50	87	6.6	1.9	< 0.2	< 0.5

← Profile #2 - Section 10					
			W %		
Distance (mils)	Ti	Al	V	C	N
0	89	2.6	1.6	0.9	1.3
1	91	2.6	1.6	0.3	1.6
2	89	3.9	1.9	0.3	1.6
3	89	5.4	1.8	0.4	1.1
4	88	5.2	1.7	0.3	1.6
5	90	5.7	2.3	0.2	1.2
6	88	5.8	1.9	0.2	1.4
8	90	5.8	1.9	0.2	0.6
10	87	6	1.8	0.2	0.7
12	91	6.1	1.9	< 0.2	< 0.5
16	91	6.3	1.9	< 0.2	0.7
20	90	6.4	1.9	< 0.2	0.9
25	90	6.5	2	< 0.2	0.7
30	91	6.2	1.9	< 0.2	< 0.5
40	91	6.4	1.9	< 0.2	< 0.5
50	91	6.2	1.9	< 0.2	0.6

Indication: B1BW3 – D

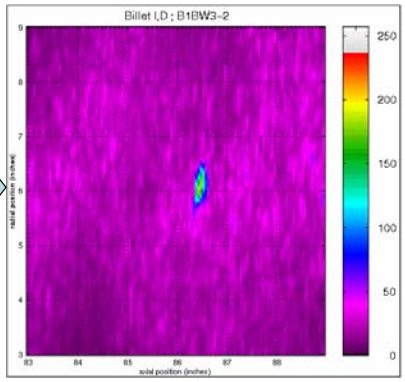
Original billet length: 107.5”



Billet inspection:

	Amplitude (%)	S/N	depth (in)	axial length (in)	radial length (in)
Multizone	74%	5.06	1.5	0.3268	0.2577
Conv. Longitudinal	%				
Conv. Angle	%				

Zone 2



Mult inspection parameters:

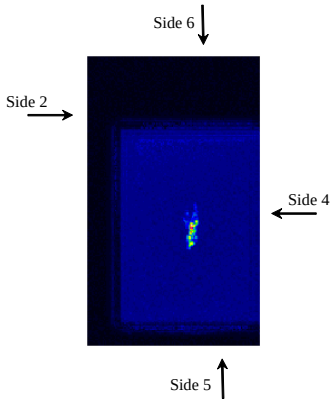
Transducer - Zone 2, 6” diameter, 5MHz
Index - 0.010
Data Acquisition Rate - 0.010
Inspection Sensitivity - #2 FBH at 80-90% in Titanium
Inspection Range - 0.8” to 1.7”
Sampling Rate - 100 MHz

Depth	Axial Length	Amplitude	Signal-to-Noise Ratio
1.5”	0.365”	74%	5.06

25 MHz inspection parameters:

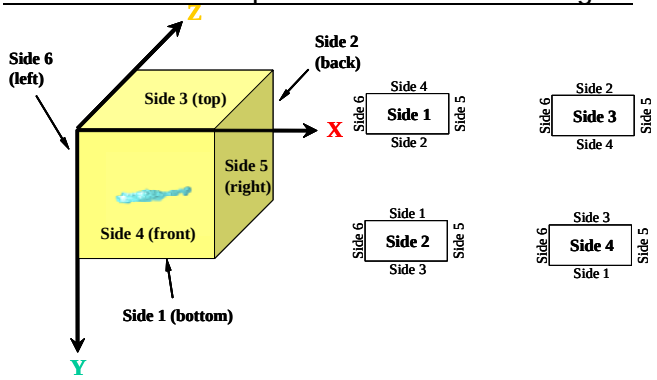
Transducer - 25 MHz, F10 - focal point positioned at indication depth
Index - 0.010
Data Acquisition Rate - 0.010
Inspection sensitivity - #1 FBH at 83% - 56 dB #2FBH at 84% at 48dB
Inspection range - C-scan , Between Front and Back / B-scan entire volume
Sampling Rate - 200 MHz

Side	Depth	Axial Length	Amplitude %	Sensitivity, dB
1	0.484”	0.365”	85	53
2	0.530”	0.365”	80	49
3	0.508”	0.365”	70	54
4	0.508”	0.365”	84	55
5	0.530”	0.365”	78	68
6	0.530”	0.365”	76	73



View is from Side 1(side which was polished). Sides 5 and 6 represent the axial ends as shown above. Sides 2 and 4 represent the hoop direction (circumferential plane.)

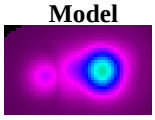
Orientation of sample block and c-scan images:



B1BW3-D 5 MHz C-scan image comparisons:

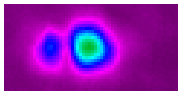
Side 2

Model



51(H) x 31(V) @10 mils, 14dB
peak amplitude @14dB=280 mv
deviation=-11.4% or -1.1 dB

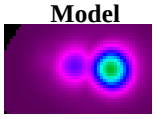
Experiment



60(H) x 30(V) @10 mils, 14dB
peak amplitude @14dB=316 mv

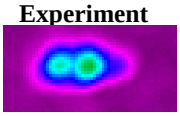
Side 4

Model



51(H) x 31(V) @10 mils, 16dB
peak amplitude @10dB=646 mv
deviation=105.7% or 6.3 dB

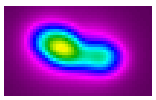
Experiment



60(H) x 30(V) @10 mils, 10dB
peak amplitude @10dB=314 mv

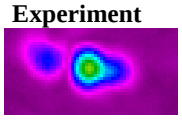
Side 1

Model



51(H) x 31(V) @10 mils, 22dB
peak amplitude @12dB=1263 mv
deviation=244.1% or 10.7 dB

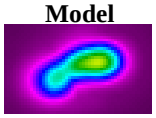
Experiment



60(H) x 30(V) @10 mils, 12dB
peak amplitude @12dB=367 mv

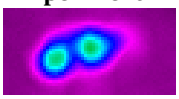
Side 3

Model

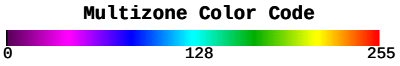


51(H) x 31(V) @10 mils, 18dB
peak amplitude @12dB=793 mv
deviation=160% or 8.3 dB

Experiment



60(H) x 30(V) @10 mils, 12dB
peak amplitude @12dB=305 mv



Experiment 255 = 500mv

B1BW3-D 3D Solid Model Parameters:

Summary:

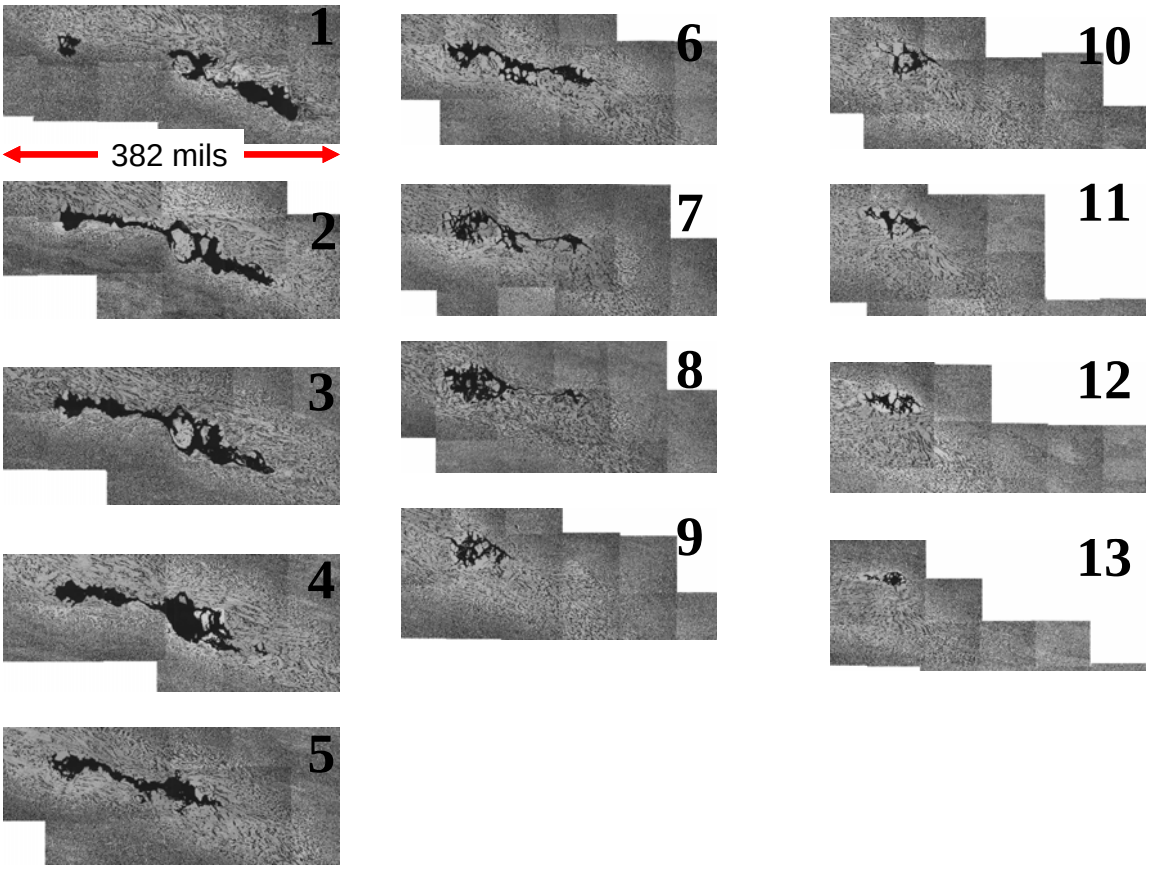
Sub-Micrograph

size - 2400(H) by 1000(V) pixels
color - 256 gray-scale
scale - 4340 pixels =690 mils

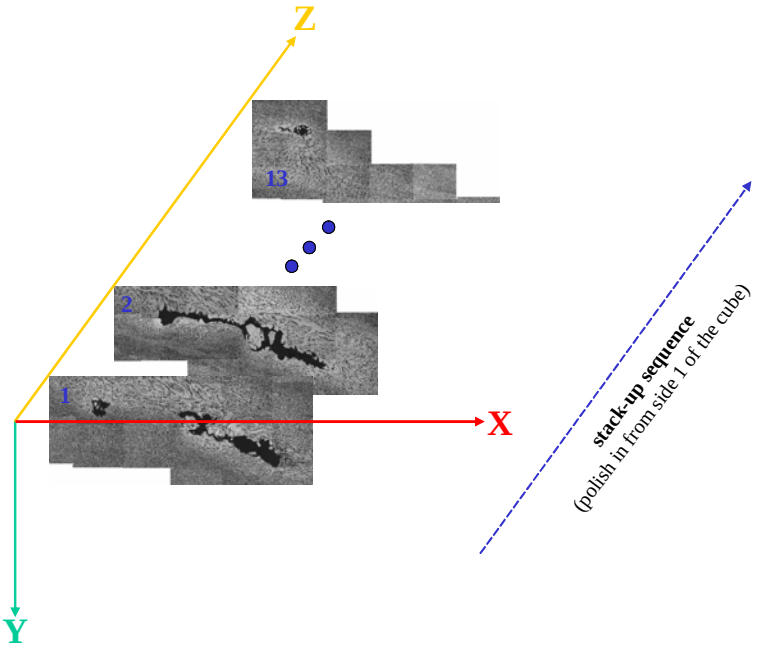
Geometric Model

1 void part
(with branches)
8 geometric model parts
21 micrograph planes
(including 8 patches)
33 void cross-section boundary traces
(model parts 5 and 8 uses 7 traces, 3 uses 4, and the rest use 3 each)

B1BW3-D

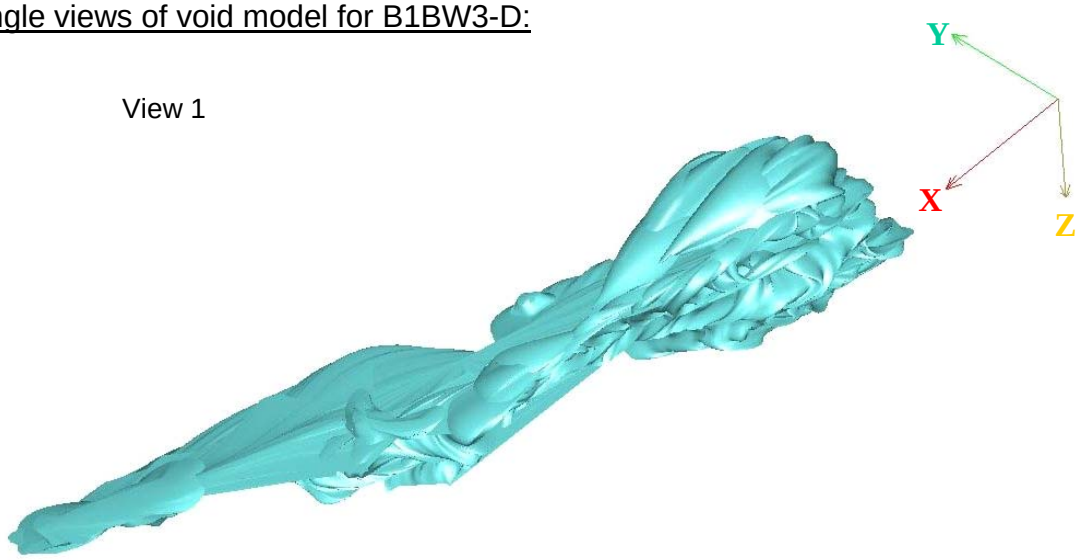


Orientation of Sub-Micrographs (B1BW3-D):

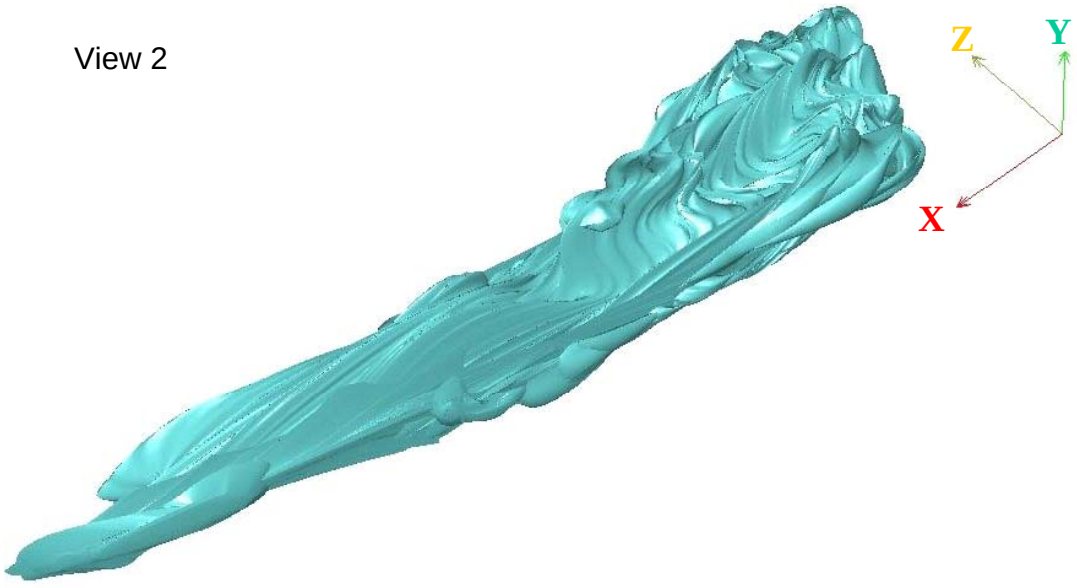


Angle views of void model for B1BW3-D:

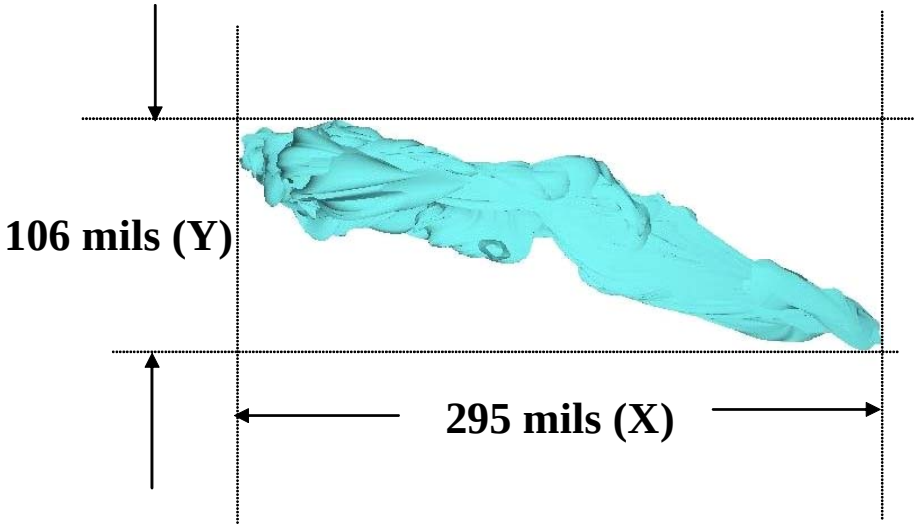
View 1



View 2



Dimensions of B1BW3-D:

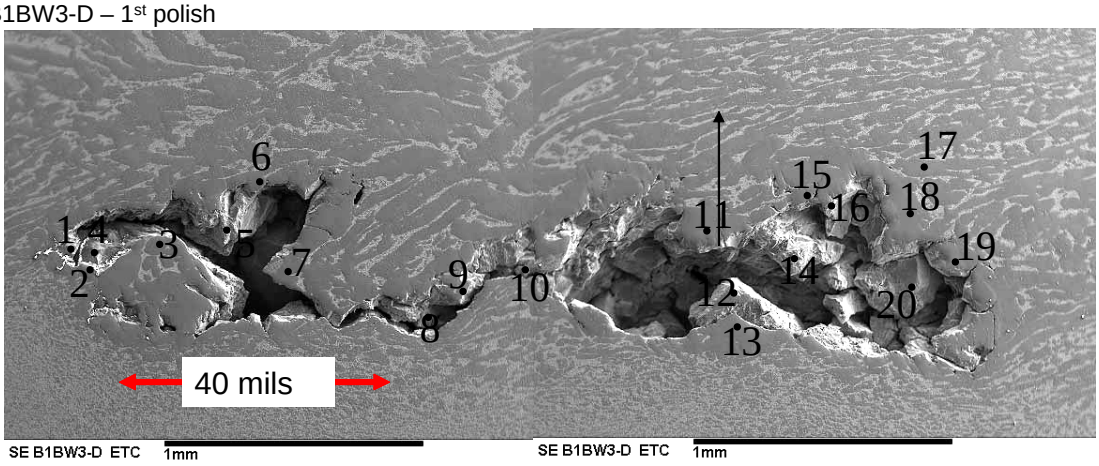


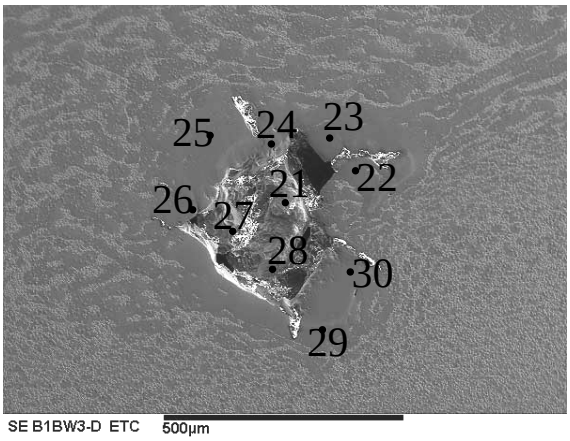
	min.	max.	size
X	38.24	332.76	294.52
Y	23.37	129.26	105.88
Z	-0.60	62.60	63.20

Unit: mils

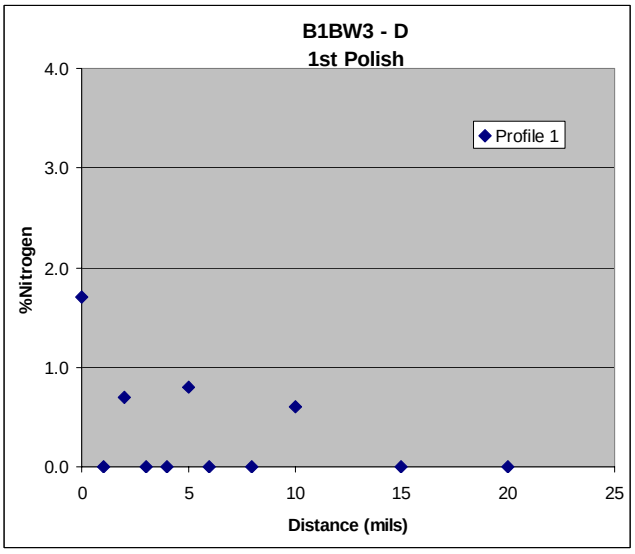
Microprobe analysis:

B1BW3-D – 1st polish



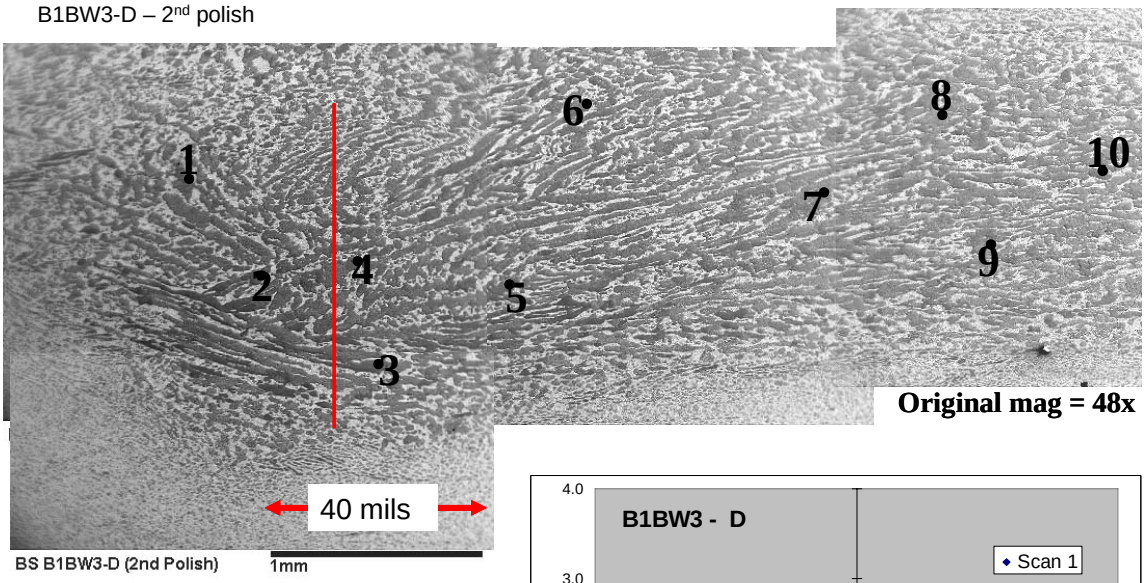


B1BW3 - D	W %			
Pt #	Ti	Al	V	N
1	86.4	3.4	1.7	4.9
2	90.2	5.7	2.5	1.5
3	89.9	7.5	2.9	0.9
4	92.2	2.9	1.1	5.8
5	88.6	2.7	1.4	4.7
6	85.4	5.6	2.0	0.5
7	90.6	6.5	2.8	0.8
8	88.3	4.5	1.9	2.9
9	88.1	5.8	3.2	1.4
10	89.5	2.2	1.4	4.8
11	85.5	3.2	1.3	2.1
12	90.2	1.2	1.6	6.4
13	95.0	4.0	1.5	0.8
14	87.7	2.2	1.7	4.6
15	88.5	4.9	2.3	0.5
16	88.3	1.5	1.6	2.6
17	90.6	5.7	2.2	< 0.5
18	90.6	4.7	1.7	1.0
19	90.4	2.5	1.4	2.5
20	91.1	3.4	2.0	3.9
21	83.6	0.4	0.6	9.4
22	89.0	6.0	2.0	0.5
23	89.0	4.7	1.6	0.9
24	89.8	1.6	0.9	2.5
25	88.9	4.2	1.1	1.3
26	89.3	4.5	1.6	< 0.5
27	88.7	1.4	1.1	3.7
28	85.0	0.9	1.1	8.3
29	90.6	4.9	1.7	0.6
30	87.7	1.7	1.5	5.5



Microprobe analysis:

B1BW3-D – 2nd polish

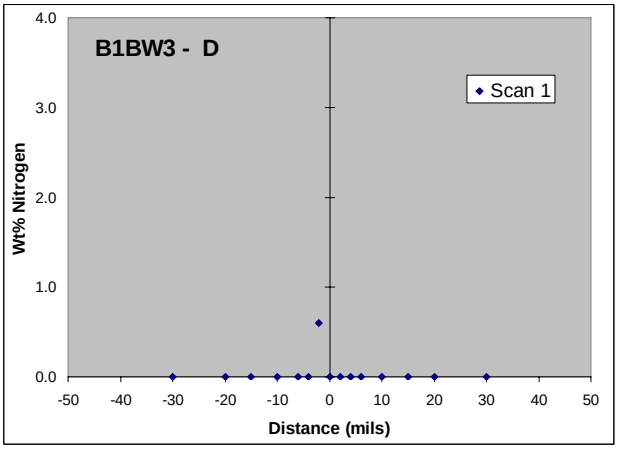


Original mag = 48x

Data for areas around the defect.

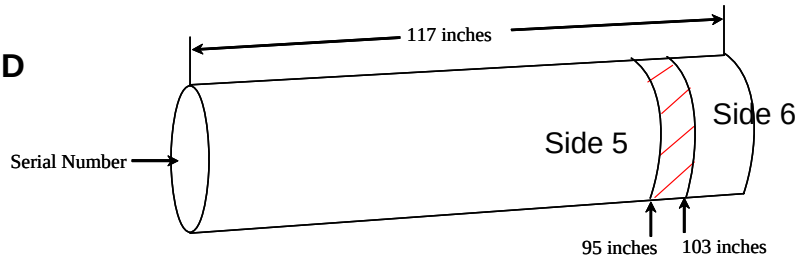
B1BW3-D(2) W %

Pt #	Ti	Al	V	N
1	91.0	6.7	1.9	< 0.5
2	93.6	6.6	1.9	< 0.5
3	92.7	6.0	1.8	0.5
4	92.1	6.6	1.6	0.6
5	92.2	6.5	2.1	< 0.5
6	92.4	6.8	2.3	< 0.5
7	91.8	6.7	2.3	< 0.5
8	91.1	6.5	2.1	< 0.5
9	92.8	6.6	2.0	< 0.5
10	91.1	6.6	2.2	0.5



Indication: B1AW2 – D

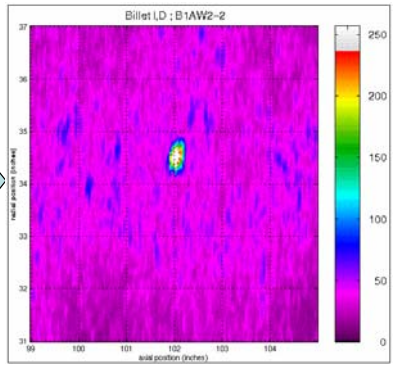
Original billet length: 117”



Billet inspection:

	Amplitude (%)	S/N	depth (in)	axial length (in)	radial length (in)
Multizone	134%	5.46	0.7	0.4217	0.2681
Conv. Longitudinal	50%	2.61			
Conv. Angle	%				

Zone 1



Mult inspection parameters:

Transducer - Zone 1, 6” diameter, 5MHz
Index - 0.010
Data Acquisition Rate - 0.010
Inspection Sensitivity - #2 FBH at 80-90% in Titanium
Inspection Range - 0.2” to 0.8”

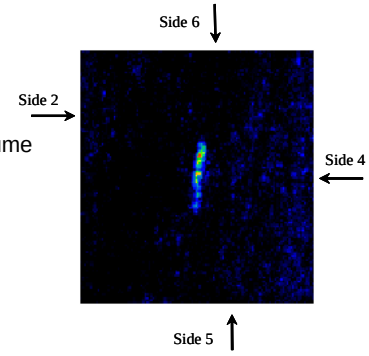
Sampling Rate - 100 MHz

Depth	Axial Length	Amplitude	Signal-to-Noise Ratio
0.780”	0.400”	134%	5.5

25 MHz inspection parameters

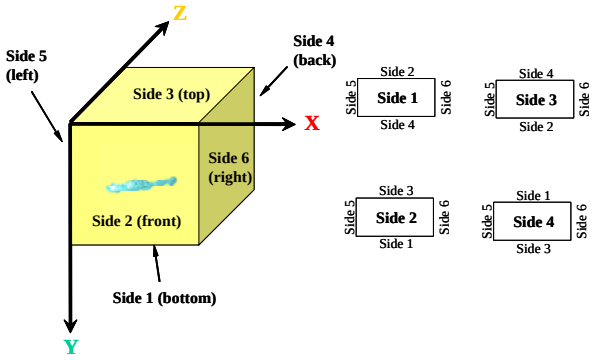
Transducer - 25 MHz, F10 - focal point positioned at indication depth
Index - 0.010
Data Acquisition Rate - 0.010
Inspection sensitivity - #1 FBH at 83% - 56 dB #2FBH at 84% at 48dB
Inspection range - C-scan , Between Front and Back / B-scan entire volume
Sampling Rate - 200 MHz

Side	Depth	Axial Length	Amplitude %	Sensitivity, dB
1	0.652”	0.400”	68	58
2	0.502”	0.400”	75	69
3	1.1011”	0.400”	58	79
4	0.472”	0.400”	65	65
5	0.508”	0.400”	75.6	75
6	0.520”	0.400”	78	79



View is from Side 1(side which was polished). Sides 5 and 6 represent the axial ends as shown above. Sides 2 and 4 represent the hoop direction (circumferential plane.)

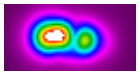
Orientation of sample block and c-scan images:



B1AW2 – D 5 MHz C-scan image comparisons:

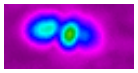
Side 1

Model



Attenuation=10dB
peak amplitude = 557 mv
deviation=64% or 4.31 dB

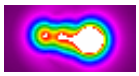
Experiment



Attenuation=10dB
peak amplitude=339 mv

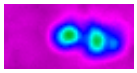
Side 2

Model



Attenuation=2dB
peak amplitude=1052 mv
deviation=258% or 11.07 dB

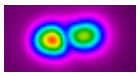
Experiment



Attenuation=2dB
peak amplitude=294 mv

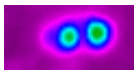
Side 3

Model



Attenuation=12dB
peak amplitude=473 mv
deviation=46% or 3.29 dB

Experiment



Attenuation=12dB
peak amplitude=324 mv

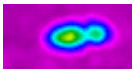
Side 4

Model



Attenuation=4dB
peak amplitude=1393 mv
deviation=312% or 12.30 dB

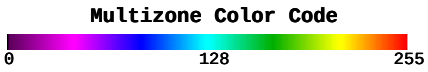
Experiment



Attenuation=4dB
peak amplitude=338 mv

Experiment image: 60(H) x 30(V) @10 mils

Model image: 61(H) x 31(V) @10 mils



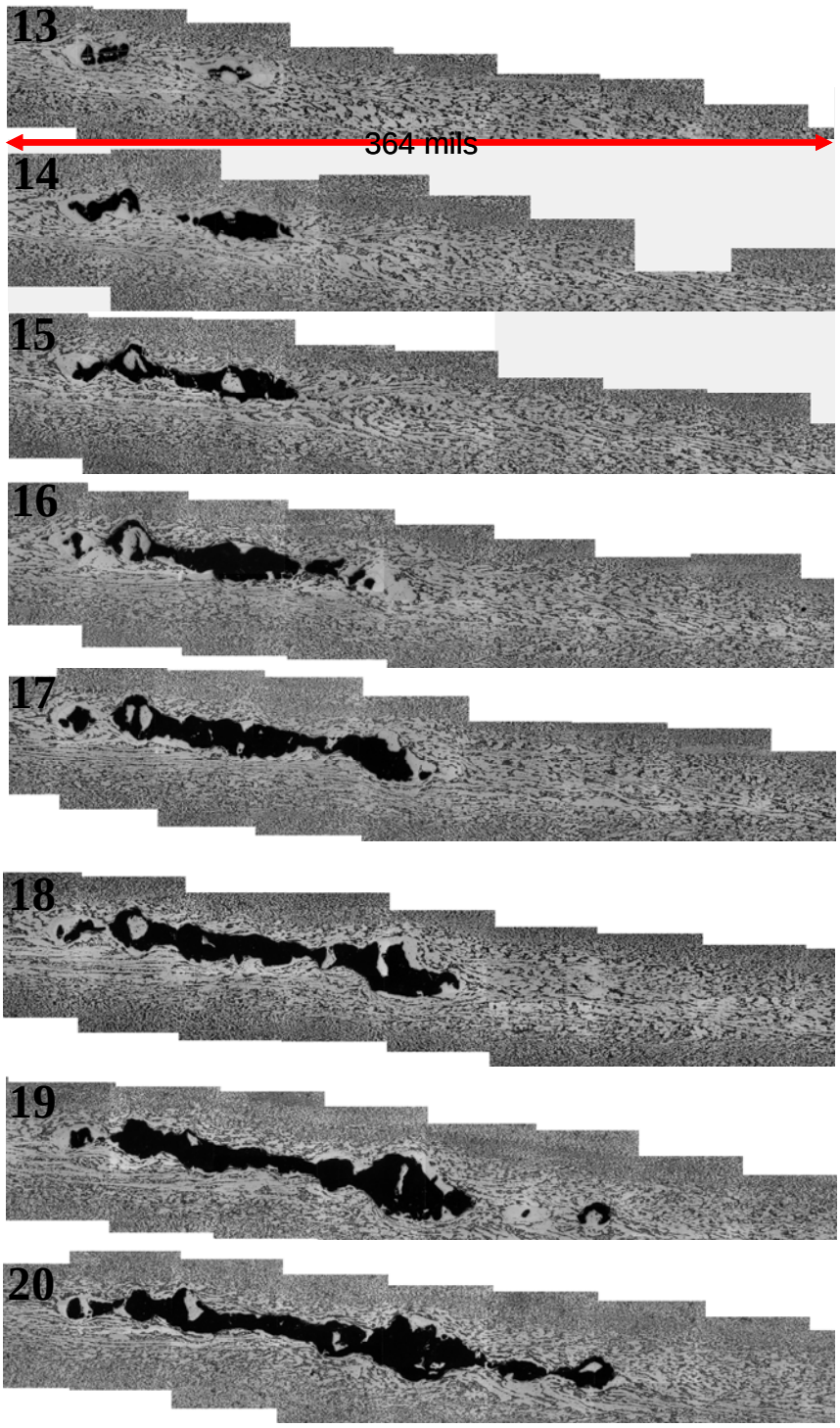
Experiment 255 = 500mv

B1AW2 – D 3D Solid Model Parameters:

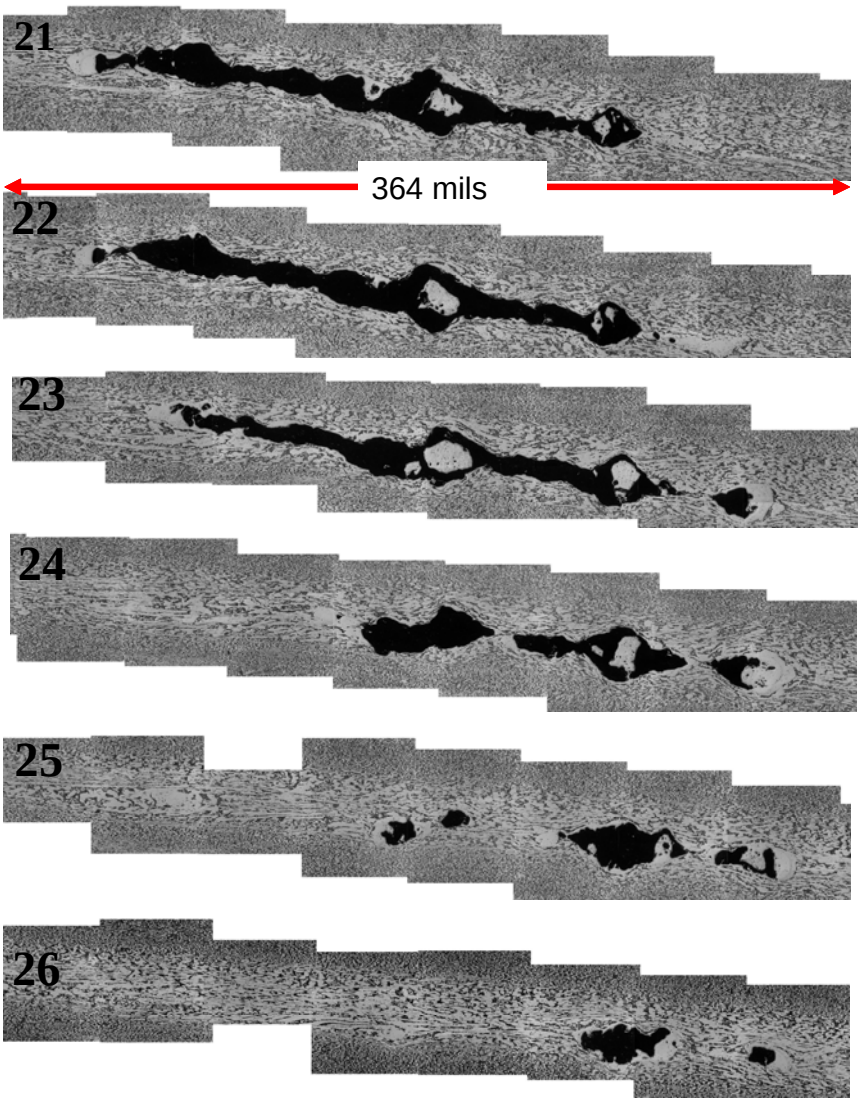
Sub-Micrograph
- size - 4800(H) by 1300(V) pixels
- color - 256 gray-scale of size
- scale - 132 pixels =10 mils

Geometric Model
- 1 void flaw part (with branches)
- 17 geometric model parts
- 23 micrograph planes (including 9 patches)
- 72 void cross-section boundary traces (model part 5 uses 11; 13 uses 8; 15,6 uses 6; 3 uses 5; the rest use 3 each)

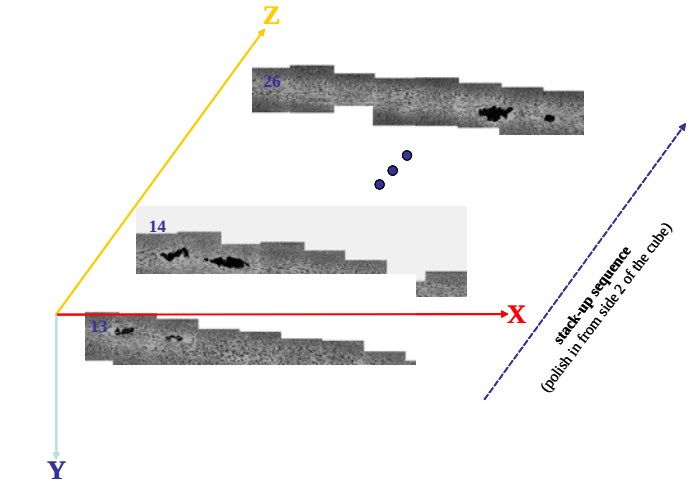
B1AW2 – D



B1AW2 – D



Orientation of Sub-Micrographs (B1AW2 – D):



Angle views of void model for B1AW2 – D:

View 1



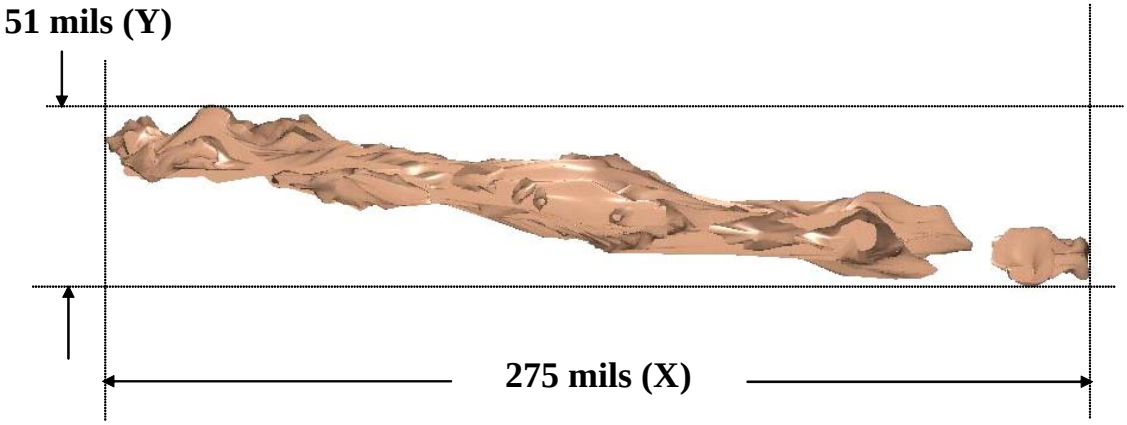


View 2





Dimensions of B1AW2 – D:

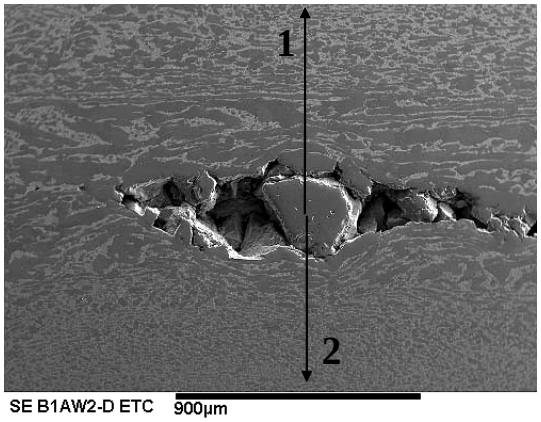


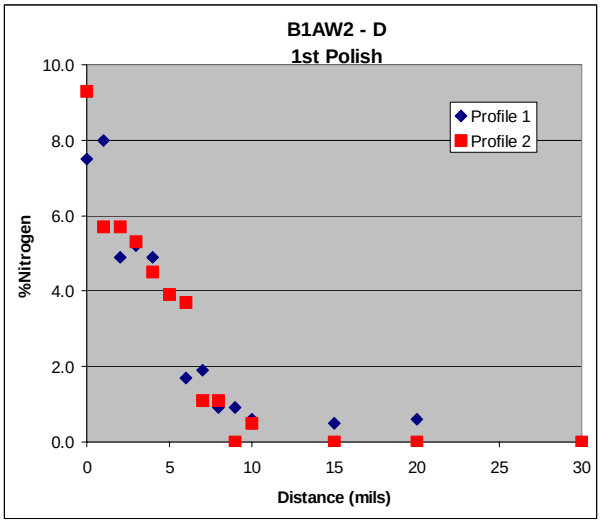
	min.	max.	size
X	19	294	275
Y	30	81	51
Z	97	154	57

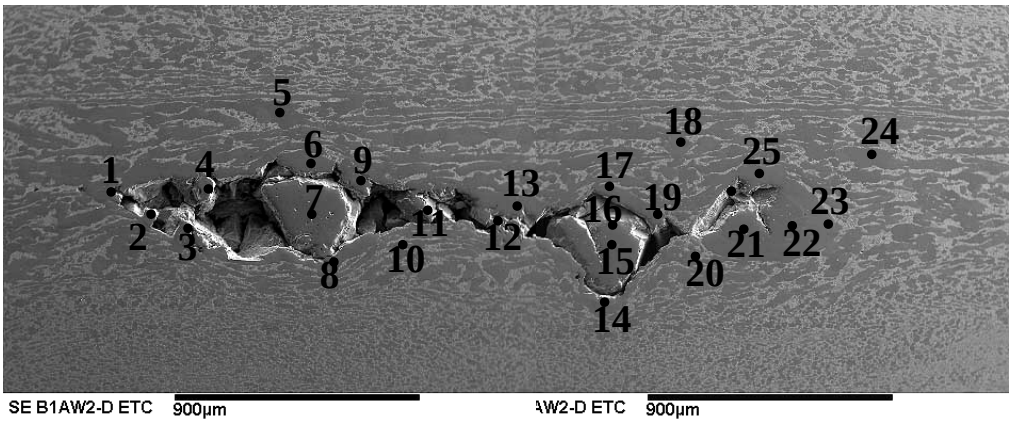
Unit: mils

Microprobe analysis:

B1AW2 – D – section 15





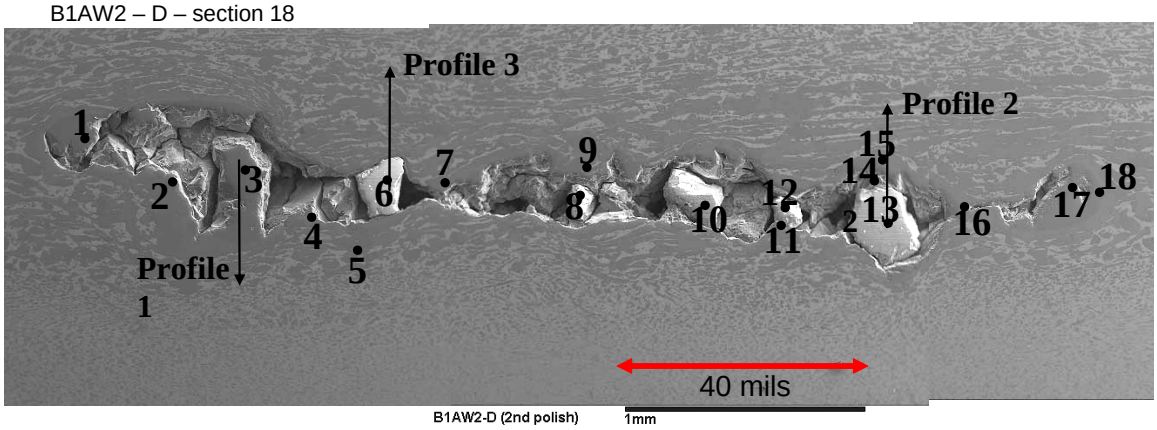


B1AW2-D	W %			
Pt #	Ti	Al	V	N
1	91.6	0.3	2.2	4.0
2	86.9	0.1	2.2	9.9
3	88.6	0.1	1.8	9.3
4	88.5	0.3	2.0	6.6
5	90.4	6.0	2.4	< 0.5
6	90.6	4.1	1.9	1.7
7	89.9	0.1	1.4	7.7
8	89.4	4.8	1.8	1.0
9	91.7	3.8	1.7	1.1
10	91.7	6.1	1.8	0.9
11	92.1	0.4	1.6	7.0
12	90.5	0.2	2.0	4.9
13	93.5	2.5	1.4	2.7

B1AW2-D	W %			
Pt #	Ti	Al	V	N
14	94.4	1.5	1.6	2.1
15	90.7	0.1	1.3	9.5
16	91.6	0.2	2.3	5.4
17	91.0	4.6	2.0	1.5
18	92.5	6.0	1.8	< 0.5
19	93.5	4.3	1.8	1.2
20	94.0	5.2	1.8	0.6
21	93.5	0.3	3.1	2.7
22	95.9	0.3	1.8	2.5
23	95.3	4.7	1.6	< 0.5
24	94.5	5.8	1.7	< 0.5
25	93.5	0.2	2.0	4.4

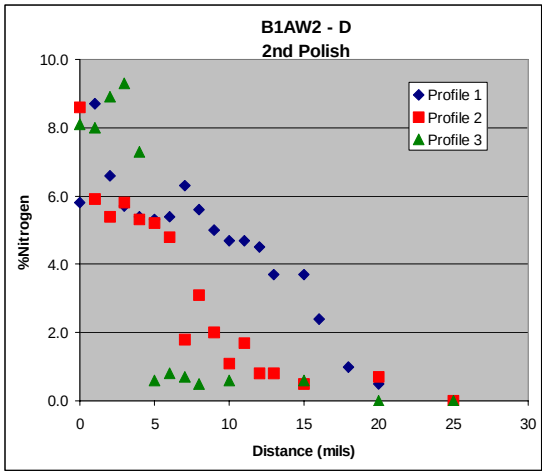
Microprobe analysis:

B1AW2 – D – section 18



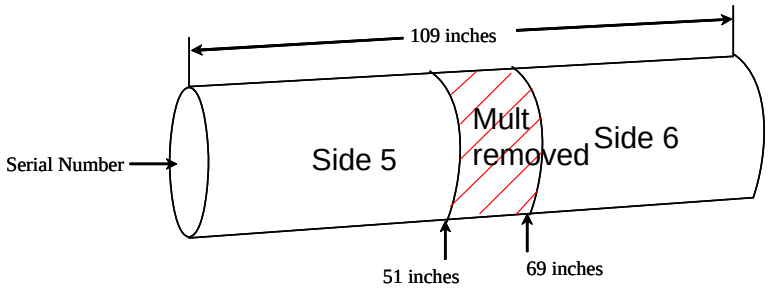
B1AW2-D (2nd polish)

B1AW2-D (2)	W %			
Pt #	Ti	Al	V	N
1	94.6	0.3	2.2	4.2
2	91.1	3.9	1.7	2.5
3	90.9	0.2	2.4	6.6
4	89.3	4.6	1.6	1.7
5	93.5	6.2	2.1	< 0.5
6	90.7	0.3	1.8	6.7
7	92.8	3.7	1.5	1.6
8	89.2	0.1	1.6	8.8
9	90.5	5.6	2.0	1.0
10	84.8	0.4	6.2	8.0
11	94.0	5.0	2.0	1.1
12	87.9	0.3	2.0	6.8
13	89.9	0.0	1.1	9.2
14	92.5	0.2	2.4	5
15	92.0	4.3	1.5	2.1
16	93.6	1.2	1.5	3.3
17	93.8	0.3	2.1	4.2
18	95.6	0.3	1.7	3.7



Indication: B1AW3 – A

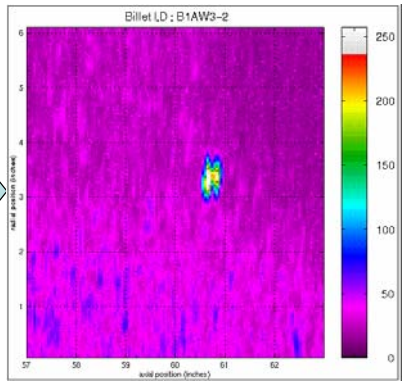
Original billet length: 107.5”



Billet inspection:

	Amplitude (%)	S/N	depth (in)	axial length (in)	radial length (in)
Multizone	142%	5.02	0.7	0.4186	0.3387
Conv. Longitudinal	50%	2.92	0.8		
Conv. Angle	60%	2.48	0.8		

Zone 2



Mult inspection parameters:

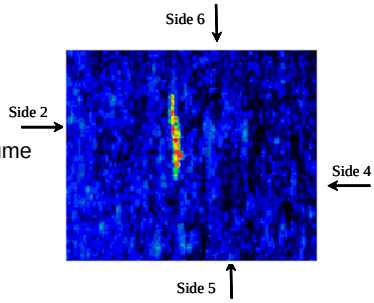
Transducer - Zone 2, 6” diameter, 5MHz
Index - 0.010
Data Acquisition Rate - 0.010
Inspection Sensitivity - #2 FBH at 80-90% in Titanium
Inspection Range - 0.8” to 1.7”
Sampling Rate - 100 MHz

Depth	Axial Length	Amplitude	Signal-to-Noise Ratio
0.812”	0.400”	142%	5.1

25 MHz inspection parameters

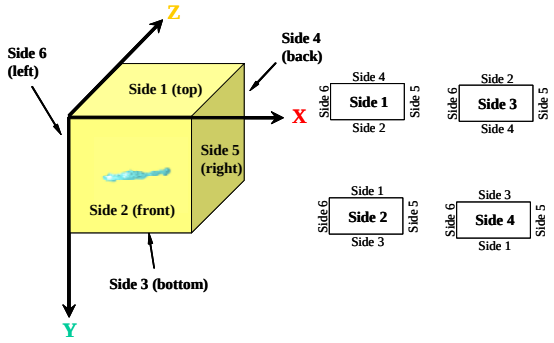
Transducer - 25 MHz, F10 - focal point positioned at indication depth
Index - 0.010
Data Acquisition Rate - 0.010
Inspection sensitivity - #1 FBH at 83% - 56 dB #2FBH at 84% at 48dB
Inspection range - C-scan , Between Front and Back / B-scan entire volume
Sampling Rate - 200 MHz

Side	Depth	Axial Length	Amplitude %	Sensitivity, dB
1	0.484”	0.365”	85	53
2	0.530”	0.365”	80	49
3	0.508”	0.365”	70	54
4	0.508”	0.365”	84	55
5	0.530”	0.365”	78	68
6	0.530”	0.365”	76	73



View is from Side 1(side which was polished). Sides 5 and 6 represent the axial ends as shown above. Sides 2 and 4 represent the hoop direction (circumferential plane.)

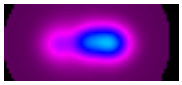
Orientation of sample block and c-scan images:



B1AW3 – A 5 MHz C-scan image comparisons:

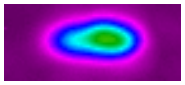
Side 1

Model



Attenuation=18dB
peak amplitude = 231 mv
deviation=-34% or -3.56 dB

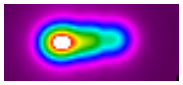
Experiment



Attenuation=18dB
peak amplitude=348 mv

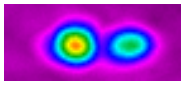
Side 2

Model



Attenuation=12dB
peak amplitude=578 mv
deviation=27% or 2.08 dB

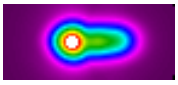
Experiment



Attenuation=12dB
peak amplitude=455 mv

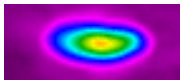
Side 3

Model



Attenuation=12dB
peak amplitude=564 mv
deviation=29% or 2.20 dB

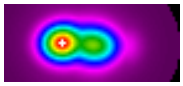
Experiment



Attenuation=12dB
peak amplitude=438 mv

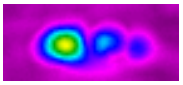
Side 4

Model



Attenuation=12dB
peak amplitude=511 mv
deviation=24% or 1.87 dB

Experiment



Attenuation=12dB
peak amplitude=412 mv

Experiment image: 70(H) x 30(V) @10 mils

Model image: 71(H) x 31(V) @10 mils



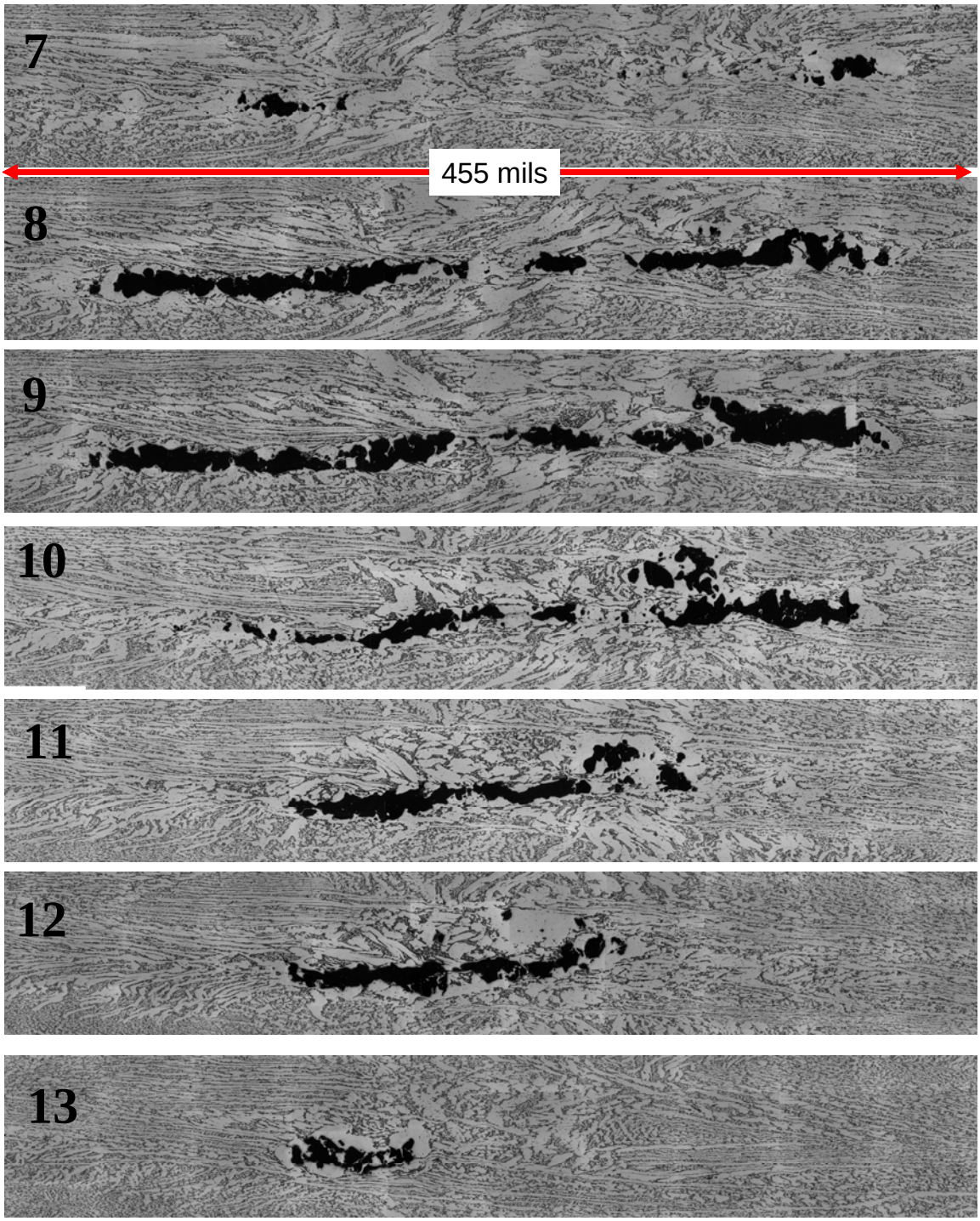
Experiment 255 = 500mv

B1AW3 – A 3D Solid Model Parameters:

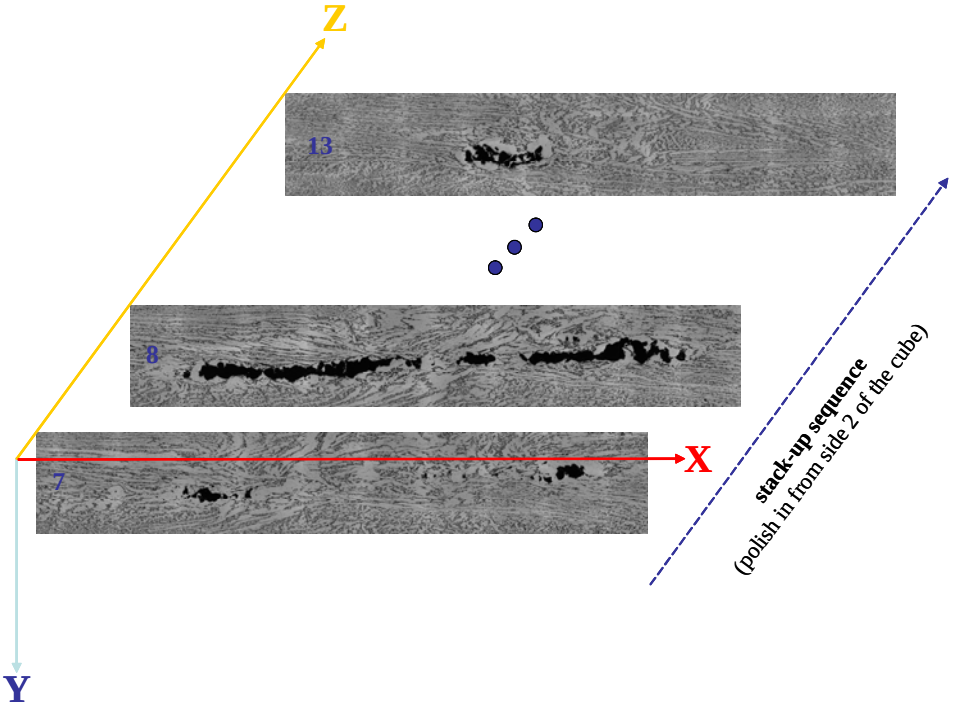
Sub-Micrograph
- size - 6000(H) by 1000(V) pixels
- color - 256 gray-scale of size
- scale - 132 pixels =10 mils

Geometric Model
- 18 void flaw parts (with branches)
- 48 geometric model parts
- 17 micrograph planes (including 6 patches)
- 154 void cross-section boundary traces (model part 18 uses 5, parts 2, 14, 15, 16, 26, 34, 35, 41 use 4 and the rest use 3 each)

B1AW3 – A

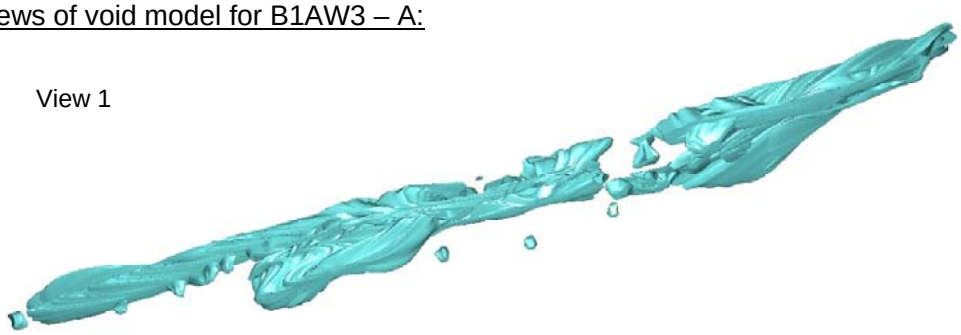


Orientation of Sub-Micrographs (B1AW3 – A):



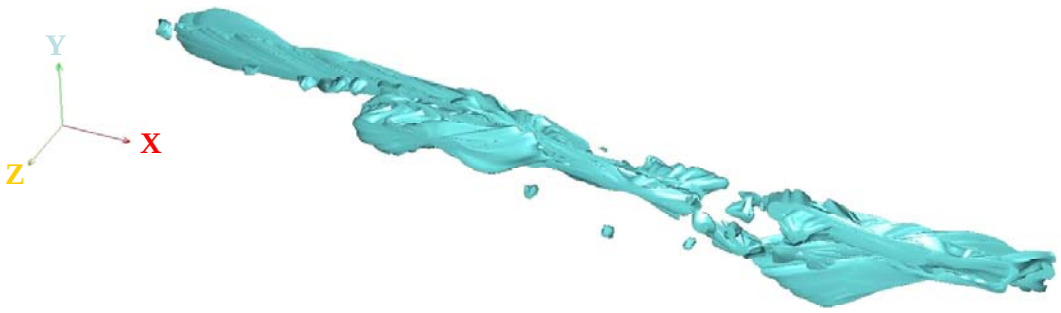
Angle views of void model for B1AW3 – A:

View 1

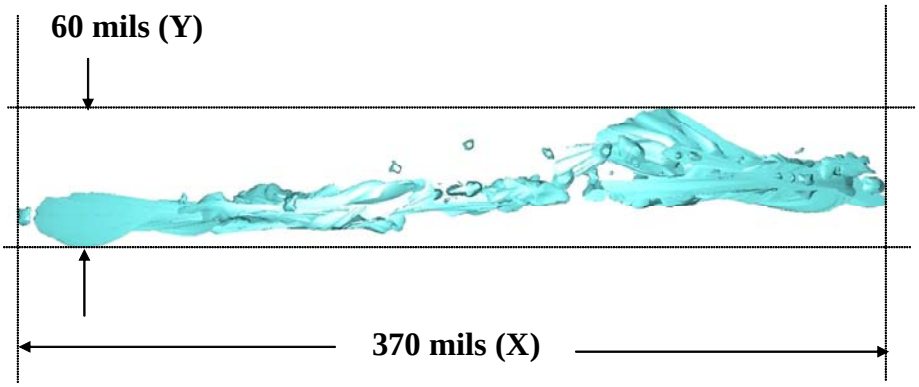




View 2



Dimensions of B1AW3 – A:

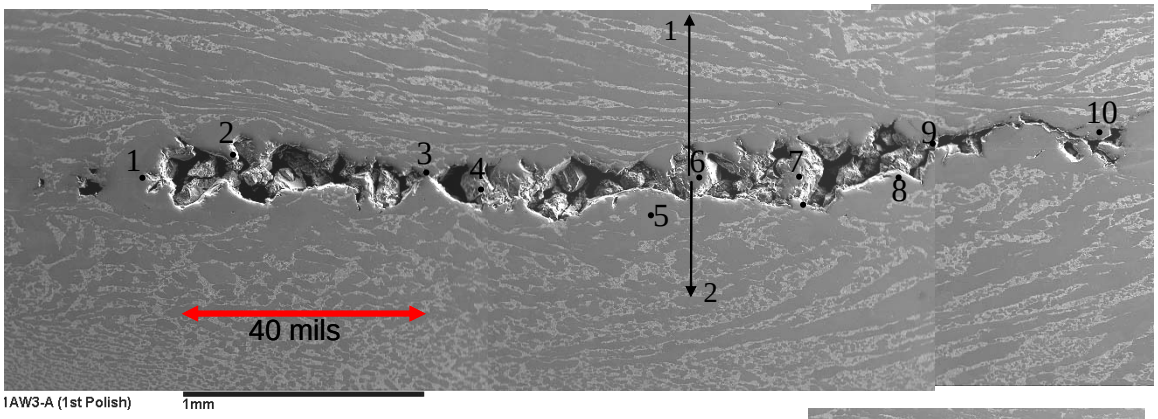


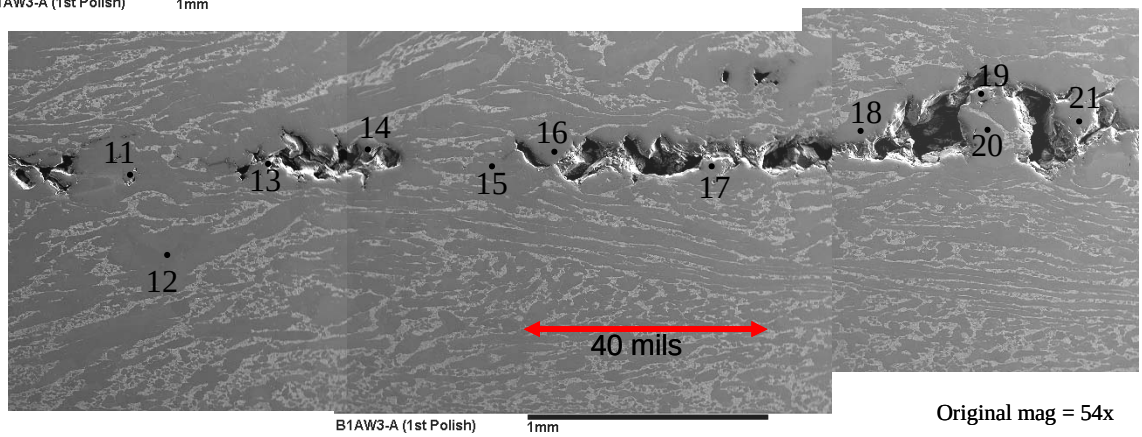
	min.	max.	size
X	39	409	370
Y	4	64	60
Z	-13	19	32

Unit: mils

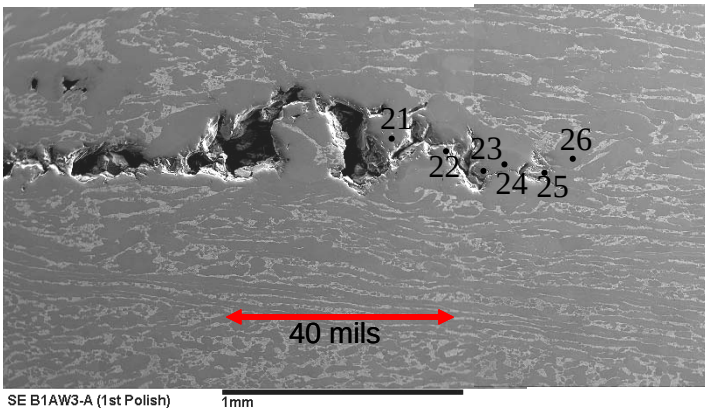
Microprobe analysis:

B1AW3 – A - section 8

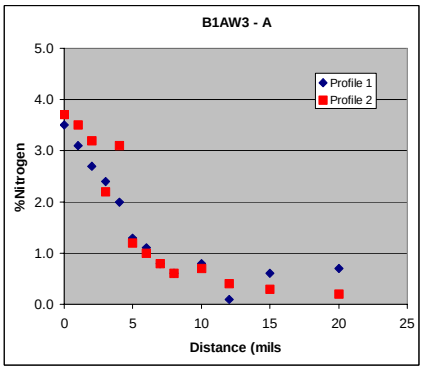




Original mag = 54x

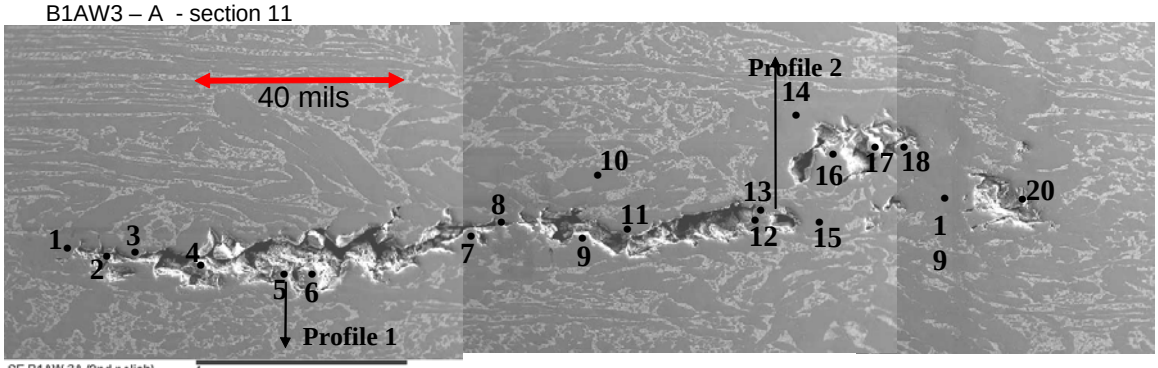


B1AW3-A (1)	W %			
Pt #	Ti	Al	V	N
1	98.0	2.3	0.8	2.8
2	86.3	2.2	1.2	3.7
3	86.7	3.4	1.4	3.1
4	83.1	1.9	1.2	4.6
5	84.4	5.3	1.1	1.7
6	90.0	2.8	1.5	3.9
7	91.1	2.9	1.7	3.0
8	89.8	4.7	1.4	2.8
9	88.8	2.9	1.2	2.5
10	89.4	5.0	1.7	1.8
11	90.7	4.1	1.4	1.9
12	89.1	5.9	2.0	0.8
13	89.2	2.1	1.1	2.2
14	87.6	2.6	1.5	2.8
15	88.3	6.1	2.0	0.8
16	88.9	2.5	1.4	3.4
17	89.9	2.4	1.1	3.6
18	87.3	5.6	1.9	1.7
19	89.1	5.5	2.0	1.5
20	87.3	5.9	2.4	1.1
21	93.3	2.5	1.6	3.3
22	92.1	2.8	1.5	3.2
23	90.1	2.7	1.6	3.5
24	92.0	2.7	1.3	2.5
25	93.1	3.7	1.4	1.5
26	89.8	5.9	1.8	0.8



Microprobe analysis:

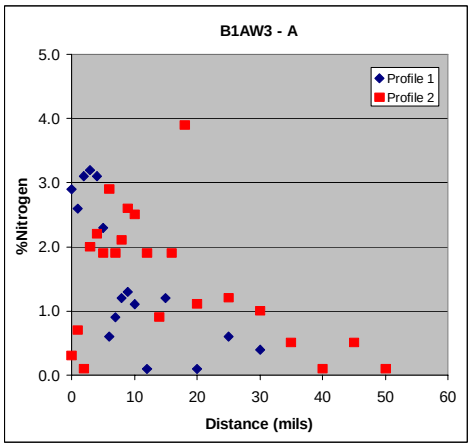
B1AW3 – A - section 11



Data for areas around the defect.

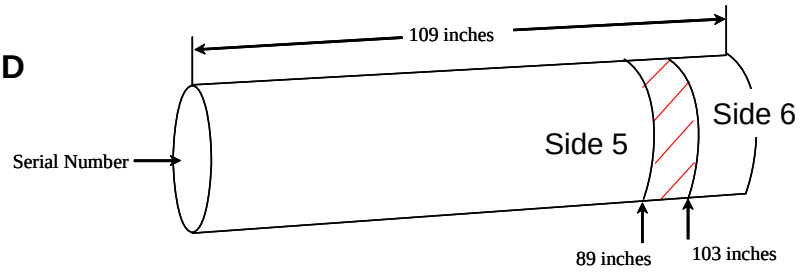
B1AW3-A(2) W %

Pt #	Ti	Al	V	N
1	92.9	4.0	1.3	1.5
2	93.9	2.5	1.1	1.4
3	92.6	4.4	1.4	1.2
4	92.2	3.3	1.5	2.8
5	93.9	3.0	1.3	2.9
6	92.4	3.1	1.4	3.2
7	90.2	6.0	2.1	1.7
8	88.9	6.1	2.2	1.7
9	90.8	5.1	1.5	2.7
10	89.3	6.9	1.7	< 0.5
11	90.9	4.7	1.4	1.7
12	90.9	3.4	1.2	4.0
13	90.3	4.5	1.6	2.8
14	92.3	3.6	1.4	2.2
15	90.5	5.3	1.7	1.6
16	90.5	3.9	1.3	2.9
17	92.0	5.3	1.7	2.6
18	94.2	3.7	1.3	2.7
19	94.3	4.2	1.3	1.6
20	93.9	2.8	1.1	2.8



Indication: B1AW3 – D

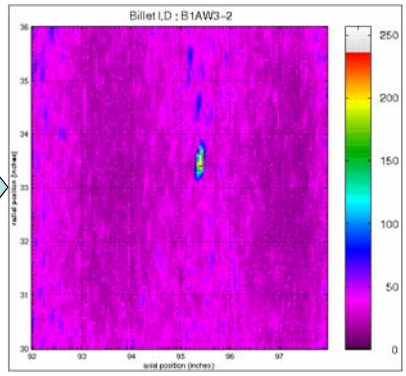
Original billet length: 109”



Billet inspection:

	Amplitude (%)	S/N	depth (in)	axial length (in)	radial length (in)
Multizone	101%	4.49	1.1	0.2326	0.2215
Conv. Longitudinal					
Conv. Angle					

Zone 2



Mult inspection parameters:

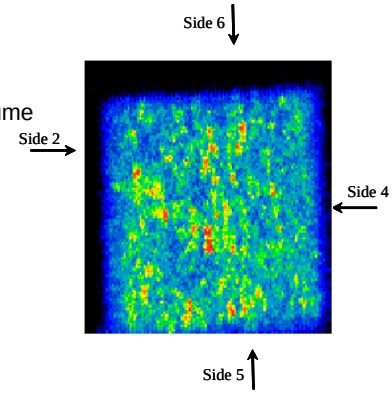
Transducer - Zone 2, 6” diameter, 5MHz
Index - 0.010
Data Acquisition Rate - 0.010
Inspection Sensitivity - #2 FBH at 80-90% in Titanium
Inspection Range - 0.8” to 1.7”
Sampling Rate - 100 MHz

Depth	Axial Length	Amplitude	Signal-to-Noise Ratio
1.1400”	0.250”	101%	4.5

25 MHz inspection parameters

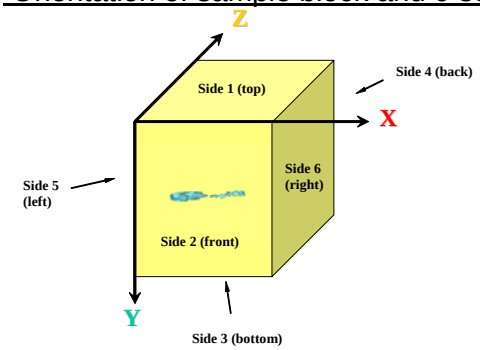
Transducer - 25 MHz, F10 - focal point positioned at indication depth
Index - 0.010
Data Acquisition Rate - 0.010
Inspection sensitivity - #1 FBH at 83% - 56 dB #2FBH at 84% at 48dB
Inspection range - C-scan , Between Front and Back / B-scan entire volume
Sampling Rate - 200 MHz

Side	Depth	Axial Length	Amplitude %	Sensitivity, dB
1	0.560”	0.250”	85	58
2	0.701”	0.250”	80	72
3	0.544”	0.250”	75	49
4	0.399”	0.250”	70	65
5	0.425”	0.250”	83	65
6	0.435”	0.250”	85	65



View is from Side 1(side which was polished). Sides 5 and 6 represent the axial ends as shown above. Sides 2 and 4 represent the hoop direction (circumferential plane.)

Orientation of sample block and c-scan images:

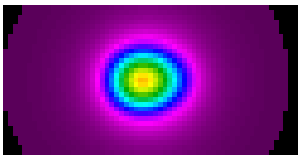


NOTE: Data were taken only from sides 1 and 3

B1AW3-D 5 MHz C-scan image comparisons:

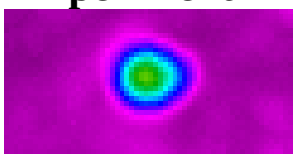
Side 1

Model



61(H) x 31(V) @10 mils, 10dB
peak amplitude @10dB=437 mv
deviation=22% or 1.8 dB

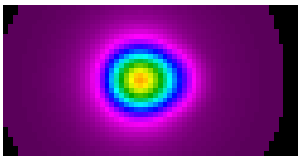
Experiment



60(H) x 30(V) @10 mils, 10dB
peak amplitude @10dB=357 mv

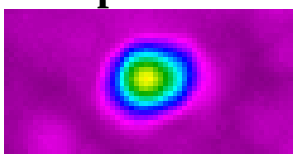
Side 3

Model

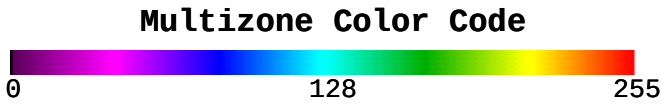


61(H) x 31(V) @10 mils, 10dB
peak amplitude@10dB = 444 mv
deviation=10% or 0.9 dB

Experiment



60(H) x 30(V) @10 mils, 10dB
peak amplitude@10dB = 402 mv



Experiment 255 = 500mv

B1AW3-D

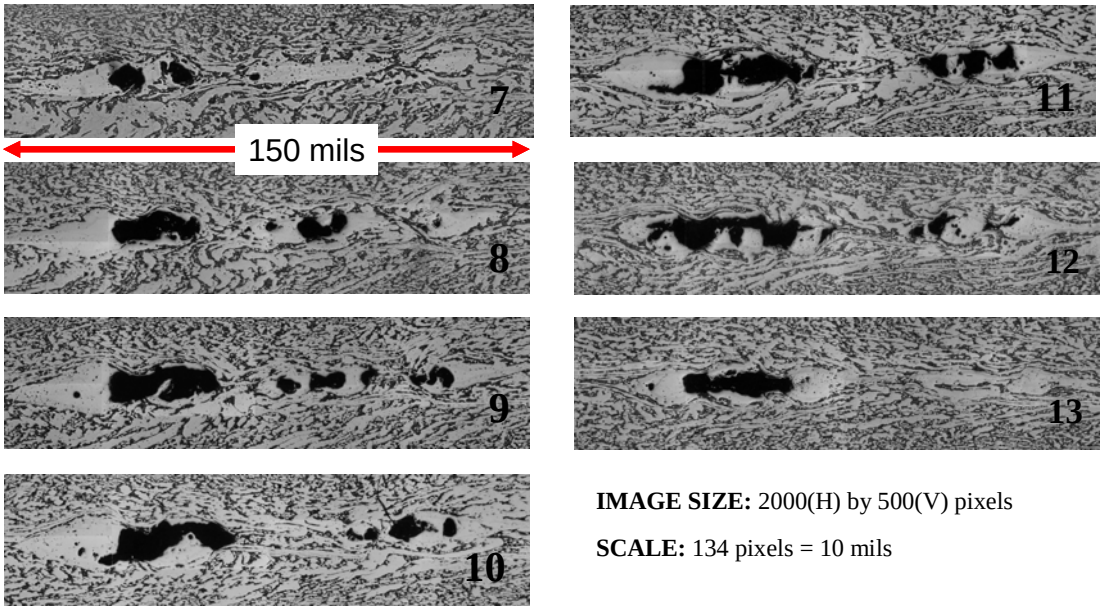
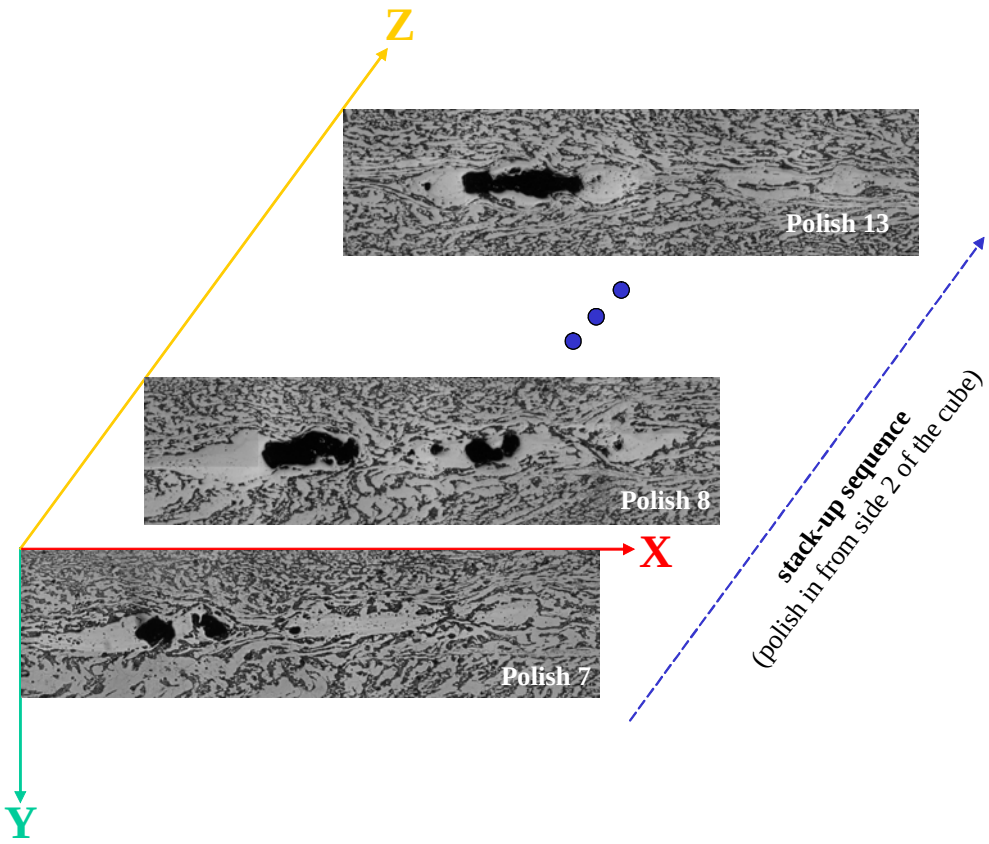


IMAGE SIZE: 2000(H) by 500(V) pixels

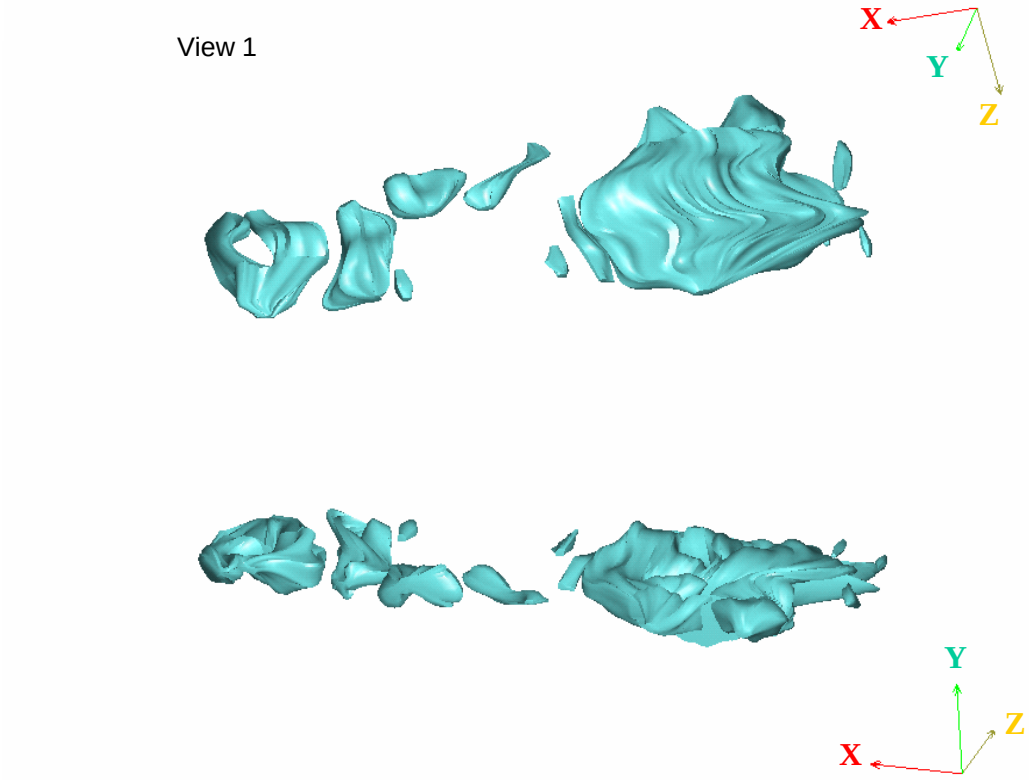
SCALE: 134 pixels = 10 mils

Orientation of Sub-Micrographs (B1AW3-D):

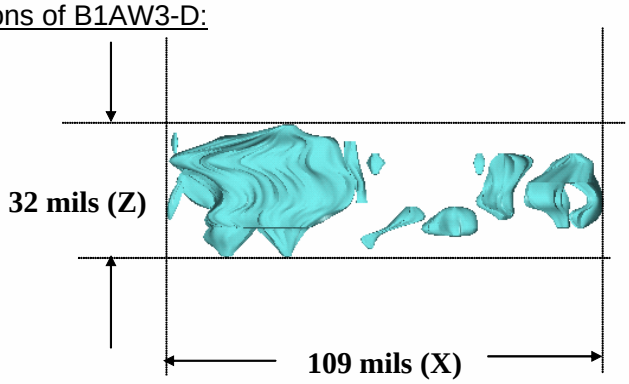


Angle views of void model for B1AW3-D:

View 1



Dimensions of B1AW3-D:

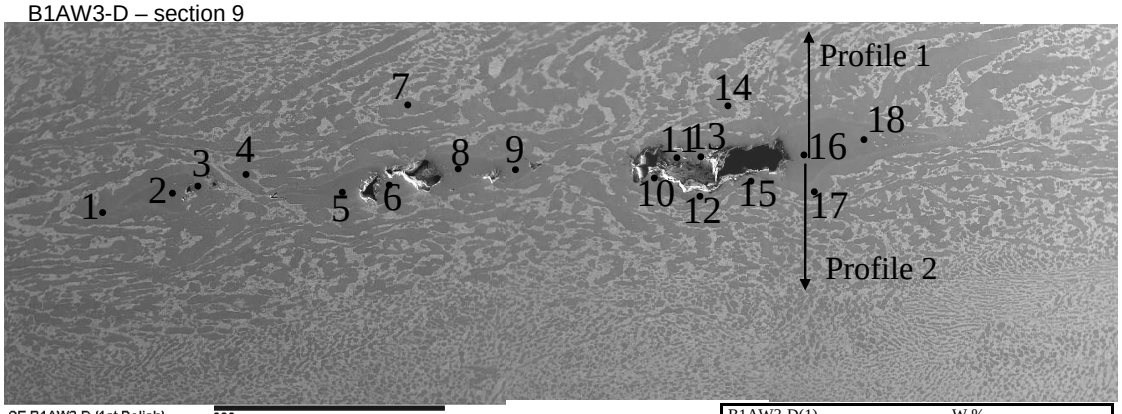


	min.	max.	size
X	20	128	109
Y	11	26	15
Z	0	32	32

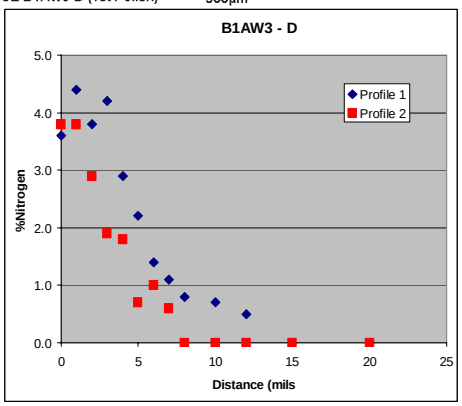
Unit: mils

Microprobe analysis:

B1AW3-D – section 9



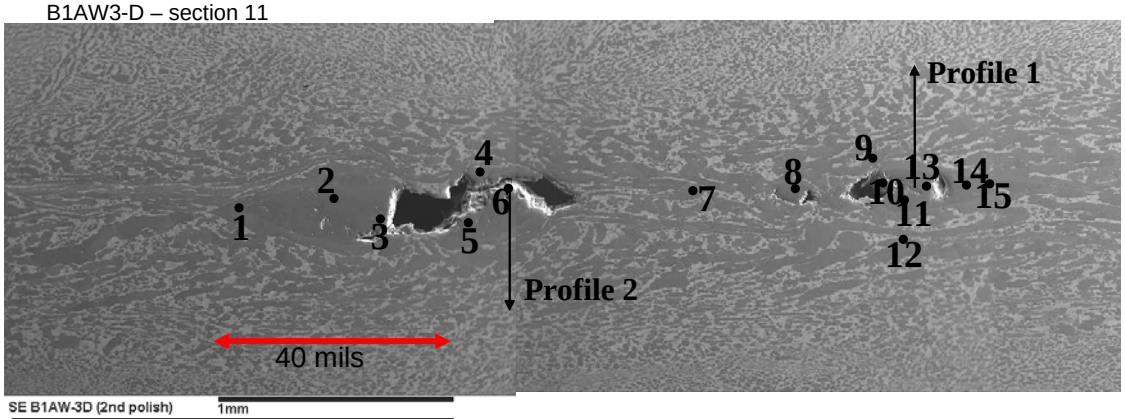
SE B1AW3-D (1st Polish) 900µm



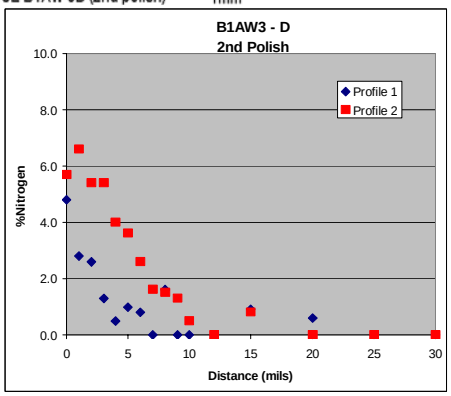
B1AW3-D(1)	W %			
Pt #	Ti	Al	V	N
1	92.8	4.7	2.0	0.8
2	94.4	0.7	2.3	3.6
3	96.4	1.9	1.9	0.9
4	93.1	5.4	2.2	5.8
5	95.1	1.5	2.1	2.6
6	94.4	1.2	2.1	2.7
7	92.4	6.3	2.0	< 0.5
8	88.8	0.4	8.5	2.2
9	94.3	0.5	2.2	3.5
10	89.4	3.3	2.5	2.2
11	93.5	0.5	2.6	3.5
12	89.5	3.9	2.3	1.8
13	93.0	0.5	2.6	3.6
14	90.4	5.7	2.4	< 0.5
15	91.7	5.4	2.0	1.5
16	91.1	0.5	2.4	4.6
17	92.0	5.1	2.0	0.7
18	93.7	0.4	2.1	3.6

Microprobe analysis:

B1AW3-D – section 11



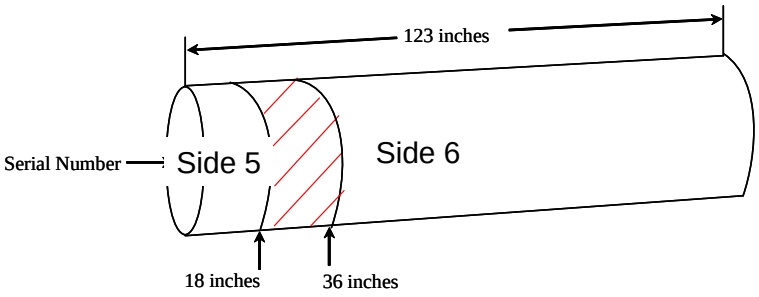
SE B1AW-3D (2nd polish) 1mm



B1AW3-D(2)	W %			
Pt #	Ti	Al	V	N
1	94.6	1.6	1.1	2.0
2	90.2	0.5	1.9	5.0
3	91.3	0.1	2.5	4.7
4	88.7	3.7	1.6	2.1
5	91.1	0.2	1.8	5.9
6	89.0	0.2	2.1	5.5
7	90.0	5.8	1.8	0.7
8	89.9	0.2	2.0	2.7
9	89.3	6.2	1.8	< 0.5
10	89.3	0.3	1.8	5.3
11	90.1	1.2	2.6	4.3
12	87.5	6.4	1.7	1.3
13	88.6	0.3	3.0	4.0
14	92.4	0.3	1.7	3.9
15	92.8	1.5	1.7	2.4

Indication: B2W2 – C

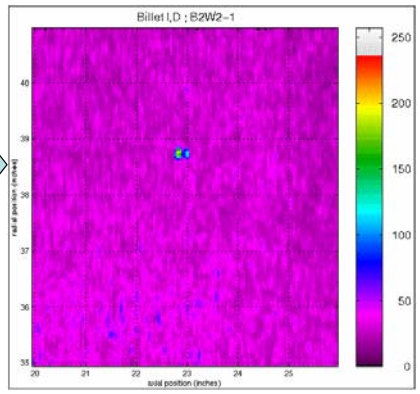
Original billet length: 123”



Billet inspection:

	Amplitude (%)	S/N	depth (in)	axial length (in)	radial length (in)
Multizone	74%	4.09	0.2	0.3273	0.1031
Conv. Longitudinal	%				
Conv. Angle	%				

Zone 1



Mult inspection parameters:

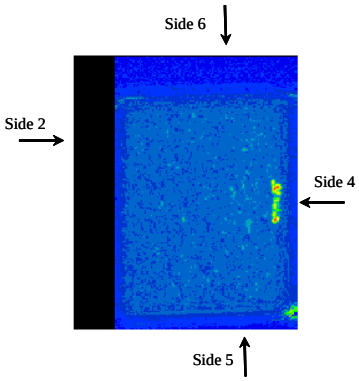
Transducer - Zone 1, 6” diameter, 5MHz
Index - 0.010
Data Acquisition Rate - 0.010
Inspection Sensitivity - #2 FBH at 80-90% in Titanium
Inspection Range - 0.2” to 0.8”
Sampling Rate - 100 MHz

Depth	Axial Length	Amplitude	Signal-to-Noise Ratio
0.195	0.350”	74%	4.09

25 MHz inspection parameters

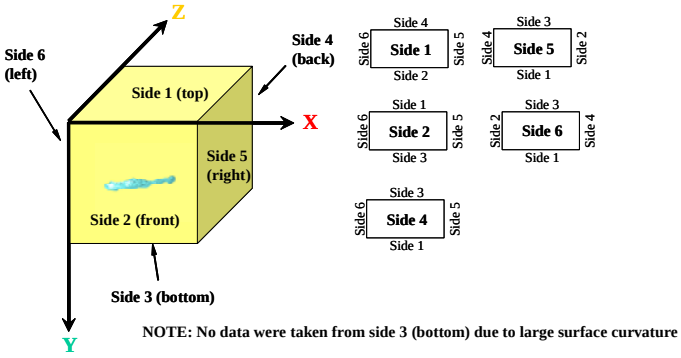
Transducer - 25 MHz, F10 - focal point positioned at indication depth
Index - 0.010
Data Acquisition Rate - 0.010
Inspection sensitivity - #1 FBH at 83% - 56 dB #2FBH at 84% at 48dB
Inspection range - C-scan , Between Front and Back / B-scan entire volume
Sampling Rate - 200 MHz

Side	Depth	Axial Length	Amplitude %	Sensitivity, dB
1				
2	0.689”	0.350”	71	55
3	1.052”	0.350”	38	71
4	0.768”	0.350”	80	54
5	0.605”	0.350	63	74
6	0.629”	0.350”	80	74



Sides 5 and 6 represent the axial ends as shown above. Sides 2 and 4 represent the hoop direction (circumferential plane.)

Orientation of sample block and c-scan images:

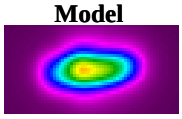


NOTE: No data were taken from side 3 (bottom) due to large surface curvature

B2W2 – C 5 MHz C-scan image comparisons:

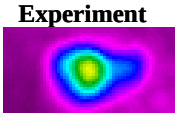
Side 2

Model



61(H) x 31(V) @10 mils, 21.5dB
peak amplitude @12dB=1316 mv
deviation=219% or 10.1 dB

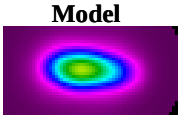
Experiment



60(H) x 30(V) @10 mils, 12dB
peak amplitude @12dB=412 mv

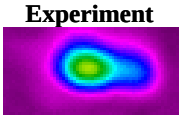
Side 4

Model



61(H) x 31(V) @10 mils, 25.5dB
peak amplitude @16dB=1167 mv
deviation=205% or 9.7 dB

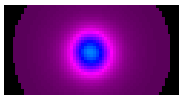
Experiment



60(H) x 30(V) @10 mils, 16dB
peak amplitude @16dB=382 mv

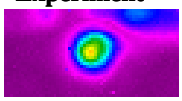
Side 5

Model



61(H) x 31(V) @10 mils, 0dB
peak amplitude @0dB=208 mv
deviation=-52% or -6.4 dB

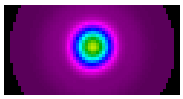
Experiment



60(H) x 30(V) @10 mils, 0dB
peak amplitude @0dB=437 mv

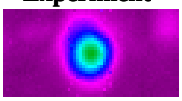
Side 6

Model



61(H) x 31(V) @10 mils, 0dB
peak amplitude @0dB=394 mv
deviation=26% or 2.0 dB

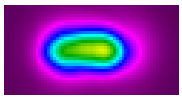
Experiment



60(H) x 30(V) @10 mils, 0dB
peak amplitude @0dB=313 mv

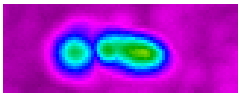
Side 1

Model

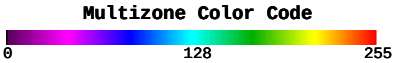


61(H) x 31(V) @10 mils, 10dB
peak amplitude@6dB = 654 mv
deviation=75% or 4.9 dB

Experiment



80(H) x 30(V) @10 mils, 6dB
peak amplitude@6dB = 373 mv



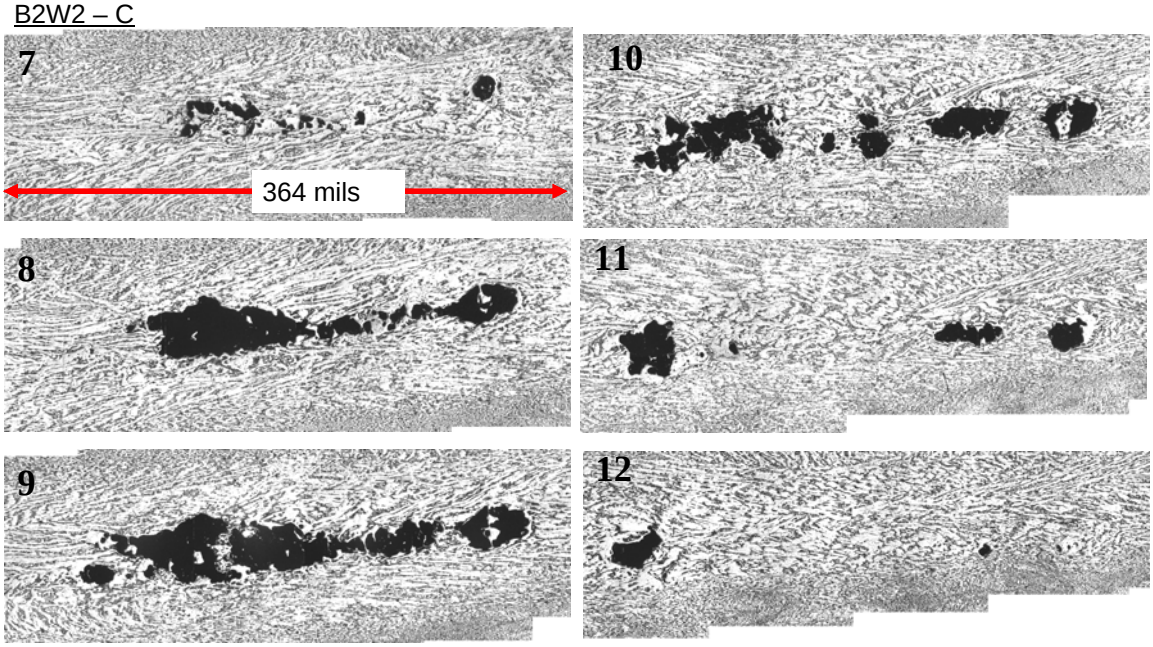
Experiment 255 = 500mv

B2W2 – C 3D Solid Model Parameters:

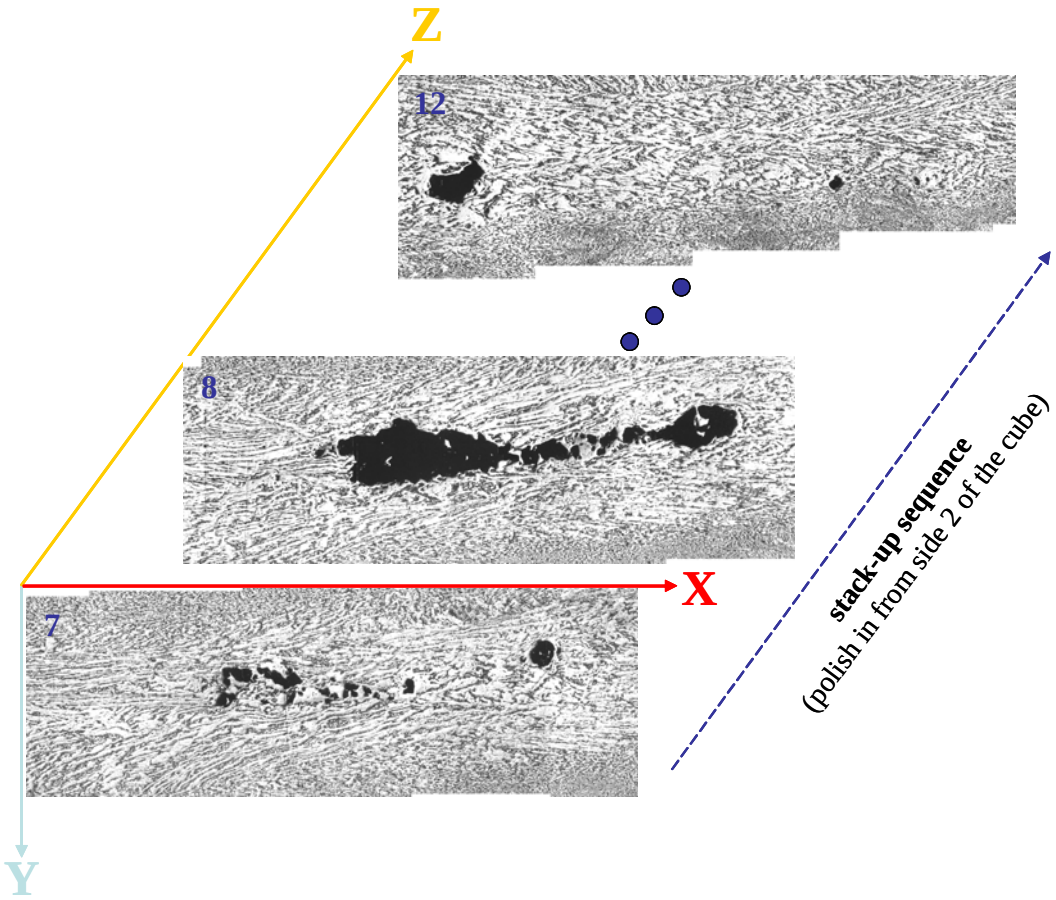
Sub-Micrograph
- size - 2400(H) by 800(V) pixels
- color - 256 gray-scale
- scale - 132 pixels =20 mils

Geometric Model
- 1 void part
  - (with branches)
- 37 geometric model parts
- 14 micrograph planes
  - (including 7 patches)
- 117 void cross-section boundary traces
  - (model part 24 uses 6 traces,
  - 34 uses 5,
  - 35 uses 4 and the rest use 3 each)

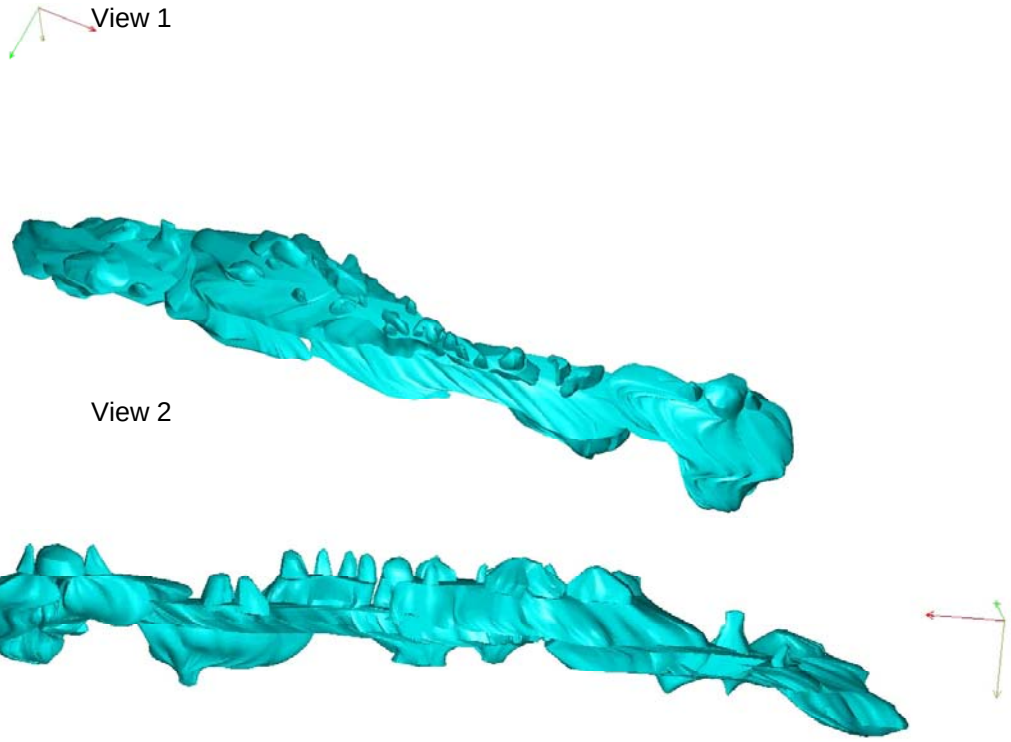
B2W2 – C



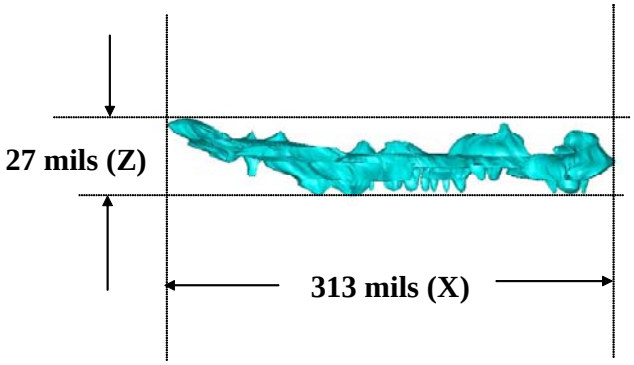
Orientation of Sub-Micrographs (B2W2 – C):



Angle views of void model for B2W2 – C:



Dimensions of B2W2 – C:

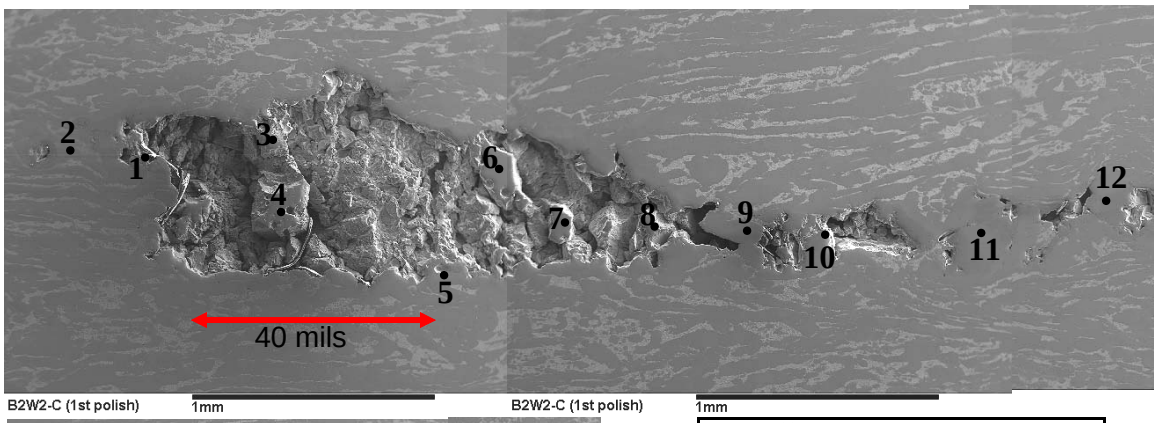


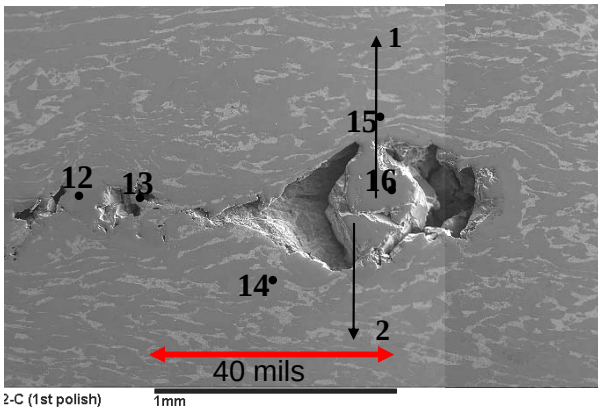
	min.	max.	size
X	19	332	313
Y	28	86	58
Z	1	28	27

Unit: mils

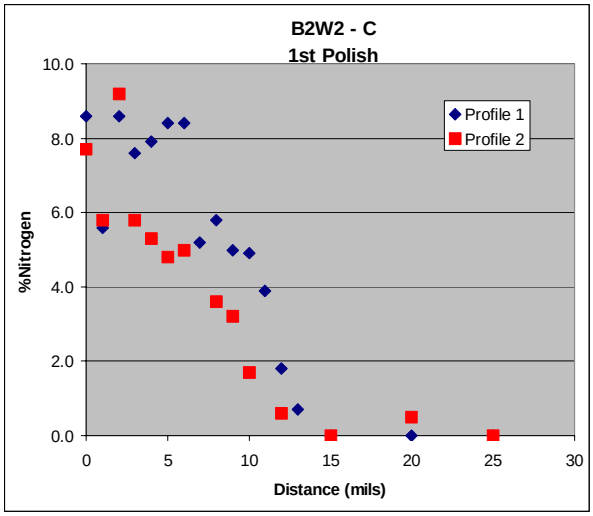
Microprobe analysis:

B2W2 – C – 8 section





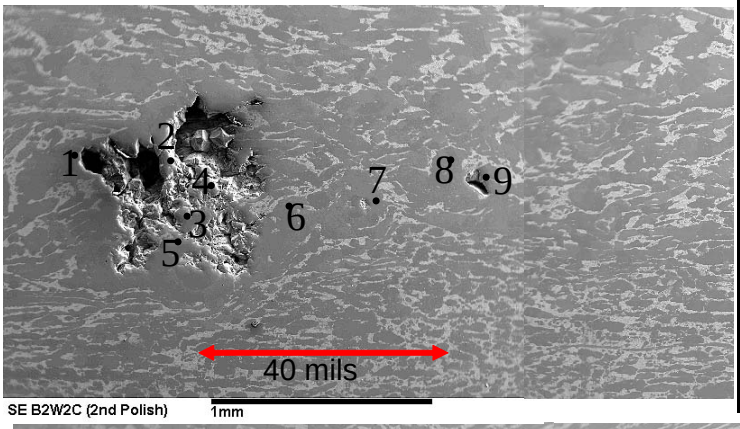
B2W2-C (1)	W %			
Pt #	Ti	Al	V	N
1	92.5	2.3	1.5	4.2
2	89.0	5.5	2.5	0.7
3	90.7	1.7	2.1	6.8
4	89.5	2.9	2.4	5.2
5	92.8	4.3	1.5	1.7
6	90.5	0.4	0.9	9.6
7	91.6	2.9	2.6	5.2
8	89.9	1.6	2.2	5.8
9	91.6	5.5	2.2	0.5
10	93.7	2.5	1.3	2.4
11	88.6	5.7	2.4	1.5
12	91.3	2.6	1.4	3.3
13	90.2	4.7	1.8	1.6
14	90.8	5.7	1.9	0.6
15	91.7	6.5	2.2	0.6
16	89.3	0.3	1.0	10.0

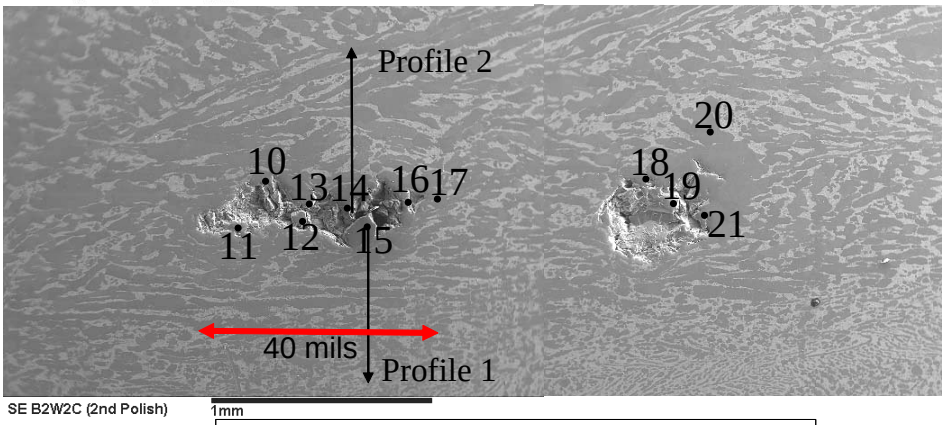


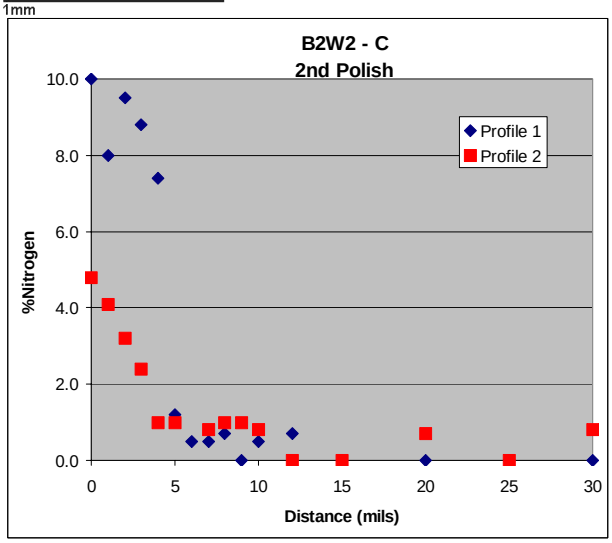
Microprobe analysis:

B2W2 – C – section 11

B2W2-C (2)	W %			
Pt #	Ti	Al	V	N
1	93.7	4.2	1.4	1.4
2	95.1	3.1	1.7	2.9
3	94.3	2.5	1.3	2.8
4	92.5	4.5	2.1	2.3
5	90.8	4.6	1.7	2.0
6	92.3	6.2	1.6	0.6
7	94.3	3.1	1.6	2.9
8	93.4	5.5	1.9	1.0
9	93.7	5.8	1.8	2.4
10	94.0	2.9	1.5	1.5
11	93.3	5.8	2.2	1.5
12	93.0	2.2	1.6	6.3
13	90.9	4.6	1.8	2.4
14	94.1	1.7	1.4	4.8
15	88.9	0.6	0.9	8.7
16	95.6	1.2	1.6	4.9
17	94.4	5.2	2.0	1.2
18	91.6	2.8	1.4	2.2
19	92.3	1.3	1.2	4.4
20	93.0	4.9	1.5	< 0.5
21	93.3	3.4	1.5	1.9

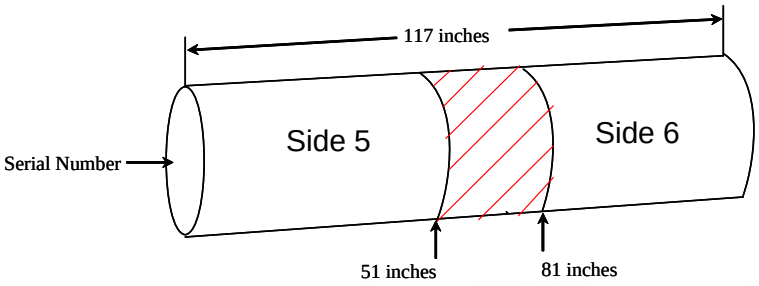






Indication: B1AW2 – B

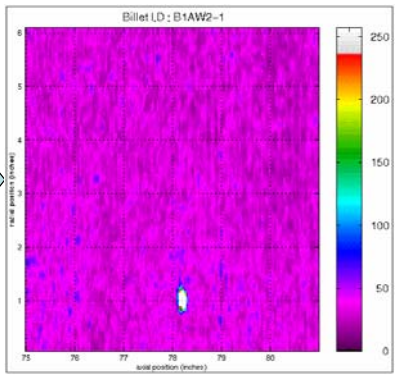
Original billet length: 117”



Billet inspection:

	Amplitude (%)	S/N	depth (in)	axial length (in)	radial length (in)
Multizone	69%	2.09	0.9	0.2300	0.4188
Conv. Longitudinal	%				
Conv. Angle	%				

Zone 1



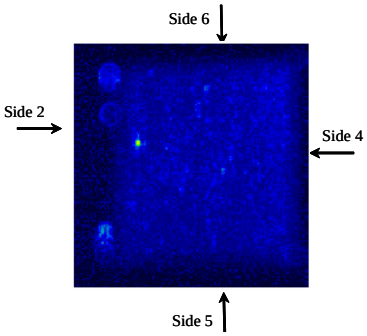
Mult inspection parameters:

Transducer - Zone 1, 6” diameter, 5MHz
Index - 0.010
Data Acquisition Rate - 0.010
Inspection Sensitivity - #2 FBH at 80-90% in Titanium
Inspection Range - 0.2” to 0.8”
Sampling Rate - 100 MHz

Depth	Axial Length	Amplitude	Signal-to-Noise Ratio
0.200”	0.180”	225%	21.7

25 MHz inspection parameters

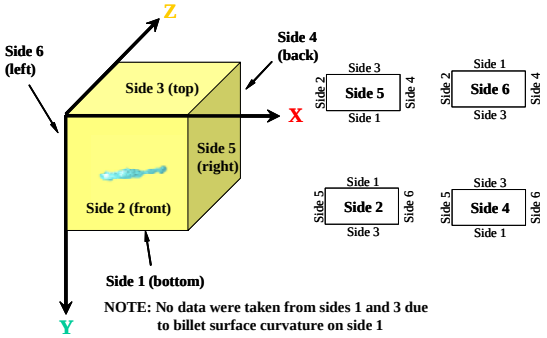
Transducer - 25 MHz, F10 - focal point positioned at indication depth
Index - 0.010
Data Acquisition Rate - 0.010
Inspection sensitivity - #1 FBH at 83% - 56 dB #2FBH at 84% at 48dB
Inspection range - C-scan , Between Front and Back / B-scan entire volume
Sampling Rate - 200 MHz



Side	Depth	Axial Length	Amplitude %	Sensitivity, dB
1	Data Not Available			
2	Cannot Detect Due to Curved Surface			
3	1.065”	0.180”	80	71
4	0.750”	0.180”	75	71
5	0.460”	0.180”	70	71
6	0.675”	0.180”	60	78

View is from Side 4, which is opposite side 2. Sides 5 and 6 represent the axial ends with Side 5 having the serial number. Sides 2 and 4 represent the hoop direction (the circumferential plane) NOTE: Data from sides 1 and 2 is unavailable.

Orientation of sample block and c-scan images:



NOTE: No data were taken from sides 1 and 3 due to billet surface curvature on side 1

B1AW2 – B 5 MHz C-scan image comparisons:

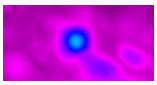
Side 2

Model



31(H) x 31(V) @10 mils, 2dB
peak amplitude @2dB=573 mv
deviation=155% or 8.1 dB

Experiment



60(H) x 30(V) @10 mils, 2dB
peak amplitude @2dB=225 mv

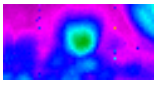
Side 4

Model



51(H) x 31(V) @10 mils, 0dB
peak amplitude @0dB=901 mv
deviation=474% or 15.2 dB

Experiment



60(H) x 30(V) @10 mils, 0dB
peak amplitude @0dB=157 mv

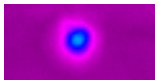
Side 5

Model



31(H) x 31(V) @10 mils, 2dB
peak amplitude @2dB=111 mv
deviation=-49% or -5.8 dB

Experiment



60(H) x 30(V) @10 mils, 2dB
peak amplitude @2dB=217 mv

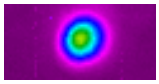
Side 6

Model

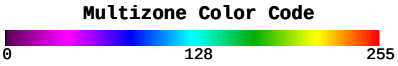


31(H) x 31(V) @10 mils, 0dB
peak amplitude @0dB=192 mv
deviation=-51% or -6.1 dB

Experiment



60(H) x 30(V) @10 mils, 0dB
peak amplitude @0dB=384 mv



Experiment 255 = 500mv for sides 2, 5 and 6
= **250mv** for side 4

B1AW2 – B 3D Solid Model Parameters:

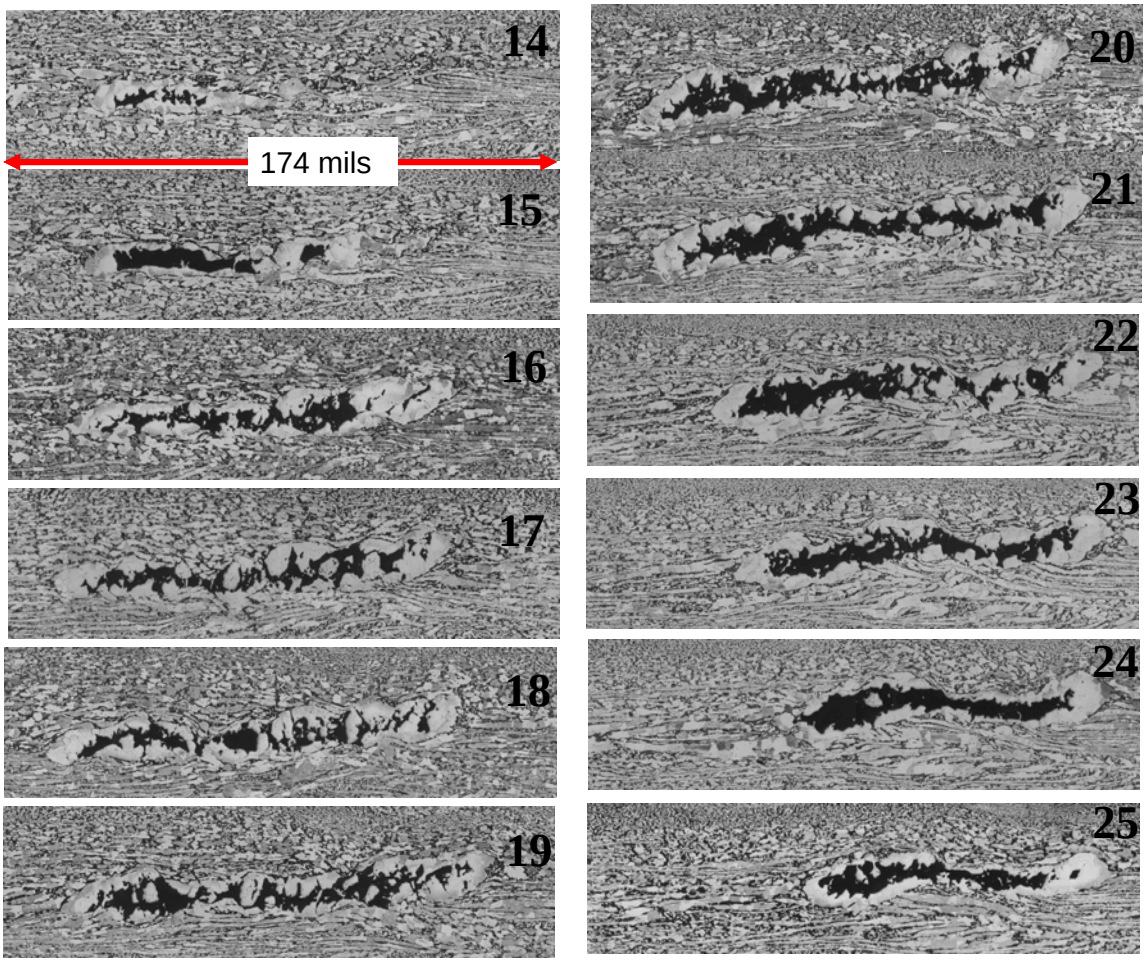
Sub-Micrograph

size - 1100(H) by 300(V) pixels
color - 256 gray-scale
scale - 5110 pixels =810 mils

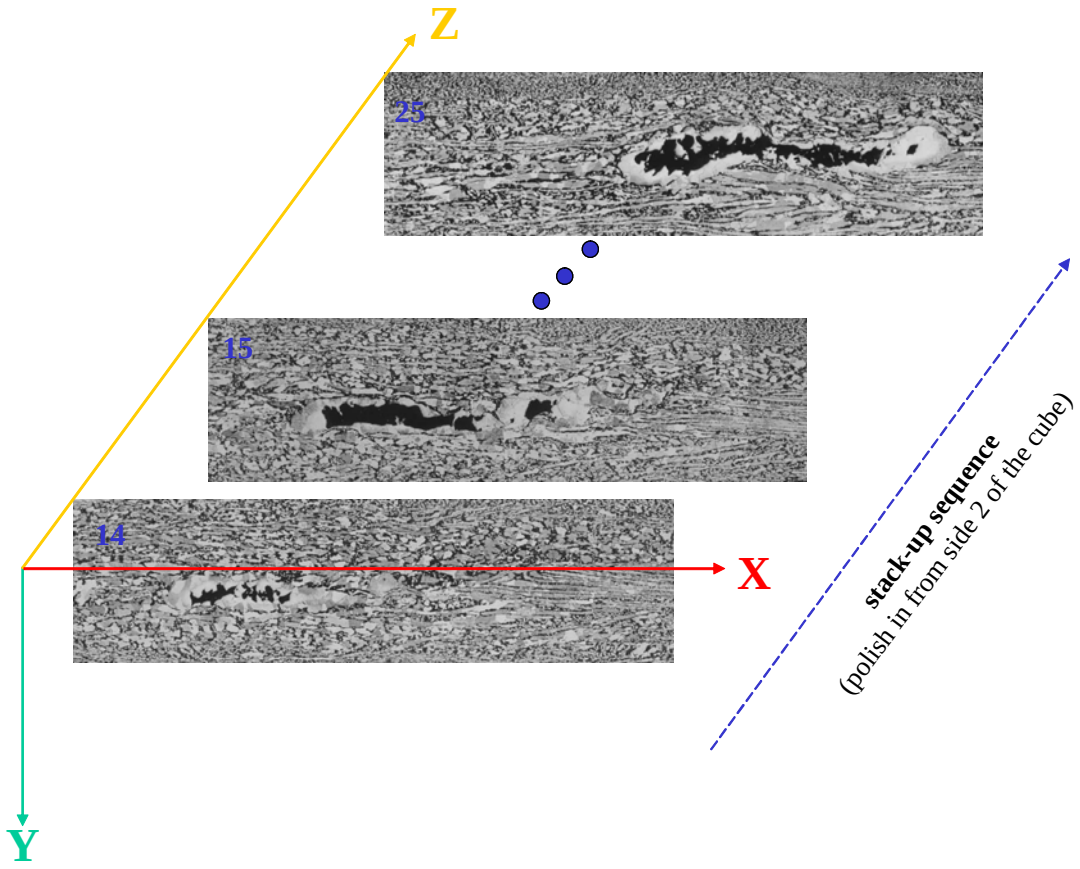
Geometric Model

1 void part
(with branches)
6 geometric model parts
17 micrograph planes
(including 4 patches)
30 void cross-section boundary traces

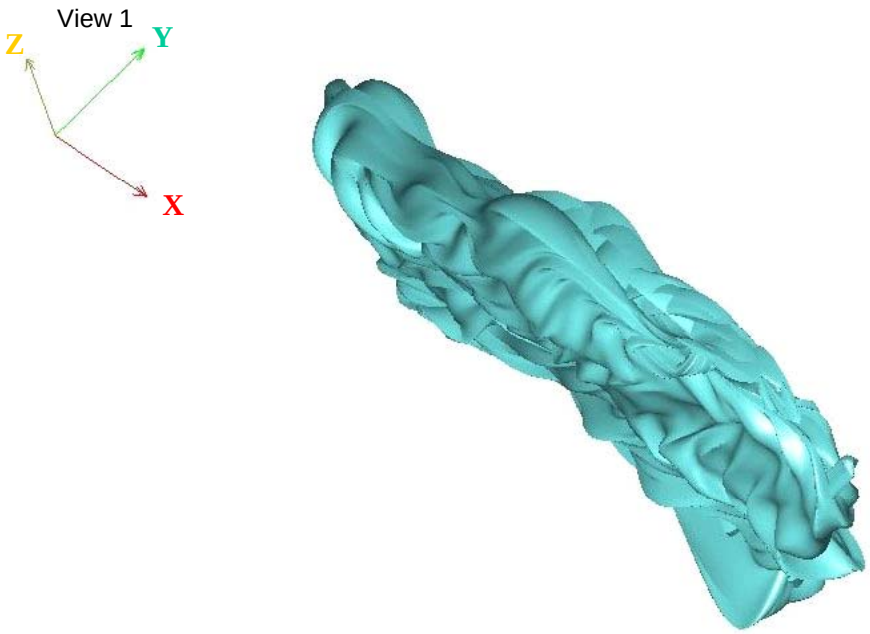
B1AW2 – B



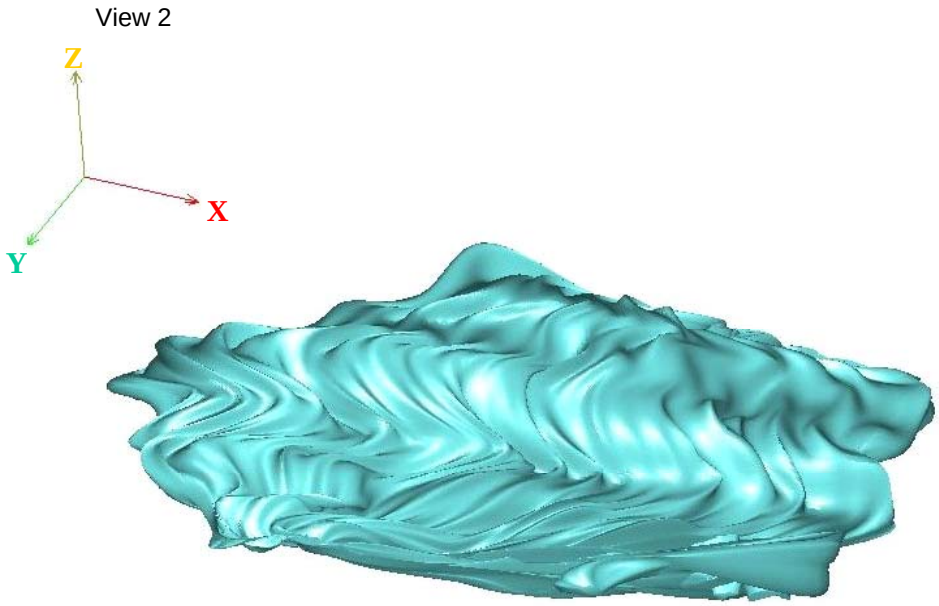
Orientation of Sub-Micrographs (B1AW2 – B):



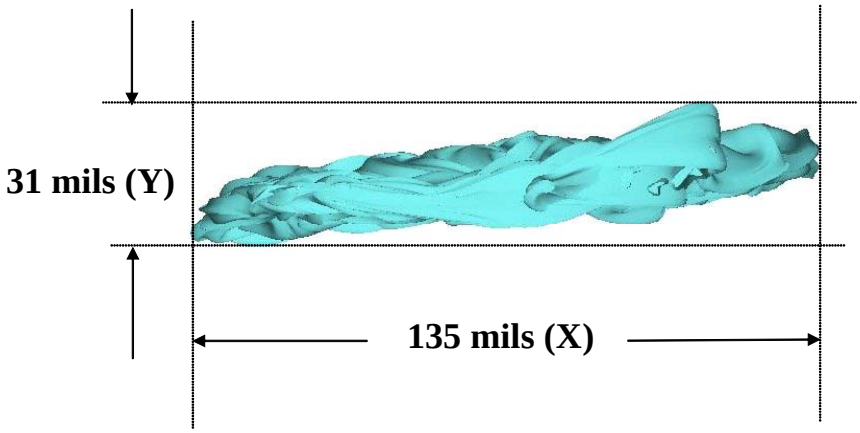
Angle views of void model for B1AW2 – B:



Angle views of void model for B1AW2 – B:



Dimensions of B1AW2 – B:

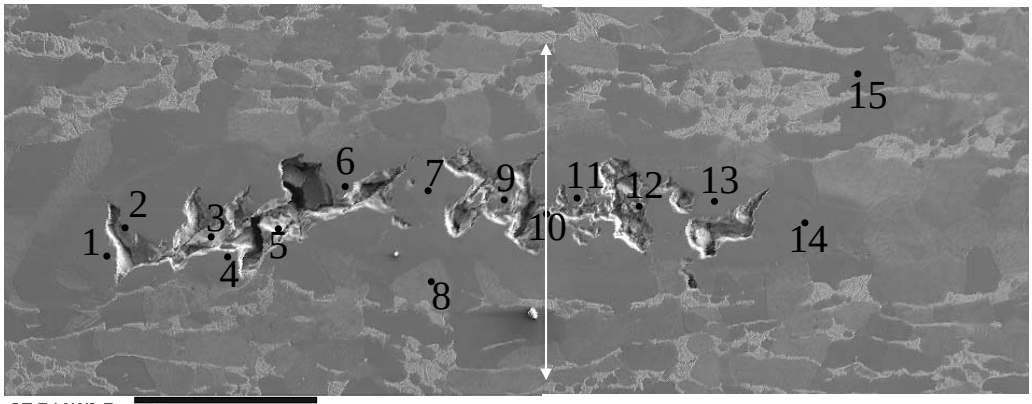


	min.	max.	size
X	21	156	135
Y	7	38	31
Z	-43	21	64

Unit: mils

Microprobe analysis:

B1AW2 – B – polish 1

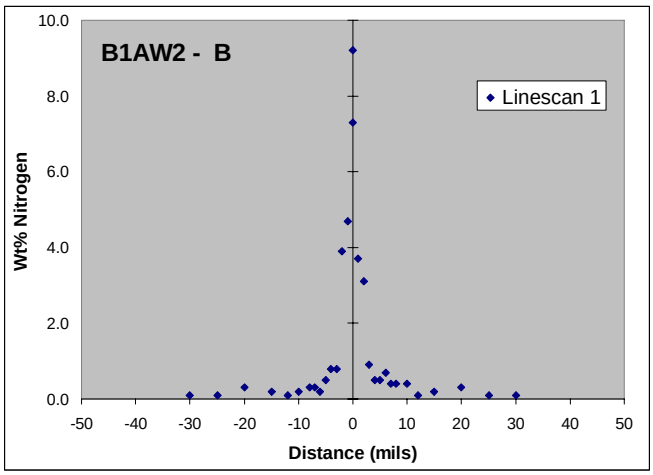


SE B1AW2-B 200um

Data for areas around the defect.

B1AW2-B W %

Pt #	Ti	Al	V	N
1	97.1	0.3	1.3	2.6
2	96.3	0.3	1.6	3.1
3	92.9	0.4	1.8	5.5
4	97.1	0.5	1.4	3.9
5	92.9	0.5	1.5	6.4
6	96.2	0.3	1.7	3.3
7	91.6	1.6	1.9	4.2
8	94.1	5.9	1.8	0.5
9	92.1	0.8	1.9	5.6
10	93.3	0.3	0.9	7.3
11	92.6	0.5	1.6	6.4
12	90.9	0.6	1.7	6.5
13	95.6	0.4	1.8	3.6
14	97.3	0.8	1.3	2.1
15	93.5	5.7	2.1	< 0.5



Indication: B1AW2 – X

Original billet length: 117”



Billet inspection:

Not detected by inspectors during production billet inspection

Mult inspection parameters:

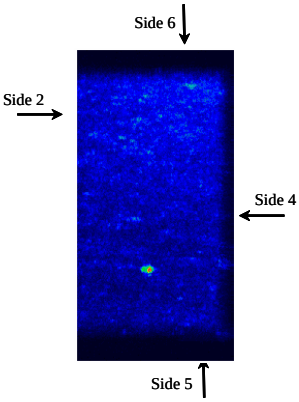
Transducer - Zone 3, 6” diameter, 5MHz
Index - 0.010
Data Acquisition Rate - 0.010
Inspection Sensitivity - #2 FBH at 80-90% in Titanium
Inspection Range - 0.8” to 1.7”
Sampling Rate - 100 MHz

Depth	Axial Length	Amplitude	Signal-to-Noise Ratio
0.618”	0.160”	Not detected in mult	

25 MHz inspection parameters

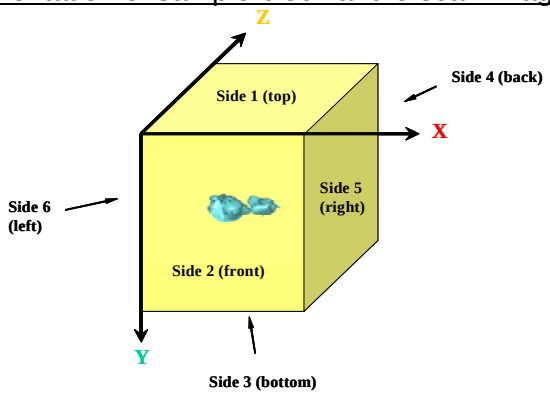
Transducer - 25 MHz, F10 - focal point positioned at indication depth
Index - 0.010
Data Acquisition Rate - 0.010
Inspection sensitivity - #1 FBH at 83% - 56 dB #2FBH at 84% at 48dB
Inspection range - C-scan , Between Front and Back / B-scan entire volume
Sampling Rate - 200 MHz

Side	Depth	Axial Length	Amplitude %	Sensitivity, dB
1	0.415”	0.160”	Data Unavailable	64
2	0.529	0.160”	80	67
3	1.247”	0.160”	37	79
4	0.485”	0.160”	80	74
5	0.487”	0.160”	76	79
6	0.498”	0.160”	78	76



View is from Side 2, the side that was polished. Sides 5 and 6 represent the axial ends with Side 5 having the serial number. Sides 2 and 4 represent the hoop direction (the circumferential plane)

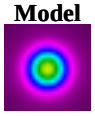
Orientation of sample block and c-scan images:



B1AW2 - X 5 MHz C-scan image comparisons:

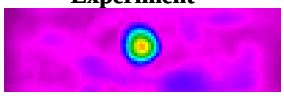
Side 1

Model



31(H) x 31(V) @10 mils, 6dB
peak amplitude @6dB=398 mv
deviation=-11% or -1.0 dB

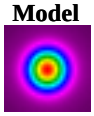
Experiment



100(H) x 30(V) @10 mils, 6dB
peak amplitude @6dB=448 mv

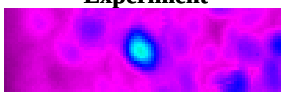
Side 2

Model



31(H) x 31(V) @10 mils, 0dB
peak amplitude @0dB=498 mv
deviation=94% or 5.7 dB

Experiment



100(H) x 30(V) @10 mils, 0dB
peak amplitude @0dB=257 mv

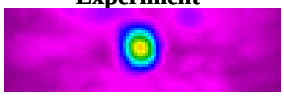
Side 3

Model



31(H) x 31(V) @10 mils, 6dB
peak amplitude @6dB=461 mv
deviation=-7.2% or -0.6 dB

Experiment



100(H) x 30(V) @10 mils, 6dB
peak amplitude @6dB=430 mv

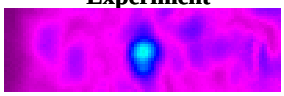
Side 4

Model



31(H) x 31(V) @10 mils, 0dB
peak amplitude @0dB=175 mv
deviation=-29% or -2.9 dB

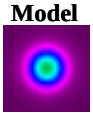
Experiment



100(H) x 30(V) @10 mils, 0dB
peak amplitude @0dB=244 mv

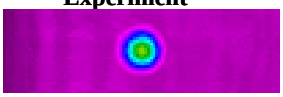
Side 5

Model



31(H) x 31(V) @10 mils, 0dB
peak amplitude@0dB = 309 mv
deviation=-17% or -1.7 dB

Experiment



100(H) x 30(V) @10 mils, 0dB
peak amplitude@0dB = 374 mv

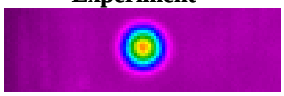
Side 6

Model



31(H) x 31(V) @10 mils, 0dB
peak amplitude@0dB = 403 mv
deviation=-10% or -1.0 dB

Experiment



100(H) x 30(V) @10 mils, 0dB
peak amplitude@0dB = 450 mv

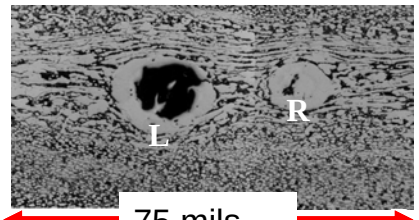
Multizone Color Code



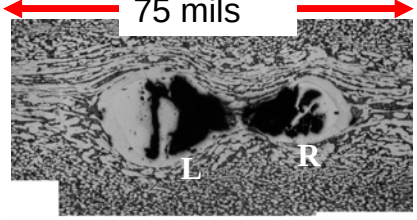
Experiment 255 = 500mv

B1AW2 - X

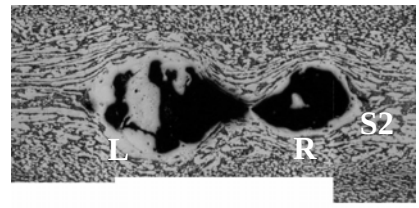
Polish 8



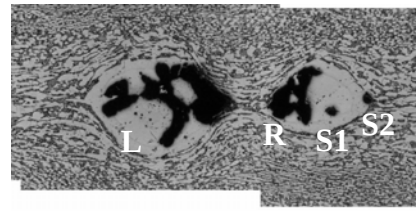
Polish 9



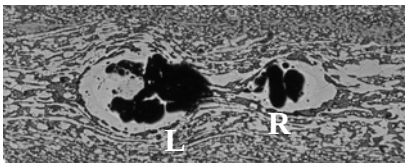
Polish 10



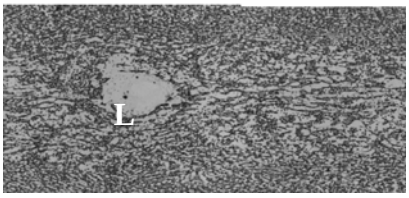
Polish 11



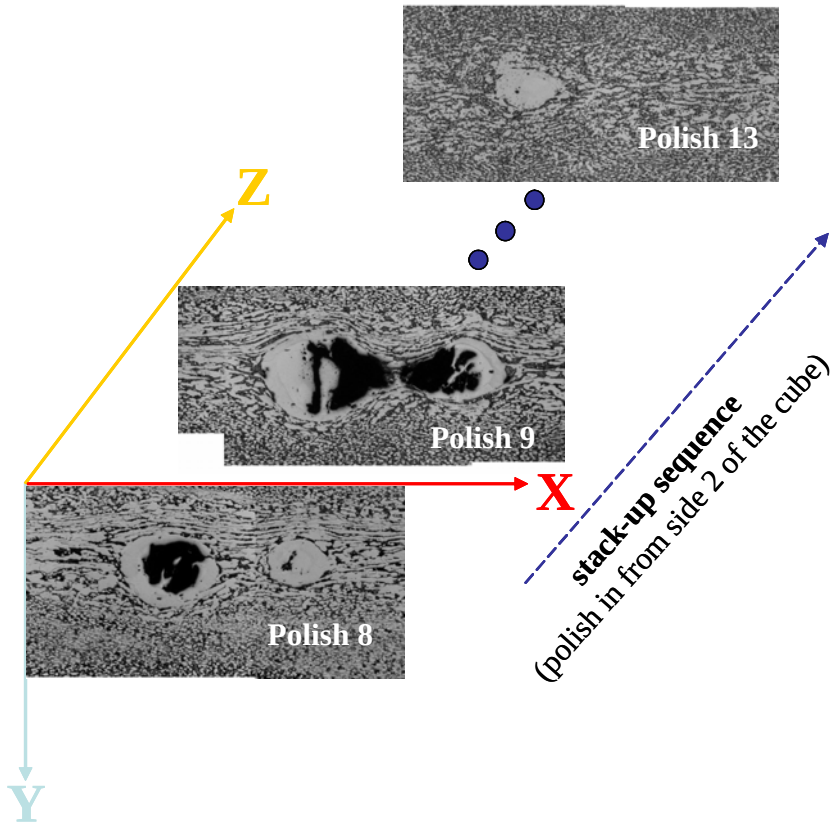
Polish 12



Polish 13

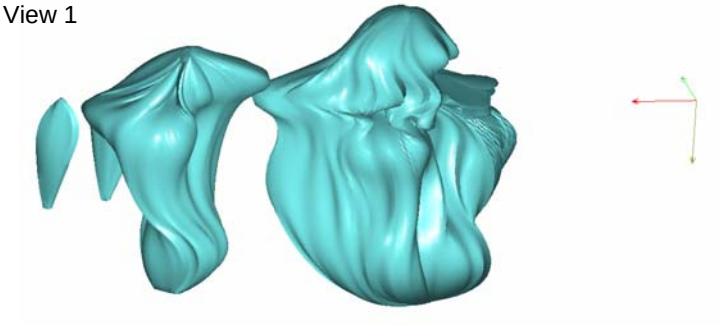


Orientation of Sub-Micrographs (B1AW2 - X):

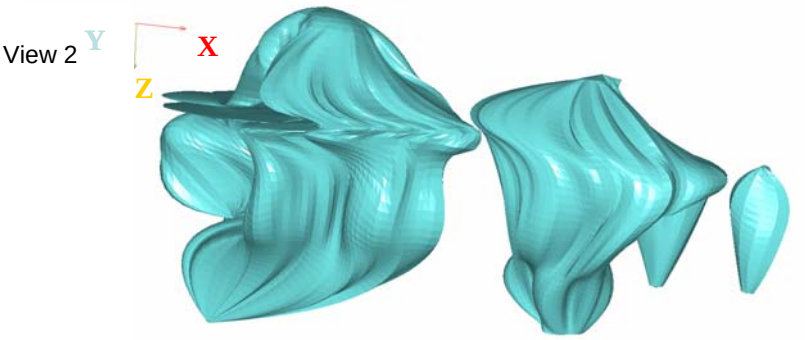


Angle views of void model for B1AW2 - X:

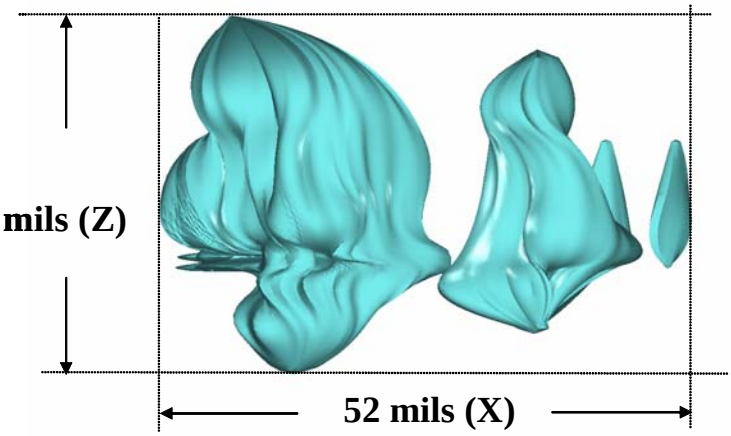
View 1



View 2



Dimensions of B1AW2 - X:

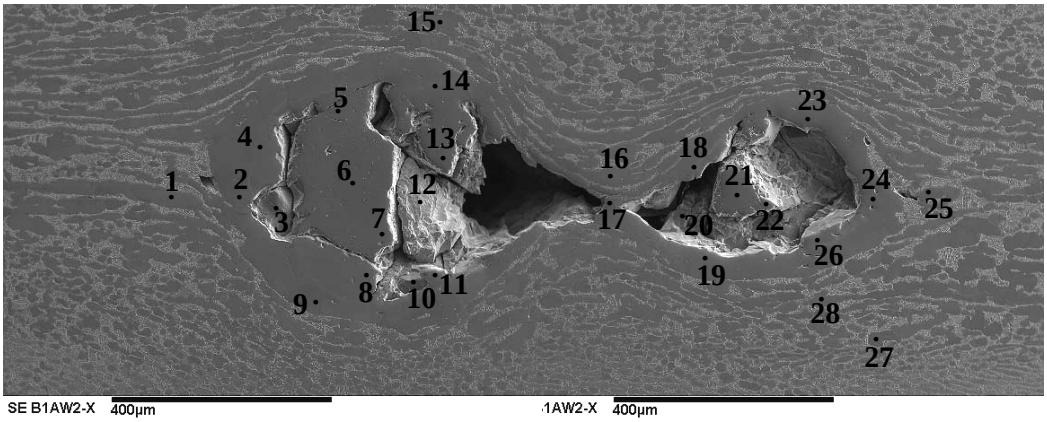


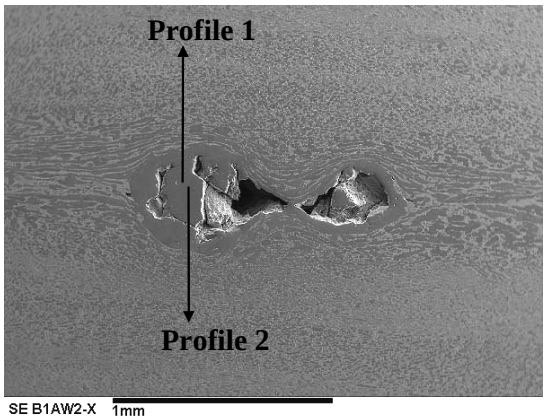
	min.	max.	size
X	15	67	52
Y	9	27	18
Z	-5	29	34

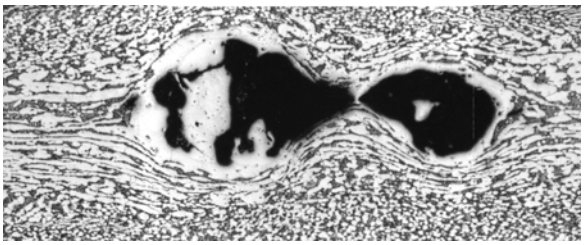
Unit: mils

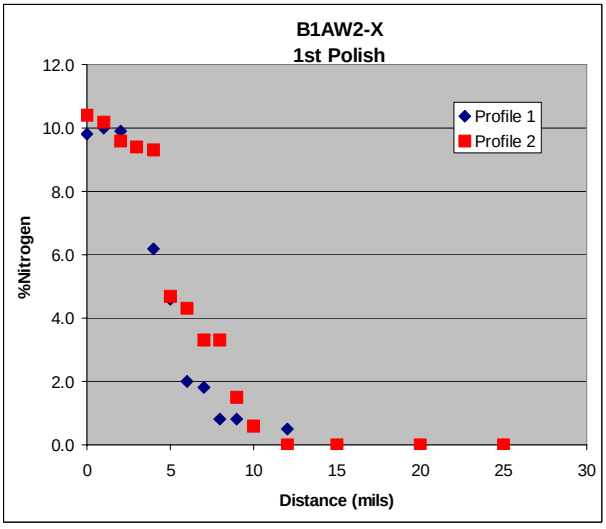
Microprobe analysis:

B1AW2 - X – section 10





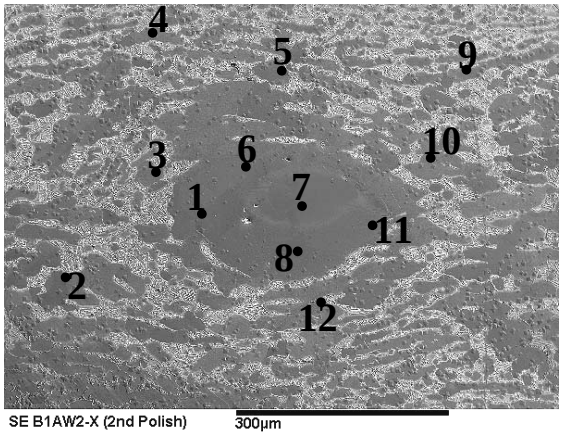


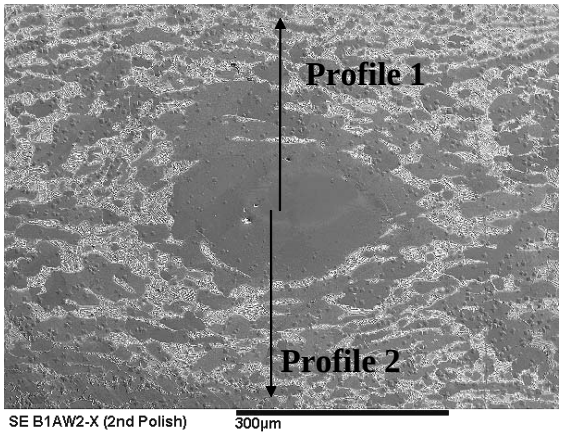


B1AW2-X	W %			
Pt #	Ti	Al	V	N
1	90.1	5.2	2.1	0.5
2	90.9	4.4	1.7	1.0
3	89.5	2.7	1.6	2.7
4	89.1	0.4	1.6	3.0
5	91.9	0.3	2.2	4.4
6	85.5	0.3	1.8	11.2
7	88.1	0.2	1.7	9.1
8	91.0	0.3	2.4	4.1
9	92.9	4.4	1.9	1.0
10	93.5	0.2	2.0	2.9
11	92.1	0.3	2.5	4.8
12	84.9	0.3	2.1	12.3
13	84.9	0.1	2.5	9.3
14	94.0	0.6	1.8	2.6
15	89.6	6.8	2.0	0.5
16	93.0	5.2	2.1	0.6
17	95.1	2.1	1.8	2.0
18	90.1	3.2	1.9	0.5
19	94.0	2.1	1.6	1.9
20	91.5	0.8	2.2	4.4
21	86.5	0.2	1.5	9.0
22	88.0	0.2	1.6	8.4
23	92.5	2.0	1.6	1.6
24	91.5	4.1	1.7	1.3
25	91.6	4.9	2.0	0.5
26	92.6	0.4	1.8	3.6
27	89.2	6.9	1.8	< 0.5
28	90.6	6.6	2.0	< 0.5

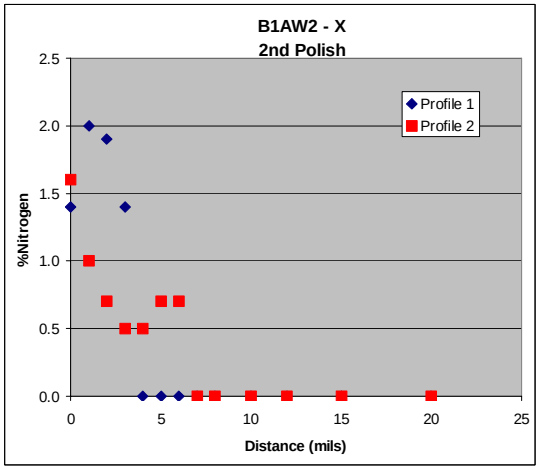
Microprobe analysis:

B1AW2 - X – section 14





B1AW2-X	W %			
Pt #	Ti	Al	V	N
1	90.3	4.7	1.8	1.1
2	92.3	5.8	1.9	0.5
3	90.7	5.1	1.9	0.5
4	91.1	6.9	2.0	< 0.5
5	91.5	6.6	1.8	< 0.5
6	93.9	4.1	1.9	< 0.5
7	94.6	0.6	1.8	1.8
8	93.6	4.3	1.7	0.7
9	91.1	6.9	2.1	< 0.5
10	92.8	5.8	2.1	0.7
11	93.0	4.5	2.0	0.8
12	93.7	5.6	1.9	< 0.5



APPENDIX F—RECONSTRUCTION OF HARD ALPHA DEFECTS USING METALLOGRAPHIC SECTIONING DATA

In this appendix, the techniques used in geometric reconstructions of the hard alpha defects are described more extensively. These were developed to build a uniform solid model of hard alpha defects using actual metallographic data. The objective of the earlier work was to develop the techniques to construct geometric models and enable testing of the ultrasonic model using output from these solid geometric models. Later efforts focused on determining the flaw boundary and using the nonuniform rational b-splines (NURBS). The appendix includes three sections:

- Description of the flaw region extraction method using primary regional growth method or the manual tracing method.
- Explanation of the scheme to determine the flaw boundary.
- Description of the theory of NURBS, which is the backbone of the geometric model reconstruction work, are both used in the early solid model and later surface model.

The geometrical models were derived from metallographic cross-section images taken from destructive sectioning of the defect regions. The reconstruction of a defect begins with the boundary determination of the respective defect regions on each of the metallographs by using some image-processing algorithms [F-1]. The three-dimensional geometrical model then follows by using the state-of-the-art NURBS techniques [F-2]. Once the geometrical models are constructed, the complete acoustical and material properties can be interpolated within the volume or on the surface of the defects.

F.1 EARLY WORK: FLAW REGION EXTRACTION.

Before the geometrical models of the flaws can be constructed, the flaw regions and their boundaries on the metallographic images need to be identified and extracted. In this work, several image-processing techniques were used for these tasks. In particular, a recursive regional growth routine was found effective in extracting the flaw regions and a boundary detection algorithm was useful for determining the flaw boundaries.

Region growing is a procedure that groups pixels or subregions into larger regions. The simplest of these approaches is pixel aggregation, which starts with a set of seed (starting) points. From these, regions are grown by adding neighboring pixels to the region if they have similar characteristics. The characteristic that was used to include a pixel in a region is that the absolute difference between the gray-scale levels of the seed be less than a prescribed threshold. Any pixel that satisfies this property will be assigned to the region. Implementation of the regional growth routine for the cracks and voids in the metallographic images were easily acceptable because the region was very distinct in nature.

Although the concept for which the regional growth routine works is easy to implement, problems arise in the actual practice. It was difficult to set a consistent threshold for a series of images with different intensity levels that would satisfy all the criteria for the boundary edge linking algorithm. A specific threshold had to be set manually for the individual image. Given

this difficulty, an alternative brute-force approach was adapted. This method works by tracking the positions of the screen locator as it passes over the metallographic images on the computer display. In this way, a rough outline of the flaw boundaries can be manually drawn to reflect the users' observation of intensity change around the flaw boundaries.

F.2 EARLY WORK: BOUNDARY DETERMINATION.

After applying the region growth technique, or the manual drawing to a metallographic image as described above, a new binary image was formed for each of the flaw regions on that image. The binary image is fully described by a set of pixels set to zero (black) and ones (white). A boundary determination algorithm was then used to detect the path around a binary image as accurately as possible. The algorithm is a recursive looped routine that uses a set of rules to detect a path around any arbitrary, binary region provided as input. The binary region of interest is indicated by a 0 or 1. The conditional statements that are used to obtain a boundary around a region are limited in number and reduce the computation by an order of magnitude over other algorithms that work on edge detection and edge linking [F-3].

The boundary determination algorithm used in this work was setup to find the least resistant path around any arbitrary binary image. The algorithm needs only three input parameters, which are the binary image, a starting point on the boundary of the region of interest, and the binary region itself. A clockwise direction and a closed boundary are assumed. The algorithm works by comparing two byte arrays as it traverses the boundary around the binary image. The first byte array stores the original binary image. The second byte array is initialized to the opposite value of the region of interest. During the traversing of the boundary around the region of interest, if any one of the conditional statements set up in the clockwise direction starting with the first test pixel are true, then the position of the satisfying pixel is added to the boundary and immediately becomes the next test position. In the occurrence of a test position being added to the boundary, the second byte array is turned to the opposite value at that location. The traversing of the boundary stops when none of the conditional statements are satisfied and the last point on the boundary is a pixel away from the starting pixel location. An example of these image-processing routines working together is shown in figure F-1.

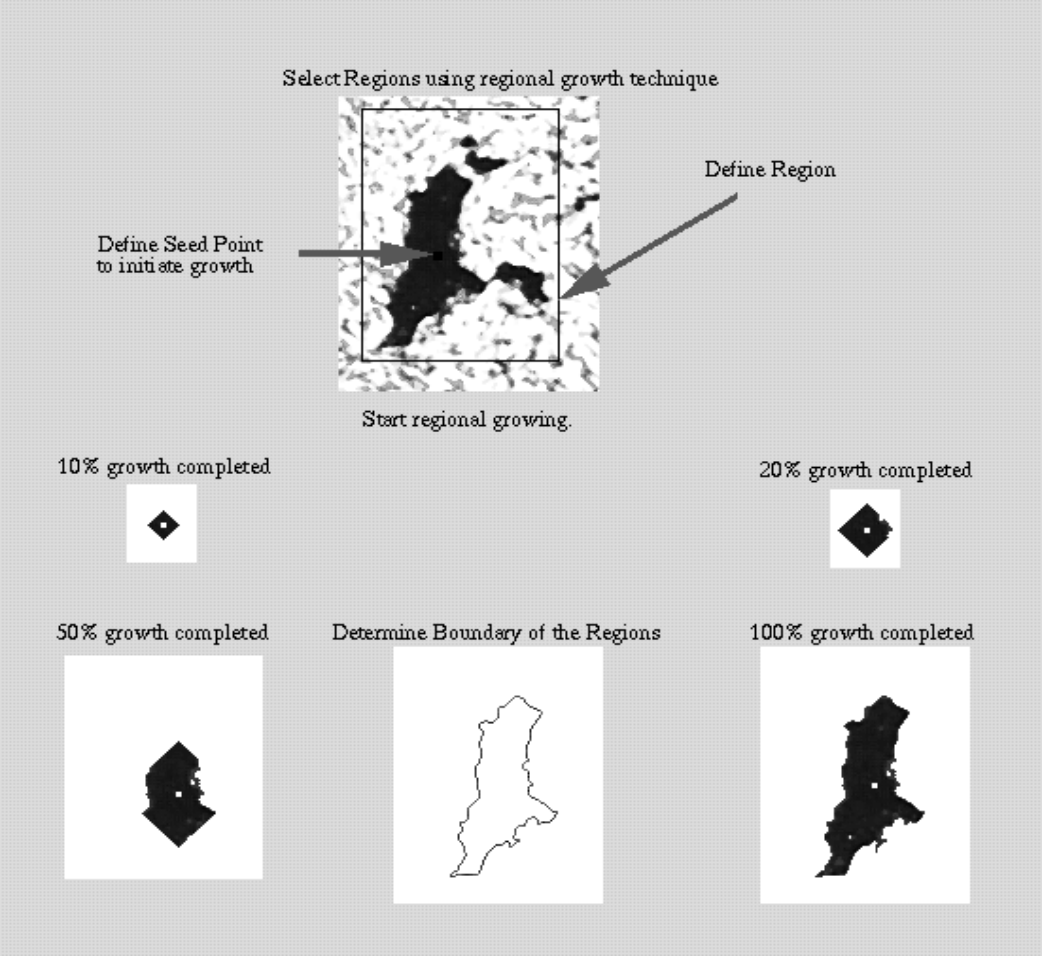


FIGURE F-1. RESULTS OF REGION GROWING AND BOUNDARY DETECTION ROUTINES

F.3 THEORY OF NURBS.

This section briefly discusses the theory of NURBS. For more details, the reader is referred to reference F-4 and the cited literature therein. The geometrical modeling of the hard alpha defects begins with the normalization of the extracted contour data from the image-processing routines. The normalization was carried out by subdividing each of the contours into *n* line segments of equal length. NURBS and their Bezier subsets are then used to interpolate the sets of contour data with *n* points into an *m* by *n* surface mesh where *m* is the number of contours being interpolated through.

A generic NURBS surface can be expressed as [F-2]

$$\vec{S}(u,v) = \sum_{i=0}^{n} \sum_{j=0}^{m} N_{i,p}(u) N_{j,q}(v) \vec{P}_{i,j} \qquad \text{(F-1)}$$

where the surface is $\vec{S}$, $\vec{P}_{i,j}$'s are the control points, and $N_{i,p}(u)N_{j,q}(v)$ are the basis functions as given by

$$N_{i,0}(u) = \begin{cases} 1 & if \quad u_i \le u \le u_{i+1} \\ 0 & otherwise \end{cases}$$

$$N_{i,p}(u) = \frac{u - u_i}{u_{i+p} - u_i} N_{i,p-1}(u) + \frac{u_{i+p+1} - u}{u_{i+p+1} - u_{i+1} N_{i+1,p-1}} \tag{F-2}$$

The p and q are the degree of interpolations in the u and v directions, respectively. For the calculation of $N_{j,q}(v)$, just substitute j for I, q for p, and v for u. v and u are knots in the knot vector given by equation F-3. Knot vectors are comprised of a set of nondecreasing real numbers called knots.

$$\vec{U} = \{u_0, u_1, \ldots, u_{m-1}) \quad i = 0, \ldots . m - 1 \tag{F-3}$$

Global surface interpolation is accomplished by using equation F-4 on a given set of points (n+1) x (m+1) data points{ $Q_{k,l}$ }, k=0,…,n and l=0,…,m. p and q are the degrees of interpolation in the u and v directions, respectively.

$$\vec{Q}_{k,l} = \vec{S}(\bar{u}_k, \bar{v}_l) = \sum_{i=0}^{n} \sum_{j=0}^{m} N_{i,p}(\bar{u}_k) N_{j,q}(\bar{v}_l) \vec{P}_{i,j} \tag{F-4}$$

An example of the flaw reconstruction procedure is illustrated in figure F-2. First, the position trace was manually drawn to define a region of interest in a metallographic image. A linear pixel interpolation followed to enclose the distance between the points and to have a one-to-one pixel boundary mapping on the image to ensure that the boundary was a closed loop defining a region of interest. Once the linear pixel interpolation was completed, the boundaries were normalized to a set of n points in a clockwise manner starting at the position having the coordinates of centroid of area in the horizontal direction and the lowest reading in the vertical direction. After the same procedure was applied to all of the metallographic images, a three-dimensional solid model was constructed, as shown in figure F-3. The model was created using a bilinear interpolation between each successive slice of data. This model also allowed for the solid to be sliced apart and the interior of the solid could be analyzed at any orientation, as shown in figures F-4 and F-5. Figure F-6 shows an improved surface model using the same manual boundary traces with Bezier interpolation routines. Finally, a global surface interpolation implementing the advanced NURBS on another set of metallographic images is depicted in figure F-7, in which the exact boundaries around void regions were extracted.

NURBS were chosen for the interpolation of the model because of the control a user would have in modifying the shape of a surface once a model was initially created. A user could change the shape of a constructed model by modifying weights or control points. B-spline basis functions have been chosen over the Bezier and linear surface interpolation for the geometrical design of

the model because of the high degree requirement by the Bezier curve function. To fit a curve containing *n* points, a Bezier curve has to complete an *n*-1 degree calculation.

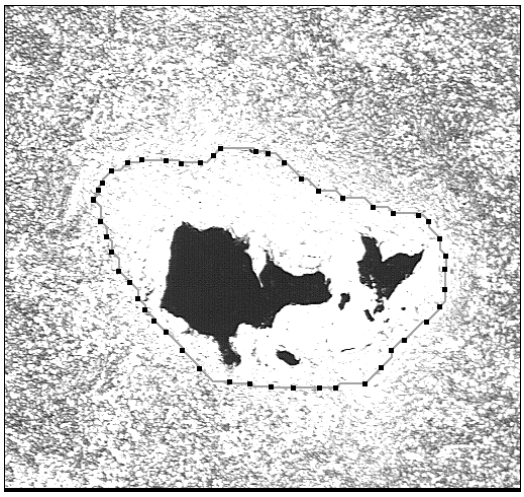


FIGURE F-2. BOUNDARY TRACE OF THE DIFFUSION ZONE OF A METALLOGRAPHIC CROSS SECTION OF A REAL HARD ALPHA DEFECT

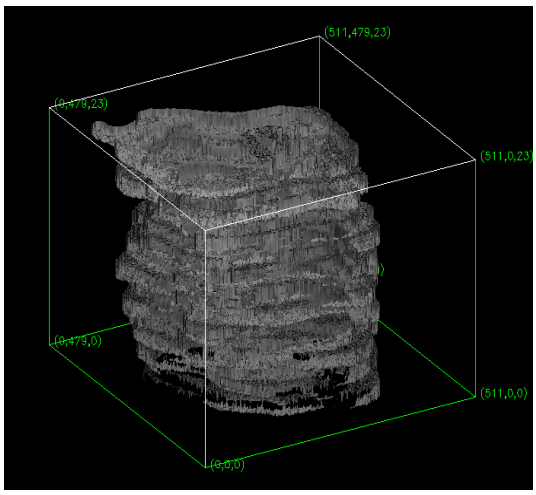


FIGURE F-3. SOLID MODEL RECONSTRUCTION AROUND A REGION OF INTEREST WITH LINEAR DYNAMIC, POSITION LOCATOR TRACES, AND PIXEL INTERPOLATION

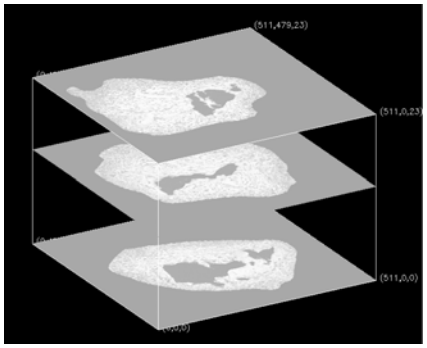


FIGURE F-4. A STACKUP OF BOUNDED SLICES

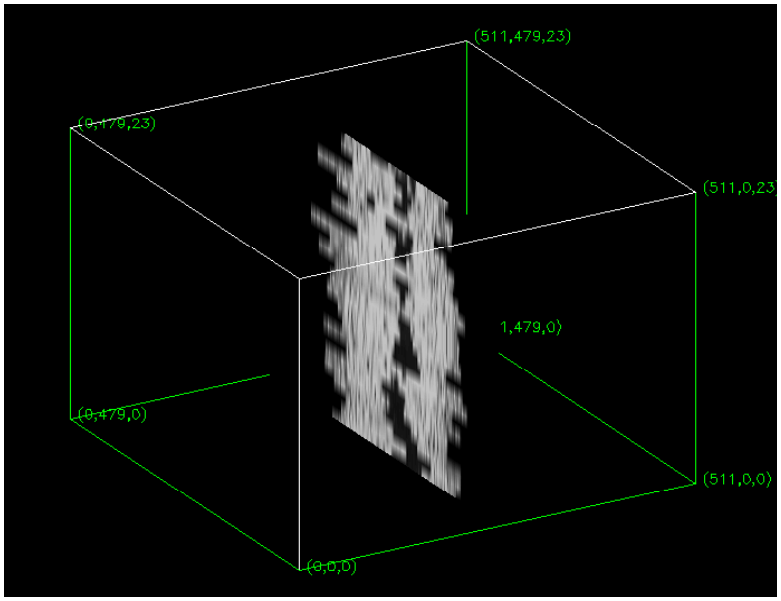


FIGURE F-5. ANALYZE INTERIOR PROFILE FOR ARBITRARY ORIENTATION

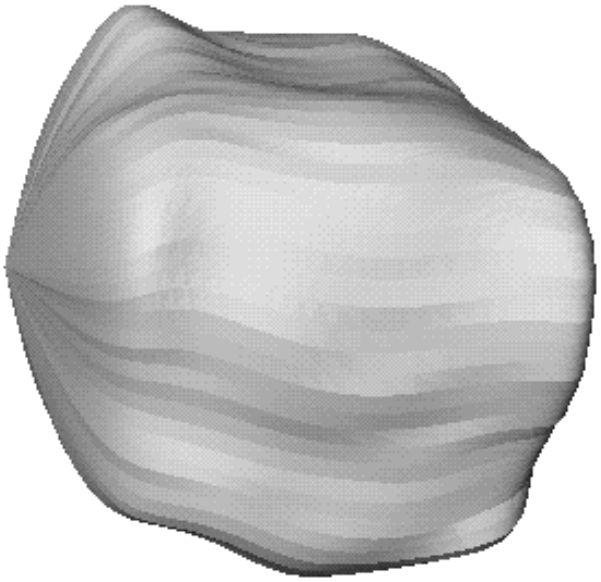


FIGURE F-6. BEZIER SURFACE MODEL OF THE TRACED BOUNDARIES

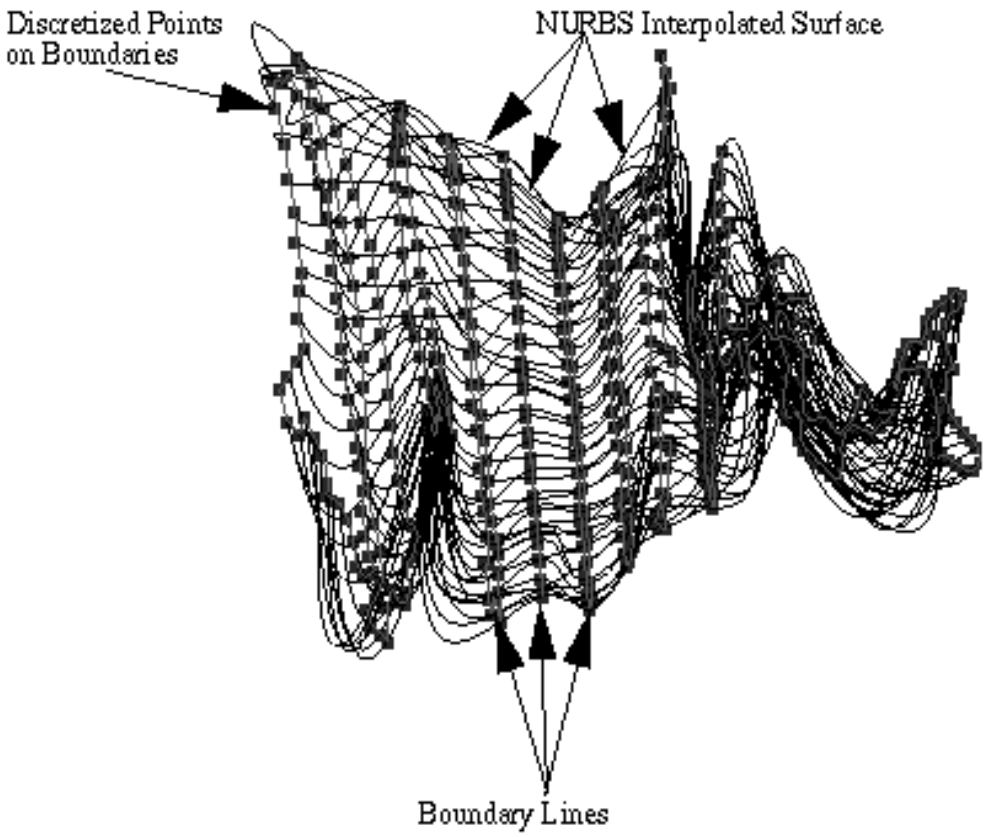


FIGURE F-7. NONUNIFORM RATIONAL B-SPLINE INTERPOLATED SURFACE MODEL OF EXACT BOUNDARY EXTRACTION OF VOIDS IN A SET METALLOGRAPHIC IMAGES

F.4 REFERENCES.

F-1. Rafael C. Gonzalez and Richard E. Woods, *Digital Image Processing*, Addison-Wesley Publishing Company, 1992.

F-2. Les Piegl and Wayne Tiller, *The NURBS Book*, Springer-Verlag Publishing Company, 1995.

F-3. C.-P. Chiou, F.J. Margetan, R.B. Thompson, and Brian Boyd, "Development of Ultrasonic Model for Hard Alpha Inclusions in Titanium Alloys," *Review of Progress in Quantitative Nondestructive Evaluation*, D.O. Thompson and D.E. Chimenti, eds., Vol. 16B, p. 1529, 1997.

F-4. B. Boyd, "Development and Application of Geometrical Models of Defects for Ultrasonic Nondestructive Evaluation in Aircraft Engine Alloys," Master thesis, Iowa State University, 1998.

APPENDIX G—ULTRASONIC MODELING OF HARD ALPHA DEFECTS

This appendix discusses the details of the ultrasonic modeling effort with emphasis on a Born model for inclusion of complex morphology, a multilayered exact model for spherical inclusions, and a multifacet Kirchhoff model (MKIR) for voids of arbitrary shape. The basic framework has been described thoroughly in appendix A1 of the Engine Titanium Consortium Phase I report on probability of detection (PoD) [G-1]. To make this report self-contained, a portion of that appendix is cited below.

G.1 MEASUREMENT MODEL FRAMEWORK.

"The ultrasonic flaw response modeling approach in this work is derived within the context of Auld's electromechanical reciprocity relation [G-2] as has been demonstrated previously in the derivation of the Thompson-Gray measurement model [G-3]. Auld's reciprocity relation provides a general and rigorous way to relate ultrasonic scattering theory to the absolute level of signals observed at the electrical ports of a transducer. The key in this process is the specification of the wavefields in the vicinity of the flaw, in terms of scattering theory. Within this framework, the Thompson-Gray measurement model describes an immersion inspection process in which the flaw is small with respect to the ultrasonic beam width. In this small flaw limit, the prediction of the overall signal is made in terms of the product of a number of factors, which may be thought of as theoretical modules which describe the flaw scattering response, beam propagation, medium attenuation, and interface transmission effects. In order to make absolute predictions of flaw response, inference of the system response obtained from a separate reference experiment is required. The measurement model is formulated in the frequency domain. For a given inspection geometry and flaw particulars, the absolute values of various radio-frequency (rf) flaw waveforms can be predicted to great accuracy through the use of inverse Fourier transform techniques.

Symbolically, the frequency domain components predicting the results of the inspection process, as predicted by the Thompson-Gray measurement model, can be summarized in the following expression:

$$\begin{bmatrix}\text{Spectral}\\ \text{component}\\ \text{of flaw signal}\end{bmatrix} \propto \begin{bmatrix}\text{probe}\\ \text{efficiency}\\ \text{factor}\end{bmatrix}\begin{bmatrix}\text{interface}\\ \text{transmission}\end{bmatrix}\begin{bmatrix}\text{diffraction,}\\ \text{focusing,}\\ \text{and other effects}\end{bmatrix}\begin{bmatrix}\text{phase \&}\\ \text{attenuation}\end{bmatrix}\begin{bmatrix}\text{flaw}\\ \text{signature}\end{bmatrix} \quad \text{(G-1)}$$

Here the "diffraction, focusing, and other effects" sub-module describing the effects of beam propagation, as influenced by the part geometry, is calculated based on the Gauss-Hermite beam model [G-4]. The "probe efficiency factor" sub-module, used to account for the system efficiency, is deduced from a measured rf reference signal for which backsurface echoes obtained from a fused quartz plate are normally used. This reference signal together with other geometry and material parameters, such as "interface transmission", "phase & attenuation", and "flaw signature", are the necessary inputs to predict the signal

> response. After the "spectral component of flaw signal" is evaluated at all frequency components within the transducer bandwidth, the time domain rf signal can then be synthesized via fast Fourier transform techniques. The main advantage of taking this approach is the reduction of computational effort, while maintaining necessary modeling complexity, through the introduction of appropriate approximations in the various modules. The use of the Gauss-Hermite beam model, for example, enables the wave fields to be rapidly calculated in the regions of interest; thereby enabling the evaluation of the "diffraction, focusing and other effects" sub-module. In contrast with other numerical methods such as finite element and boundary element, this beam model consumes much less computation time."

The key component of all these submodules is the flaw signature, which depends on the actual flaw morphology as well the illuminating ultrasonic beam pattern. The specific flaw signature for each of the three models mentioned above are discussed in the following paragraphs.

G.2 BORN MODEL FOR INCLUSIONS.

The basic Born inclusion model is the same as described in Appendix A.1 of the Phase I PoD report. For the sake of completeness, here again the related portions are cited.

> "In modeling weak scatterers such as the hard alpha inclusions, one good choice is the Born approximation, which has been extensively studied in the literature."

See, for example, references G-5 and G-6.

> "This approximation greatly simplifies the modeling effort by replacing the otherwise unknown scattered field quantities that appear within the kernel of various integral representations by their incident counterparts on the surface or within the volume of the flaw. In our new formulation, the Auld's surface reciprocity relationship was first converted into a volumetric form via Gauss' theorem. The paraxial and Born approximations were then utilized to reduce the new form to a three-dimensional volumetric integral involving the square of incident displacement field and the inclusion properties." In the ordinary context of the Born approximation, both the density and wave speed are assumed to be very close to those of the host materials, i.e., the flaw is assumed to possess a weak (small) impedance mismatch. Intuitively, this weak impedance assumption is consistent with the Born approximation that replaces the wavefield quantities within the inclusion by the incident field counterparts. However, from a comparative study with the high-frequency Kirchhoff approximation [G-7], both approximations (Born & Kirchhoff) have been shown to be equivalent in modeling the leading specular (front surface) responses. As such, it has become unnecessary to impose this weak impedance assumption."

As was shown in the previous study [G-8], the normal Born model without the weak impedance assumption actually offers better accuracy in comparison with the experimental data for inclusions of higher impedance.

In order to accommodate the complex geometry and composition of the Contaminated Billet Study hard alpha defect, a new implementation was adapted using a simple linear approximation. This was done by approximating the three-dimensional volumetric integral of the Born model as the linear sum of a series of two-dimensional planar surface integrals. The stackup sequence of the metallographic images (figure F-4 in appendix F of this report) provides a natural way of implementing such linear sum. For an inhomogeneous inclusion embedded in an otherwise isotropic, homogeneous media, the symbolic form of the flaw signature (equation G-1) for this implementation can be expressed as

$$\left[\textit{flaw signature}\right] \approx \sum_{i=1}^{M}\left[\iint_{A_i}\left(\begin{matrix}\textit{incident}\\ \textit{displacement field}\end{matrix}\right)^2 f\left(\begin{matrix}\textit{material and}\\ \textit{acoustic property}\end{matrix}\right)dA\right]dL_i \qquad \text{(G-2)}$$

in which the double area integral is done on the flaw area A_i on each of the cross-section metallograph. The integrand consists of the square of displacement field of the incident ultrasonic beam as predicted by the beam model, and an expression as function of the material and acoustic properties that fully describe the inhomogeneity everywhere within the inclusion. dL_i denotes the spacing distance in between the adjacent metallographic cross sections. The flaw signature at a specific frequency is then the linear summation of the product of the double integration and the spacing dL_i over all metallographs.

To demonstrate the capability of this model, a calculation was performed using the geometrical model constructed in figure F-6 in appendix F of this report as input. In figure G-1, the A-scan model predictions are compared between the test defect model and a cylindrical model of equivalent size. In both cases, the acoustic properties of pure titanium with 5.9% nitrogen contamination were assumed. The inspection scenario simulated was for both flaws orientated at their side-on positions at a depth of 1.5 inches scanned by a 5-MHz transducer at normal incidence. As was expected, due to its irregularities in shape, the front and back surface echoes of the test defect cannot be resolved as those of the same-size flaw of cylindrical shape. In addition, the peak amplitude of test defect is significantly lower than the cylindrical flaw counterpart.

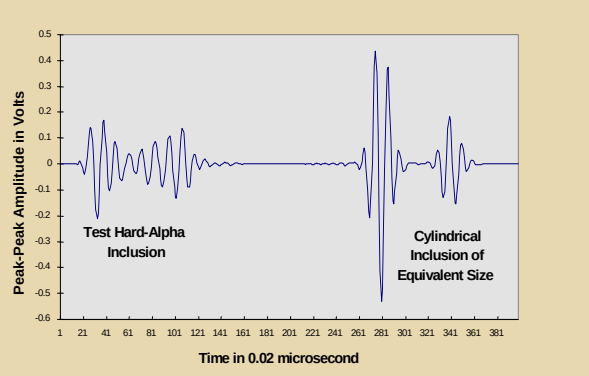


FIGURE G-1. A-SCAN COMPARISON BETWEEN THE TEST HARD ALPHA INCLUSION AND A CYLINDRICAL INCLUSION OF EQUIVALENT SIZE (Both are 0.175″ diameter by 0.11″ length at 1.5″ depth, scanned by a 5-MHz transducer at central side-on position.)

G.3 MULTILAYERED EXACT MODEL FOR SPHERICAL INCLUSIONS/VOIDS.

As described previously, the material properties of the hard alpha defects and their surrounding regions were obtained by a material model using the metallographic images from destructive sectioning of the defects. These material property data are then input to the ultrasonic model to calculate the flaw signal predictions. In order to quantify the accuracy of the approximate Born models used in the inhomogeneous hard alpha defect calculations (discussed above and in references G-8 and G-9), other theoretical solutions are sought for independent verifications. However, to the authors' best knowledge, an exact model suitable for real hard alpha defects of complicated morphology is not yet available today. At the first attempt to develop such a model, a classic exact series solution has been extended for spherical inclusion/void, which was first derived by Ying and Truell [G-10] and later integrated with void result by Pao and Mow [G-11], both using the separation-of-variable method.

To accommodate the inhomogeneous structure of the hard alpha defects (in the spherical shape), a hard alpha defect was approximated by a number of concentrically homogeneous layers and applied the Pao and Mow building block solution to each layer. At each frequency, an overall matrix equation is assembled and solved for the coefficients of which the outer-most layer represents the out-going wave solution of interest. Following the basic framework as stated above, this layered spherical inclusion/void model is also cast into the Thompson-Gray measurement model framework in conjunction with the Auld's reciprocity formulation. The symbolic form for flaw signature (equation G-1) in the far field can be expressed as

$$\left[\textit{flaw signature}\right] \approx \sum_{i=1}^{N} C_i \Phi_i \qquad \text{(G-3)}$$

where C_i's are the out-going wave coefficients from the matrix solutions and the Φ_i's are combinations of spherical wave phase terms, Legendre functions and their derivatives. The series are truncated at N terms when convergence is reached.

This new layered inclusion/void model has been tested against the Born model in cases of spherical inclusion and void cores, both surrounded by the hard alpha layers profiled by the material model, as shown in figure 34 of this report. Overall good agreement between the layered exact model and Born model is clearly shown in figure G-2. It is also observed that the 30 mils thickness of the hard alpha layer seems to be insufficient to make a significant change on the overall ultrasonic response of the hard alpha defects. As was stated previously, this observation justifies the use of the Kirchhoff model (see section G.4), which was employed to calculate the ultrasonic response from void portions of the hard alpha defects.

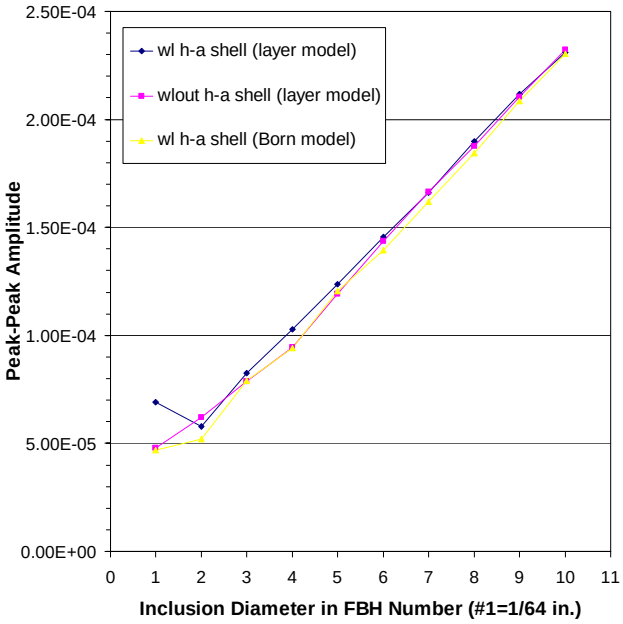


FIGURE G-2. PEAK AMPLITUDE COMPARISON BETWEEN MULTILAYERED EXACT MODEL AND BORN MODEL

G.4 MULTIFACET KIRCHHOFF MODEL FOR VOIDS.

As described previously, the morphology of hard alpha defects is complicated. Exact models capable of predicting the ultrasonic responses of real defects with such complexity, to the authors' best knowledge, are not available. Even if such exact models were available, current technology does not provide sufficient and accurate morphological data. Thus, modeling efforts were focused on the use of approximations to reduce the complexity. An approximate ultrasonic model using the high-frequency Kirchhoff approximation has proven to be successful for modeling various volumetric voids or cracks. The Kirchhoff model is particularly suitable for making use of the multifaceted data of the defect surfaces provided by the geometric model. It should be noted that the modeling emphasis was placed on the void portions of these hard alpha defects because of their dominance in determining the ultrasonic responses. This choice of emphasis was justified by studies that have been conducted on the ultrasonic response from spherical inclusions/voids using exact series solutions, as discussed in appendix F. In these studies, the hard alpha layer was estimated to contribute at most 10% of the overall ultrasonic response of a typical hard alpha defect.

In the frequency domain, the symbolic form of flaw signature for the general Kirchhoff model can be expressed as

$$\left[flaw\ signature\right] \approx \iint_{lit\ surface} \left[\begin{matrix} incident \\ wave\ field \end{matrix}\right]^2 dA \qquad \text{(G-4)}$$

where the incident wave field amplitudes and phases are calculated by a Gauss-Hermite beam model.

Under the high-frequency Kirchhoff assumption, only the portions being illuminated by the ultrasonic beam contribute to the flaw response. This is indicated by the lit surface in the double surface integral of equation G-4. When plane-wave illumination and simple flaw geometry such as an elliptical crack or an ellipsoidal void are considered, analytic solutions to the surface integral are available. In dealing with finite-beam effect and complex flaw geometry, however, the integration has to be accomplished numerically. For the latter case, involving the intricate void components of the natural hard alpha defects, detailed geometrical information of the reflecting surface are required. By way of geometrical modeling, complete parameterization of the void surface has been established. In the current implementation, the geometrical information is given in terms of triangular element (facet) connections and the corresponding nodal coordinates. Using the geometrical information, one can proceed to compute the local contributions to the integral in each facet. The total surface integration is then the sum of contributions from all facets. Here, a simple scheme is adopted that numerically resembles the mean-value theorem, with the centroid points of the facets used to approximate the mean-value locations. This integration procedure is summarized below.

$$\iint_{\textit{lit surface}} \left[\begin{matrix} \textit{incident} \\ \textit{wave field} \end{matrix} \right]^2 dA \quad \cong \quad \sum_{i=1}^{\textit{total lit facets}} \left[\begin{matrix} \textit{incident wave field} \\ \textit{at centroid of facet } i \end{matrix} \right]^2 [\textit{area of facet } i] \qquad \text{(G-5)}$$

Numerical experience has shown that equation G-5 gives a stable result when the proper ratio between wavelength and facet size is maintained.

For each scan position, a ray-tracing algorithm was employed to determine the portions of the defect surface that were illuminated by the incoming ultrasonic beam and the strength of illumination on each of the triangular surface facets. Equation G-5 was then used to calculate the overall ultrasonic response of the defect as the sum of contributions from each of the illuminated facets. Finally, the time domain radio frequency (RF) waveform can be obtained via numerical inversion of the Fourier transform. From the RF waveform output, C- or B-scan can then be predicted for a specified scan plan.

This new multifacet void model has been validated in the case of spherical void under plane-wave illumination for which, as was noted previously, an analytic solution known as plane-wave Kirchhoff model is available. Figure G-3 shows the comparison of the on-axis peak amplitude profile between the two models for a 5-mm-diameter spherical void located at various depths and illuminated by a 10-MHz immersion planar transducer with a fixed water path. Overall good agreement has been obtained. It is also observed that the agreement improves as the void depth increases toward the far-field region because the accuracy of the plane-wave Kirchhoff model increases as well.

The performance of the multifacet Kirchhoff model is also quite encouraging when put to a real test on the naturally occurring hard alpha defects. At each scan position, the illuminated facets on the flaw surface model were indexed and their geometrical coordinates were used as the input to drive the multifacet Kirchhoff model calculations. An example of the results was demonstrated in section 3.4 for hard alpha defect B1AW2-X. As was shown in figure 43 of this report, it is evident that the shape and orientation of the experimental C-scan images of B1AW2-X are in good agreement with the geometrical model. The overall performance summary and

error analyses have also been provided in earlier sections. For a comparison of the individual defects of the ten selected hard alpha defects, the reader is referred to appendix E.

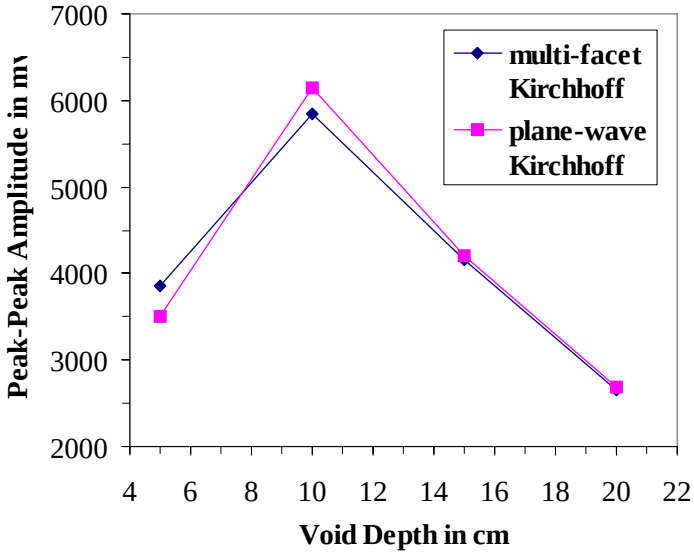


FIGURE G-3. MODEL COMPARISON BETWEEN MULTIFACET KIRCHHOFF MODEL AND PLANE-WAVE KIRCHHOFF MODEL FOR THE ON-AXIS PEAK AMPLITUDES OF A SPHERICAL VOID AT DIFFERENT DEPTHS UNDER PLANE-WAVE ILLUMINATION

G.5 REFERENCES.

G-1. "A Methodology for the Assessment of the Capability of Inspection Systems for Detection of Subsurface Flaws in Engine Components," FAA Report DOT/FAA/AR-01/96, September 2002.

G-2. B.A. Auld, "General Electromechanical Reciprocity Relations Applied to the Calculation of Elastic Wave Scattering Coefficients," Wave Motion, 1, 1979, pp. 3-10.

G-3. R.B. Thompson and T.A. Gray, "A Model Relating Ultrasonic Scattering Measurements Through Liquid-Solid Interfaces to Unbounded Medium Scattering Amplitudes," *Journal of Acoustical Society of America*, 74 (4), 1983, pp. 1279-1290.

G-4. B.P. Newberry, R.B. Thompson, and E.F. Lopez, "Development and Comparison of Beam Models for Two-Media Ultrasonic Inspection," *Review of Progress in Quantitative NDE*, Vol. 6A, D.O. Thompson and D.E. Chimenti, eds., 1987, pp. 639-647.

G-5. J.E. Gubernatis, E. Domany, J.A. Krumhansl, and M. Huberman, "The Born Approximation in the Theory of the Scattering of Elastic Waves by Flaws," *Journal of Applied Physics*, 48 (7), 1977, pp. 2812-2819.

G-6. J.H. Rose and J.M. Richardson, "Time Domain Born Approximation," *Journal of Nondestr. Eval.,* 3 (1), 1982, pp. 45-53.

G-7. L.W. Schmerr, Jr., *Fundamentals of Ultrasonic Nondestructive Evaluation – A Modeling Approach*, Kluwer Academic Publishers, June 1998.

G-8. C.-P. Chiou, F.J. Margetan, R.B. Thompson, and Brian Boyd, "Development of Ultrasonic Model for Hard Alpha Inclusions in Titanium Alloys," *Review of Progress in Quantitative Nondestructive Evaluation*, D.O. Thompson and D.E. Chimenti, eds., Vol. 16B, 1997, p. 1529.

G-9. C.-P. Chiou, F.J. Margetan, and R.B. Thompson, "Modeling of Ultrasonic Signals From Weak Inclusions," *Review of Progress in Quantitative Nondestructive Evaluation*, D.O. Thompson and D.E. Chimenti, eds., Vol. 15A, 1996, pp. 49-55.

G-10. C.F. Ying and R. Truell, "Scattering of a Plane Longitudinal Wave by a Spherical Obstacle in an Isotropically Elastic Solid," *Journal of Applied Physics*, Vol. 27, No. 9, 1956, pp. 1086-1097.

G-11. Y-H. Pao and C.C. Mow, "Scattering of Plane Compressional Waves by a Spherical Obstacle," *Journal of Applied Physics*, Vol. 34, No. 3, 1963, pp. 493-499.